

THESIS / THÈSE

MASTER IN CHEMISTRY RESEARCH FOCUS

Quantum Chemical Study of a Dihydroazulene-Spiropyran Multi-State Multi-Functional Molecular Switch

Deveaux, Noah

Award date:
2024

Awarding institution:
University of Namur

[Link to publication](#)

General rights

Copyright and moral rights for the publications made accessible in the public portal are retained by the authors and/or other copyright owners and it is a condition of accessing publications that users recognise and abide by the legal requirements associated with these rights.

- Users may download and print one copy of any publication from the public portal for the purpose of private study or research.
- You may not further distribute the material or use it for any profit-making activity or commercial gain
- You may freely distribute the URL identifying the publication in the public portal ?

Take down policy

If you believe that this document breaches copyright please contact us providing details, and we will remove access to the work immediately and investigate your claim.



Université de Namur
Faculté des Sciences



Quantum Chemical Study of a Dihydroazulene-Spiropyran

Multi-State Multi-Functional Molecular Switch

Mémoire présenté pour l'obtention du grade académique de Master Chimie "Chimie du Vivant et des Nanomatériaux" : Finalité Approfondie

Noah DEVEAUX

Janvier 2024

UNIVERSITE DE NAMUR**Faculté des Sciences**

Secrétariat du Département de Chimie

Rue de Bruxelles 61 – 5000 NAMUR

Téléphone : +32(0)81 72.54.44 – Téléfax : +32(0)81 72.54.40

E-mail : enseignement.chimie@unamur.be - www.unamur.be/sciences

Quantum Chemical Study of a Dihydroazulene-Spiropyran Multi-State Multi-Functional Molecular Switch

DEVEAUX Noah

Résumé

Les interrupteurs moléculaires sont des systèmes qui peuvent réversiblement commuter entre deux états ou plus sous l'influence de stimuli externes, modifiant ainsi leurs structures géométriques et électroniques, et par conséquent, leurs propriétés moléculaires. Un nouvel interrupteur multi-états et multi-fonctionnel a récemment été proposé, démontrant expérimentalement huit formes différentes. Celui-ci est composé d'une unité photochromique dihydroazulène (DHA) connectée à un spiropyran (SP).

Ce travail explore les aspects multi-fonctionnels de la dyade DHA-SP *via* la chimie quantique, en utilisant la théorie de la fonctionnelle de la densité (dépendante du temps). En complément de la caractérisation expérimentale, les réponses optiques non linéaires du deuxième ordre sont introduites comme un nouvel "output" du point de vue de la logique moléculaire, afin d'étendre la nature multi-fonctionnelle de cette dyade. Les calculs démontrent que les propriétés, plus spécifiquement les réponses de génération de seconde harmonique (SHG), sont de bons "outputs" vu leurs contrastes entre les différentes formes de la dyade. Les calculs révèlent également que (i) commuter une unité n'a qu'un impact négligeable sur les paramètres géométriques de l'autre, et que (ii) les spectres d'absorption UV/visible sont, en bonne approximation, une superposition de ceux des unités parentes. Cependant, cette additivité n'est pas systématiquement observée pour les réponses SHG, et ces propriétés présentent des comportements intrigants par rapport aux caractéristiques géométriques et aux énergies d'excitation. Ce mémoire montre aussi comment l'utilisation des méthodes de chimie quantique permet de rationaliser ces résultats en prenant en compte l'orientation des réponses, dévoilée grâce à la représentation en sphère unitaire. Une compréhension plus approfondie est ensuite obtenue grâce au modèle à quelques états et à l'analyse des états manquants, identifiant les états excités clés pour les réponses SHG.

Mémoire de Master en Sciences Chimiques à Finalité Approfondie.

Janvier 2024

Promoteur: B. CHAMPAGNE

UNIVERSITY OF NAMUR**Faculty of Sciences**

Chemistry Department Secretariat

Rue de Bruxelles 61 – 5000 NAMUR

Phone: +32(0)81 72.54.44 - Fax: +32(0)81 72.54.40

E-mail : enseignement.chimie@unamur.be - www.unamur.be/sciences

Quantum Chemical Study of a Dihydroazulene-Spiropyran Multi-State Multi-Functional Molecular Switch

DEVEAUX Noah

Summary

Molecular switches are a class of molecular systems that can reversibly interconvert between two or more different states upon external stimuli, giving rise to changes in their geometrical and electronic structures and, therefore, to modifications of their molecular properties. Recently, a new multi-state multi-functional switch was proposed, which has been experimentally demonstrated to display eight different states. It combines a dihydroazulene (DHA) photochromic unit with a spiropyran (SP), connected through a linker.

This work consists in a quantum chemical study of the multi-functional properties of the DHA-SP dyad, by employing (time-dependent) density functional theory. With respect to the experimental characterizations, the second-order nonlinear optical (NLO) responses are introduced as a novel output signal from the viewpoint of molecular logic, with the aim of extending the multi-functional nature of this dyad. The calculations demonstrate that these properties, more precisely, the second harmonic generation (SHG) responses, are good outputs owing to their contrasts between the different forms of the dyad. The calculations also highlight that (i) switching either unit has only a negligible impact on the geometrical parameters of the other one, and that (ii) UV/vis absorption spectra are, in good approximation, a superposition of those from the parent units. However, this additivity trend is not consistently observed for the SHG responses, and these properties present intriguing behaviors in comparison to the geometrical features and the excitation energies. This Master thesis shows how these SHG results are rationalized by considering the oriented character of the responses, which is unraveled thanks to the unit sphere representations. Then, a deeper understanding is grasped by resorting to the few-state approximation and the missing state analysis. The latter pinpoints the key excited states of the SHG responses.

Master thesis in Chemical Sciences focused on Research.

January 2024

Supervisor: B. CHAMPAGNE

Remerciements

Je tiens à remercier tous ceux qui, de près ou de loin, ont contribué au bon déroulement de ce travail. Je voudrais tout d’abord exprimer ma gratitude envers mon promoteur, le Professeur Benoît Champagne, pour son accueil au sein de son laboratoire et sa guidance tout au long de mon mémoire. Je souhaite également le remercier pour l’opportunité qu’il m’a offerte d’aller présenter et discuter mes résultats à l’université de Bordeaux. Par la même occasion, je remercie Frédéric Castet pour les précieux conseils.

Ensuite, je me dois d’exprimer une reconnaissance immense à Pierre, sans qui l’obtention de ces résultats n’aurait jamais été possible. Je tiens également à souligner son implication et son dévouement dans l’implémentation des codes Python essentiels à la réalisation de ce travail. En résumé, merci pour tout le temps que tu as pu me consacrer, toujours dans la bonne humeur.

Ce mémoire a été très plaisant, notamment grâce à l’ambiance conviviale qui règne dans le laboratoire. Je remercie donc tous les membres du LCT pour les discussions (plus ou moins scientifiques), avec une attention particulière pour Charlotte et Tarcus qui m’ont également beaucoup aidé dans mon travail, et qui ont répondu à toutes les questions, plus ou moins bêtes, que j’ai pu poser. Différentes figures présentes dans ce travail ont pu voir le jour grâce à Vincent qui, à plusieurs reprises, a spécifiquement implémenté de nouvelles fonctionnalités dans la suite DrawMol.

Bien qu’ils n’aient probablement pas une idée précise de ce que j’ai fait pendant un an, je suis également reconnaissant envers ma famille et surtout mes parents pour leur soutien.

Enfin, un grand merci à Juliette, la petite surprise de ces années d’étude, pour son soutien et les moments passés ensemble. Merci de m’avoir fait sortir, ne serait-ce qu’un peu, de mes livres de chimie, et d’avoir écouté mes râleries à maintes reprises.

Les calculs ont été effectués sur les ressources informatiques fournies par le Consortium des Équipements de Calcul Intensif (CÉCI), et en particulier celles de la Plate-forme Technologique

de Calcul à Haute Performance (PTCI).

Grâce à toutes ces personnes, et les nombreuses autres que j'ai omises, ces 11 mois consacrés à mon mémoire ont représenté les moments les plus enrichissants de mon parcours académique. Cette expérience m'a enfin offert l'opportunité d'associer travail et passion, élargissant ainsi mes connaissances tout en unifiant ce que j'ai pu apprendre au cours de mes années d'études.

List of acronyms

NLO Nonlinear optics/optical

CT Charge transfer

ES Excited state

DHA Dihydroazulene

SP Spiropyran

VHF Vinylheptafulvene

OR Optical rectification

SHG Second harmonic generation

SFG Sum-frequency generation

DFG Difference-frequency generation

EFISHG Electric-field-induced second harmonic generation

HRS Hyper-Rayleigh scattering

SHS Second harmonic scattering

DR Depolarization ratio

QC Quantum chemistry

HF Hartree-Fock

LCAO Linear Combination of Atomic Orbitals

MO Molecular orbital

AO Atomic Orbital

GTO Gaussian-Type Orbital

ECP Effective core potential

BSSE Basis set superposition error

NBO Natural bond orbital

NHO Natural hybrid orbital

NAO Natural atomic orbital

OWSO Occupancy-weighted symmetric orthogonalization

NPA Natural population analysis

LEP Lone electron pair

LSO Löwdin symmetric orthogonalization

GS Ground state

CI Configuration interaction

CSF Configuration state function

FCI Full configuration interaction

DFT Density functional theory

LDA Local density approximation

GGA Generalized gradient approximation

HK Hohenberg and Kohn

KS Kohn-Sham

SCF Self-consistent field

XCF Exchange-correlation functional

PT Perturbation theory

RG Runge and Gross

RD Time-dependent

TDDFT Time-dependent density functional theory

PCM Polarizable continuum model

IEF Integral equation formalism

ASC apparent surface charges

MB Maxwell-Boltzmann

SMD Solvation Model Density

FWHM Full width at half-maximum

USR Unit sphere representation

OWB Orr-Ward-Bishop

SOS Summation over excited states

BLA Bond length alternation

ICT Intramolecular charge transfer

Contents

I	Introduction, objectives and methods	1
1	Introduction and objectives	3
1.1	Molecular switches	4
1.2	NLO switches	6
1.3	System of interest	7
1.4	Objectives	11
2	Elements of nonlinear optics	17
2.1	Second harmonic generation	18
2.2	Hyper-Rayleigh Scattering - principles	21
2.3	Notes on isotropic rotational averages	23
2.4	HRS isotropic rotational averages	25
2.5	Analysis of $\langle\beta_{HRS}^2\rangle$	27
3	Quantum chemistry methods	33
3.1	The Schrödinger equation and the wavefunction - general aspects	34
3.2	The antisymmetry of the wavefunction and Slater determinants	38
3.3	Electron correlation	45
3.4	Density functional theory	47
3.5	Exchange-correlation functionals	55
3.6	Molecular properties	58
3.7	Analysis of the excited states and of their electronic distributions	65
3.8	Effects of the surrounding	67

II	Strategies, results, conclusions and perspectives	77
4	Strategies and computational details	79
4.1	General strategies	80
4.2	Interpretation of the NLO responses	83
5	Results and discussions	91
5.1	Structural properties	92
5.2	Thermodynamical analysis	99
5.3	UV/vis absorption spectra and related properties	104
5.4	Nonlinear optical properties	112
6	Conclusions and outlooks	129
III	Appendices	135
A	Supporting information to Chapter 4	137
B	Supporting information to Section 5.1	141
B.1	Conformational search	141
B.2	Geometry optimizations	149
C	Supporting information to Section 5.2	153
D	Supporting information to Section 5.3	155
E	Supporting information to Section 5.4	169
E.1	HRS quantities	169
E.2	Few-state approximation	178

Part I

Introduction, objectives and methods

Chapter 1

Introduction and objectives

1.1 Molecular switches

Molecular switches are a class of molecular systems that can reversibly interconvert between two or more different states upon the application of external stimuli, giving rise to changes in their geometrical and electronic structures and, therefore, to modifications of their molecular properties.¹ These transformations result in chromism phenomena, the most common one being the photochromism. This opens the use of molecular switches in various applications, *e.g.* in electronic devices,^{2–4} in drug delivery,⁵ for the control of biological functions,^{6–8} as molecular machines and motors when switching involves large nuclear motions,^{9–11} as sensors,¹² and in data storage.^{1,13} Molecular switches are also involved in the process of vision. For instance, when reading this sentence, the retinoid encompasses numerous *cis-trans* photoisomerizations.¹⁴ Among photochromic systems, azobenzenes,^{15,16} dithienylethenes,¹⁷ dihydroazulenes,^{18–20} and spiro-compounds (spiropyrans, spiroxazines)^{21–23} have received much attention over the years. Other chromism phenomena involve halo- or acido-chromism, thermochromism, electrochromism, and piezochromism.

For the purpose of memory devices, for which destructive reading should be prevented, a general strategy involves integrating more than one switching unit addressed by means of at least two different stimuli (multi-functional).^{24,25} So, in the case of the dual-mode stimulation, compounds having the ability to exist in more than two states (multi-state) can be switched by means of two distinct stimuli.¹

From the viewpoint of molecular logic,²⁶ bistable systems perform *YES/NOT* functions while multi-state/multi-functional systems are basic units for the *AND*, *OR*, exclusive *OR* (*XOR*), and *XNOR* logic operations. Indeed, to reach higher-level operations at the single molecule level, the assembly of several multi-state systems from one or several families, covalently linked, should be considered. In molecular logic, the molecule generally constitutes the substrate (or the logic device) even though, in an alternative view, the constitutive units could also be seen as connected inputs (chromophore functional groups), which communicate through a linker. Since a molecule is a specific entity, its presence or its absence can be associated with a bit of information. In this context, the stimuli are generally referred to as the inputs. These concepts broaden beyond photons, as myriads of inputs of different natures exist, such as a variation of the pH or of the redox potential, an addition of ions or ligands, electric currents, heat, pressure, and even a combination of different stimuli.^{1,27,28}

Furthermore, the access to one or several specific forms of a molecular switch can be or-

thogonal or path-dependent.²⁹ To illustrate these concepts, a hypothetical system comprising two bistable switching units addressable by two distinct inputs is considered. The different switching schemes are summarized in Fig. 1.1, using a binary code representation of the four switching states of the system, namely [00], [01], [10], and [11]. On the one hand, in the case of non-orthogonal switching (Fig. 1.1a), the first input switches one unit, while leaving the state of the second unit not affected ([00] \rightarrow [01]). Subsequent application of the second input results in the [11] state, which can originate from both [00] and [01]. Consequently, the [10] switching state remains inaccessible. On the other hand, in the case of an orthogonal switching path (Fig. 1.1b), each input exclusively affects one unit, rendering all four states accessible. Finally, path-dependency (Fig. 1.1c) enables each state to be addressed specifically, but the [11] state can only be reached from one specific sequence of inputs.

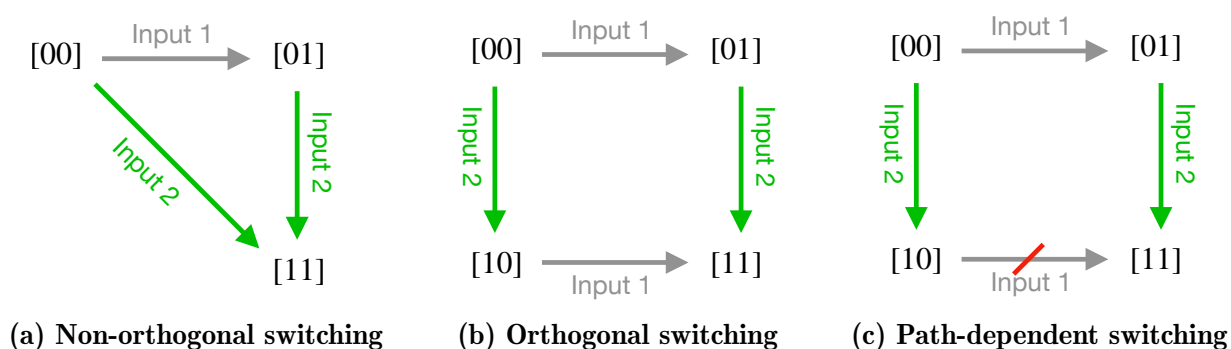


Fig. 1.1: Stimuli-dependent switching processes in a system composed by two switching units (adapted from Ref. 29).

In addition to the triggering of switching transitions, which corresponds to writing or erasing information, the use of (photo)chemical inputs is extended to the reading of information, *i.e.* to probe the state of the system. The resulting outputs can be gathered through a range of techniques, frequently involving spectroscopic experiments.²⁶ In single input-single output devices, linear optical responses (*e.g.* UV/vis absorbance, fluorescence lifetime or intensity, and the signal ellipticity in electronic circular dichroism) are among the most useful readouts for fast and relatively inexpensive analyses. Taking a step further, nonlinear optical (NLO) responses can also be considered as outputs, and become particularly advantageous in scenarios where inputs in the UV/visible region of the electromagnetic spectra trigger switching reactions. This attribution leads to the designation of the device as a NLO molecular switch (*vide infra*).^{30–32} In all cases, large contrasts of molecular responses between the forms of a molecular switch must be achieved for an output to be adequate to characterize the different states of a molecular system.

1.2 NLO switches

NLO molecular switches present a change of their nonlinear responses when triggered by stimuli. NLO effects appear when the relation between the total dipole moment and the amplitude of the irradiating field is no longer linear, which occurs when using intense light irradiations, typically with lasers (Fig. 1.2).³³ At the molecular level, these polarization effects are described using a Taylor expansion of the dipole moment as a function of the external field (here, electric field only), \mathbf{E} ,

$$\mu(\mathbf{E}) = \mu_0 + \alpha\mathbf{E} + \frac{1}{2}\beta\mathbf{E}^2 + \dots, \quad (1.1)$$

where μ_0 is the permanent dipole moment, α is the polarizability, and β is the first hyperpolarizability. The latter quantity and its measurement in bulks are the main objects of Chapter 2.

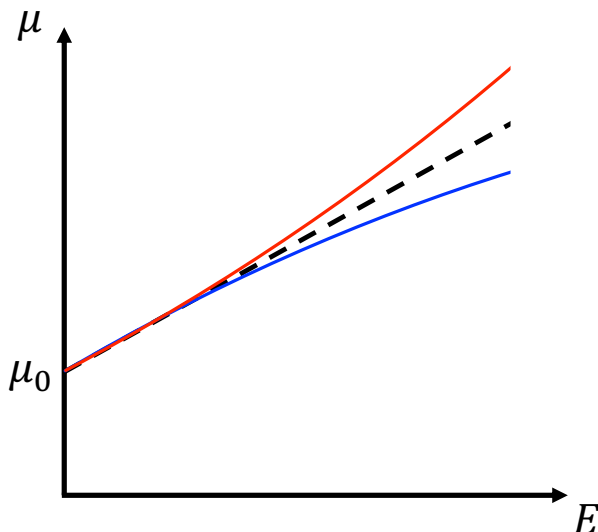


Fig. 1.2: Schematic evolution of the amplitude of the total dipole moment as a function of the amplitude of the incident electric field. The dashed line corresponds to the linear regime while the red and blue curves represent the nonlinear deviations associated with positive and negative β values.

A large variety of compounds exhibit a β response. Those that achieve large β values are usually push-pull systems, composed by (i) an electron donor group (D), (ii) an electron acceptor group (A), and (iii) a π -conjugated segment that links the donor to the acceptor.³⁰ Such dipolar one-dimensional molecules are often characterized by a low-energy charge transfer (CT) excited state (ES) dominating the linear optical properties. In good approximation, their β response can be described by a two-state model:³⁴

$$\beta \propto \frac{f_{0n}\Delta\mu_{0n}}{\Delta E_{0n}^3}. \quad (1.2)$$

Consequently, large β responses require (i) a small excitation energy between the ground state and this CT excited state (ΔE_{0n}), (ii) a large oscillator strength (f_{0n}), and (iii) a large variation of dipole moment between these electronic states ($\Delta\mu_{0n}$).

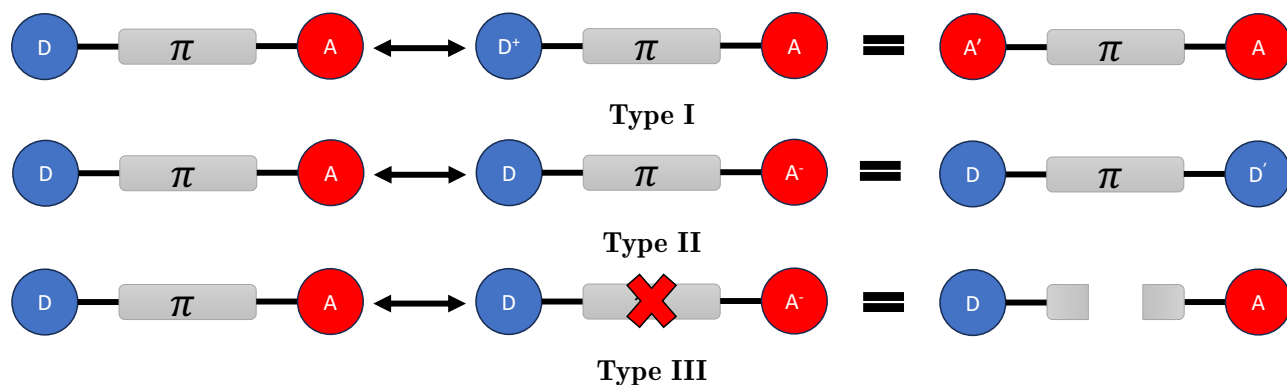
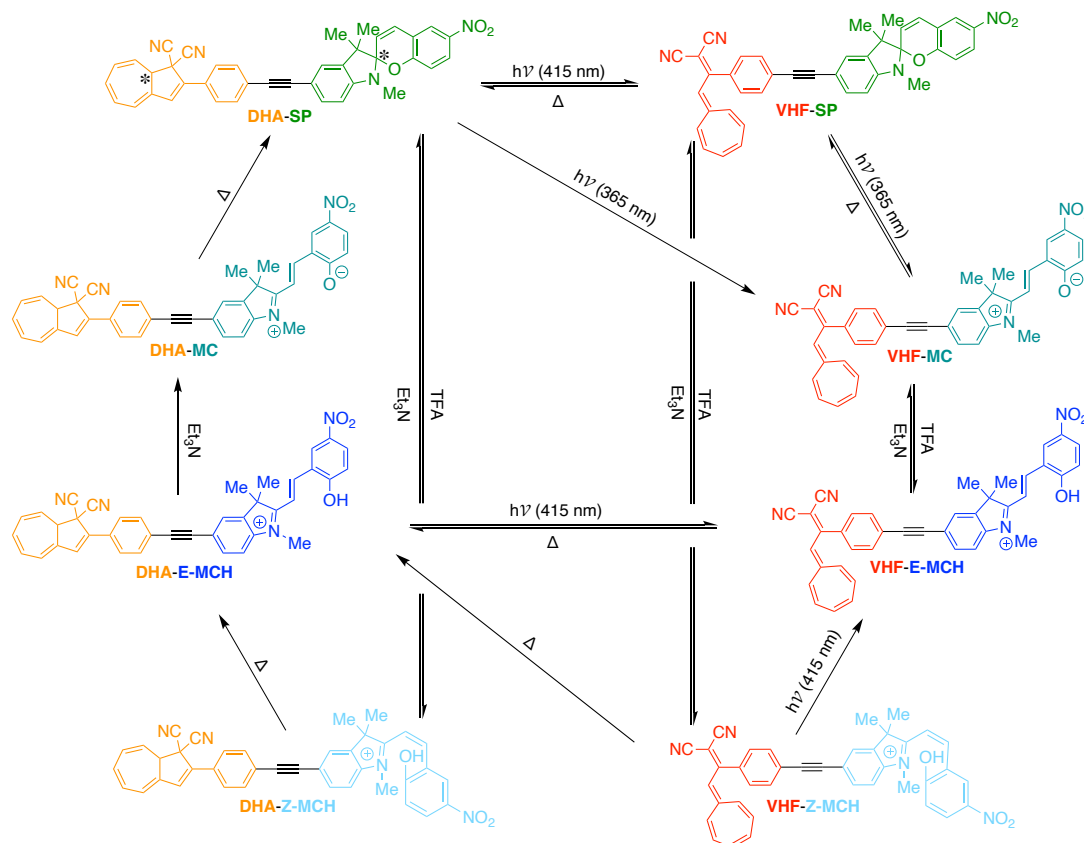


Fig. 1.3: Schematic representation of the D- π -A molecular patterns to obtain efficient NLO switches (adapted from Ref. 30).

When this concept of D- π -A NLO material is applied to simple bistable molecular switches, different strategies arise to modulate the β responses, in order to observe high contrasts between the forms of the switches. This leads to three main types of switching behaviors, based on three manners to alter the electronic structures of the functional units upon switching (Fig. 1.3). Types I and II molecular switches typically rely on acidochromism or redox control, while types III are based on structural changes that interrupt the π -conjugation between the donor and acceptor moieties.³⁰ In addition, in an efficient switch, the two forms must be stable, and have a sufficiently large activation barrier. Afterwards, an extension of these NLO switches consists in the combination of two or more D-A units, addressed by a multi-modal stimulation.

1.3 System of interest

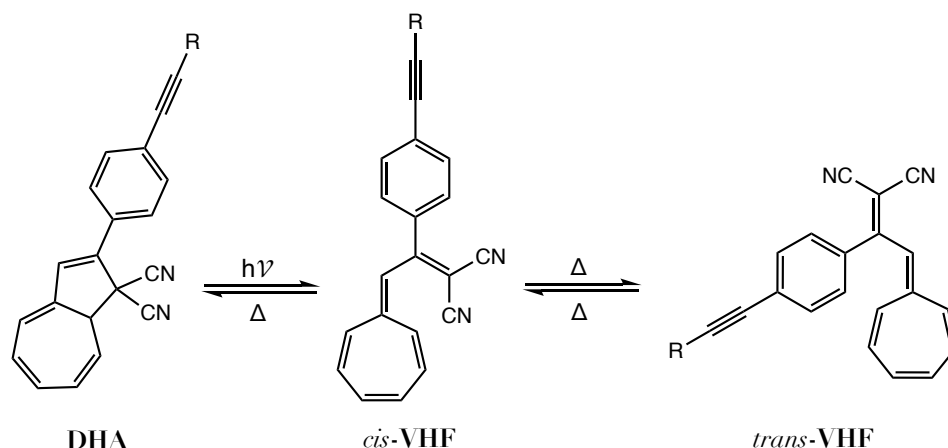
In this work, one of these multi-state multi-functional switches is studied. It consists of the combination of the 2-phenyl-1,1-dicyano-1,8a-dihydroazulene (DHA) T-type photochromic bistable unit with the photochromic multi-state 1',3',3'-trimethyl-6-nitroindolinobenzospiropyran (SP) moiety. Scheme 1.1 presents the switching behavior of this DHA-SP dyad, which, experimentally, has been demonstrated by Dowds *et al.*²⁹ to display eight different states (ignoring stereoisomers). They also reported the synthesis and experimental characterizations of the linear optical properties of this dyad in its different states. In their work, the inputs are monochromatic light irradiations and pH variations while the outputs (or readouts) are light



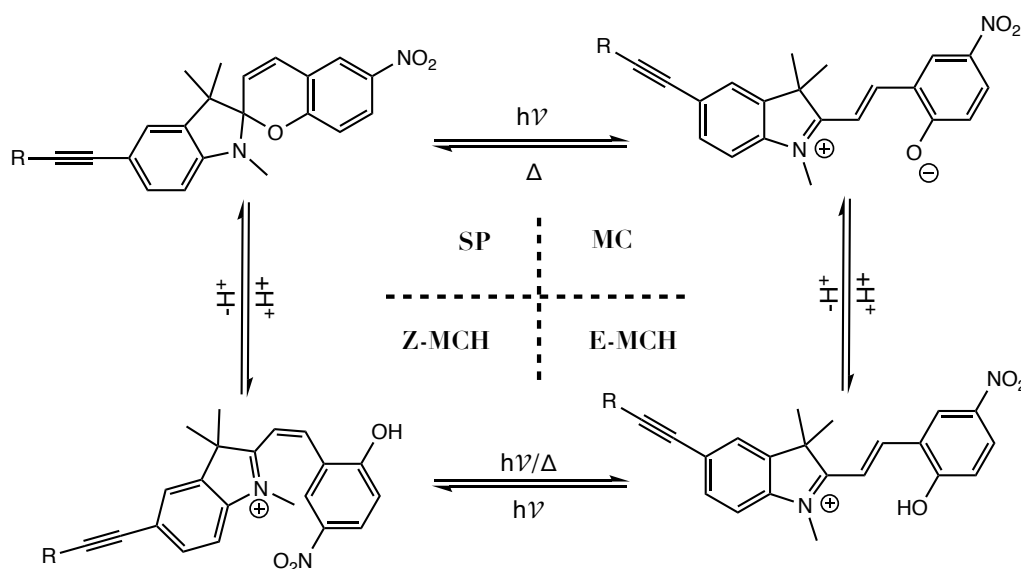
Scheme 1.1: Overview of the switching reactions of the DHA-SP dyad (adapted from Ref. 29), TFA: trifluoroacetic acid, '*' refers to the chiral centers of the DHA-SP form.

absorption and fluorescence. They found that photo-excitation at 415 nm causes the inter-conversion from the stable DHA isomer to the corresponding higher-energy vinylheptafulvene (VHF) isomer.^{35,36} The reverse reaction is spontaneous and thermally induced. In individual DHA, upon light absorption, this moiety is excited from the electronic ground state to the first (lowest-energy) singlet excited state (S_1). The excited molecule undergoes a ring-opening, leading to the metastable *cis*-VHF isomer (Scheme 1.2) through a conical intersection.^{18,19} This metastable *cis*-form either recaptures the DHA, or thermally isomerizes to the *trans*-VHF.

Then, upon a light-triggered (365 nm) cleavage of the $C-O$ bond, SP of VHF-SP undergoes a ring opening to form a zwitterionic colored merocyanine (VHF-MC).³⁷⁻⁴¹ VHF-MC reacts back to VHF-SP via thermal relaxation (Scheme 1.3). Moreover, the DHA and SP units of DHA-SP can simultaneously switch to the VHF-MC form, in a non-orthogonal way when irradiated at 365 nm, without passing through the VHF-SP state. Unsubstituted spiropyrans generally switch to the corresponding merocyanines following a singlet manifold pathway, which involves a conical intersection between the S_1 potential energy surface of SP and one excited state of the cisoid form of the merocyanine, often referred to as the "X" species (see Ref. 42 for an extensive



Scheme 1.2: Photo and thermochromic isomerization of the dihydroazulene (DHA)/vinylheptafulvene (VHF) moiety.



Scheme 1.3: General switching equilibria of spiropyran (SP)/merocyanine (MC)/protonated Z merocyanine (Z-MCH)/protonated E-merocyanine (E-MCH).

review). Relaxation from the latter leads to both the stable transoid merocyanine (MC) and thermally unstable cisoid form of the merocyanine (CCC in Fig. 1.4), which falls back to the ground state of SP. In the case of nitro-substituted spiropyrans, the ring-opening often implies a triplet manifold pathway, where intersystem crossing of S_1 and T_1 of SP increases the quantum efficiency of the switching process.⁴²

Protonation of MC in its photo-metastable state yields a protonated transoid merocyanine (E-MCH). The VHF-SP, VHF-MC and VHF-E-MCH trio of states can then act as an *AND* logic gate: going from VHF-SP to the fluorescence emitting VHF-E-MCH form necessitates (i) irradiation by light at 365 nm *AND* (ii) the addition of acid. If one condition is not satisfied, the emission readout can not be observed. Finally, the addition of acid on SP (for both

DHA and VHF forms) gives directly the protonated cisoid merocyanine (in the 'Z' configuration), Z-MCH.^{42,43} Hence, the switching processes encompassing the eight states integrate both orthogonality and path-dependency concepts.²⁹

Remarkably, for the merocyanines, time resolved studies and theoretical calculations have highlighted eight stable conformations (Fig. 1.4).^{44–46} The energetically most stable zwitterionic merocyanine is the TTC conformer, followed by the TTT form. It is also known that the cisoid forms (*i.e.*, CCT, TCT, CCC, and TCC) are only stable in their protonated state, Z-MCH.

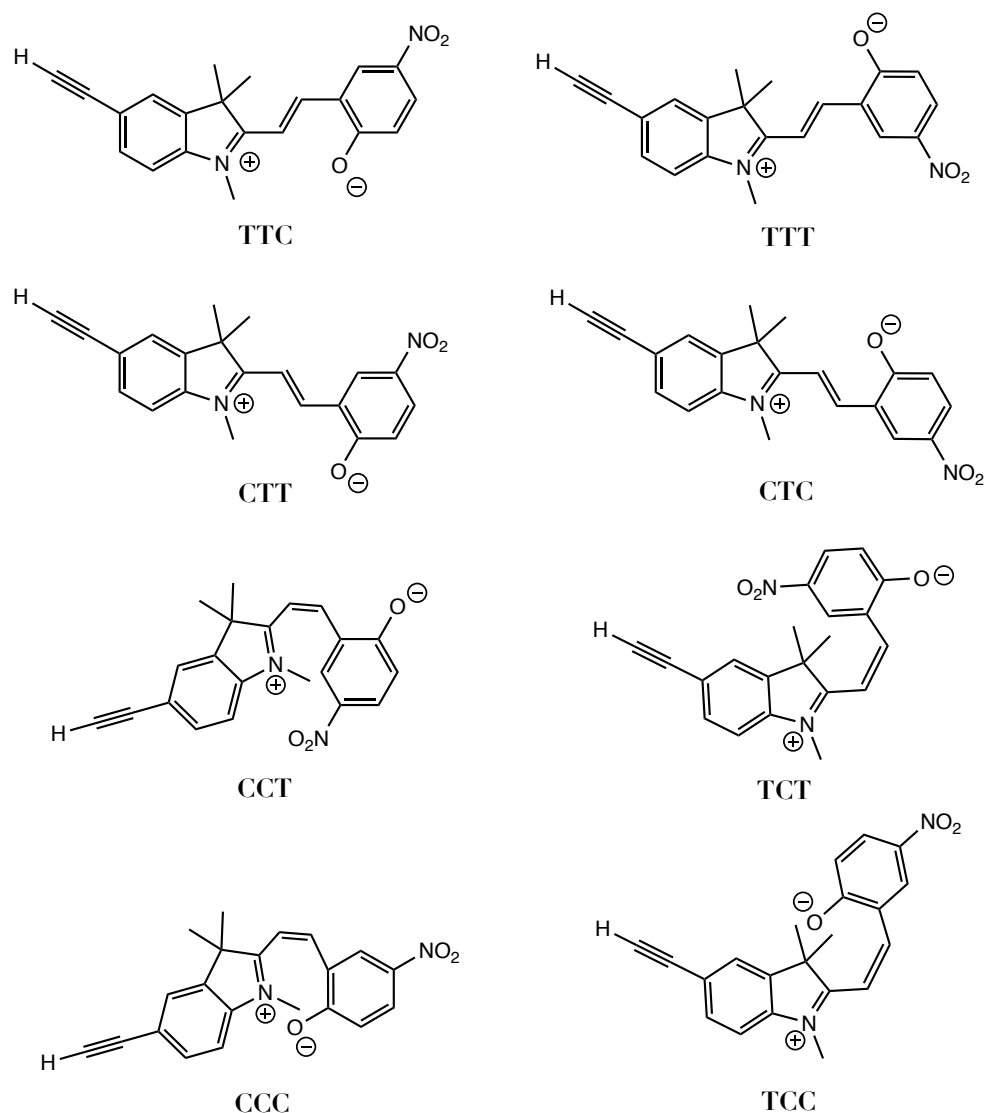


Fig. 1.4: Molecular structures of the eight possible isomers of the merocyanine constitutive unit. Note that the forms with a *cis* central alkene are always protonated in our dyad of interest, which corresponds to the Z-MCH states.

1.4 Objectives

This Master thesis consists in a quantum chemical study of the multi-functional aspects of the DHA-SP molecular dyad. With respect to the experimental characterizations of Dowds and coworkers,²⁹ the second-order nonlinear optical (NLO) responses are introduced as a novel output signal from the viewpoint of molecular logic, with the aim of extending the multi-functional nature of this dyad. The subsequent objective of this work is to understand how the DHA/VHF and the SP/MC units influence each other linear and nonlinear optical properties. This thesis is divided in three main Parts, and it is structured as follows. The first Part, which includes this Chapter sets a general, as well as a theoretical context, and browses the interest to study such dyads as NLO switches. Chapter 2 exposes the theoretical aspects associated with the first hyperpolarizability of molecules in solution, and its measurement by Hyper-Rayleigh scattering. Then, Chapter 3 introduces the quantum chemistry methods employed in this work.

With all the required theoretical background in the hands of the reader, Part II enters the practical viewpoint of the work, starting with the presentation of the strategies and of the detailed computational approach followed to tackle the multi-functional properties of the targeted system (Chapter 4). The results are then exposed in Chapter 5, beginning with a geometrical analysis of the structures in the ground state, and their thermodynamical features. This analysis is followed by an exploration of the mutual influence of the two switching units on the UV/vis absorption properties and the related charge transfer characteristics, completed by calculations on their constitutive units (with the alkyne linker). Then, the Hyper-Rayleigh scattering responses are presented and discussed. Their adequacy as an efficient output between the different forms of the DHA-SP dyad is scrutinized. Subsequently, the NLO properties of this molecular switch are rationalized by considering their oriented character, and the contribution of specific electronic excited states. Finally, conclusions are drawn and several perspectives are proposed.

Part III collects the appendices from the different Chapters and Sections.

Bibliography

- [1] Feringa, B. L., Brown, W. R., Eds. *Molecular Switches*; Wiley-VCH, Weinheim, Germany, 2011.
- [2] Kudernac, T.; Katsonis, N.; Browne, W. R.; Feringa, B. L. Nano-Electronic Switches: Light-Induced Switching of the Conductance of Molecular Systems. *J. Mater. Chem.* **2009**, *19*, 7168–7177.
- [3] Browne, W. R.; Feringa, B. L. Light Switching of Molecules on Surfaces. *Annu. Rev. Phys. Chem.* **2009**, *60*, 407–428.
- [4] Huang, X.; Li, T. Recent Progress in the Development of Molecular-Scale Electronics Based on Photoswitchable Molecules. *J. Mater. Chem. C* **2020**, *8*, 821–848.
- [5] Fitzmaurice, O.; Bartkowski, M.; Giordani, S. Molecular Switches-Tools for Imparting Control in Drug Delivery Systems. *Front. Chem.* **2022**, *10*, 859450.
- [6] Folgering, J. H.; Kuiper, J. M.; Vies, A. H. D.; Engberts, J. B.; Poolman, B. Lipid-Mediated Light Activation of a Mechanosensitive Channel of Large Conductance. *Langmuir* **2004**, *20*, 6985–6987.
- [7] Koçer, A.; Walko, M.; Meijberg, W.; Feringa, B. L. Chemistry: A Light-Actuated Nanovalve Derived from a Channel Protein. *Science* **2005**, *309*, 755–758.
- [8] Volgraf, M.; Gorostiza, P.; Numano, R.; Kramer, R. H.; Isacoff, E. Y.; Trauner, D. Allosteric Control of an Ionotropic Glutamate Receptor with an Optical Switch. *Nat. Chem. Biol.* **2006**, *2*, 47–52.
- [9] Harris, J. D.; Moran, M. J.; Aprahamian, I. New Molecular Switch Architectures. *Proc. Natl. Acad. Sci. U.S.A.* **2018**, *115*, 9414–9422.
- [10] Tierney, H. L.; Murphy, C. J.; Jewell, A. D.; Baber, A. E.; Iski, E. V.; Khodaverdian, H. Y.; McGuire, A. F.; Klebanov, N.; Sykes, E. C. H. Experimental Demonstration of a Single-Molecule Electric Motor. *Nat. Nanotechnol.* **2011**, *6*, 625–629.
- [11] Kudernac, T.; Ruangsupapichat, N.; Parschau, M.; Maciá, B.; Katsonis, N.; Harutyunyan, S. R.; Ernst, K. H.; Feringa, B. L. Electrically Driven Directional Motion of a Four-Wheeled Molecule on a Metal Surface. *Nature* **2011**, *479*, 208–211.
- [12] Plaxco, K. W.; Soh, H. T. Switch-Based Biosensors: a New Approach Towards Real-Time, In Vivo Molecular Detection. *Trends Biotechnol.* **2011**, *29*, 1–5.

- [13] Mishra, A.; Betal, A.; Pal, N.; Kumar, R.; Lama, P.; Sahu, S.; Metre, R. K. Molecular Memory Switching Device Based on a Tetranuclear Organotin Sulfide Cage $[(RS_n^{IV})_4(\mu - S)_6] \bullet 2CHCl_3 \bullet 4H_2O$ ($R = 2$ -(Phenylazo)phenyl): Synthesis, Structure, DFT Studies, and Memristive Behavior. *ACS Appl. Electron. Mater.* **2020**, *2*, 220–229.
- [14] Kiser, P. D.; Golczak, M.; Palczewski, K. Chemistry of the Retinoid (Visual) Cycle. *Chem. Rev.* **2014**, *114*, 194–232.
- [15] Jerca, F. A.; Hoogenboom, R. Advances and Opportunities in the Exciting World of Azobenzenes. *Nat. Rev. Chem.* **2022**, *6*, 51–59.
- [16] Bandara, H. M. D.; Burdette, S. C. Photoisomerization in Different Classes of Azobenzene. *Chem. Soc. Rev.* **2012**, *41*, 1809–1825.
- [17] Irie, M.; Fukaminato, T.; Matsuda, K.; Kobatake, S. Photochromism of Diarylethene Molecules and Crystals: Memories, Switches, and Actuators. *Chem. Rev.* **2014**, *114*, 12174–12277.
- [18] Abedi, M.; Pápai, M.; Mikkelsen, K. V.; Henriksen, N. E.; Møller, K. B. Mechanism of Photoinduced Dihydroazulene Ring-Opening Reaction. *J. Phys. Chem. Lett.* **2019**, *10*, 3944–3949.
- [19] Shostak, S.; Park, W.; Oh, J.; Kim, J.; Lee, S.; Nam, H.; Filatov, M.; Kim, D.; Choi, C. H. Ultrafast Excited State Aromatization in Dihydroazulene. *J. Am. Chem. Soc.* **2023**, *145*, 1638–1648.
- [20] Bayach, I.; Al-Faiyz, Y. S. S.; Alkhalifah, M. A.; Almutlaq, N.; Ayub, K.; Sheikh, N. S. Phototunable Absorption and Nonlinear Optical Properties of Thermally Stable Dihydroazulene-Vinylheptafulvene Photochrome Pair. *ACS Omega* **2022**, *7*, 35863–35874.
- [21] Antipin, S.; Petrukhin, A.; Gostev, F.; Marevtsev, V.; Titov, A.; Barachevsky, V.; Strokach, Y.; Sarkisov, O. Femtosecond Transient Absorption Spectroscopy of Non-Substituted Photochromic Spirocompounds. *Chem. Phys. Lett.* **2000**, *331*, 378–386.
- [22] Berkovic, G.; Krongauz, V.; Weis, V. Spiropyran and Spirooxazines for Memories and Switches. *Chem. Rev.* **2000**, *100*, 1741–1753.
- [23] Gómez, I.; Reguero, M.; Robb, M. A. Efficient Photochemical Merocyanine-to-Spiropyran Ring Closure Mechanism through an Extended Conical Intersection Seam. A Model CASSCF/CASPT2 Study. *J. Phys. Chem. A* **2006**, *110*, 3986–3991.

- [24] Uchidal, M.; Irie, M. Two-Photon Photochromism of a Naphthopyran Derivative. *J. Am. Chem. Soc.* **1993**, *115*, 6442–6443.
- [25] Wang, Z. Y.; Todd, E. K.; Meng, X. S.; Gao, J. P. Dual Modulation of a Molecular Switch with Exceptional Chiroptical Properties. *J. Am. Chem. Soc.* **2005**, *127*, 11552–11553.
- [26] de Silva, A. P. *Molecular Logic-Based Computation*, 1st ed.; RSC Publishing, Cambridge, UK, 2013.
- [27] Otsuki, J.; Akasaka, T.; Araki, K. Molecular Switches for Electron and Energy Transfer Processes Based on Metal Complexes. *Coord. Chem. Rev.* **2008**, *252*, 32–56.
- [28] Zhang, J. L.; Zhong, J. Q.; Lin, J. D.; Hu, W. P.; Wu, K.; Xu, G. Q.; Weeb, A. T. S.; Chen, W. Towards Single Molecule Switches. *Chem. Soc. Rev.* **2015**, *44*, 2998–3022.
- [29] Dowds, M.; Stenspil, S. G.; de Souza, J. H.; Laursen, B. W.; Cacciarini, M.; Nielsen, M. B. Orthogonal- and Path-Dependent Photo/Acidswitching in an Eight-State Dihydroazulene-Spiropyran Dyad. *ChemPhotoChem* **2022**, *6*, e202200152.
- [30] Coe, B. J. Molecular Materials Possessing Switchable Quadratic Nonlinear Optical Properties. *Chem. Eur. J.* **1999**, *5*, 2464–2471.
- [31] Delaire, J. A.; Nakatani, K. Linear and Nonlinear Optical Properties of Photochromic Molecules and Materials. *Chem. Rev.* **2000**, *100*, 1817–1845.
- [32] Castet, F.; Rodriguez, V.; Pozzo, J.-L.; Ducasse, L.; Plaquet, A.; Champagne, B. Design and Characterization of Molecular Nonlinear Optical Switches. *Acc. Chem. Res.* **2013**, *46*, 2656–2665.
- [33] Verbiest, T.; Clays, K.; Rodriguez, V. *Second-Order Nonlinear Optical Characterization Techniques*; CRC Press, New York, 2009.
- [34] Oudar, J. L.; Chemla, D. S. Hyperpolarizabilities of the Nitroanilines and their Relations to the Excited State Dipole Moment. *J. Chem. Phys.* **1977**, *66*, 2664–2668.
- [35] Daub, J.; Knöchel, T.; Mannschreck, A. Photosensitive Dihydroazulenes with Chromogenic Properties. *Angew. Chem. Int. Ed. Engl.* **1984**, *23*, 960–961.
- [36] Cardenuto, M. H.; Cezar, H. M.; Mikkelsen, K. V.; Sauer, S. P.; Coutinho, K.; Canuto, S. A QM/MM Study of the Conformation Stability and Electronic Structure of the Photochromic Switches Derivatives of DHA/VHF in Acetonitrile Solution. *Spectrochim. Acta A: Mol. Biomol. Spectrosc.* **2021**, *251*, 119434.
- [37] Heiligman-Rim, R.; Hirshberg, Y.; Fischer, E. Photochromism in Spiropyrans. Part IV.

- Evidence for the Existence of Several Forms of the Colored Modification. *J. Phys. Chem.* **1962**, *66*, 2465–2470.
- [38] Bercovici, T.; Heiligman-Rim, R.; Fischer, E. Photochromism in Spiropyran, VI. Trimethylindolinobenzospiropyran and its Derivatives. *Mol. Photochem.* **1969**, *1*, 23–25.
- [39] Lenoble, C.; Becker, R. S. Photophysics, Photochemistry, Kinetics, and Mechanism of the Photochromism of 6'-Nitroindolinospiropyran. *J. Phys. Chem.* **1986**, *90*, 62–65.
- [40] Celani, P.; Bernardi, F.; Olivucci, M.; Robb, M. A. Conical Intersection Mechanism for Photochemical Ring Opening in Benzospiropyran Compounds. *J. Am. Chem. Soc.* **1997**, *119*, 10815–10820.
- [41] Maurel, F.; Aubard, J.; Rajzmann, M.; Guglielmetti, R.; Samat, A. A Quantum Chemical Study of the Ground State Ring Opening/Closing of Photochromic 1,3,3-Trimethylspiro[Indoline-2,3'-Naphtho[2,1-b][1,4]Oxazine]. *J. Chem. Soc., Perkin Trans. 2* **2002**, *2*, 1307–1315.
- [42] Kortekaas, L.; Browne, W. R. The Evolution of Spiropyran: Fundamentals and Progress of an Extraordinarily Versatile Photochrome. *Chem. Soc. Rev.* **2019**, *48*, 3406–3424.
- [43] Kortekaas, L.; Chen, J.; Jacquemin, D.; Browne, W. R. Proton-Stabilized Photochemically Reversible E/Z Isomerization of Spiropyran. *J. Phys. Chem. B* **2018**, *122*, 6423–6430.
- [44] Futami, Y.; Chin, M. L. S.; Kudoh, S.; Takayanagi, M.; Nakata, M. Conformations of Nitro-Substituted Spiropyran and Merocyanine Studied by Low-Temperature Matrix-Isolation Infrared Spectroscopy and Density-Functional-Theory Calculation. *Chem. Phys. Lett.* **2003**, *370*, 460–468.
- [45] Minkin, V. I. Photo-, Thermo-, Solvato-, and Electrochromic Spiroheterocyclic Compounds. *Chem. Rev.* **2004**, *104*, 2751–2776.
- [46] Wang, P. X.; Bai, F. Q.; Zhang, Z. X.; Wang, Y. P.; Wang, J.; Zhang, H. X. The Theoretical Study of Substituent and Charge Effects in the Conformational Transformation Process of Molecular Machine Unit Spiropyran. *Org. Electron.* **2017**, *45*, 33–41.

Chapter 2

Elements of nonlinear optics

2.1 Second harmonic generation

Nonlinear optics deals with phenomena where matter modifies the properties of light, and *vice versa*. When an intense electric field interacts with a NLO medium, different NLO processes can occur. Contrary to linear optics, NLO processes can involve more than a single light field. At the macroscopic level (*i.e.*, for crystals, or solids in general), and considering the simplified case of a unique dynamic incident electric field oscillating at frequency ω , nonlinear effects are described using the expansion of the polarization as a function of this field,¹

$$\frac{P(\mathbf{E})}{\epsilon_0} = \frac{P_0}{\epsilon_0} + \chi^{(1)}\mathbf{E}(\omega) + \chi^{(2)}\mathbf{E}(\omega)\mathbf{E}(\omega) + \dots, \quad (2.1)$$

where ϵ_0 is the vacuum permittivity, while $\chi^{(1)}$ and $\chi^{(2)}$ are the linear and second-order nonlinear susceptibilities, respectively. However, this work focuses on the molecular level, where, as mentioned in Section 1.2, the expression of the molecular dipole moment in nonlinear regime is given by:

$$\mu(\mathbf{E}) = \mu_0 + \alpha\mathbf{E}(\omega) + \frac{1}{2}\beta\mathbf{E}(\omega)\mathbf{E}(\omega) + \dots \quad (2.2)$$

A more complete description is however achieved by considering multiple incident electric fields, and their directions. For instance, the ζ -component of the total electric dipole moment (within the T convention) of a NLO compound reads:²

$$\mu_\zeta(\mathbf{E}) = \mu_{0\zeta} + \sum_{\eta}^{x,y,z} \alpha_{\zeta\eta}(-\omega_\sigma; \omega_1) E_\eta(\omega_1) + \frac{1}{2!} \sum_{\eta,\xi}^{x,y,z} \beta_{\zeta\eta\xi}(-\omega_\sigma; \omega_1, \omega_2) E_\eta(\omega_1) E_\xi(\omega_2) + \dots, \quad (2.3)$$

where β is a rank-3 tensor with 27 elements (represented in Eq. (2.4) as a 3×9 matrix), defined in terms of the molecular axis coordinates (x, y, z) ,

$$\beta = \begin{bmatrix} \beta_{xxx} & \beta_{xyy} & \beta_{xzz} & \beta_{xyz} & \beta_{xzy} & \beta_{xxz} & \beta_{xxz} & \beta_{xxy} & \beta_{xyx} \\ \beta_{yxx} & \beta_{yyy} & \beta_{yzz} & \beta_{yyz} & \beta_{yzy} & \beta_{yzz} & \beta_{yzz} & \beta_{yyx} & \beta_{yyx} \\ \beta_{zxx} & \beta_{zyy} & \beta_{zzz} & \beta_{zxy} & \beta_{zzy} & \beta_{zzx} & \beta_{zzx} & \beta_{zxy} & \beta_{zyx} \end{bmatrix}. \quad (2.4)$$

In Eq. (2.3), $E_\eta(\omega_1)$ is the amplitude of the η -component of the field oscillating at frequency ω_1 , and $\omega_\sigma = \sum_i \omega_i$. When the unique incident field reads:

$$E_\eta(t) = E(t) = E_0 \cos(\omega t), \quad (2.5)$$

which corresponds to the case where $\omega_1 = \omega_2$, for the corresponding ζ -component of μ (the indices have been dropped for clarity) Eq. (2.3) becomes:

$$\mu(E) = \mu_0 + \alpha E_0 \cos(\omega t) + \frac{1}{2} \beta [E_0 \cos(\omega t)]^2 + \dots \quad (2.6)$$

$$= \mu_0 + \alpha E_0 \cos(\omega t) + \frac{1}{4} \beta E_0^2 + \frac{1}{4} \beta E_0^2 \cos(2\omega t) + \dots \quad (2.7)$$

Thus, after applying Carnot formula, an additional frequency independent (static) term and a term of frequency doubling arise in the induced dipole moment. The former corresponds to the optical rectification (OR), while the latter is associated with the second harmonic generation (SHG) phenomenon.¹ Here, $E(t)$ was taken as a scalar quantity for simplicity but the vector character of this field and its phase could be equally treated, for instance by expressing it as follows:

$$\mathbf{E}(\mathbf{r}, t) = \mathbf{E}_0(e^{i\mathbf{k}\mathbf{r} - i\omega t} + cc), \quad (2.8)$$

where $\mathbf{k} = n\omega/c$ is the wavevector (n is the refractive index, and c is the speed of light in vacuum), and cc denotes the complex conjugate. More generally, at the second-order NLO level, using two irradiating fields at frequencies ω_1 and ω_2 leads to additional contributions at $(\omega_1 + \omega_2)$ and $(\omega_1 - \omega_2)$, representing the sum-frequency and the difference-frequency generations (SFG and DFG), respectively. In molecular logic,³ this corresponds to "double input-single output" devices because there are two inputs (the two electric fields) that can independently be switched on or off while a unique signal is observed. This results in the emergence of 16 logic gates. SHG, SFG, DFG as well as the trivial case where the system does not emit any NLO signal are among these patterns.

Moreover, it can be deduced from Eq. (2.2) that, in a centrosymmetric system, the dipole must change sign if the electric field is applied in the opposite direction:²

$$\mu(\mathbf{E}) = -\mu(-\mathbf{E}). \quad (2.9)$$

After substitution of $\mu(\mathbf{E})$ with its expression, one gets:

$$\mu_0 + \alpha \mathbf{E}(\omega) + \frac{1}{2} \beta \mathbf{E}^2(\omega) + \dots = -[\mu_0 - \alpha \mathbf{E}(\omega) + \frac{1}{2} \beta \mathbf{E}^2(\omega) + \dots] \quad (2.10)$$

$$= -\mu_0 + \alpha \mathbf{E}(\omega) - \frac{1}{2} \beta \mathbf{E}^2(\omega) + \dots, \quad (2.11)$$

which demonstrates that the odd terms vanish in centrosymmetric systems, *i.e.* $\mu_0 = 0$ and

$\beta = 0$. This holds true for molecules, as well as for solids or supramolecular complexes. It is also of interest to note that the formalism presented in this chapter is restricted to the electric-dipole approximation, but other contributions (*e.g.* magnetization, and quadrupolarization) may occur.¹

From the viewpoint of quantum electrodynamics, the SHG phenomenon consists in the conversion of two photons of the same frequency into a new one with twice the frequency, as schematically shown in Fig. 2.1.² The first experimental observation of second harmonic generation was achieved by Franken *et al.*⁴ in 1961 (Fig. 2.2).

From analyzing Eq. (2.3), in the case of SHG, the $\beta_{\zeta\eta\xi}$ and $\beta_{\zeta\xi\eta}$ components are identical. Thus, the SHG first hyperpolarizability tensor reduces to 18 independent components (for a general C_1 point group of symmetry).¹ This permutation rule originates from the fact that the last two β -tensor component indices translate the polarization direction of the incident photons. These photons having the same frequencies, they can not be distinguished. Hence, considering two incident beams with frequencies ω_1 and ω_2 , the permutation of the indices is accompanied by the permutation of the frequencies, such that $\beta_{\zeta\eta\xi}(-\omega_1 - \omega_2; \omega_1, \omega_2) = \beta_{\zeta\xi\eta}(-\omega_1 - \omega_2; \omega_2, \omega_1)$. Therefore, in the case of SHG ($\omega_1 = \omega_2$), $\beta_{\zeta\eta\xi}(-2\omega; \omega, \omega) = \beta_{\zeta\xi\eta}(-2\omega; \omega, \omega)$. The minus sign in

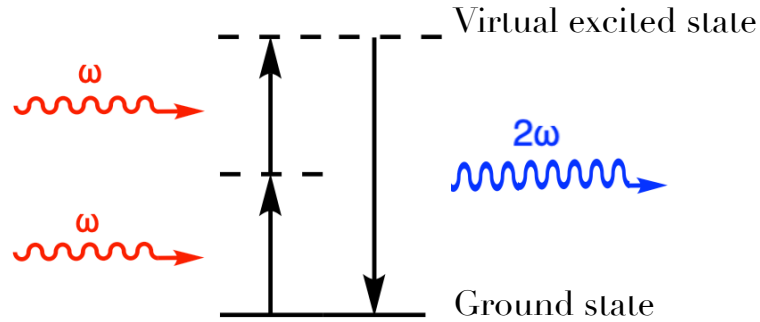


Fig. 2.1: Energy level diagram associated with the second harmonic generation phenomenon.

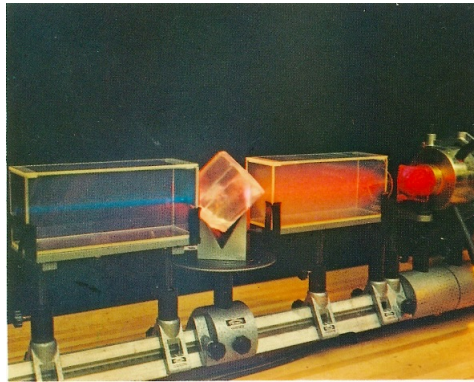


Fig. 2.2: Illustration of second harmonic generation by an ammonium dihydrogenophosphate crystal. Red light at 700 nm is converted into blue light at 350 nm (from Ref. 5).

front of the frequency $\omega_1 + \omega_2$ (or 2ω) means that the associated photon is emitted. In addition, for a transparent or weakly/non-optically dispersive medium, Kleinman symmetry conditions⁶ can be assumed. This approximation stipulates that the β -tensor components are invariant with respect to the permutations of any of their Cartesian indices. In this way, $\beta_{\zeta\eta\xi} = \beta_{\xi\eta\zeta}$, which reduces to 10 the number of independent components of the SHG β tensor.

Two main experimental techniques are used to determine β from the measurement of the SHG responses of gases and solutions: the electric-field-induced second harmonic generation (EFISHG)^{7,8} and the Hyper-Rayleigh scattering (HRS).^{9,10} Note that ionic compounds can not be analyzed by EFISHG measurements, since a static electric field is applied on the sample to align the molecules, which induces their motions (towards one of the electrodes). In this work, one concentrates on the HRS technique because the switching processes involve charged species. In addition, in the frame of the LCT investigations, the SHG responses are usually characterized on the HRS setups of UBordeaux or KULeuven.

2.2 Hyper-Rayleigh Scattering - principles

Experimental setup and measured quantities

In this work, the measurement of $\beta(-2\omega; \omega, \omega)$ is assumed to be obtained from second harmonic scattering (SHS), and more precisely, from Hyper-Rayleigh scattering. Therefore, β_{SHG} and β_{HRS} are considered as the same quantities. Hyper-Rayleigh scattering, first observed by Terhune *et al.*¹¹ in 1965, is the equivalent to Rayleigh scattering but where second-order NLO responses are targeted. For a liquid composed of identical molecules, the expression of the nonlinear scattered light intensity is given as a function of the squared incident light intensity, and a quadratic form of the molecular first hyperpolarizability:¹²

$$I^{2\omega} = G f_{\omega}^4 f_{2\omega}^2 C \langle \beta_{HRS}^2 \rangle (I^{\omega})^2, \quad (2.12)$$

where G is a constant containing geometrical, optical and electrical factors of the experimental setup, C is the molar concentration of the liquid and $f_{\omega}^4 f_{2\omega}^2$ is a local field correction, commonly approximated using the high frequency Lorentz-Lorenz spherical cavity expression, f_L ,¹

$$f_L = \left(\frac{n_{\omega}^2 + 2}{3} \right)^2 \left(\frac{n_{2\omega}^2 + 2}{3} \right). \quad (2.13)$$

Eq. (2.13) involves the refractive index of the liquid at optical frequencies ω and 2ω . The bracket in Eq. (2.12) refers to an average over all possible molecular orientations, since the liquid is isotropic.

A schematic view of a classical 90° angle Hyper-Rayleigh scattering experimental setup is presented in Fig. 2.3. One assumes (i) an initial light beam propagating along the Y direction of a laboratory frame with a state of polarization described by two angles (Ψ, δ) , where Ψ is the tilt angle of the polarization plane and δ is the phase retardation, (ii) a scattered beam collected at 90° along the X axis, and (iii) only the incoherent contributions to SHS, neglecting therefore the cooperative scattering originating from the correlation between the positions/orientations of the neighboring molecules.¹³ The intensity of the vertically (V) polarized (along the Z direction) scattered light beam is obtained by the Bersohn expression:¹³

$$I_{\Psi V}^{2\omega} \propto \langle \beta_{ZXX}^2 \rangle \cos^4 \Psi + \langle \beta_{ZZZ}^2 \rangle \sin^4 \Psi + \langle (\beta_{ZXZ} + \beta_{ZZX})^2 - 2\beta_{ZZZ}\beta_{ZXX} \cos(2\delta) \rangle \cos^2 \Psi \sin^2 \Psi. \quad (2.14)$$

Note that the incident light could not only be linearly or circularly polarized but also elliptically polarized to measure all five observables of the macroscopic $\langle \dots \rangle$ quantities present in Eq. (2.14). When the incident beam is horizontally polarized (H) or vertically polarized, it results in two possible polarization combinations: VV (vertically polarized incident and scattered beams) and HV (horizontally polarized incident beam and vertically polarized scattered beam). Experimentally, $\langle \beta_{ZZZ}^2 \rangle$ and $\langle \beta_{ZXX}^2 \rangle$ can be obtained individually from $I_{VV}^{2\omega}$ and $I_{HV}^{2\omega}$, respectively. Since both combinations are detected with equal probability for a non polarized incident light, the corresponding orientational average β_{HRS} is written as the sum of the two

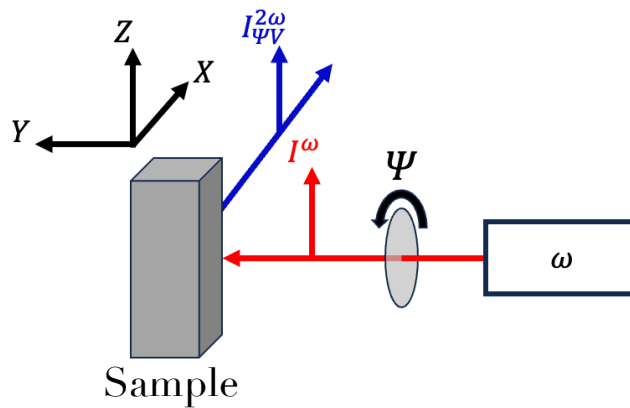


Fig. 2.3: Schematic view of a classical 90° angle Hyper-Rayleigh scattering experimental setup. X , Y and Z are the axes laboratory frames.

contributions,¹

$$\beta_{HRS}(-2\omega; \omega, \omega) = \sqrt{\langle \beta_{ZZZ}^2 \rangle + \langle \beta_{ZXX}^2 \rangle}. \quad (2.15)$$

Because of the isotropy of the solution, terms like $\langle \beta_{ZXX}^2 \rangle$ and $\langle \beta_{XZZ}^2 \rangle$ are the same.¹³ Within the $\langle \beta_{ZXX}^2 \rangle$ notation, the two X (or the two last Z for $\langle \beta_{ZZZ}^2 \rangle$) refer to the polarization state of the incident photons while the first Z means that the scattered beam is vertically polarized along the Z direction.

The $I_{VV}^{2\omega}/I_{HV}^{2\omega}$ ratio or the ratio between $\langle \beta_{ZZZ}^2 \rangle$ and $\langle \beta_{ZXX}^2 \rangle$ defines the depolarization ratio (DR),

$$DR = \frac{I_{VV}^{2\omega}}{I_{HV}^{2\omega}} = \frac{\langle \beta_{ZZZ}^2 \rangle}{\langle \beta_{ZXX}^2 \rangle}. \quad (2.16)$$

Assuming Kleinman's conditions, DR ranges from 1.5 to 9. Yet, a more general description of the HRS response is obtained covering the full range of Ψ angles (see Eq. (2.14)) of the incident light.¹⁴

For a solution of two noncentrosymmetric components (*i.e.* solute and solvent), which both contribute to the HRS response, Eq. (2.12) becomes:

$$I^{2\omega} = G f_{\omega}^4 f_{2\omega}^2 \left(C_{solvent} \langle \beta_{HRS}^2 \rangle_{solvent} + C_{solute} \langle \beta_{HRS}^2 \rangle_{solute} \right) (I^{\omega})^2, \quad (2.17)$$

where $C_{solvent}$ and C_{solute} are the number densities (concentrations) of solvent and solute molecules in the sample, respectively. Note that, considering time and space average, a simple solution, *i.e.*, an isotropic ensemble of solute molecules randomly dissolved in a solvent, is centrosymmetric. Nevertheless, HRS signals are obtained for solutions. In fact, the measured incoherent responses originate from the density and rotational fluctuations that occur locally in space and time, inducing deviations from the centrosymmetry.¹ Experimentally, pulsed lasers and tight focusing are required in order to record an exploitable HRS intensity. For that purpose, a Q -switched YAG Neodymium laser and nanosecond pulses are of common use.¹⁵ Moreover, in general, β_{HRS} responses are obtained from their relative values with respect to a well-characterized standard reference chromophore/solvent (external/internal reference method).

2.3 Notes on isotropic rotational averages

As seen in the previous section, measurements of bulk samples lead to the deduction of properties of individual molecules. However, when a molecule "interacts with the experimental

system” (or, for example, when radiations interact with matter), the response depends on the molecule orientation. The objective of this section is to calculate bulk properties in terms of microscopic molecular parameters. Hence, it is necessary to take into account all possible random orientations of the molecules.¹⁶ This can be achieved by calculating a statistical average over all molecular orientations.¹⁷ According to Andrews and coworkers,¹⁶ the signal of any spectroscopic observable Γ reads:

$$\Gamma = \sum_{i_1, \dots, i_n} A_{i_1 \dots i_n}^{(n)} \wp_{i_1 \dots i_n}^{(n)}, \quad (2.18)$$

where $\wp_{i_1 \dots i_n}$ is the response tensor of a molecule and $A_{i_1 \dots i_n}$ is a tensor of the same rank, n , associated with the initial external perturbation. Γ is then a scalar quantity. The tensor components of A and \wp are expressed in a laboratory frame (also called the space-fixed reference frame, $i_1, \dots = X, Y, Z$). On the other hand, in quantum chemistry calculations, the responses to an external perturbation are generally computed with respect to the molecular frame (x, y, z). Hence, the laboratory axes are usually defined so that the components of A are expressed in relatively simple way, *videlicet* by choosing a frame sharing the same origin as the molecular frame, though with a different orientation (Fig. 2.4). Subsequently, the molecular property tensor \wp is re-specified with respect to a molecular frame (a molecule-fixed reference frame, $\lambda_1, \dots = x, y, z$):

$$\Gamma = \sum_{i_1, \dots, i_n} \sum_{\lambda_1, \dots, \lambda_n} A_{i_1 \dots i_n}^{(n)} l_{i_1 \lambda_1 \dots i_n \lambda_n} \wp_{\lambda_1 \dots \lambda_n}^{(n)}, \quad (2.19)$$

where $l_{i_p \lambda_p}$ are the elements of the direction cosines matrix, which contains information about the molecule orientation in the laboratory frame. The direction cosines in Eq. (2.19) are usually expressed in terms of Euler angles. The molecule orientation in the laboratory frame axes is then given by the Euler angles θ , ϕ and τ as shown in Fig. 2.4.

For an isotropic sample, one can consider any possible orientation with respect to the fixed laboratory frame. Consequently, Γ is replaced by its isotropic/rotational average, $\langle \Gamma \rangle$,

$$\langle \Gamma \rangle = \sum_{i_1, \dots, i_n} \sum_{\lambda_1, \dots, \lambda_n} A_{i_1 \dots i_n}^{(n)} \langle l_{i_1 \lambda_1 \dots i_n \lambda_n} \rangle \wp_{\lambda_1 \dots \lambda_n}^{(n)}. \quad (2.20)$$

where $\langle l_{i_1 \lambda_1 \dots i_n \lambda_n} \rangle$ is the rotational average of the direction cosines matrix. Different mathematical methods can be employed to compute these rotational averages: (i) a trigonometric approach and (ii) an approach resorting to the fundamental isotropic tensors. The former consists in

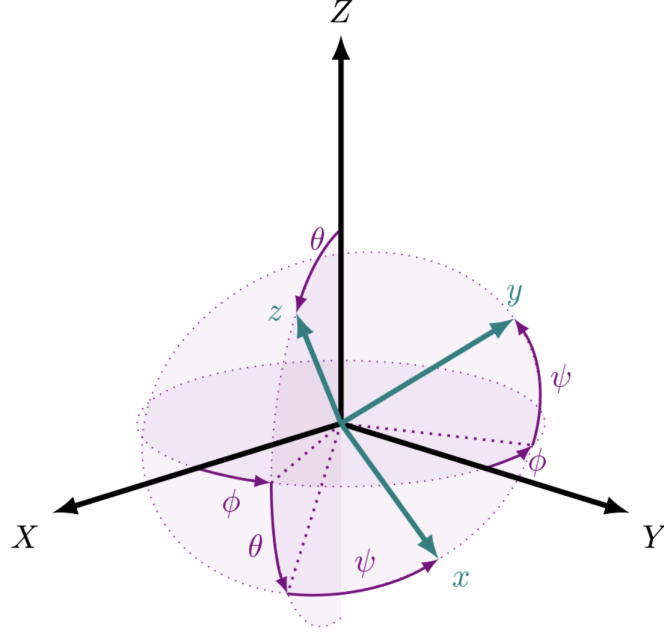


Fig. 2.4: Laboratory reference frame axes (X , Y and Z) and molecular reference frames (x , y and z). For clarity, only z is represented; x and y are perpendicular to each other and to z . θ , ϕ and ψ are the Euler angles that relate the coordinate systems (Reprinted from Ref. 18).

computing directly the rotational average of the direction cosines matrix as follows:¹⁹

$$\langle l_{i_1 \lambda_1 \dots i_n \lambda_n} \rangle = \frac{1}{8\pi^2} \int_0^\pi \int_0^{2\pi} \int_0^{2\pi} l_{i_1 \lambda_1 \dots i_n \lambda_n} \sin \theta \, d\theta \, d\phi \, d\psi. \quad (2.21)$$

This requires the calculation of 3^{2n} integrals, which is a tremendous task, and not adapted for high-rank tensors. The second approach relies on considering $\langle l_{i_1 \lambda_1 \dots i_n \lambda_n} \rangle$ as rotational invariant,¹⁶ and allows to discuss solutions for Cartesian tensors up to rank 12.^{18,20}

2.4 HRS isotropic rotational averages

In HRS, the response and the polarization tensors are both tensors of rank 6. Following Bersohn *et al.*,¹³ the rotational invariants $\langle \beta_{ZZZ}^2 \rangle$ and $\langle \beta_{ZXX}^2 \rangle$ can be expressed as functions of the molecular β -tensor components:

$$\begin{aligned} \langle \beta_{ZZZ}^2 \rangle = & \frac{1}{7} \sum_{\zeta}^{x,y,z} \beta_{\zeta\zeta\zeta}^2 + \frac{4}{35} \sum_{\zeta \neq \eta}^{x,y,z} \beta_{\zeta\zeta\eta}^2 + \frac{1}{35} \sum_{\zeta \neq \eta}^{x,y,z} \beta_{\eta\zeta\zeta}^2 + \frac{4}{35} \sum_{\zeta \neq \eta}^{x,y,z} \beta_{\zeta\zeta\zeta} \beta_{\eta\eta\zeta} \\ & + \frac{2}{35} \sum_{\zeta \neq \eta}^{x,y,z} \beta_{\zeta\zeta\zeta} \beta_{\zeta\eta\eta} + \frac{4}{35} \sum_{\zeta \neq \eta}^{x,y,z} \beta_{\eta\zeta\zeta} \beta_{\zeta\zeta\eta} + \frac{2}{105} \sum_{\zeta \neq \eta \neq \xi}^{x,y,z} \beta_{\zeta\eta\xi}^2 + \frac{4}{105} \sum_{\zeta \neq \eta \neq \xi}^{x,y,z} \beta_{\zeta\zeta\eta} \beta_{\eta\xi\xi} \\ & + \frac{4}{105} \sum_{\zeta \neq \eta \neq \xi}^{x,y,z} \beta_{\zeta\zeta\eta} \beta_{\xi\xi\eta} + \frac{1}{105} \sum_{\zeta \neq \eta \neq \xi}^{x,y,z} \beta_{\eta\zeta\zeta} \beta_{\eta\xi\xi} + \frac{4}{105} \sum_{\zeta \neq \eta \neq \xi}^{x,y,z} \beta_{\zeta\eta\xi} \beta_{\eta\xi\xi}, \end{aligned} \quad (2.22)$$

$$\begin{aligned}
\langle \beta_{ZXX}^2 \rangle &= \frac{1}{35} \sum_{\zeta}^{x,y,z} \beta_{\zeta\zeta\zeta}^2 + \frac{8}{105} \sum_{\zeta \neq \eta}^{x,y,z} \beta_{\zeta\zeta\eta}^2 + \frac{3}{35} \sum_{\zeta \neq \eta}^{x,y,z} \beta_{\zeta\eta\eta}^2 - \frac{2}{35} \sum_{\zeta \neq \eta}^{x,y,z} \beta_{\zeta\zeta\zeta} \beta_{\eta\eta\eta} \\
&+ \frac{4}{105} \sum_{\zeta \neq \eta}^{x,y,z} \beta_{\zeta\zeta\zeta} \beta_{\zeta\eta\eta} - \frac{2}{35} \sum_{\zeta \neq \eta}^{x,y,z} \beta_{\zeta\zeta\eta} \beta_{\eta\eta\zeta} + \frac{2}{35} \sum_{\zeta \neq \eta \neq \xi}^{x,y,z} \beta_{\zeta\eta\xi}^2 - \frac{2}{105} \sum_{\zeta \neq \eta \neq \xi}^{x,y,z} \beta_{\zeta\zeta\eta} \beta_{\eta\xi\xi} \\
&+ \frac{1}{35} \sum_{\zeta \neq \eta \neq \xi}^{x,y,z} \beta_{\zeta\eta\eta} \beta_{\zeta\xi\xi} - \frac{2}{105} \sum_{\zeta \neq \eta \neq \xi}^{x,y,z} \beta_{\zeta\zeta\zeta} \beta_{\eta\eta\xi} - \frac{2}{105} \sum_{\zeta \neq \eta \neq \xi}^{x,y,z} \beta_{\zeta\eta\xi} \beta_{\eta\xi\xi}.
\end{aligned} \tag{2.23}$$

The incomplete summations can be transformed in complete summations using the following relationships:

$$\sum_{\zeta\eta}^{x,y,z} = \sum_{\zeta \neq \eta}^{x,y,z} + \sum_{\zeta}^{x,y,z} \delta_{\zeta\eta}, \tag{2.24}$$

$$\sum_{\zeta\eta\xi}^{x,y,z} = \sum_{\zeta \neq \eta \neq \xi}^{x,y,z} + \sum_{\zeta \neq \eta}^{x,y,z} \delta_{\eta\xi} + \sum_{\zeta \neq \eta}^{x,y,z} \delta_{\zeta\xi} + \sum_{\zeta \neq \eta}^{x,y,z} \delta_{\zeta\eta} + \sum_{\zeta}^{x,y,z} \delta_{\zeta\eta} \delta_{\zeta\xi}. \tag{2.25}$$

Subsequently, Eqs. (2.22) and (2.23) simplify in more implementation friendly forms:

$$\langle \beta_{ZZZ}^2 \rangle = \frac{1}{105} \sum_{\zeta\eta\xi}^{xyz} 2\beta_{\zeta\eta\xi}^2 + \beta_{\zeta\eta\eta} \beta_{\zeta\xi\xi} + 4\beta_{\zeta\zeta\eta} \beta_{\eta\xi\xi} + 4\beta_{\zeta\zeta\eta} \beta_{\eta\eta\xi} + 4\beta_{\zeta\eta\xi} \beta_{\eta\xi\xi}, \tag{2.26}$$

$$\langle \beta_{ZXX}^2 \rangle = \frac{1}{105} \sum_{\zeta\eta\xi}^{xyz} 6\beta_{\zeta\eta\xi}^2 + 3\beta_{\zeta\eta\eta} \beta_{\zeta\xi\xi} - 2\beta_{\zeta\zeta\eta} \beta_{\eta\xi\xi} - 2\beta_{\zeta\zeta\eta} \beta_{\eta\eta\xi} - 2\beta_{\zeta\eta\xi} \beta_{\eta\xi\xi}. \tag{2.27}$$

In addition, if Kleinman symmetry conditions apply, Eqs. (2.22) and (2.23) reduce to the analysis of Cyvin *et al.*,²¹ and are rewritten as follows:

$$\langle \beta_{ZZZ}^2 \rangle = \frac{1}{7} \sum_{\zeta}^{x,y,z} \beta_{\zeta\zeta\zeta}^2 + \frac{9}{35} \sum_{\zeta \neq \eta}^{x,y,z} \beta_{\zeta\zeta\eta}^2 + \frac{6}{35} \sum_{\zeta \neq \eta}^{x,y,z} \beta_{\zeta\zeta\zeta} \beta_{\zeta\eta\eta} + \frac{2}{35} \sum_{\zeta \neq \eta \neq \xi}^{x,y,z} \beta_{\zeta\eta\xi}^2 + \frac{3}{35} \sum_{\zeta \neq \eta \neq \xi}^{x,y,z} \beta_{\zeta\zeta\eta} \beta_{\eta\xi\xi}, \tag{2.28}$$

$$\langle \beta_{ZXX}^2 \rangle = \frac{1}{35} \sum_{\zeta}^{x,y,z} \beta_{\zeta\zeta\zeta}^2 + \frac{11}{105} \sum_{\zeta \neq \eta}^{x,y,z} \beta_{\zeta\zeta\eta}^2 - \frac{2}{105} \sum_{\zeta \neq \eta}^{x,y,z} \beta_{\zeta\zeta\zeta} \beta_{\zeta\eta\eta} + \frac{4}{105} \sum_{\zeta \neq \eta \neq \xi}^{x,y,z} \beta_{\zeta\eta\xi}^2 - \frac{1}{105} \sum_{\zeta \neq \eta \neq \xi}^{x,y,z} \beta_{\zeta\zeta\eta} \beta_{\eta\xi\xi}. \tag{2.29}$$

It is also convenient to express the rotational invariants in terms of irreducible spherical tensors (irreducible spherical representations of the β tensor).^{22,23} In this way, the β tensor is decomposed as a sum of a dipolar ($J = 1$) and an octupolar ($J = 3$) tensorial β_J -components. This invariance holds for $\langle \beta_{ZZZ}^2 \rangle$ and $\langle \beta_{ZXX}^2 \rangle$,

$$\langle \beta_{ZZZ}^2 \rangle = \frac{1}{5} |\beta_{J=1}|^2 + \frac{2}{35} |\beta_{J=3}|^2, \tag{2.30}$$

$$\langle \beta_{ZXX}^2 \rangle = \frac{1}{45} |\beta_{J=1}|^2 + \frac{4}{105} |\beta_{J=3}|^2. \tag{2.31}$$

These equations are obtained assuming Kleinman's conditions. Moreover, the two spherical

invariants $|\beta_{J=1}|^2$ and $|\beta_{J=3}|^2$ can be written as a function of the Cartesian β -tensor components:^{24,25}

$$|\beta_{J=1}|^2 = \frac{3}{5} \sum_{\zeta}^{x,y,z} \beta_{\zeta\zeta\zeta}^2 + \frac{3}{5} \sum_{\zeta \neq \eta}^{x,y,z} \beta_{\zeta\zeta\eta}^2 + \frac{6}{5} \sum_{\zeta \neq \eta}^{x,y,z} \beta_{\zeta\zeta\zeta} \beta_{\zeta\eta\eta} + \frac{3}{5} \sum_{\zeta \neq \eta \neq \xi}^{x,y,z} \beta_{\zeta\zeta\eta} \beta_{\eta\xi\xi}, \quad (2.32)$$

$$|\beta_{J=3}|^2 = \frac{2}{5} \sum_{\zeta}^{x,y,z} \beta_{\zeta\zeta\zeta}^2 + \frac{12}{35} \sum_{\zeta \neq \eta}^{x,y,z} \beta_{\zeta\zeta\eta}^2 - \frac{6}{5} \sum_{\zeta \neq \eta}^{x,y,z} \beta_{\zeta\zeta\zeta} \beta_{\zeta\eta\eta} + \frac{1}{4} \sum_{\zeta \neq \eta \neq \xi}^{x,y,z} \beta_{\zeta\eta\xi}^2 - \frac{3}{5} \sum_{\zeta \neq \eta \neq \xi}^{x,y,z} \beta_{\zeta\zeta\eta} \beta_{\eta\xi\xi}. \quad (2.33)$$

The ratio between the latter quantities is referred to as the nonlinear anisotropy $\rho = |\beta_{J=3}|/|\beta_{J=1}|$.

It therefore leads to alternative expressions for DR and β_{HRS} :²⁵

$$DR = 9 \frac{\left(1 + \frac{2}{7}\rho^2\right)}{\left(1 + \frac{12}{7}\rho^2\right)}, \quad (2.34)$$

$$\beta_{HRS} = \sqrt{\frac{2}{9}|\beta_{J=1}|^2 + \frac{2}{21}|\beta_{J=3}|^2} \quad (2.35)$$

$$= |\beta_{J=1}| \sqrt{\frac{2}{3} \left(\frac{1}{3} + \frac{1}{7}\rho^2 \right)}. \quad (2.36)$$

2.5 Analysis of $\langle \beta_{HRS}^2 \rangle$

The evolution of the static depolarization ratio as a function of nonlinear anisotropy factor ρ is presented in Fig. 2.5, highlighting the evolution of DR from 9 where $\rho = 0$ to 1.5 when ρ tends to infinity. Another way to illustrate these variations is shown in Fig. 2.6, which portrays the

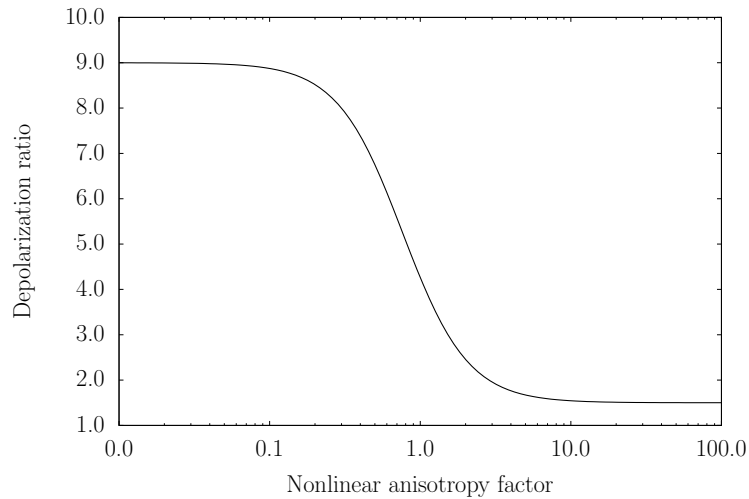


Fig. 2.5: Evolution of the static depolarization ratio as a function of the nonlinear anisotropy factor.

evolution of the static $\langle\beta_{ZZZ}^2\rangle$ and $\langle\beta_{ZXX}^2\rangle$ quantities as a function of ρ . These evolutions have a similar appearance and were obtained by fixing $|\beta_{J=1}|^2$ as equal to 1 (for any other $|\beta_{J=1}|$ value, both $\langle\beta_{ZZZ}^2\rangle$ and $\langle\beta_{ZXX}^2\rangle$ would be scaled in the same way). Following the trend of their DR values, the difference between the $\langle\beta_{ZZZ}^2\rangle$ and $\langle\beta_{ZXX}^2\rangle$ values is larger for dipolar compounds than for octupolar ones.

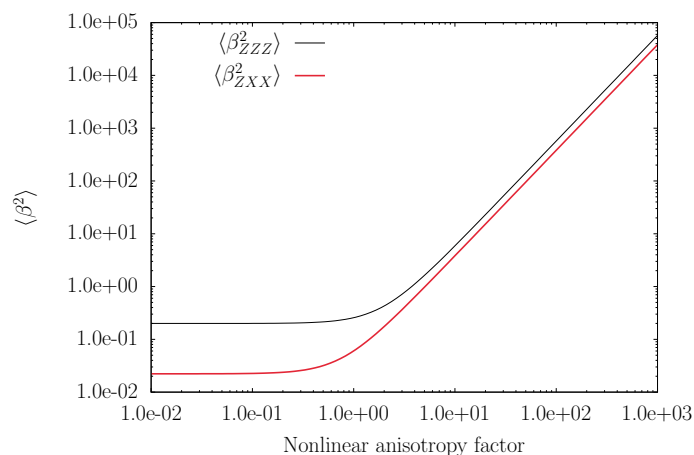


Fig. 2.6: Evolution of the static $\langle\beta_{ZZZ}^2\rangle$ and $\langle\beta_{ZXX}^2\rangle$ averages as a function of the nonlinear anisotropy factor.

A third illustration is provided by plotting, as a function of ρ , the static $\langle\beta_{ZZZ}^2\rangle$ and $\langle\beta_{ZXX}^2\rangle$ averages divided by the total $\langle\beta_{HRS}^2\rangle$ response (Fig. 2.7). The latter highlights that $\langle\beta_{ZZZ}^2\rangle$ is always larger than $\langle\beta_{ZXX}^2\rangle$ but that they get closer (up to a ratio of 1.5) when the molecular β response is fully octupolar.

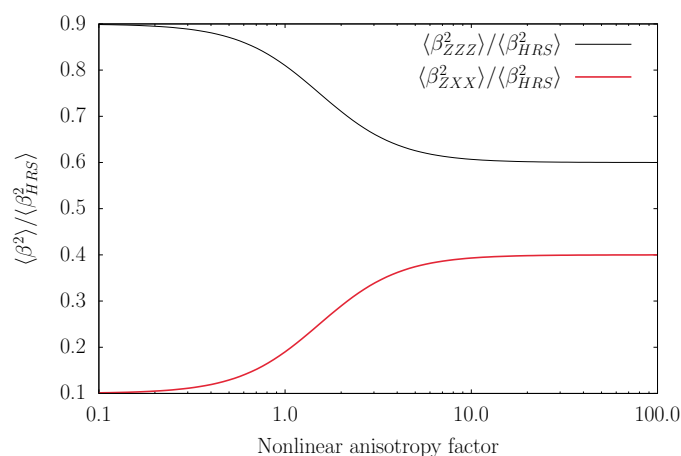


Fig. 2.7: Evolution of the static $\langle\beta_{ZZZ}^2\rangle/\langle\beta_{HRS}^2\rangle$ and $\langle\beta_{ZXX}^2\rangle/\langle\beta_{HRS}^2\rangle$ ratios as a function of the nonlinear anisotropy factor.

Let's have a look at molecular structures belonging to the C_{2v} point group. This is of interest for the present work because several structures behave like C_{2v} compounds. Here, the molecule

is lying in a mean xz molecular plane with z as the twofold symmetry axis, the SHG β tensor is simplified with respect to Eq. (2.4) and it reduces to:¹

$$\beta_{(C_{2v})} = \begin{bmatrix} 0 & 0 & 0 & 0 & 0 & \beta_{xxz} & \beta_{xxz} & 0 & 0 \\ 0 & 0 & 0 & \beta_{yyz} & \beta_{yyz} & 0 & 0 & 0 & 0 \\ \beta_{zxx} & \beta_{zyy} & \beta_{zzz} & 0 & 0 & 0 & 0 & 0 & 0 \end{bmatrix}. \quad (2.37)$$

If further assuming that the molecule is planar and that Kleinman symmetry applies, $\beta_{yyz} = \beta_{zyy} = \beta_{yzy} = 0$, $\beta_{zxx} = \beta_{xxz} = \beta_{xzx} \neq 0$ and $\beta_{zzz} \neq 0$. Thus, it is of interest to portray the evolution of DR as a function of the ratio of two molecular β -tensor components, such that $R = \beta_{zxx}/\beta_{zzz}$. Eqs. (2.28) and (2.29) can be rewritten as:

$$\langle \beta_{ZZZ}^2 \rangle = \frac{1}{7}\beta_{zzz}^2 + \frac{6}{35}\beta_{zzz}\beta_{zxx} + \frac{9}{35}\beta_{zxx}^2, \quad (2.38)$$

$$\langle \beta_{ZXX}^2 \rangle = \frac{1}{35}\beta_{zzz}^2 - \frac{2}{105}\beta_{zzz}\beta_{zxx} + \frac{11}{105}\beta_{zxx}^2. \quad (2.39)$$

Finally, dividing these two expressions by β_{zzz}^2 provides the expression of DR as a function of R :

$$DR_{(C_{2v})} = \frac{\frac{1}{7} + \frac{6}{35}R + \frac{9}{35}R^2}{\frac{1}{35} - \frac{2}{105}R + \frac{11}{105}R^2}. \quad (2.40)$$

The evolution of DR and of ρ as a function of R are sketched in Fig. 2.8. Both curves show an asymptotic behavior when $R = \pm\infty$. DR and ρ tend to $\frac{27}{11}$ and 2, respectively, for these two limits. Consequently, the experimentally measured DR for this type of molecules corresponds to two possible values of R unless the DR is equal to $\frac{27}{11}$.

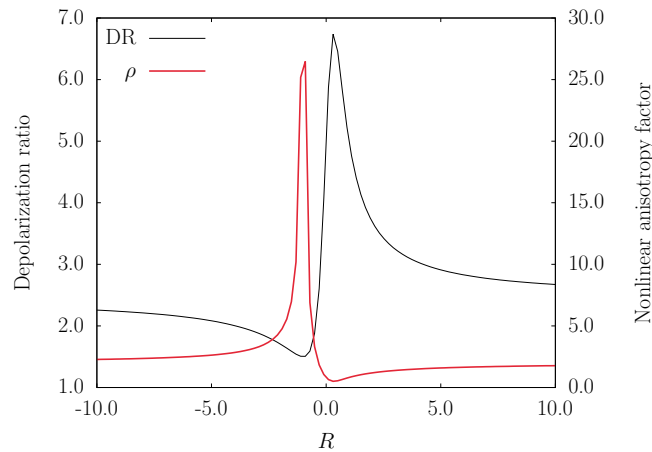


Fig. 2.8: Evolution of the depolarization ratio and of the nonlinear anisotropy factor as a function of $R = \beta_{zxx}/\beta_{zzz}$ when assuming Kleinman symmetry conditions and a C_{2v} point group.

Bibliography

- [1] Verbiest, T.; Clays, K.; Rodriguez, V. *Second-Order Nonlinear Optical Characterization Techniques*; CRC Press, New York, 2009.
- [2] Boyd, R. W. *Nonlinear Optics*, 4th ed.; Academic Press, Rochester, New York, 2020.
- [3] de Silva, A. P. *Molecular Logic-Based Computation*, 1st ed.; RSC Publishing, Cambridge, UK, 2013.
- [4] Franken, P. A.; Hill, A. E.; Peters, C.; Weinreich, G. Generation of Optical Harmonics. *Phys. Rev. Lett.* **1961**, *7*, 118–119.
- [5] Yariv, A. *Quantum electronics*; John Wiley & Sons, New York, 1989.
- [6] Kleinman, D. A. Nonlinear Dielectric Polarization in Optical Media. *Phys. Rev.* **1962**, *126*, 1977–1979.
- [7] Levine, B. F.; Bethea, C. G. Molecular Hyperpolarizabilities Determined from Conjugated and Nonconjugated Organic Liquids. *Appl. Phys. Lett.* **1974**, *24*, 445–447.
- [8] Levine, B. F.; Bethea, C. G. Second and Third Order Hyperpolarizabilities of Organic Molecules. *J. Chem. Phys.* **1975**, *63*, 2666–2682.
- [9] Clays, K.; Persoons, A. Hyper-Rayleigh Scattering in Solution. *Phys. Rev. Lett.* **1991**, *66*, 2980–2983.
- [10] Hendrickx, E.; Clays, K.; Persoons, A. Hyper-Rayleigh Scattering in Isotropic Solution. *Acc. Chem. Res.* **1998**, *31*, 675–683.
- [11] Terhune, R. W.; Maker, P. D.; Savage, C. M. Measurements of Nonlinear Light Scattering. *Phys. Rev. Lett.* **1965**, *14*, 681–684.
- [12] Clays, K.; Persoons, A.; De Maeyer, L. Hyper-Rayleigh Scattering in Solution. *Adv. Chem. Phys.* **1994**, *85*, 455–498.
- [13] Bersohn, R.; Yoh-Han, P. A.; Frisch, H. L. Double-Quantum Light Scattering by Molecules. *J. Chem. Phys.* **1966**, *45*, 3184–3198.
- [14] Castet, F.; Gillet, A.; Bureš, F.; Plaquet, A.; Rodriguez, V.; Champagne, B. Second-Order Nonlinear Optical Properties of \wedge -shaped Pyrazine Derivatives. *Dyes Pigm.* **2021**, *184*, 108850.
- [15] Clays, K.; Persoons, A. Hyper-Rayleigh Scattering in Solution. *Rev. Sci. Instrum.* **1992**, *63*, 3285–3289.

- [16] Andrews, D. L.; Thirunamachandran, T. On Three-Dimensional Rotational Averages. *J. Chem. Phys.* **1977**, *67*, 5026–5033.
- [17] Andrews, S. S. Using Rotational Averaging to Calculate the Bulk Response of Isotropic and Anisotropic Samples from Molecular Parameters. *J. Chem. Educ.* **2004**, *81*, 877–885.
- [18] Bonvicini, A.; Champagne, B. The Evaluation of Three-Dimensional Rotational Averages. *J. Chem. Theory Comput.* **2023**, *19*, 7801–7815.
- [19] Nessler, R.; Gegzjav, T. K. A General Method for Rotational Averages. *J. Phys. Conf. Ser.* **2021**, *2090*, 012041.
- [20] Wagnière, G. The Evaluation of Three-Dimensional Rotational Averages. *J. Chem. Phys.* **1982**, *76*, 473–480.
- [21] Cyvin, S. J.; Rauch, J. E.; Decius, J. C. Theory of Hyper-Raman Effects: Selection Rules and Depolarization Ratios for Second-Order Polarizability. *J. Chem. Phys.* **1965**, *43*, 4083–4095.
- [22] Coope, J. A. R.; Snider, R. F.; McCourt, F. R. The Evaluation of Three-Dimensional Rotational Averages. *J. Chem. Phys.* **1965**, *43*, 2269–2275.
- [23] Chemla, D. S.; Ouder, J. L.; Jerphagnon, J. Origin of the Second-Order Optical Susceptibilities of Crystalline Substituted Benzene. *Phys. Rev. B* **1975**, *12*, 4534–4546.
- [24] Brasselet, S.; Zyss, J. Multipolar Molecules and Multipolar Fields: Probing and Controlling the Tensorial Nature of Nonlinear Molecular Media. *J. Opt. Soc. Am. B* **1998**, *15*, 257–288.
- [25] Rodriguez, V.; Grondin, J.; Adamietz, F.; Danten, Y. Local Structure in Ionic Liquids Investigated by Hyper-Rayleigh Scattering. *J. Phys. Chem. B* **2010**, *114*, 15057–15065.

Chapter 3

Quantum chemistry methods

3.1 The Schrödinger equation and the wavefunction - general aspects

In quantum chemistry (QC), where the chemical phenomena are studied using quantum mechanics, the evolution of a system in space and time is determined by the non-relativistic time-dependent Schrödinger equation,¹

$$\hat{\mathcal{H}}\Psi = i\hbar\frac{\partial\Psi}{\partial t}, \quad (3.1)$$

where $\hat{\mathcal{H}}$ is the Hamiltonian operator, the hermitian quantum mechanical operator of the total energy. The quantum state of the system is described by the wavefunction $\Psi(\{\mathbf{x}_i\}, t)$, depending on the spin-space variables of the particles, $\{\mathbf{x}_i\}$, and time, t . More rigorously, one could use the Dirac notation, $|\Psi(\{\mathbf{x}_i\}, t)\rangle$, which translates that the wavefunction is a complex vector in a N-dimensional vector space. This equation was proven to be equivalent to the matrix equation proposed by Heisenberg in 1925.² The relativistic adaptation of the Schrödinger equation was formulated by Dirac two years later (1928).³ The time-dependent Schrödinger equation can be established using analytical mechanics (see, for instance, the book by Tsuneda⁴) from the least action principle leading to the Euler-Lagrange and the time-dependent Hamilton-Jacobi equations. Eq. (3.1) was then obtained by combining the Hamilton-Jacobi equation with de Broglie's concept of matter waves. Schrödinger defined the wavefunction as

$$\Psi = \exp\left(\frac{-i\mathcal{S}}{\hbar}\right), \quad (3.2)$$

where \mathcal{S} is the action. Ψ translates the amplitude of matter waves, and the finiteness of the wavefunction is presumed by a normalization condition:

$$\int |\Psi|^2 d\tau = 1, \quad (3.3)$$

$d\tau$ being an infinitesimal spin-space element (for each particle).

The interpretation of the wavefunction was vigorously discussed since the publication of the Schrödinger equation. The most accepted interpretation (advocated by the Copenhagen school) was suggested by Born,⁵ which states that the wavefunction is probabilistic in nature. According to this interpretation, the wavefunction only targets the existence probability P of

particle(s) in a differential spin-volume element $d\tau$,

$$P(\tau)d\tau = |\Psi|^2 d\tau. \quad (3.4)$$

For an energy (E) conservative system, the wavefunction can be separated into a factor depending only on the coordinates, Ψ_0 , and a factor depending on time:

$$\Psi = \Psi_0 \exp\left(\frac{-iEt}{\hbar}\right). \quad (3.5)$$

Substituting the action using the wavefunction in the time-independent Hamilton-Jacobi equation gives:

$$\hat{\mathcal{H}}\Psi = E\Psi, \quad (3.6)$$

the time-independent Schrödinger equation, an eigenvalue equation describing the stationary states of the system. For time-independent (and independent particles) system, Eq. (3.6) reads:

$$-\sum_i \frac{\hbar^2}{2m_i} \nabla_i^2 \Psi + (V - E)\Psi = 0. \quad (3.7)$$

The momentum quantum operator $\hat{\mathbf{p}}_i$,

$$\hat{\mathbf{p}}_i = -i\hbar \nabla_i, \quad (3.8)$$

produces discrete energy levels (the eigenvalues), associated with the corresponding wavefunctions (the eigenfunctions or eigenstates), under the boundary conditions of a potential V to make the wavefunctions finite.⁴

The electronic problem

For a molecular system, the Hamiltonian operator is described by the position vector of the nuclei and the electrons, \mathbf{R}_A and \mathbf{r}_i , respectively. The distance between the i^{th} electron and the A^{th} nucleus is $r_{iA} = |\mathbf{r}_{iA}| = |\mathbf{r}_i - \mathbf{R}_A|$, while the distance between the i^{th} and j^{th} electrons is $r_{ij} = |\mathbf{r}_i - \mathbf{r}_j|$, and the distance between the A^{th} and B^{th} nuclei is $R_{AB} = |\mathbf{R}_A - \mathbf{R}_B|$. As from this point, the following equations are expressed in atomic units (a.u.). Hence, the electron charge, e , electron mass, m_e , reduced Planck constant, \hbar , and Coulomb force constant, $1/(4\pi\epsilon_0)$ are all of unit magnitude. In these units, the Hamiltonian operator for N electrons

and M nuclei is written as follows:⁶

$$\hat{\mathcal{H}} = -\frac{1}{2} \sum_i^N \nabla_i^2 - \frac{1}{2} \sum_A^M \frac{\nabla_A^2}{M_A} - \sum_i^N \sum_A^M \frac{Z_A}{r_{iA}} + \frac{1}{2} \sum_i^N \sum_{j \neq i}^N \frac{1}{r_{ij}} + \frac{1}{2} \sum_A^M \sum_{B \neq A}^M \frac{Z_A Z_B}{R_{AB}}, \quad (3.9)$$

where M_A is the ratio of the mass of the nucleus A to the mass of an electron (which is the mass of the nucleus in a.u.), and Z_A is the charge of the nucleus A . The first two terms in Eq. (3.9) are the kinetic energies of the electrons and the nuclei, respectively; the third term is the Coulomb attraction between the electrons and the nuclei; and the last two terms represent the repulsion between the electrons and between the nuclei, respectively.

Although the Schrödinger equation is exact, the three-body (or more) problems can not be solved exactly. Hence, approximations are needed, the first one being the Born-Oppenheimer approximation.⁷ In the latter, one can consider the electron in a molecule to be moving (rapidly) in the field of fixed nuclei, and the repulsion energy between the nuclei is assumed to be constant. The wavefunction can be separated into an electronic and a nuclear contribution⁶

$$\Psi(\{\mathbf{r}_i\}, \{\mathbf{R}_A\}) = \Phi_{nuc}(\{\mathbf{R}_A\}) \Psi_{elec}(\{\mathbf{r}_i\}, \{\mathbf{R}_A\}). \quad (3.10)$$

The electronic Schrödinger equation reads

$$\hat{\mathcal{H}}_{elec} \Psi_{elec} = E_{elec} \Psi_{elec}, \quad (3.11)$$

where the electronic Hamiltonian is defined by:

$$\hat{\mathcal{H}}_{elec} = -\sum_i^N \frac{1}{2} \nabla_i^2 - \sum_i^N \sum_A^M \frac{Z_A}{r_{iA}} + \frac{1}{2} \sum_i^N \sum_{j \neq i}^N \frac{1}{r_{ij}}, \quad (3.12)$$

and the electronic wavefunction,

$$\Psi_{elec} = \Psi_{elec}(\{\mathbf{r}_i\}, \{\mathbf{R}_A\}), \quad (3.13)$$

describes the electronic motions, and depends explicitly on the electronic coordinates but also parametrically on the nuclear coordinates. This parametric dependency induces a different Ψ_{elec} for each nuclear configuration of the molecular system, and therefore, a different electronic energy,

$$E_{elec} = E_{elec}(\{\mathbf{R}_A\}). \quad (3.14)$$

It should be noted that the nuclear coordinates do not appear explicitly in the expression of Ψ_{elec} . Finally, the total energy for a fixed nuclear configuration reads:

$$E_{tot} = E_{elec} + \frac{1}{2} \sum_A^M \sum_{B \neq A}^M \frac{Z_A Z_B}{R_{AB}}. \quad (3.15)$$

Subsequently, it is possible to solve the nuclear equation. Since electrons move faster than the nuclei, the electronic coordinates can be replaced by their average values (over the electronic wavefunction), meaning that the nuclei perceive the electronic distribution as an average field. In other words, E_{tot} provides a potential for the nuclear motions. The solutions to the nuclear equation,

$$\hat{\mathcal{H}}_{nucl} \Phi_{nucl} = E \Phi_{nucl}, \quad (3.16)$$

describe the vibrations, rotations, and translations of the system, and E is the total energy in the Born-Oppenheimer approximation, which contains electronic, vibrational, rotational, and translational energy. This approximation is extremely efficient, and is used by default in quantum chemical calculations.

The variation principle

The first target of quantum chemistry is to solve the Schrödinger equation for the electronic motions in molecules. To address this challenge, approximate solutions to the eigenvalue problem,

$$\hat{\mathcal{H}} |\Psi\rangle = E |\Psi\rangle, \quad (3.17)$$

are required, since the Schrödinger equation cannot be solved exactly, except for simple cases like hydrogenoids. Note that the "elec" subscripts are dropped for clarity in the rest of this chapter. The variational method,⁸ which follows the variation theorem is useful to find approximate solutions to Eq. (3.17). The variation theorem (or variation principle) states that the energy of an approximate wavefunction is always higher or equal than the exact energy of the lowest energy state (namely, the exact ground state in a non-relativistic regime, with the unconstrained variational space).⁶ Hence, a normalized trial wavefunction, $|\tilde{\Psi}\rangle$, satisfies

$$\langle \tilde{\Psi} | \hat{\mathcal{H}} | \tilde{\Psi} \rangle \geq E_0 = \langle \Psi_0 | \hat{\mathcal{H}} | \Psi_0 \rangle, \quad (3.18)$$

considering the fact that the eigenfunctions of the Hamiltonian are orthonormal and form a complete set, which allows defining all wavefunctions,

$$\tilde{\Psi} = \sum_{\alpha} c_{\alpha} \Psi_{\alpha}. \quad (3.19)$$

Determining the approximate wavefunction of a system resumes in (i) choosing the initial wavefunction (*e.g.* its form) depending on variational parameters, and (ii) minimizing its energy with respect to these parameters.

3.2 The antisymmetry of the wavefunction and Slater determinants

As mentioned previously in this section, the complete description of an electron includes its spin. However, the Hamiltonian operator depends only on the spatial coordinates of the particles. The reader should note that in a non-relativistic approach, the spin functions $\alpha(\omega)$ and $\beta(\omega)$, corresponding to spin up and down, respectively (ω is an unspecified spin variable), are simply added to the description but they derive naturally from the Dirac equation. Consequently, Dirac⁹ and Heisenberg¹⁰ independently proposed that: *the wavefunction of electronic motions must be antisymmetric with respect to the interchange of the spin-space coordinates of any electron pair*,

$$\Psi(\mathbf{x}_1, \mathbf{x}_2, \dots, \mathbf{x}_i, \dots, \mathbf{x}_j, \dots, \mathbf{x}_N) = -\Psi(\mathbf{x}_1, \mathbf{x}_2, \dots, \mathbf{x}_j, \dots, \mathbf{x}_i, \dots, \mathbf{x}_N), \quad (3.20)$$

to satisfy the Pauli exclusion principle.¹¹ This antisymmetry principle, which subsequently leads to the inclusion of the so-called exchange interaction, is enforced by using Slater determinants.¹² That is, for an N -electron system,

$$\Psi(\mathbf{x}_1, \mathbf{x}_2, \dots, \mathbf{x}_N) = \frac{1}{\sqrt{N!}} \begin{vmatrix} \Theta_1(\mathbf{x}_1) & \Theta_2(\mathbf{x}_1) & \cdots & \Theta_N(\mathbf{x}_1) \\ \Theta_1(\mathbf{x}_2) & \Theta_2(\mathbf{x}_2) & \cdots & \Theta_N(\mathbf{x}_2) \\ \vdots & \vdots & \ddots & \vdots \\ \Theta_1(\mathbf{x}_N) & \Theta_2(\mathbf{x}_N) & \cdots & \Theta_N(\mathbf{x}_N) \end{vmatrix} = |\Theta_i \Theta_j \dots \Theta_k\rangle, \quad (3.21)$$

where $1/\sqrt{N!}$ is a normalization factor. The wavefunction of Eq. (3.21) is a (single) Slater determinant built out of the occupied molecular spinorbitals $\Theta_i(\mathbf{x}_1) = \phi_i(\mathbf{r}_1)\sigma_i(\omega_1)$ where ϕ is

the space function and σ is the spin function, which may be either α or β . This corresponds to the wavefunction optimized within the Hartree-Fock (HF) approximation,¹³ where the motions of electrons with antiparallel spins are independent and have no correlation with each other. Subsequently, the electron correlation effects can be included by considering linear combinations of Slater determinants (Section 3.3).

The LCAO approximation and the atomic basis sets

Quantum chemistry methods often involve the Linear Combination of Atomic Orbitals (LCAO) approximation¹⁴ to resolve integro-differential equations, such as the Kohn-Sham equation (Section 3.4). In this algebraic approach, spatial parts of the spin orbitals, or molecular orbitals (MOs), are expanded as

$$\phi_i(\mathbf{r}) = \sum_p^K C_{pi} \chi_p(\mathbf{r}), \quad (3.22)$$

where K is the size of the basis set, C_{pi} are the expansion coefficients, also called MO coefficients, and $\{\chi_p\}$ is the set of atomic orbitals. These MO coefficients are typically obtained to minimize the electronic energy of system (Section 3.1).

From Eq. (3.22), it becomes evident that the accuracy of the wavefunction and its related computational time (CPU) depend on the quality and number of basis functions. At first sight, Slater functions ($e^{-\zeta r}$) are best, since actual atomic orbitals, like those of hydrogenoids, present that mathematical form. However, for the matter of the speed of evaluation of two-electron integrals (Section 3.4), Gaussian-Type Orbitals (GTO) are preferred.⁶ A good compromise, proposed by Boys,¹⁵ is obtained by using contracted Gaussian-type basis functions, which are linear combinations of GTO. Contracted Cartesian Gaussian-type functions are expressed as follows:¹⁶

$$\chi_q(\mathbf{r} - \mathbf{R}_A) = \sum_{\mu}^{N_{cont}} c_{\mu q} (r_x - R_{A,x})^a (r_y - R_{A,y})^b (r_z - R_{A,z})^c N_{\mu q} e^{-\alpha_{\mu q} |\mathbf{r} - \mathbf{R}_A|^2}. \quad (3.23)$$

In this equation, the original Gaussian functions are called primitive functions, $c_{\mu q}$, $\alpha_{\mu q}$, and $N_{\mu q}$ are the contraction coefficients and exponents, and normalization factors of the primitives, respectively, and the sum of a , b , c defines the angular momentum number ℓ . \mathbf{R}_A is the point where the function is centered, usually a nucleus. For a QC calculation using the HF method and contracted GTOs, the CPU time needed scales in K^4 .¹⁷

Several types of contracted Gaussian-type basis functions were developed over the years,

and many of them are available on the Basis Set Exchange platform.¹⁸ In this section, a non-extensive summary^{4,6} of the different basis sets families is presented, with a particular focus on the Pople basis sets,¹⁹⁻²³ since they are used in this Master thesis:

- **Minimal basis sets (or single- ζ)** contain only the least number of functions per atom required to describe the occupied atomic orbitals (AOs) of that isolated atom. Since a small number of functions is used, one prefers to employ the terminology Slater-type functions, *e.g.* the STO-LG sets,¹⁹ which consist in one contraction of L primitives for each basis function; where the contraction coefficients and exponents are chosen to minimize the deviation from reference Slater orbitals.
- **Multiple- ζ basis sets** include multiple contractions of primitive Gaussians for each occupied AO. For example, TZP, a triple- ζ basis set, contains three basis functions for each occupied AO in the isolated atom.
- **Split valence basis sets** use one contraction for the core orbitals, but multiple contractions for the valence orbitals, *i.e.* there is a single- ζ representation of the core shells and a multiple- ζ representation of the valence shells. Indeed, in a non-relativistic approach, the inner shells contribute slightly to most molecular properties, and do not vary much between different molecules. In this family, the Pople basis sets are named from the number of contractions and primitives, *e.g.* the valence double- ζ 6-31G²⁴ basis set consists in one contraction of 6 primitives for each core AO, and in the doubly-split basis functions combining one contraction of 3 primitives and one uncontracted Gaussian function for each outermost orbital of the atom. Triply-split basis functions for valence orbitals, such as in 6-311G,²² are constructed in a similar way. Note that Dunning-Huzinaga-type^{25,26} (DZ, TZ, and QZ) and Ahlrichs-type^{27,28} (DZV, TZV, and QZV) basis sets are also included in this category.
- **Polarized basis sets** improve the previously discussed basis sets by adding polarization functions, which take into account the anisotropy of the MOs, caused by the chemical bonds. Without these polarization functions, only orbitals with the same symmetries as those of the occupied AOs in the isolated atoms are included into the basis sets. Nevertheless, the MOs show lower symmetry than those occupied AOs, and functions of different symmetry can contribute to the wavefunction of the molecular system. Hence, functions of higher angular momentum, the polarization functions, describe the polarization of the

charge distribution upon chemical bonding. For example, adding *d*-symmetry GTOs with similar radial size as *p*-functions on carbon *C*-atoms allows the *p* and *d* functions to be combined through the LCAO process to form π bonds. This combination produces in fact a *p* function, bent on one side.¹⁷ One can see this improvement in the following way: while going from minimal to multiple- ζ basis improves the radial part of the wavefunction, adding polarization functions improves the angular part of the latter.²⁹ In Pople basis sets, including one set of polarization functions on heavy atoms (starting from the second row of the periodic table of elements) is symbolized by "*", such as 6-311G*²¹; while including additional *p* functions on the hydrogen atoms is represented by "**", such as 6-311G**.²¹ One could also specify all the types of added higher angular momentum functions, which can lead to very extended basis sets, *e.g.* 6-311G(3*df*,2*pd*).

- **Diffuse-function-augmented basis sets** add basis functions with very small exponents, which are called diffuse functions, in order to describe the distribution of weakly bonded electrons. Adding one set of *sp* diffuse functions on all atoms except hydrogen atoms is represented by a "+" in Pople basis sets, such as in 6-311+G*.²³ Then, a second set of diffuse functions for all atoms except hydrogens, and one set of functions for hydrogens is shown by "++", such as in 6-311++G*.²⁴
- **Correlation-consistent basis sets** developed by Dunning *et al.*,^{30,31} noted cc-pVXZ, are another family of basis sets. The "p" stands for the polarization functions that are added on all atoms, and "X" is the cardinal number referring to the number of contractions per AO.²⁹ Augmenting these sets with diffuse functions is noted by adding the prefix "aug", such as aug-cc-pVTZ.

The list of basis sets families presented above is not complete. Basis sets such as **effective core potential (ECP)**³² also exist (widely used for adding implicitly relativistic effects to inner shells), but are out of the scope of this work. One should also note that an artificial energy stabilization can originate from the overlap of the nonorthogonal Gaussian-type basis functions, making the atoms closer to each other. The error is called basis set superposition error (BSSE), and should be corrected to reproduce correctly weak bonds.⁴ However large basis sets lead to a more flexible description of the wavefunction, which reduces the BSSE.

Natural bond orbitals

The Lewis structure of a molecular system can help predicting its physical properties, and it furnishes powerful clues for investigating hyperconjugative interactions. One way to obtain the Lewis structure is to consider a somewhat "chemist basis set", the natural bond orbitals (NBO).³³ In the rest of this section, we are only concerned with the closed-shell NBOs. The NBO for a localized σ bond between two atoms A and B, σ_{AB} , is built out of the orthonormal natural hybrid orbitals (NHOs), h_A , h_B , and their c_A and c_B coefficients,

$$\sigma_{AB} = c_A h_A + c_B h_B, \quad (3.24)$$

and the NHOs are formed from the natural atomic orbitals (NAOs),^{34,35}

$$\{\chi_q\} \longrightarrow NAOs \longrightarrow NHOs \longrightarrow NBOs. \quad (3.25)$$

Similarly, the generated unoccupied orbitals (in the formal Lewis structure), σ^* , are constructed from the same atomic valence-shell hybrids as the occupied NBOs,

$$\sigma_{AB}^* = c_B h_A - c_A h_B. \quad (3.26)$$

Let's now detail the procedure schematized by Eq. (3.25). The first stage to form the NAOs (and subsequently the NBOs) is an occupancy-weighted symmetric orthogonalization (OWSO) of the chosen AO basis set:³⁶

$$\mathbf{T}_{OWSO}\{\chi_p\} = \{\chi'_p\}, \quad \langle \chi'_p | \chi'_q \rangle = \delta_{pq}. \quad (3.27)$$

The transformation matrix \mathbf{T}_{OWSO} in the OWSO procedure minimizes the mean-squares deviations of the orthogonal χ'_p from the initially chosen AOs, χ_p ,

$$\sum_p w_p \int |\chi'_p - \chi_p|^2 d\tau, \quad (3.28)$$

where w_p is the weighting factor corresponding to the occupancy of χ_p , the diagonal expectation value of the density matrix \mathbf{P} ,

$$w_p = \langle \chi_p | \mathbf{P} | \chi_p \rangle. \quad (3.29)$$

So, the orbitals of maximum occupancies (maximum-occupancy hybrid orbitals) can be computed from the full density matrix, \mathbf{P} . However, in the search for the optimal natural hybrid orbitals for each atom, \mathbf{P} should first be partitioned into subblocks: the submatrices $\mathbf{P}^{(A)}$ (for all A), associated with atomic orbitals on any center A , and the two-center submatrices $\mathbf{P}^{(AB)}$, associated with bond orbitals, σ_{AB} , between any pair of A and B atoms.³³

Diagonalizing the localized block $\mathbf{P}^{(A)}$ leads to pre-NAOs, which are eigenfunctions of the one-electron density matrix, and the associated eigenvalues, the occupancies, represent a measure of the contributions that the different natural atomic orbitals make to the full density matrix.²⁹ The final NAOs are obtained by removing the interatomic overlaps by the OWSO procedure (Eqs. (3.28) and (3.29)). This corresponds to solving the following eigenvalue problem,

$$\mathbf{P}^{(A)}\chi'_p = q_p^{(A)}\chi'_p. \quad (3.30)$$

The orthonormal NAOs, $\{\chi'_q\}$, allow one to achieve a natural population analysis (NPA),³⁵ which is an improvement of the commonly used Mulliken population analysis.³⁷ The natural populations on centers A , $q_p^{(A)}$, are simply the occupancies of the NAO,

$$q_p^{(A)} = \langle \chi'_p | \mathbf{P}^{(A)} | \chi'_p \rangle, \quad (3.31)$$

and the atomic population is given by

$$q^{(A)} = \sum_p q_p^{(A)}, \quad N_{elec} = \sum_A^{atoms} q^{(A)}. \quad (3.32)$$

The second stage consists in the search for the optimal natural Lewis structure. In a practical way, in the NBO program,^{35,38} NAOs with occupancies superior to 1.999 e are considered as unhybridized core orbitals. Then, the one center eigenfunctions whose occupancies exceed a certain threshold are taken as lone electron pairs (LEPs). After that, a similar operation is performed on the two-center submatrices, where the program looks for bond orbitals with occupancies superior to another threshold. Finally, each σ_{AB} is decomposed into its hybrid contributions, following Eq. (3.24). The natural hybrids (NHOs) are obtained, once again, after a symmetric orthogonalization to remove the atomic overlaps.

One could note that the OSWO procedure is similar to the Löwdin symmetric orthogonalization (LSO).³⁹ In the latter, w_p is chosen as equal to 1 for each p . Therefore, the OWSO method tends to preserve the shape of the valence orbitals of atoms with nearly filled valence shells,

while LSO treats nearly filled and nearly empty valence shells in the same manner. However, for minimal basis sets, the two methods should produce similar orbital, meaning that

$$\mathbf{T}_{OWSO} \simeq \mathbf{T}_{LSO} = \mathbf{S}^{-\frac{1}{2}}, \quad (3.33)$$

where \mathbf{S} is the overlap matrix.

On this basis, the total energy, E , can be decomposed into a covalent part, $E_{\sigma\sigma} = E_{Lewis}$, and into a noncovalent contribution, $E_{\sigma\sigma^*} = E_{non-Lewis}$:

$$E = E_{\sigma\sigma} + E_{\sigma\sigma^*}. \quad (3.34)$$

Here, the " σ " and " σ^* " notations refer to filled and unfilled orbitals in the ideal Lewis structure, respectively. These orbitals can be core orbitals, LEP, actual σ or π bonds, etc.

The general quality of the natural valence Lewis structure description used for this analysis is given in terms of the percentage of the total Lewis electron density. The deviations from the ideal Lewis structure are usually so small that simple second-order perturbative expressions are a good approximation to describe the corrections to these deviations.³⁶ Eq. (3.35) gives the second-order energy lowering, $\Delta E_{\sigma\sigma^*}^{(2)}$, the interaction energy between a filled orbital σ and an unfilled antibonding orbital σ^* (in the SCF-MO theory frame) as pictured in Fig. 3.1:

$$\Delta E_{\sigma\sigma^*}^{(2)} = -2 \frac{|\langle \sigma | \hat{F} | \sigma^* \rangle|^2}{\epsilon_{\sigma^*} - \epsilon_{\sigma}}, \quad (3.35)$$

where \hat{F} is the Fock operator, while ϵ_{σ^*} and ϵ_{σ} are the corresponding NBO energies.

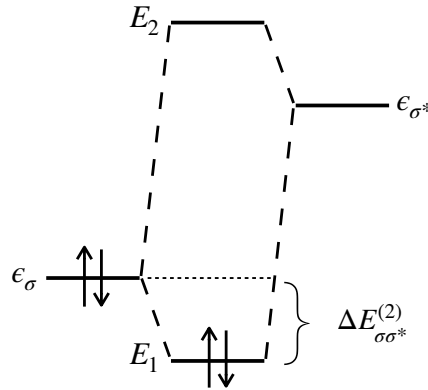


Fig. 3.1: Noncovalent energy lowering resulting from the perturbative interaction between a filled orbital σ and a unfilled antibonding orbital σ^* (reproduced from Ref. 36).

3.3 Electron correlation

The Hartree-Fock wavefunction is the simplest way to treat many-electron systems since it is built out of a single Slater determinant, which is based on the independent particle model with the correct antisymmetry. However, it is well known that this method is not adapted to reach high chemical accuracy. This problem is attributed to the lack of electron correlation, firstly introduced by Löwdin⁴⁰ as the difference between the exact and the HF energy,

$$E_{corr} = E_{exact} - E_{HF}. \quad (3.36)$$

This difference is generally of the order of 1% on the total energy of the system but it has a huge impact on the energies of reaction and molecular properties, to name a few.

Coulomb hole and Coulomb cusp

From the expression of the electronic Hamiltonian operator,

$$\hat{\mathcal{H}} = -\frac{1}{2} \sum_i^N \nabla_i^2 - \sum_i^N \sum_A^M \frac{Z_A}{r_{iA}} + \frac{1}{2} \sum_i^N \sum_{j \neq i}^N \frac{1}{r_{ij}}, \quad (3.37)$$

it is easily conceivable that $\hat{\mathcal{H}}$ should have singularities for $r_{iA} = 0$ and $r_{ij} = 0$. Considering the exact wavefunction, and assuming a hypothetical two-electron system where one of these electrons is at a fixed position, the probability amplitude of the other electron is shifted away from the fixed electron. This indicates that Ψ has a hole at $r_{ij} = 0$, which is called a Coulomb hole. This hole reduces Coulomb interaction between the two electrons, and lowers the total energy.

At the singularities, in a non-relativistic regime, the wavefunction is finite, and these singularities must be counterbalanced by other contributions of the exact solution to the Schrödinger equation to ensure that the local energy is conserved equal to the eigenvalue (see Ref. 29 for more details). The only possible other contribution is the kinetic energy, and to produce an infinite local kinetic energy, the wavefunction must be nondifferentiable at the singularities. Hence, Kato⁴¹ established a cusp condition for the behavior of the wavefunction in the vicinity of the singularities, which reads, for nearly coinciding electrons:

$$\lim_{r_{ij} \rightarrow 0} \left(\frac{\partial \Psi}{\partial r_{ij}} \right) = \frac{1}{2} \Psi(r_{ij} = 0). \quad (3.38)$$

Consequently, Ψ has discontinuous first-order derivatives at $r_{ij} = 0$, and can be approximated by an exponential function in that region. Nevertheless, the latter should not vanish for coinciding electrons.⁴

The HF wavefunction violates the cusp condition, and allows anti-parallel-spin electrons to be found at the same position. Moreover Ψ_{HF} is vanishing at this same singularity for parallel-spin electrons, which is translated into a hole for these electron pairs. This arises from the antisymmetrization of the wavefunction, and is referred to as Fermi correlation (or exchange correlation), but has nothing to do with the correlation energy.

Static and dynamical correlation

The preceding discussion exhibited the fact that the HF wavefunction is not adequate to describe electron correlation since it does not respect the Coulomb cusp condition, which decreases the Coulomb overlap between ϕ_i and ϕ_j , leading to an energy stabilization. The correlation cusp condition is also called dynamic correlation, because it is a short-range effect connected to the actual motion of individual electrons. Additionally, there is static electron correlation (or nondynamical), which arises from direct interaction between (near-)degenerate electron configurations (long-range interactions). In these cases, the ground state (GS) HF Slater determinant is not sufficient to describe the real GS, since other determinants present similar energies.⁴² This is particularly important at the dissociation limit where bonding and anti-bonding electron configurations interact strongly.^{4,29}

To account for both correlation effects, one should consider linear combinations of electronic configurations, given by Slater determinants. A straightforward (and variational) method to do so is called the configuration interaction (CI) method, where each determinant corresponds to a configuration state function (CSF). The exact wavefunction, called full configuration interaction (FCI), is built over all possible CSFs (and in theory, with an infinite AO basis set),

$$|FCI\rangle = \sum_I C_I |\Psi_I\rangle, \quad (3.39)$$

where the C_I are the CI coefficients, and take an amplitude between 0 and 1.

Practically, using the FCI method with an extensive basis set is extremely computationally expensive, and other state-of-the-art post-HF methods are preferred, even though, also limited to small systems. Indeed, the overall CPU time for such methods is tremendous, as it also depends on the number of CSFs.¹⁷ For routine computations on large systems, the density

functional theory method (DFT) is widespread. The density functional theory method is a quantum chemistry method based on the electron density, that incorporates electron correlation through exchange-correlation functionals, as described in the next Section.

3.4 Density functional theory

The probability interpretation of the wavefunction gives access to the one-electron density, or rigorously speaking, the one-electron probability density, $\rho(\mathbf{r})$,

$$\rho(\mathbf{r}) = N \int \cdots \int \Psi^*(\mathbf{x}, \mathbf{x}_2, \dots, \mathbf{x}_N) \Psi(\mathbf{x}, \mathbf{x}_2, \dots, \mathbf{x}_N) d\omega d\mathbf{x}_2 \dots d\mathbf{x}_N, \quad (3.40)$$

which determines the probability of finding any of the N electrons (with arbitrary spin) within the volume element $d\mathbf{r}$, and the $N-1$ other electrons anywhere else. $\rho(\mathbf{r})$ is a positive function, which vanishes at infinity, and that integrates to the total number of electrons:

$$\rho(\mathbf{r} \rightarrow \infty) = 0, \quad (3.41)$$

$$\int \rho(\mathbf{r}) d\mathbf{r} = N. \quad (3.42)$$

Moreover, the electron density is an observable that presents a finite value for each \mathbf{r} . Therefore, $\rho(\mathbf{r})$ exhibits a cusp for $r_{iA} \rightarrow 0$, *i.e.* when the Hamiltonian operator has singularities.

Back to electron correlation

Similarly to Eq. (3.40), the pair density,

$$\rho_2(\mathbf{x}_1, \mathbf{x}_2) = N(N-1) \int \cdots \int \Psi^*(\mathbf{x}_1, \mathbf{x}_2, \dots, \mathbf{x}_N) \Psi(\mathbf{x}_1, \mathbf{x}_2, \dots, \mathbf{x}_N) d\mathbf{x}_3 \dots d\mathbf{x}_N, \quad (3.43)$$

defines the probability of finding simultaneously two electrons, here with spins σ_1 and σ_2 , within two volume elements $d\mathbf{r}_1$ and $d\mathbf{r}_2$, and the $N-2$ other electrons anywhere else. $\rho_2(\mathbf{x}_1, \mathbf{x}_2)$ is also a non-negative quantity, and contains all the information about electron correlation.⁴²

First, it can be seen that, in the case of coinciding electrons and with respect to the anti-symmetry principle,

$$\rho_2(\mathbf{x}_1, \mathbf{x}_1) = -\rho_2(\mathbf{x}_1, \mathbf{x}_1), \quad (3.44)$$

which is only possible if $\rho_2(\mathbf{x}_1, \mathbf{x}_1) = 0$. As for Ψ_{HF} , there is no probability of finding two

parallel-spin electrons at the same position, due to the Pauli principle. Hence, the Fermi correlation also holds for the electron density.

Then, the inclusion of the Coulomb correlation (as well as the Fermi correlation) is obtained by expressing the pair density as follows:

$$\rho_2(\mathbf{x}_1, \mathbf{x}_2) = \rho(\mathbf{x}_1)\rho(\mathbf{x}_2)[1 + f(\mathbf{x}_1, \mathbf{x}_2)], \quad (3.45)$$

where $f(\mathbf{x}_1, \mathbf{x}_2)$ is the correlation factor. For an independent-particle system, $f(\mathbf{x}_1, \mathbf{x}_2) = 0$, and the pair density resumes in the product of the one-electron densities. Consequently, one can express the total hole (Coulomb and Fermi) as a function of the correlation factor,

$$h_{XC}(\mathbf{x}_1, \mathbf{x}_2) = \rho(\mathbf{x}_2)f(\mathbf{x}_1, \mathbf{x}_2), \quad (3.46)$$

where $h_{XC}(\mathbf{x}_1, \mathbf{x}_2)$ is called the exchange-correlation hole, and integrates to the charge of one electron,

$$\int h_{XC}(\mathbf{x}_1, \mathbf{x}_2)d\mathbf{x}_2 = -1. \quad (3.47)$$

Finally, the expectation value of the electron-electron repulsion part of the electronic Hamiltonian operator, V_{ee} , corresponding to the potential energy due to electrostatic repulsion,

$$V_{ee} = \left\langle \Psi \left| \frac{1}{2} \sum_i^N \sum_{j \neq i}^N \frac{1}{r_{ij}} \right| \Psi \right\rangle = \frac{1}{2} \int \int \frac{\rho_2(\mathbf{r}_1, \mathbf{r}_2)}{r_{12}} d\mathbf{r}_1 d\mathbf{r}_2, \quad (3.48)$$

can be expressed in terms of the exchange-correlation hole:

$$V_{ee} = \frac{1}{2} \int \int \frac{\rho(\mathbf{r}_1)\rho(\mathbf{r}_2)}{r_{12}} d\mathbf{r}_1 d\mathbf{r}_2 + \frac{1}{2} \int \int \frac{\rho(\mathbf{r}_1)h_{XC}(\mathbf{r}_1, \mathbf{r}_2)}{r_{12}} d\mathbf{r}_1 d\mathbf{r}_2 \quad (3.49)$$

$$= \frac{1}{2} \int \rho(\mathbf{r}_1)J(\mathbf{r}_1)d\mathbf{r}_1 + \frac{1}{2} \int \int \frac{\rho(\mathbf{r}_1)h_{XC}(\mathbf{r}_1, \mathbf{r}_2)}{r_{12}} d\mathbf{r}_1 d\mathbf{r}_2. \quad (3.50)$$

The first term in the right hand side is the classical repulsion energy, while the second term includes exchange and correlation effects (non-classical part). The former is related to the Coulomb potential, $J[\rho(\mathbf{r})]$, due to the electron density $\rho(\mathbf{r})$, which describes the Coulombic repulsion of an electron at \mathbf{r} with the full electron density $\rho(\mathbf{r}')$. One should note that $J[\rho(\mathbf{r})]$ also includes the self-interaction, but h_{XC} contains a correction to this nonphysical contribution.

Principle of DFT

So far in this Section, it was seen that electron correlation could be well included in the electron density to describe the electron-electron interactions. Furthermore, the electronic Hamiltonian operator contains only terms that act on one electron, namely the electron kinetic energy operator (\hat{T}) and the nuclei-electron attraction (\hat{V}_{ne}), or on two electrons at the most (\hat{V}_{ee}). On that basis, the density functional theory was developed. This method aims at replacing the complicated wavefunction that depends on $4N$ variables by the electron density, $\rho(\mathbf{r})$, that depends only on the three spatial variables.^{4,42}

The first attempt of a density functional for the energy of an atom (nucleus of atomic number Z at the origin) was accomplished by the Thomas-Fermi method,^{43,44}

$$E_{TF}[\rho(\mathbf{r})] = \frac{3}{10}(3\pi^2)^{\frac{2}{3}} \int \rho(\mathbf{r})^{\frac{5}{3}} d\mathbf{r} - Z \int \frac{\rho(\mathbf{r})}{r} d\mathbf{r} + \frac{1}{2} \iint \frac{\rho(\mathbf{r})\rho(\mathbf{r}')}{|\mathbf{r} - \mathbf{r}'|} d\mathbf{r} d\mathbf{r}', \quad (3.51)$$

where the first term, the kinetic energy, is a rough approximation that neglects all correlation effects. This kinetic energy functional was the first local density approximation (LDA). This model is not adapted for molecules due to its inability to describe chemical bonding.⁴⁵ Then, to solve partially the problem, Dirac proposed the first exchange functional,⁴⁶

$$E_{LDA} = -\frac{3}{4} \left(\frac{3}{\pi} \right)^{\frac{1}{3}} \int \rho(\mathbf{r})^{\frac{4}{3}} d\mathbf{r}, \quad (3.52)$$

which is known as the exact LDA exchange functional. Later, a correction including the gradient of the electron density, $\nabla\rho(\mathbf{r})$, was proposed by von Weizsäcker,⁴⁷ which is considered as the first generalized gradient approximation (GGA),

$$T_W = \frac{1}{8} \int \frac{|\nabla\rho(\mathbf{r})|^2}{\rho(\mathbf{r})} d\mathbf{r}. \quad (3.53)$$

However, these models stay not reliable, even for qualitative discussions, and therefore, the density functional theory was forgotten until the publication of the Hohenberg and Kohn (HK) theorems in 1964,⁴⁸ the central concepts of modern DFT.

On the one hand, the first theorem actually proves the previous assumptions, that the electron density completely defines the Hamiltonian operator. Indeed, the first theorem states that: *the external potential $V_{ext}(\mathbf{r})$ is (to within a constant) a unique functional of $\rho(\mathbf{r})$; since, in turn $V_{ext}(\mathbf{r})$ fixes $\hat{\mathcal{H}}$, the full many-particle ground state is a unique functional of $\rho(\mathbf{r})$.*

Hence, the GS electronic energy can be written as a functional of the GS electron density,⁴²

$$E_0[\rho_0(\mathbf{r})] = T[\rho_0(\mathbf{r})] + V_{Ne}[\rho_0(\mathbf{r})] + V_{ee}[\rho_0(\mathbf{r})], \quad (3.54)$$

where the external potential is generally specified as the attraction due to the nuclei. This equation can be rewritten in the following way:

$$E_0[\rho_0(\mathbf{r})] = \int \rho_0(\mathbf{r}) V_{ext}(\mathbf{r}) d\mathbf{r} + F_{HK}[\rho_0(\mathbf{r})], \quad (3.55)$$

where the first term is the external potential. This equation also introduced the Hohenberg-Kohn functional, which sums the expectation values of the kinetic energy and electron-electron repulsion operators,

$$F_{HK}[\rho(\mathbf{r})] = T[\rho(\mathbf{r})] + V_{ee}[\rho(\mathbf{r})] = \langle \Psi | \hat{T} + \hat{V}_{ee} | \Psi \rangle. \quad (3.56)$$

It is important to note that the functional form of F_{HK} cannot be determined. However, if it were known, the Schrödinger equation would be solved exactly, since this functional contains all the information about the kinetic energy and the electron-electron interactions.

On the other hand, the second theorem states that *the energy variational principle is always established for any electron density*. This proves that the Hamiltonian operator, defined by $\rho(\mathbf{r})$, has a solution of minimum energy.⁴ Therefore, the ground state of an electronic system can be completely described by its electron density, and $\rho_0(\mathbf{r})$ can be determined by minimizing the energy of the system.

Kohn-Sham Method

From the HK functional, rewritten by separating V_{ee} into its classical and non-classical contributions,

$$F_{HK}[\rho(\mathbf{r})] = T[\rho(\mathbf{r})] + J[\rho(\mathbf{r})] + V_{non-classical}[\rho(\mathbf{r})], \quad (3.57)$$

one issue to apply the Hohenberg and Kohn theorems is to find an accurate expression for $T[\rho(\mathbf{r})]$. Indeed, representations where kinetic energy (and exchange contribution) are explicit functionals of the electron density, such as the Thomas-Fermi-Dirac model, failed badly to obtain accurate results. To solve the problem, the Kohn-Sham (KS) method⁴⁹ was developed, which is an exact application of the Hohenberg and Kohn theorems.

The Kohn-Sham method consists of substituting the real interacting-electron system by a fictitious system of non-interacting electrons moving in a effective potential. These non-interacting electrons obey the antisymmetry principle. In Section 3.1, it was established that the exact wavefunction of a non-interacting electronic system is a single Slater determinant, such as the HF wavefunction (Eq. (3.21)). Consequently, the molecular spinorbitals are reintroduced, here as Kohn-Sham spinorbitals, $\Theta_{KS,i}(\mathbf{r}, \omega)$; so that the one-electron density in Eq. (3.40) becomes:

$$\rho(\mathbf{r}) = \sum_i^N \int |\Theta_{KS,i}(\mathbf{r}, \omega)|^2 d\omega, \quad (3.58)$$

which is exactly equal to the GS electron density of the real interacting system. The non-interacting Hamiltonian operator, $\hat{\mathcal{H}}_S$, is not defined by an explicit repulsion potential, V_{ee} , but by an effective local potential, $V_{eff}(\mathbf{r})$,⁴²

$$\hat{\mathcal{H}}_S = -\frac{1}{2} \sum_i^N \nabla_i^2 + \sum_i^N V_{eff}(\mathbf{r}_i), \quad (3.59)$$

so the kinetic energy can be computed in a simple and approximate way,

$$T_S = \sum_i^N \left\langle \Theta_{KS,i} \left| -\frac{1}{2} \nabla^2 \right| \Theta_{KS,i} \right\rangle. \quad (3.60)$$

Hence, the new density functional, $F_{KS}[\rho(\mathbf{r})]$, reads:

$$F_{KS}[\rho(\mathbf{r})] = T_S[\rho(\mathbf{r})] + J[\rho(\mathbf{r})] + E_{XC}[\rho(\mathbf{r})], \quad (3.61)$$

and the energy functional of the real interacting system is given by:

$$E[\rho(\mathbf{r})] = T_S[\rho(\mathbf{r})] + J[\rho(\mathbf{r})] + E_{XC}[\rho(\mathbf{r})] + V_{Ne}[\rho(\mathbf{r})], \quad (3.62)$$

where E_{XC} is the exchange-correlation energy, which incorporates the remaining part of the real kinetic energy, since the non-interacting kinetic energy, $T_S[\rho(\mathbf{r})]$, is not equal to $T[\rho(\mathbf{r})]$. In addition, $E_{XC}[\rho(\mathbf{r})]$ contains all the non-classical electrostatic contributions. To quote the book by Koch and Holthausen,⁴² *E_{XC} is the functional, which contains everything that is unknown, a kind of junkyard where everything is stowed away, which we do not know how to handle exactly.*

The energies of the spinorbitals, ϵ_i , are computed by solving the Kohn-Sham integro-differential equation,

$$\hat{f}^{KS}(\mathbf{r}) \Theta_{KS,i}(\mathbf{x}) = \epsilon_i \Theta_{KS,i}(\mathbf{x}). \quad (3.63)$$

which derives from the minimization of the energy in Eq. (3.62) using the Lagrange multiplier method, under the orthogonality constraint, $\langle \Theta_{KS,i} | \Theta_{KS,j} \rangle = \delta_{ij}$. In this equation, $\hat{f}^{KS}(\mathbf{r})$ is the Kohn-Sham operator,

$$\hat{f}^{KS}(\mathbf{r}) = -\frac{1}{2}\nabla^2 + \hat{J}(\mathbf{r}) + \hat{V}_{XC}(\mathbf{r}) + \hat{V}_{Ne}(\mathbf{r}) \quad (3.64)$$

$$= -\frac{1}{2}\nabla^2 + \int \frac{\rho(\mathbf{r}')d\mathbf{r}'}{|\mathbf{r} - \mathbf{r}'|} + \hat{V}_{XC}(\mathbf{r}) - \sum_A^M \frac{Z_A}{|\mathbf{r} - \mathbf{R}_A|} \quad (3.65)$$

$$= -\frac{1}{2}\nabla^2 + \hat{V}_{eff}(\mathbf{r}), \quad (3.66)$$

where the exchange-correlation potential corresponds to the functional derivative of the exchange-correlation energy with respect to the electron density,

$$\hat{V}_{XC}[\rho(\mathbf{r})] = \frac{\delta E_{XC}[\rho(\mathbf{r})]}{\delta \rho(\mathbf{r})}. \quad (3.67)$$

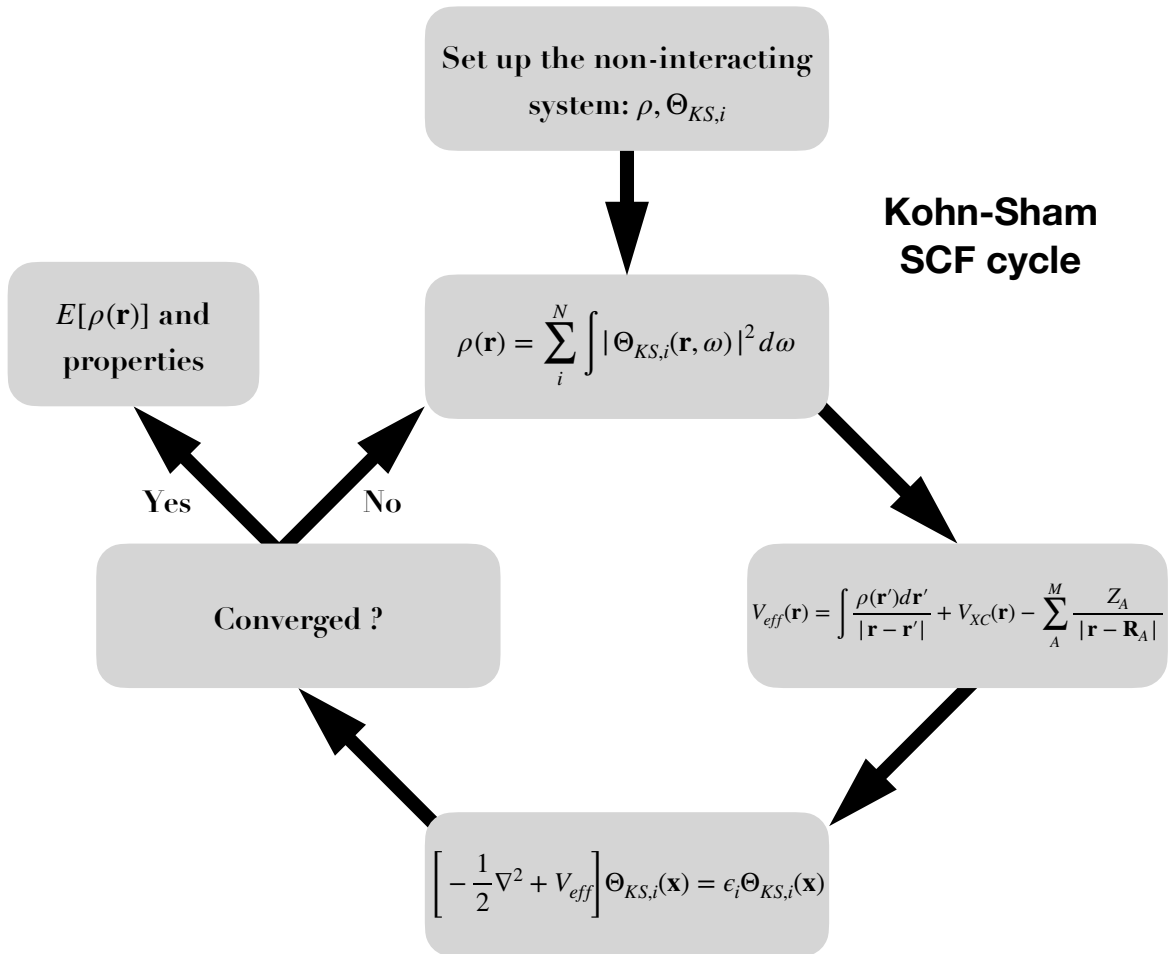


Fig. 3.2: Schematic view of the Kohn-Sham SCF iterative procedure.

Finally, one can express the total electronic energy of the system as follows:

$$E = \sum_i^N h_{ii} + \frac{1}{2} \sum_i^N \sum_j^N J_{ij} + E_{XC}. \quad (3.68)$$

where:

$$h_{ii} = \langle \Theta_{KS,i}(\mathbf{x}) | \hat{h}(\mathbf{r}) | \Theta_{KS,j}(\mathbf{x}) \rangle, \quad (3.69)$$

with $\hat{h}(\mathbf{r})$, the one-electron part of the KS operator,

$$\hat{h}(\mathbf{r}) = -\frac{1}{2} \nabla^2 + V_{Ne}(\mathbf{r}). \quad (3.70)$$

It should be noted that since V_{eff} depends on the spinorbitals, through the electron density in the Coulomb and exchange-correlation potential terms, *i.e.* it depends on the solutions of the KS equations. The Kohn-Sham method is therefore solved iteratively by the self-consistent field (SCF) procedure until self-consistency on the spinorbital energy is achieved as shown in Fig. 3.2.

Roothaan-Hall formulation

So far in this chapter, no method for practically solving the Kohn-Sham equations has been presented. For molecular systems, the Roothaan-Hall method^{50,51} is generally employed. The strategy is based on the LCAO-MO approximation (see Eq. (3.22)), and consists of converting the KS equation into a matrix equation,

$$\mathbf{F}^{KS} \mathbf{C} = \mathbf{S} \mathbf{C} \mathbf{E}, \quad (3.71)$$

where \mathbf{C} is the LCAO coefficient matrix, \mathbf{S} is the overlap matrix, *i.e.* the metric tensor linking the elements of \mathbf{F}^{KS} to those of \mathbf{C} , since the AO basis is not orthogonal,

$$S_{pq} = \langle \chi_p | \chi_q \rangle, \quad (3.72)$$

and \mathbf{E} is the diagonal matrix containing the orbital energies, ϵ_i . Using the expression of the density matrix elements (for a closed-shell system),

$$P_{rs} = \sum_j^{N/2} C_{rj} C_{sj}^*, \quad (3.73)$$

the elements of the \mathbf{F}^{KS} matrix are given as:

$$F_{pq}^{KS} = \langle \chi_p | \hat{f}^{KS} | \chi_q \rangle \quad (3.74)$$

$$= h_{pq} + 2 \sum_{r,s=1}^K P_{rs} \langle pr | qs \rangle + (V_{XC})_{pq}, \quad (3.75)$$

where the one-electron integrals, h_{pq} , are:

$$h_{pq} = \int \chi_p^*(\mathbf{r}) \left\{ -\frac{1}{2} \nabla^2 + V_{Ne}(\mathbf{r}) \right\} \chi_q(\mathbf{r}) d\mathbf{r}, \quad (3.76)$$

the two-electron integral, corresponding to the Coulomb term expressed in the AO basis, read:

$$\langle pr | qs \rangle = \int \int \chi_p^*(\mathbf{r}) \chi_r^*(\mathbf{r}') \frac{1}{|\mathbf{r} - \mathbf{r}'|} \chi_q(\mathbf{r}) \chi_s(\mathbf{r}') d\mathbf{r} d\mathbf{r}', \quad (3.77)$$

and $(V_{XC})_{pq}$ are the expectation values of the exchange-correlation potential using the given atomic orbitals,

$$(V_{XC})_{pq} = \langle \chi_p | \hat{V}_{XC} | \chi_q \rangle. \quad (3.78)$$

Solving the generalized eigenvalue problem in Eq. (3.71) is achieved by the SCF-LCAO-MO iterative procedure (Fig. 3.3). It involves i) Building \mathbf{F}^{KS} from an initial evaluation of the density matrix, ii) the transformation to a usual eigenvalue problem,

$$(\mathbf{F}^{KS})' \mathbf{C}' = \mathbf{C}' \mathbf{E}, \quad (3.79)$$

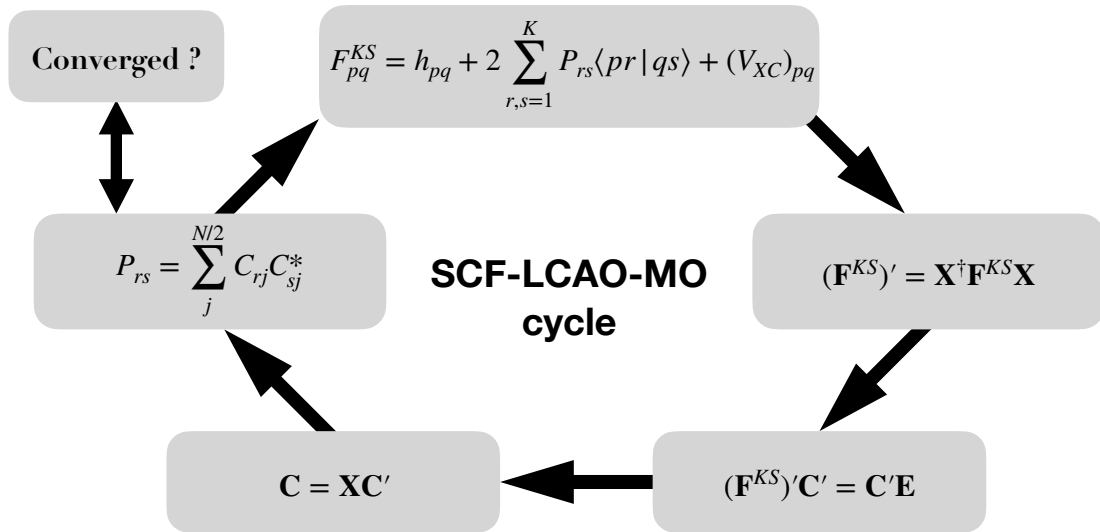


Fig. 3.3: Schematic view of the SCF-LCAO-MO iterative procedure.

which summarizes into the orthogonalization of the AO basis set, iii) diagonalizing $(\mathbf{F}^{KS})'$, which leads to \mathbf{C}' and \mathbf{E} , iv) evaluating \mathbf{C} from \mathbf{C}' , and finally v) computing \mathbf{P} to get back to the F_{pq}^{KS} matrix elements. Note that the orthogonalization in ii) can be either symmetric, with the transformation matrix equals to $\mathbf{S}^{1/2}$ as mentioned in previous discussions, or canonical.

3.5 Exchange-correlation functionals

Although the Kohn-Sham method is exact, the exchange-correlation energy, $E_{XC}[\rho(\mathbf{r})]$, (and so $V_{XC}[\rho(\mathbf{r})]$) remains unknown. The accuracy of the Kohn-Sham based DFT therefore relies on the quality of the exchange-correlation energy density functional, obtained thanks to an exchange-correlation functional (XCF). In this Section, the quest for more and more accurate XCFs is summarized by going through each rung of the Jacob's ladder,^{52,53} which separates the XCF families according to the number, kind, and locality of their contributions.

Local density approximation

The first rung regroups the functionals derived by applying uniform electron gas results directly on infinitesimal portions of the non-uniform densities. In general, LDA functionals have the simple following form:

$$E_{XC}^{LDA}[\rho(\mathbf{r})] = \int \rho(\mathbf{r}) \epsilon_{XC}^{LDA}[\rho(\mathbf{r})] d\mathbf{r}, \quad (3.80)$$

where the exchange-correlation energy per particle of the electron gas, $\epsilon_{XC}[\rho(\mathbf{r})]$, at position \mathbf{r} is a function of the density only, at point \mathbf{r} .⁵⁴ In Eq. (3.80), the energy per particle is weighted with the probability density, $\rho(\mathbf{r})$.⁴²

Furthermore, $\epsilon_{XC}^{LDA}[\rho(\mathbf{r})]$ can be split into its exchange and correlation contributions,

$$\epsilon_{XC}^{LDA}[\rho(\mathbf{r})] = \epsilon_X^{LDA}[\rho(\mathbf{r})] + \epsilon_C^{LDA}[\rho(\mathbf{r})]. \quad (3.81)$$

The former contribution is given by the Dirac expression (Eq. (3.52)), which is exact for an uniform electron gas, as briefly discussed in the Thomas-Fermi model. The correlation part is derived from quantum Monte-Carlo simulations.⁵⁵ One famous example of LDA XCF is SVWN, which combines the Vosko-Wilk-Nusair correlation functional⁵⁶ with the LDA exchange functional from Slater.⁵⁷

Density Gradient Expansions

Even if $E_{XC}[\rho(\mathbf{r})]$ is a functional of $\rho(\mathbf{r})$ alone, the dependence on $\rho(\mathbf{r})$ is nonlocal, *i.e.* the exchange-correlation potential at \mathbf{r} may be highly impacted by changes of density at \mathbf{r}' , and small variations of densities may lead to large modifications of $V_{XC}[\rho(\mathbf{r})]$.⁵⁴

The logical rung beyond LDA is the generalized gradient approximation, as already mentioned with the von Weizsacker improvement of the Thomas-Fermi-Dirac model.⁴⁷ This allows to compensate for the nonlocality by adding semilocal (or indirectly nonlocal) contributions. GGA functionals usually present the form:

$$E_{XC}^{GGA}[\rho(\mathbf{r})] = \int \rho(\mathbf{r}) \epsilon_{XC}^{GGA}[\rho(\mathbf{r}), \nabla \rho(\mathbf{r})] d\mathbf{r}, \quad (3.82)$$

where the energy per particle depends also on the gradient of the electron density at \mathbf{r} . One of the most famous GGA exchange functional is the B88 from Becke,⁵⁸ and combined with Lee-Yang-Parr correlation functional,⁵⁹ one obtains the BLYP XCF. Systematic improvements to B88 were achieved, for instance, B97,⁶⁰ but the limits of the generalized gradient approximation seemed reached.

One step further is the meta-GGA rung, where one more term from the expansion of the density is added, the kinetic energy density, τ_σ :

$$E_{XC}^{m-GGA}[\rho(\mathbf{r})] = \int \rho(\mathbf{r}) \epsilon_{XC}^{m-GGA} \left[\rho_\sigma(\mathbf{r}), \nabla \rho_\sigma(\mathbf{r}), \tau_\sigma = \frac{1}{2} \sum_i^{occ.} |\nabla \Theta_{KS,i\sigma}(\mathbf{r})|^2 \right] d\mathbf{r}. \quad (3.83)$$

The nonempirical Tao-Perdew-Staroverov-Scuseria (TPSS)⁶¹ XCF is found in this group.

Hybrid functionals

The fourth rung of Jacob's ladder is occupied by hybrid XCFs, which include a certain amount of HF exchange since the analytic form of the Hartree-Fock exchange is exact. The latter is evaluated from the following integrals,⁴ $\langle ij|ji \rangle$,

$$\langle ij|ji \rangle = K_{ij} = \iint \Theta_i^*(\mathbf{x}_1) \Theta_j^*(\mathbf{x}_2) \frac{1}{r_{12}} \Theta_j(\mathbf{x}_1) \Theta_i(\mathbf{x}_2) d\mathbf{x}_1 d\mathbf{x}_2. \quad (3.84)$$

In hybrid functionals, one distinguishes two subgroups:

- **Global hybrids** that mix a constant percentage of HF exchange with GGA exchange functional, based on the adiabatic principle,^{62–64} which links the KS system to the real

system,

$$E_X = \int_0^1 E_X^\lambda d\lambda \approx E_X^{(m-)^{GGA}} + \lambda(E_X^{HF} - E_X^{(m-)^{GGA}}), \quad (3.85)$$

where λ is the coupling strength parameter. $\lambda = 0$ corresponds to the KS system, and $\lambda = 1$ is associated with the real "correlated" system. The first, and still frequently used global hybrid GGA XCF is B3LYP.⁶⁵

- **Range-separated hybrids** include HF exchange whose percentage depends on the interatomic distance, r_{12} . In the case of long-range corrected hybrids, the two-electron operator, $1/r_{12}$, is divided by the error function, using the following Ewald split:⁶⁶

$$\frac{1}{r_{12}} = \frac{1 - [\alpha + \beta \operatorname{erf}(\omega r_{12})]}{r_{12}} + \frac{[\alpha + \beta \operatorname{erf}(\omega r_{12})]}{r_{12}}, \quad (3.86)$$

where the α parameter defines the amount of HF exchange at short range, and $\alpha + \beta$ at the HF percentage at long range. The ω range-separating parameter links smoothly the short- and long-range contributions. In this category, the ω B97 and ω B97X exchange-correlation density functionals⁶⁷ were developed by Head-Gordon and colleagues. The long-range correction improves drastically the description of the electronic excitation spectra, and the optical responses, *i.e.* the targeted properties in this study.⁶⁸

Note that the attention was emphasized on the long-range corrected XCFs, since they are used in this work, but short-range, and eventually middle-range corrected hybrids also exist.

Double hybrids

Double hybrid functionals occupy the last rung of Jacob's Ladder. In this family, correlation correction from the second-order perturbation theory (PT2)⁶⁹ is introduced, in addition to the HF exchange. The most popular double hybrid is certainly B2-PLYP,⁷⁰ based on B3LYP (but includes 47 % of HF exchange) with 27% of PT2 correlation.

Dispersion correction

In Kohn-Sham DFT calculations using conventional XCFs (not the double hybrids), London dispersion interactions,⁷¹ which are pure two-body interactions (and thus, a part of the electron correlation), are not accounted. To include dispersion effects, Grimme proposed several

semiempirical dispersion corrections,^{72–74} namely, the DFT-D2, -D3, and -D4 schemes such as:

$$E_{DFT-D} = E_{KS-DFT} + E_{disp}. \quad (3.87)$$

The semiempirical exchange-correlation functional put to work in this Master thesis, ω B97X-D,⁷⁵ is a long-range corrected hybrid whose HF exchange ranges from 22% at short-range to 100% at long-range, and the ω parameter equals 0.2 Bohr^{-1} . This XCF incorporates atom-atom London dispersion thanks to a version of Grimme’s D2 dispersion model, and the dispersion energy reads:

$$E_{disp} = -s_6 \sum_{A>B}^M \frac{C_6^{AB}}{R_{AB}^6} f_{damp}(R_{AB}), \quad (3.88)$$

where s_6 is the scaling factor, and C_6^{AB} is the dispersion coefficient for atom pair AB . In Eq. (3.88), the damping factor, $f_{damp}(R_{AB})$, is expressed as:

$$f_{damp}(R_{AB}) = \frac{1}{1 + a(R_{AB}/R_{AB,vdW})^{-12}}, \quad (3.89)$$

with $R_{AB,vdW}$, the sum of van der Waals radii for atom pair AB , and $a = 6$ for ω B97X-D.

3.6 Molecular properties

In the previous Sections, the density functional theory was presented as a method to determine extensive Schrödinger energies, *i.e.* total GS energies of molecular systems. However, most molecular properties are intensive.¹⁷ Properties are responses to perturbations, *e.g.*, geometrical distortions, electric fields, or both. For instance, if a static perturbation, $\hat{\mathcal{V}}$, is applied on the system, the perturbed Hamiltonian reads:

$$\hat{\mathcal{H}} = \hat{\mathcal{H}}_0 + \lambda \hat{\mathcal{V}}, \quad (3.90)$$

where $\hat{\mathcal{H}}_0$ is the unperturbed Hamiltonian of the isolated system, and $\lambda \in [0, 1]$. It is therefore necessary to know the quantum state of the molecular system before the perturbation is applied. For that purpose, the electronic ground state $|0\rangle$ is computed using an approximate method, such as KS-DFT. The objective of this Section is then to briefly introduce the theoretical aspects involved in the computation of the targeted molecular properties (see Ref. 76 for an extensive review).

Geometry optimization

The assessment of molecular properties generally begins with the optimization of the system geometry in its ground state, which consists in locating stationary points on the potential energy surface. Starting from a guess geometry, this procedure implies to compute the forces on the nuclei, which are the gradients of the energy with respect to the nuclear coordinates.

For a $3M$ -dimensional system, the energy expansion (in the clamped-nucleus Born-Oppenheimer approximation) is expressed in terms of position vectors at equilibrium, \mathbf{R}_{eq} , as a function of the position vectors at the initial atomic distribution, \mathbf{R}_0 ,

$$E_{tot}(\{\mathbf{R}_{eq}\}) = E_{tot}(\{\mathbf{R}_0\}) + \sum_A^{3M} \left(\frac{\partial E_{tot}}{\partial \mathbf{R}_A} \right)_{\{\mathbf{R}_0\}} \Delta \mathbf{R}_A + \frac{1}{2} \sum_{A,B}^{3M} \left(\frac{\partial^2 E_{tot}}{\partial \mathbf{R}_A \partial \mathbf{R}_B} \right)_{\{\mathbf{R}_0\}} \Delta \mathbf{R}_A \Delta \mathbf{R}_B + \dots, \quad (3.91)$$

where $\Delta \mathbf{R}_A$ is the change of position of the A nuclei. In the harmonic approximation of the potential energy surface, the Taylor expansion is truncated to the second-order. Since at equilibrium the gradients vanish, the simultaneous knowledge of the gradient and of the Hessian allows obtaining an approximate (*i.e.* updated) geometry. In reality, the potential energy surfaces are anharmonic, and cubic terms (third order derivatives, ...) should be computed for anharmonic corrections. Consequently, several steps of optimization are necessary.

From a practical viewpoint, the forces are directly computed from the ground state wavefunction. Indeed, the Wigner $2n + 1$ rule⁷⁷ states that *for variational wavefunctions, derivatives of the wavefunction to order n determine the derivatives of the energy to the $2n + 1^{th}$ order.* Furthermore, in most geometry optimization calculations, the Hessian is not explicitly computed at each optimization step, but is rather approximated numerically by making use of analytical energy gradients at the consecutive steps.¹⁷ One can note that, for specific cases (*e.g.*, flat potential energy surfaces), the Hessian must be computed at each optimization step.

Then, *i.e.* when the geometry is optimized (forces \leq threshold) the second-order derivatives are calculated analytically to obtain the harmonic vibrational frequencies, and so, the thermodynamical state functions (Gibbs free energies, enthalpies, and entropies).

Response functions to electric field perturbations

Knowing the approximate wavefunction of the GS provides information on the electronic structures at equilibrium, their electronic densities, and therefore also on the electric multipole moments. Then, when a molecule is irradiated by external (static or dynamic) electric fields,

the quantum state of the system becomes a superposition of many electronic states.⁷⁸ In response theory,⁷⁸ this wavefunction change is accounted for by computing the successive response functions of the ground state, which also allow to get the excited state properties without explicitly computing the wavefunctions of these excited states. That is, response theory is the formulation of the Rayleigh-Schrödinger perturbation theory^{79,80} for both exact and approximate wavefunctions. Hence, the time evolution of the expectation value of a Hermitian operator $\hat{\mathcal{A}}$ (*e.g.* the electric dipole moment) is described by the perturbation expansion as a function of the successive orders of the dynamical electric fields,⁷⁸

$$\begin{aligned} \langle \Psi(t) | \hat{\mathcal{A}} | \Psi(t) \rangle &= \langle 0 | \hat{\mathcal{A}} | 0 \rangle \\ &+ \int \langle \langle \hat{\mathcal{A}}; \hat{\mathcal{V}}(\omega_1) \rangle \rangle_{\omega_1} | \mathbf{E}(\omega_1) | e^{-i\omega_1 t} d\omega_1 \\ &+ \int \int \langle \langle \hat{\mathcal{A}}; \hat{\mathcal{V}}(\omega_1), \hat{\mathcal{V}}(\omega_2) \rangle \rangle_{\omega_1, \omega_2} | \mathbf{E}(\omega_1) | | \mathbf{E}(\omega_2) | e^{-i(\omega_1 + \omega_2)t} d\omega_1 d\omega_2 \\ &+ \dots, \end{aligned} \quad (3.92)$$

where the second and third terms are the linear and second-order perturbative corrections, corresponding to linear and quadratic response functions, respectively. $| \mathbf{E}(\omega_1) |$ is the amplitude of the external electric field oscillating at frequency ω_1 . Response theory for approximate quantum chemical models is often referred to as "time-dependent", but in practice, it appears that no explicit reference to the temporal evolution of the quantum states of the system is made. Indeed, response functions are computed for a limited number of perturbation frequencies. Nonetheless, the latter are related to time by Fourier transforms.

The linear response function in Eq. (3.92) provides the dynamic electric polarizability,⁷⁸

$$\alpha_{\zeta\eta}(-\omega; \omega) = -\langle \langle \hat{\mu}_\zeta; \hat{\mu}_\eta \rangle \rangle_\omega, \quad (3.93)$$

where $\hat{\mu}_\zeta$ is the ζ -component of the electric dipole moment operator,

$$\hat{\mu}_\zeta = - \sum_i^N r_i^\zeta. \quad (3.94)$$

Eq. (3.93) is obtained by performing the following substitutions, $\hat{\mathcal{A}} \rightarrow \hat{\mu}_\zeta$ and $\hat{\mathcal{V}}(\omega_1) | \mathbf{E}(\omega_1) | \rightarrow \hat{\mu}_\eta E_\eta(\omega_1)$ in the linear term of Eq. (3.92). The exact linear response function is then expressed

in terms of the ground and excited states $|n\rangle$, solving the stationary Schrödinger equation,

$$\hat{\mathcal{H}}_0 |n\rangle = E_n |n\rangle, \quad (3.95)$$

and is given by a sum-over-state formula:

$$\alpha_{\zeta\eta}(-\omega; \omega) = \sum_n \frac{\langle 0 | \hat{\mu}_\zeta | n \rangle \langle n | \hat{\mu}_\eta | 0 \rangle}{E_{0n} - \omega} + \frac{\langle 0 | \hat{\mu}_\eta | n \rangle \langle n | \hat{\mu}_\zeta | 0 \rangle}{E_{0n} + \omega}, \quad (3.96)$$

with $E_{0n} = E_n - E_0$, which corresponds to the vertical excitation energy from the ground state to the n^{th} excited state.

The linear response function is singular at the excitation energies, since it has poles at $\omega = \pm E_{0n}$. These poles are exploited in approximate QC calculations to determine the excitation energies (*vide infra*). In addition, the residues of this function at the excitation energies furnish the components of the ground to excited state electric transition dipole moments, μ_{0n} , and therefore the one-photon absorption oscillator strengths, f_{0n} . For instance, in the case of an excitation of the GS to the n^{th} ES,

$$f_{0n} = \frac{2}{3} E_{0n} \sum_{\zeta} \lim_{\omega \rightarrow E_{0n}} (\omega - E_{0n}) \alpha_{\zeta\zeta}(-\omega; \omega) \quad (3.97)$$

$$= \frac{2}{3} E_{0n} \langle 0 | \hat{\boldsymbol{\mu}} | n \rangle \langle n | \hat{\boldsymbol{\mu}} | 0 \rangle \quad (3.98)$$

$$= \frac{2}{3} E_{0n} \mu_{0n}^2. \quad (3.99)$$

Similarly, the elements of the first hyperpolarizability tensor are obtained from the quadratic response functions,

$$\beta_{\zeta\eta\xi}(-\omega_\sigma; \omega_1, \omega_2) = -\langle \langle \hat{\mu}_\zeta; \hat{\mu}_\eta, \hat{\mu}_\xi \rangle \rangle_{\omega_1, \omega_2}. \quad (3.100)$$

The exact quadratic response function is also calculated from the excitation energies and the transition matrix elements:^{81,82}

$$\beta_{\zeta\eta\xi}(-\omega_\sigma; \omega_1, \omega_2) = \sum P_{-\sigma,1,2} \sum_{n \neq 0} \sum_{m \neq 0} \frac{\langle 0 | \hat{\mu}_\zeta | m \rangle \langle m | \bar{\hat{\mu}}_\eta | n \rangle \langle n | \hat{\mu}_\xi | 0 \rangle}{(E_{0n} - \omega_\sigma)(E_{0m} - \omega_2)}, \quad (3.101)$$

where the summations run over all excited states $|n\rangle$ and $|m\rangle$ of energies E_n and E_m . $\sum P_{-\sigma,1,2}$ denotes the summation over the six permutation of the pairs made of the frequencies and Cartesian components $(-\omega_\sigma, \zeta)$, (ω_1, η) , and (ω_2, ξ) . The bar on $\hat{\mu}_\eta$ means that the operator

is shifted by its ground state expectation value,

$$\bar{\hat{\mu}}_\eta = \hat{\mu}_\eta - \langle 0 | \hat{\mu}_\eta | 0 \rangle \hat{I}. \quad (3.102)$$

where \hat{I} is the identity operator. $\bar{\hat{\mu}}$ is commonly referred to as the fluctuation operator.

The quadratic response function is also singular at the excitation energies. So, one important residue determines the transition matrix elements of two-photon excitation from the ground state to the excited state $|m\rangle$:⁷⁸

$$\lim_{\omega_2 \rightarrow E_{0m}} (\omega_2 - E_{0m}) \langle \langle \hat{\mu}_\zeta; \hat{\mu}_\eta, \hat{\mu}_\xi \rangle \rangle_{\omega_1, \omega_2} = \left[\sum_n \frac{\langle 0 | \hat{\mu}_\zeta | n \rangle \langle n | \hat{\mu}_\eta | m \rangle}{E_{nm} - \omega_1} + \frac{\langle 0 | \hat{\mu}_\eta | n \rangle \langle n | \hat{\mu}_\zeta | m \rangle}{E_{0n} + \omega_1} \right] \langle m | \hat{\mu}_\xi | 0 \rangle. \quad (3.103)$$

Then, another crucial (double) residue is:

$$\begin{aligned} & \lim_{\omega_1 \rightarrow -E_{0n}} (\omega_1 + E_{0n}) \left[\lim_{\omega_2 \rightarrow E_{0m}} (\omega_2 - E_{0m}) \langle \langle \hat{\mu}_\zeta; \hat{\mu}_\eta, \hat{\mu}_\xi \rangle \rangle_{\omega_1, \omega_2} \right] \\ &= \delta_{nm} \langle 0 | \hat{\mu}_\zeta | 0 \rangle \langle 0 | \hat{\mu}_\eta | n \rangle \langle n | \hat{\mu}_\xi | 0 \rangle - \langle 0 | \hat{\mu}_\eta | n \rangle \langle n | \hat{\mu}_\zeta | m \rangle \langle m | \hat{\mu}_\xi | 0 \rangle, \end{aligned} \quad (3.104)$$

which allows to compute the excited-to-excited state electric transition dipole moments. In addition, it allows extracting the dipole moments of the excited states, with the specific choice of $n = m$.

Time-dependent density functional theory

In practice, Kohn-Sham DFT method does not apply when time-dependency (or frequency dependency) is introduced, since the Hohenberg and Kohn theorems are limited to stationary cases. Thankfully, Runge and Gross (RG) proposed an analogous time-dependent theorem,^{83,84} assuming that the time-dependent external potential, $V_{ext}(\mathbf{r}, t)$, depends periodically on time, and that it can be expanded as a Taylor series around t_0 . The latter is in fact separated in four theorems that are not discussed in details here. They showed that the time evolution of the density, $\rho(\mathbf{r}, t)$, arises from the density of current, $\mathbf{j}(\mathbf{r}, t)$, induced by the time-dependent external potential. As a matter of fact, the RG theorems demonstrate the one-to-one correspondence between $V_{ext}(\mathbf{r}, t)$ and $\rho(\mathbf{r}, t)$ (like the one-to-one correspondence between $V_{ext}(\mathbf{r})$ and $\rho(\mathbf{r})$ within Hohenberg and Kohn) for a ground state Ψ_0 , so that within the Kohn-Sham

approach, the exact time-dependent one-electron density of the non-interacting system reads:

$$\rho(\mathbf{r}, t) = \sum_i^N \int |\Theta_{KS,i}(\mathbf{r}, \omega, t)|^2 d\omega.^1 \quad (3.105)$$

The time-dependent KS orbitals, $\{\Theta_{KS,i}(\mathbf{r}, \omega, t)\}$, satisfy the time-dependent Schrödinger equation for the particle-independent system, referred to as the time-dependent (TD) KS equation,⁸⁵

$$\left(-\frac{1}{2}\nabla^2 + V_{eff}[\mathbf{r}, t; \rho(\mathbf{r}, t)]\right) \Theta_{KS,i}(\mathbf{r}, t) = i \frac{\partial}{\partial t} \Theta_{KS,i}(\mathbf{r}, t). \quad (3.106)$$

where the effective potential is given by:

$$\hat{V}_{eff}[\mathbf{r}, t; \rho(\mathbf{r}, t)] = \hat{V}_{ext}(\mathbf{r}, t) + \int \frac{\rho(\mathbf{r}', t) d\mathbf{r}'}{|\mathbf{r} - \mathbf{r}'|} + \hat{V}_{XC}(\mathbf{r}, t). \quad (3.107)$$

The TD exchange-correlation potential, $\hat{V}_{XC}(\mathbf{r}, t)$ is a function of $\rho(\mathbf{r}', t')$. A very common approximation is to employ the ground state exchange-correlation potential, and to take its functional derivative with respect to the actual TD density,

$$\hat{V}_{XC}[\rho(\mathbf{r}, t)] \simeq \hat{V}_{XC}(\mathbf{r}, t)|_{\rho(t)} = \frac{\delta E_{XC}[\rho(\mathbf{r})]}{\delta \rho(\mathbf{r}, t)}. \quad (3.108)$$

This corresponds to the adiabatic approximation, which assumes that the quantum eigenstate is conserved upon the application of the perturbation. In other words, the perturbation induces a rearrangement of the energy levels, but their population remains the same, *i.e.*, it assumes an instantaneous relaxation or reaction of the self-consistent field to the temporal changes in the electron density.

Within this time-dependent density functional theory (TDDFT) approach, the Fourier-transformed linear electron density response to a perturbation reads:

$$\rho^1(\mathbf{r}, \omega) = \int \chi_{eff}(\mathbf{r}, \mathbf{r}', \omega) V_{eff}^1(\mathbf{r}', \omega) d\mathbf{r}', \quad (3.109)$$

where $\chi_{eff}(\mathbf{r}, \mathbf{r}', \omega)$ is the linear response kernel describing how a small change in the effective potential in every \mathbf{r}' affects the density in every other \mathbf{r} , and $V_{eff}^1(\mathbf{r}', \omega)$ is the first-order

¹Be careful, here ω is the spin variable.

perturbed effective potential. The latter is given by:

$$V_{eff}^1(\mathbf{r}, \omega) = V_{ext}^1(\mathbf{r}, \omega) + \int \left[\frac{1}{|\mathbf{r} - \mathbf{r}'|} + \mathbf{f}_{XC}(\mathbf{r}, \mathbf{r}', \omega = 0) \right] \rho^1(\mathbf{r}', \omega) d\mathbf{r}', \quad (3.110)$$

with \mathbf{f}_{XC} , the first-order exchange-correlation kernel, that is, the functional derivative of the XC potential expressed in the frequency domain,

$$\mathbf{f}_{XC}(\mathbf{r}, \mathbf{r}') = \frac{\delta V_{XC}(\mathbf{r})}{\delta \rho(\mathbf{r}')}. \quad (3.111)$$

Since, $V_{eff}^1(\mathbf{r}, \omega)$ and $\rho^1(\mathbf{r}, \omega)$ are interdependent, finding the response function implies an iterative procedure. Within this formalism, the linear response function takes the form of a sum-over-state expression build out from the occupied and unoccupied KS molecular spinorbitals (here, without including a damping factor),⁴

$$\begin{aligned} \chi_{KS}(\mathbf{r}, \mathbf{r}', \omega) = & \sum_i^{occ} \sum_a^{unocc} \frac{\Theta_{KS,i}^*(\mathbf{r}) \Theta_{KS,a}(\mathbf{r}) \Theta_{KS,i}(\mathbf{r}') \Theta_{KS,a}^*(\mathbf{r}')}{\omega - (\epsilon_a - \epsilon_i)} \\ & - \frac{\Theta_{KS,i}(\mathbf{r}) \Theta_{KS,a}^*(\mathbf{r}) \Theta_{KS,i}^*(\mathbf{r}') \Theta_{KS,a}(\mathbf{r}')}{\omega + (\epsilon_a - \epsilon_i)}. \end{aligned} \quad (3.112)$$

Finding the poles of Eq. (3.112) corresponds to computing the vertical excitation energies. This is generally achieved using the matrix formulation proposed by Casida.⁸⁶

Taking one step further, computing the first hyperpolarizability at the TDDFT level requires the second-order derivatives of the density matrix with respect to the external electric field components, such that:

$$\beta_{\zeta\eta\xi}(-\omega_\sigma; \omega_1, \omega_2) = -2 \sum_{p,q}^K M_{pq}^\zeta D_{qp}^{\eta\xi}(\omega_1, \omega_2), \quad (3.113)$$

where the M_{pq}^ζ are the elements of the dipole moment matrix expressed in the AO basis, and $D_{qp}^{\eta\xi}$ are the second-order derivatives of the density matrix elements, or more precisely, the second-order derivatives of the LCAO coefficients. The evaluation of the latter is not a trivial task, and necessitates the knowledge of the second-order exchange-correlation kernel, $\mathbf{g}_{XC}(\mathbf{r}, \mathbf{r}', \mathbf{r}'')$, given by:

$$\mathbf{g}_{XC}(\mathbf{r}, \mathbf{r}', \mathbf{r}'') = \frac{\delta^2 V_{XC}(\mathbf{r})}{\delta \rho(\mathbf{r}') \delta \rho(\mathbf{r}'')}. \quad (3.114)$$

The complete procedure was introduced by van Gisbergen *et al.*,⁸⁷ and is not detailed in this work. In practice, one also takes advantage of the $2n + 1$ rule.⁷⁷

3.7 Analysis of the excited states and of their electronic distributions

Different schemes allow characterizing several properties of the excited states. Following the procedure described by Le Bahers and colleagues,⁸⁸ the differences between the electronic densities of the ground state and of the key excited states, $|n\rangle$, $\Delta\rho_{n0}(\mathbf{r}) = \rho_n(\mathbf{r}) - \rho_0(\mathbf{r})$ can be evaluated. The nonequilibrium solvation approach (see Section 3.8) must be employed since the electronic excitation processes are much faster than the solvent structural reorganizations (changes of orientation).⁸⁹ Using this method, the regions of space where an increase ($\Delta\rho^+(\mathbf{r})$) or a depletion ($\Delta\rho^-(\mathbf{r})$) of the electronic density is produced upon excitation are defined as follows:

$$\Delta\rho^+(\mathbf{r}) = \begin{cases} \Delta\rho_{0n}(\mathbf{r}) & \text{if } \Delta\rho_{0n}(\mathbf{r}) > 0 \\ 0 & \text{if } \Delta\rho_{0n}(\mathbf{r}) < 0 \end{cases}, \quad (3.115)$$

$$\Delta\rho^-(\mathbf{r}) = \begin{cases} \Delta\rho_{0n}(\mathbf{r}) & \text{if } \Delta\rho_{0n}(\mathbf{r}) < 0 \\ 0 & \text{if } \Delta\rho_{0n}(\mathbf{r}) > 0 \end{cases}. \quad (3.116)$$

$\Delta\rho_{0n}(\mathbf{r})$ ($\Delta\rho^+(\mathbf{r})$ and $\Delta\rho^-(\mathbf{r})$) can be evaluated on a three-dimensional grid of points around the molecule, and be depicted graphically. The integration of ($\Delta\rho^{+/-}(\mathbf{r})$) over the whole space gives the amount of charge transfer (q_{CT}). Then, the barycenters of the positive (\mathbf{R}^+) and negative (\mathbf{R}^-) electronic density variations read:

$$\mathbf{R}^+ = \frac{\int \mathbf{r} \Delta\rho^+(\mathbf{r}) d\mathbf{r}}{\int \Delta\rho^+(\mathbf{r}) d\mathbf{r}}, \quad (3.117)$$

$$\mathbf{R}^- = \frac{\int \mathbf{r} \Delta\rho^-(\mathbf{r}) d\mathbf{r}}{\int \Delta\rho^-(\mathbf{r}) d\mathbf{r}}, \quad (3.118)$$

and the distance between the latter, d_{CT} ,

$$d_{CT} = |\mathbf{R}^+ - \mathbf{R}^-|, \quad (3.119)$$

quantifies the CT excitation length. The product between d_{CT} and q_{CT} equals the difference between the ground state and excited state dipole moments,^{88,90}

$$\Delta\mu_{0n} = d_{CT}q_{CT} = \mu_n - \mu_0. \quad (3.120)$$

In addition, a charge transfer vector connecting the two barycenters can be plotted, going from \mathbf{R}^+ to \mathbf{R}^- . This CT vector indicates the global displacement of the electrons during the excitation. This method is general and can therefore be applied within the TDDFT scheme, as done in this Master thesis.

The positive and negative $\Delta\rho(\mathbf{r})$ are also referred to as the densities of the hole ($\rho^{hole}(\mathbf{r})$) and of the electron ($\rho^{elec}(\mathbf{r})$), respectively,⁹¹ so that:

$$\Delta\rho_{0n}(\mathbf{r}) = \rho^{hole}(\mathbf{r}) - \rho^{elec}(\mathbf{r}). \quad (3.121)$$

However, parts of hole and electron distributions cancel each other, since $\Delta\rho^+(\mathbf{r})$ and $\Delta\rho^-(\mathbf{r})$ do not integrate to 1. Hence, $\Delta\rho_{0n}$ does not represent completely the intrinsic distributions of the hole and of the electron. In fact, within TDDFT in general and Casida's scheme more precisely, the hole and electron densities are build out of the sets of occupied (i,j) and virtual (a,b) MOs, respectively, following Eqs. (3.122) and (3.123):

$$\rho^{hole}(\mathbf{r}) = \rho_{loc}^{hole}(\mathbf{r}) + \rho_{cross}^{hole}(\mathbf{r}) = \sum_i \sum_a^{occ \ unocc} (C_i^a)^2 \phi_i(\mathbf{r}) \phi_i(\mathbf{r}) + \sum_i \sum_{j \neq i}^{occ \ occ} \sum_a^{unocc} C_i^a C_j^a \phi_i(\mathbf{r}) \phi_j(\mathbf{r}), \quad (3.122)$$

$$\rho^{elec}(\mathbf{r}) = \rho_{loc}^{elec}(\mathbf{r}) + \rho_{cross}^{elec}(\mathbf{r}) = \sum_i \sum_a^{occ \ unocc} (C_i^a)^2 \phi_a(\mathbf{r}) \phi_a(\mathbf{r}) + \sum_i \sum_a^{occ \ unocc} \sum_{b \neq a}^{unocc} C_i^a C_i^b \phi_a(\mathbf{r}) \phi_b(\mathbf{r}), \quad (3.123)$$

where C_i^a is the coefficient of the excitation from orbital i to orbital a . The "loc" and "cross" subscripts denote the contributions of local and cross terms to the hole and electron coefficients. As (i) the MOs are orthonormal and (ii) the sum of squares of C_i^a of any excited state amounts to 1, both $\rho^{hole}(\mathbf{r})$ and $\rho^{elec}(\mathbf{r})$ integrate to unity:

$$\int \rho^{hole}(\mathbf{r}) d\mathbf{r} = 1, \quad (3.124)$$

$$\int \rho^{elec}(\mathbf{r}) d\mathbf{r} = 1. \quad (3.125)$$

Note that the hole and the electron do not have phase, due to their definitions in density forms.

To complement this quantitative analysis of $\Delta\rho_{0n}$, one can take advantage of this formalism to characterize their overlap, *i.e.* the overlap function between the hole and the electron densities, defined as:

$$S_r(\mathbf{r}) = \sqrt{\rho^{hole}(\mathbf{r}) \rho^{elec}(\mathbf{r})}, \quad (3.126)$$

Finally the overlap coefficient, O_{h-e} , is obtained by integration of this function over the whole space,

$$O_{h-e} = \int S_r(\mathbf{r}) d\mathbf{r}. \quad (3.127)$$

It ranges between 0 and 1.

3.8 Effects of the surrounding

In the realm of quantum chemical calculations, a critical aspect lies in faithfully describing the effects of the environment. Indeed, this work concentrates on elucidating molecular properties in solution. Two primary approaches for representing the solvent environment have emerged: explicit solvation, wherein solvent molecules are treated at quantum or classical levels, and implicit solvation methods, relying on a surrounding continuum described by its dielectric constant. Because it is employed in this Master thesis, this Section focuses on the latter, and briefly exposes its principle.

Most implicit solvent treatments are based on the Onsager reaction spherical cavity field method,⁹² and the Poisson equation. With respect to explicit solvation, this approach is computationally much less costly. Indeed, it mostly accounts for electrostatic interactions while it neglects specific solute-solvent interactions (*e.g.*, hydrogen bonds). Among these implicit solvation methods, the polarizable continuum model (PCM)⁹³ is widely employed. It consists in placing the solute in a void cavity created in a continuous dielectric medium. In this study, the integral equation formalism (IEF)⁹⁴ of the PCM model was employed. It is available in the Gaussian16 package.⁹⁵ The cavity is defined by the set of interpenetrating atomic spheres with radii close to the van der Waals values as illustrated in Fig. 3.4 for one form of the targeted molecular switch.

Within IEF-PCM, the charge distribution of the solute inside the cavity polarizes the continuum, and *vice versa*. In fact, the continuum polarization is described by an induced charge distribution on the surface of the cavity, called the apparent surface charges (ASC),⁹⁶ $\sigma(\mathbf{s})$, determined by both the solute and the surface potentials,

$$\sigma(\mathbf{s}) = \frac{\epsilon - 1}{4\pi\epsilon} \frac{\partial}{\partial \mathbf{n}} (V_p + V_\sigma), \quad (3.128)$$

where \mathbf{s} is a position vector on the surface, ϵ is the dielectric constant of the solvent, \mathbf{n} is the normal to the surface, V_p is the potential due to the charge distribution of the solute, and

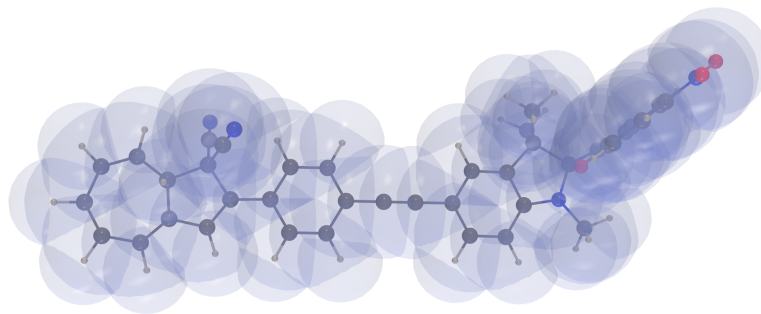


Fig. 3.4: Illustration of the PCM cavity of the DHA-SP form of the molecular switch of interest.

V_σ is the potential originating from the surface of the cavity. In practice, V_σ is added to the Hamiltonian operator to account for solute-solvent interactions,

$$\hat{\mathcal{H}} = \hat{\mathcal{H}}_{solute} + \hat{V}_\sigma. \quad (3.129)$$

Consequently, in KS-DFT calculations, a second iterative cycle is added inside the SCF procedure to compute V_σ and $\sigma(\mathbf{s})$.

Bibliography

- [1] Schrödinger, E. An Undulatory Theory of the Mechanics of Atoms and Molecules. *Phys. Rev.* **1926**, *28*, 1049–1070.
- [2] Heisenberg, W. Über Quantentheoretische Umdeutung Kinematischer und Mechanischer Beziehungen. *Z. Phys.* **1925**, *33*, 879–893.
- [3] Dirac, P. A. M. The Quantum Theory of the Electron. *Proc. R. Soc. A* **1928**, *117*, 610–624.
- [4] Tsuneda, T. *Density Functional Theory in Quantum Chemistry*; Springer, Tokyo, Japan, 2014.
- [5] Born, M. Quantenmechanik der Stossvorgänge. *Z. Phys.* **1926**, *38*, 803–827.
- [6] Szabo, A.; Ostlund, N. S. *Modern Quantum Chemistry: Introduction to Advanced Electronic Structure Theory*; Dover, Mineola, New York, 1996.
- [7] Born, M.; Oppenheimer, R. Zur Quantentheorie der Molekeln. *Ann. Phys.* **1927**, *389*, 457–484.
- [8] Ritz, W. Über Eine Neue Methode zur Lösung Gewisser Variationsprobleme der Mathematischen Physik. *J. Reine Angew. Math.* **1909**, *135*, 1–61.
- [9] Dirac, P. A. M. On the Theory of Quantum Mechanics. *Proc. R. Soc. Lond. A* **1926**, *112*, 661–667.
- [10] Heisenberg, W. Mehrkörperproblem und Resonanz in der Quantenmechanik. *Z. Phys.* **1926**, *38*, 411–426.
- [11] Pauli, W. Über den Zusammenhang des Abschlusses der Elektronengruppen im Atom mit der Komplexstruktur der Spektren. *Z. Phys.* **1925**, *31*, 765–783.
- [12] Slater, J. C. The Theory of Complex Spectra. *Phys. Rev.* **1929**, *34*, 1293–1322.
- [13] Fock, V. Näherungsmethode zur Lösung des Quantenmechanischen Mehrkörperproblems. *Z. Phys.* **1930**, *61*, 126–148.
- [14] Lennard-Jones, J. E. The Electronic Structure of some Diatomic Molecules. *Trans. Faraday Soc.* **1929**, *25*, 668–676.
- [15] Boys, S. F. Electronic Wave Functions. I. A General Method of Calculation for the Stationary States of Any Molecular System. *Proc. R. Soc. Lond. A* **1950**, *200*, 542–554.

- [16] Jensen, F. Atomic Orbital Basis Sets. *Wiley Interdiscip. Rev. Comput. Mol. Sci.* **2013**, *3*, 273–295.
- [17] Simons, J. Why Is Quantum Chemistry So Complicated? *J. Am. Chem. Soc.* **2023**, *145*, 4343–4354.
- [18] Pritchard, B. P.; Altarawy, D.; Didier, B.; Gibbsom, T. D.; Windus, T. L. A New Basis Set Exchange: An Open, Up-to-date Resource for the Molecular Sciences Community. *J. Chem. Inf. Model.* **2019**, *59*, 4814–4820.
- [19] Hehre, W. J.; Stewart, R. F.; Pople, J. A. Self-Consistent Molecular-Orbital Methods. I. Use of Gaussian Expansions of Slater-Type Atomic Orbitals. *J. Chem. Phys.* **1969**, *51*, 2657–2664.
- [20] Hehre, W. J.; Ditchfield, R.; Stewart, R. F.; Pople, J. A. Self-Consistent Molecular Orbital Methods. IV. Use of Gaussian Expansions of Slater-Type Orbitals. Extension to Second-Row Molecules. *J. Chem. Phys.* **1970**, *52*, 2769–2773.
- [21] Krishnan, R.; Binkley, J. S.; Seeger, R.; Pople, J. A. Self-Consistent Molecular Orbital Methods. XX. A Basis Set for Correlated Wave Functions. *J. Chem. Phys.* **1980**, *72*, 650–654.
- [22] McLean, A. D.; Chandler, G. S. Contracted Gaussian Basis Sets for Molecular Calculations. I. Second Row Atoms, Z=11–18. *J. Chem. Phys.* **1980**, *72*, 5639–5648.
- [23] Clark, T.; Chandrasekhar, J.; Spitznagel, G. W.; Von Ragué Schleyer, P. Efficient Diffuse Function-Augmented Basis Sets for Anion Calculations. III. The 3-21+G Basis Set for First-Row Elements, Li–F. *J. Comput. Chem.* **1983**, *4*, 294–301.
- [24] Ditchfield, R.; Hehre, W. J.; Pople, J. A. Self-Consistent Molecular-Orbital Methods. IX. An Extended Gaussian-Type Basis for Molecular-Orbital Studies of Organic Molecules. *J. Chem. Phys.* **1971**, *54*, 724–728.
- [25] Dunning, T. H. Gaussian Basis Functions for Use in Molecular Calculations. I. Contraction of (9s5p) Atomic Basis Sets for the First-Row Atoms. *J. Chem. Phys.* **1970**, *53*, 2823–2833.
- [26] Dunning, T. H. Gaussian Basis Functions for Use in Molecular Calculations. III. Contraction of (10s6p) Atomic Basis Sets for the First-Row Atoms. *J. Chem. Phys.* **1971**, *55*, 716–723.
- [27] Schaefer, A.; Horn, H.; Ahlrichs, R. Fully Optimized Contracted Gaussian-Basis Sets for Atoms Li to Kr. *J. Chem. Phys.* **1992**, *97*, 2571–2577.

- [28] Schaefer, A.; Huber, C.; Ahlrichs, R. Fully Optimized Contracted Gaussian-Basis Sets of Triple Zeta Valence Quality for Atoms Li to Kr. *J. Chem. Phys.* **1994**, *100*, 5829–5835.
- [29] Helgaker, T.; Jørgensen, P.; Olsen, J. *Molecular Electronic-Structure Theory*; John Wiley & Sons, Chichester, England, 2000.
- [30] Dunning, T. H. Gaussian Basis Sets for Use in Correlated Molecular Calculations. I. The Atoms Boron Through Neon and Hydrogen. *J. Chem. Phys.* **1989**, *90*, 1007–1023.
- [31] Kendall, R. A.; Dunning, T. H.; Harrison, R. J. Electron Affinities of the First-Row Atoms Revisited. Systematic Basis Sets and Wave Functions. *J. Chem. Phys.* **1992**, *96*, 6796–6806.
- [32] Hay, P. J.; Wadt, W. R. Ab initio Effective Core Potentials for Molecular Calculations. Potentials for the Transition Metal Atoms Sc to Hg. *J. Chem. Phys.* **1985**, *82*, 270–283.
- [33] Foster, J. P.; Weinhold, F. Natural Hybrid Orbitals. *J. Am. Chem. Soc.* **1980**, *102*, 7211–7218.
- [34] Reed, A. E.; Weinhold, F. Natural Bond Orbital Analysis of Near-Hartree-Fock Water Dimer. *J. Chem. Phys.* **1983**, *78*, 4066–4073.
- [35] Reed, A. E.; Weinstock, R. B.; Weinhold, F. Natural Population Analysis. *J. Chem. Phys.* **1985**, *83*, 735–746.
- [36] Reed, A. E.; Curtiss, L. A.; Weinhold, F. Intermolecular Interactions from a Natural Bond Orbital, Donor-Acceptor Viewpoint. *Chem. Rev.* **1988**, *88*, 899–926.
- [37] Mulliken, R. S. Electronic Population Analysis on LCAO-MO Molecular Wave Functions. I. *J. Chem. Phys.* **1955**, *23*, 1833–1840.
- [38] Reed, A. E.; Weinhold, F. Natural Localized Molecular Orbitals. *J. Chem. Phys.* **1985**, *83*, 1736–1740.
- [39] Löwdin, P. O. On the Non-Orthogonality Problem Connected with the Use of Atomic Wave Functions in the Theory of Molecules and Crystals. *J. Chem. Phys.* **1950**, *18*, 365–375.
- [40] Löwdin, P. O. Quantum Theory of Many-Particle Systems. III. Extension of the Hartree-Fock Scheme to Include Degenerate Systems and Correlation Effects. *Phys. Rev.* **1955**, *97*, 1509–1520.
- [41] Kato, T. On the Eigenfunctions of Many-Particle Systems in Quantum Mechanics. *Commun. Pure Appl. Math.* **1957**, *10*, 151–177.
- [42] Koch, W.; Holthausen, M. C. *A Chemist's Guide to Density Functional Theory*, 2nd ed.; Wiley VCH, Verlag GmbH, Germany, 2001.

- [43] Thomas, L. H. The Calculation of Atomic Fields. *Math. Proc. Camb. Philos. Soc.* **1927**, *23*, 542–548.
- [44] Fermi, E. Eine Statistische Methode zur Bestimmung Einer Eigenschaften des Atoms und ihre Anwendung auf die Theorie des Periodischen Systems der Elemente. *Z. Phys.* **1928**, *48*, 73–79.
- [45] Teller, E. On the Stability of Molecules in the Thomas-Fermi Theory. *Rev. Mod. Phys.* **1962**, *34*, 627–631.
- [46] Dirac, P. A. M. Note on Exchange Phenomena in the Thomas Atom. *Math. Proc. Camb. Philos. Soc.* **1930**, *26*, 376–385.
- [47] von Weizsäcker, C. F. Zur Theorie der Kernmassen. *Z. Phys.* **1935**, *96*, 431–458.
- [48] Hohenberg, P.; Kohn, W. Inhomogeneous Electron Gas. *Phys. Rev.* **1964**, *136*, 864–871.
- [49] Kohn, W.; Sham, L. J. Self-Consistent Equations Including Exchange and Correlation Effects. *Phys. Rev.* **1965**, *140*, 1133–1138.
- [50] Roothaan, C. C. J. New Developments in Molecular Orbital Theory. *Rev. Mod. Phys.* **1951**, *23*, 69–89.
- [51] Hall, G. G. The Molecular Orbital Theory of Chemical Valency. VIII. A Method of Calculating Ionization Potentials. *Proc. R. Soc. Lond. A* **1951**, *205*, 541–552.
- [52] Perdrew, J. P.; Schmidt, K. *Density Functional Theory and Its Application to Materials*; AIP, Melville, New-York, 2001.
- [53] Perdrew, J. P.; Ruzsinszky, A.; Tao, J.; Staroverov, V. N.; Scuseria, G. E.; Csonka, G. I. Prescription for the Design and Selection of Density Functional Approximations: More Constraint Satisfaction with Fewer Fits. *J. Chem. Phys.* **2005**, *123*, 062201.
- [54] Scuseria, G. E.; Staroverov, V. N. *Progress in the Development of Exchange-correlation Functionals. In Theory and Applications of Computational Chemistry*; Elsevier, Amsterdam, 2005; pp 669–724.
- [55] Ceperley, D. M.; Alder, B. J. Ground State of the Electron Gas by a Stochastic Method. *Phys. Rev. Lett.* **1980**, *45*, 566–569.
- [56] Vosko, S. H.; Wilk, L.; Nusair, M. Accurate Spin-Dependent Electron Liquid Correlation Energies for Local Spin Density Calculations: A Critical Analysis. *Can. J. Phys.* **1980**, *58*, 1200–1211.
- [57] Slater, J. C. A Simplification of the Hartree-Fock Method. *Phys. Rev.* **1951**, *81*, 385–390.

- [58] Becke, A. D. Density-Functional Exchange-Energy Approximation with Correct Asymptotic Behavior. *Phys. Rev. A* **1988**, *38*, 3098–3100.
- [59] Lee, C.; Yang, W.; Parr, R. G. Development of the Colle-Salvetti Correlation-Energy Formula into a Functional of the Electron Density. *Phys. Rev. B* **1988**, *37*, 785–789.
- [60] Becke, A. D. Density-Functional Thermochemistry. V. Systematic Optimization of Exchange-Correlation Functionals. *J. Chem. Phys.* **1997**, *107*, 8554–8560.
- [61] Tao, J.; Perdrew, J. P.; Staroverov, V. N.; Scuseria, G. E. Climbing the Density Functional Ladder: Nonempirical Meta-Generalized Gradient Approximation Designed for Molecules and Solids. *Phys. Rev. Lett.* **2003**, *91*, 146401.
- [62] Harris, J.; Jones, R. O. The Surface Energy of a Bounded Electron Gas. *J. Phys. F: Met Phys* **1974**, *4*, 1170–1186.
- [63] Langreth, D. C.; Perdrew, J. P. Exchange-Correlation Energy of a Metallic Surface: Wave-Vector Analysis. *Phys. Rev. B* **1977**, *15*, 2884–2901.
- [64] Burke, K.; Ernzerhof, M.; Perdrew, J. P. The Adiabatic Connection Method: A Non-Empirical Hybrid. *Chem. Phys. Lett.* **1997**, *265*, 115–120.
- [65] Becke, A. D. Density-Functional Thermochemistry. III. The Role of Exact Exchange. *J. Chem. Phys.* **1993**, *98*, 5648–5652.
- [66] Yanai, T.; Tew, D. P.; Handy, N. C. A New Hybrid Exchange–Correlation Functional Using the Coulomb-Attenuating Method (CAM-B3LYP). *Chem. Phys. Lett.* **2004**, *91*, 51–57.
- [67] Chai, J.-D.; Head-Gordon, M. Systematic Optimization of Long-Range Corrected Hybrid Density Functionals. *J. Chem. Phys.* **2008**, *128*, 084106.
- [68] Garrett, K.; Vazquez, X. S.; Egri, S. B.; Wilmer, J.; Johnson, L. E.; Robinson, B. H.; Isborn, C. M. Optimum Exchange for Calculation of Excitation Energies and Hyperpolarizabilities of Organic Electro-optic Chromophores. *J. Chem. Theory Comput.* **2014**, *10*, 3821–3831.
- [69] Møller, C.; Plesset, M. S. Note on an Approximation Treatment for Many-Electron Systems. *Phys. Rev.* **1934**, *46*, 618–622.
- [70] Grimme, S. Semiempirical Hybrid Density Functional with Perturbative Second-Order Correlation. *J. Chem. Phys* **2006**, *124*, 034108.
- [71] London, F. W. Zur Theorie und Systematik der Molekularkräfte. *Z. Phys.* **1930**, *63*, 245–279.

- [72] Grimme, S. Accurate Description of van der Waals Complexes by Density Functional Theory Including Empirical Corrections. *J. Comput. Chem.* **2004**, *25*, 1463–1473.
- [73] Grimme, S. Semiempirical GGA-type Density Functional Constructed with a Long-Range Dispersion Correction. *J. Comput. Chem.* **2006**, *27*, 1787–1799.
- [74] Grimme, S. A Consistent and Accurate Ab Initio Parameterization of Density Functional Dispersion Correction (DFT-D) for the 94 Elements H-Pu. *J. chem. Phys.* **2010**, *132*, 154104.
- [75] Chai, J.-D.; Head-Gordon, M. Long-Range Corrected Hybrid Density Functionals with Damped Atom-atom Dispersion Corrections. *Phys. Chem. Chem. Phys.* **2008**, *10*, 6615–6620.
- [76] Helgaker, T.; Coriani, S.; Jørgensen, P.; Kristensen, K.; Olsen, J.; Ruud, K. Recent Advances in Wave Function-Based Methods of Molecular-Property Calculations. *Chem. Rev.* **2012**, *112*, 543–631.
- [77] von Neumann, J. Über das Verhalten von Eigenwerten bei adiabatischen Prozessen. *Phys. Z.* **1929**, *30*, 467–470.
- [78] Pedersen, T. B. *Introduction to Response Theory*, in: Leszczynski J. (Eds), *Handbook of Computational Chemistry*; Springer, Dordrecht, 2015; pp 269–294.
- [79] Rayleigh, J. W. S. B. *The Theory of Sound*; Macmillan Publishing, New-York, 1896.
- [80] Schrödinger, E. Quantisierung als Eigenwertproblem. *Ann. Phys.* **1926**, *385*, 437–490.
- [81] Orr, B. J.; Ward, J. F. Perturbation Theory of the Non-Linear Optical polarization of an Isolated System. *Mol. Phys.* **1971**, *20*, 513–526.
- [82] Bishop, D. M. Explicit Nondivergent Formulas for Atomic and Molecular Dynamic Hyperpolarizabilities. *J. Chem. Phys.* **1994**, *100*, 6535–6542.
- [83] Runge, E.; Gross, E. K. U. Density-Functional Theory for Time-Dependent Systems. *Phys. Rev. Lett.* **1984**, *52*, 997–1000.
- [84] Gross, E. K. U.; Dobson, J. F.; Petersilka, M. Density-Functional Theory of Time-Dependent Phenomena. *Top. Curr. Chem.* **1996**, *181*, 81–172.
- [85] van Leeuwen, R. Causality and Symmetry in Time-Dependent Density-Functional Theory. *Phys. Rev. Lett.* **1998**, *80*, 1280–1283.
- [86] Casida, M. E. *Density Functional Theory II*; Springer, Heidelberg, 1995.
- [87] van Gisbergen, S. J. A.; Snijders, J. G.; Baerends, E. J. Calculating Frequency-Dependent

- Hyperpolarizabilities using Time-Dependent Density Functional Theory. *J. Chem. Phys.* **1998**, *109*, 10644–10656.
- [88] Le Bahers, T.; Adamo, C.; Ciofini, I. A Qualitative Index of Spatial Extent in Charge-transfer Excitations. *J. Chem. Theory Comp.* **2011**, *7*, 2498–2506.
- [89] Scalmani, G.; Frisch, M. J.; Mennucci, B.; Tomasi, J.; Cammi, R.; Barone, V. Geometries and Properties of Excited States in the Gas Phase and in Solution: Theory and Application of a Time-Dependent Density Functional Theory Polarizable Continuum Model. *J. Chem. Phys.* **2006**, *124*, 094107.
- [90] Jacquemin, D.; Le Bahers, T.; Adamo, C.; Ciofini, I. What Is the "Best" Atomic Charge Model to Describe Through-Space Charge-Transfer Excitations? *Phys. Chem. Chem. Phys.* **2012**, *14*, 5383–5388.
- [91] Liu, Z.; Lu, T.; Chen, Q. An sp-Hybridized All-Carboatomic Ring, Cyclo[18]carbon: Electronic Structure, Electronic Spectrum, and Optical Nonlinearity. *Carbon* **2020**, *165*, 461–467.
- [92] Onsager, L. Electric Moments of Molecules in Liquids. *J. Am. Chem. Soc.* **1936**, *58*, 1486–1493.
- [93] Cancès, E.; Mennucci, B.; Tomasi, J. A New Integral Equation Formalism for the Polarizable Continuum Model: Theoretical Background and Applications to Isotropic and Anisotropic Dielectrics. *J. Chem. Phys.* **1997**, *107*, 3032–3041.
- [94] Tomasi, J.; Mennucci, B.; Cammi, R. Quantum Mechanical Continuum Solvation Models. *Chem. Rev.* **2005**, *105*, 2999–3093.
- [95] Frisch, M. J. et al. Gaussian 16 Revision A.03. 2016; Gaussian Inc. Wallingford CT.
- [96] Tomasi, J.; Persico, M. Molecular Interactions in Solution: An Overview of Methods Based on Continuous Distributions of the Solvent. *Chem. Rev.* **1994**, *94*, 2027–2094.

Part II

Strategies, results, conclusions and perspectives

Chapter 4

Strategies and computational details

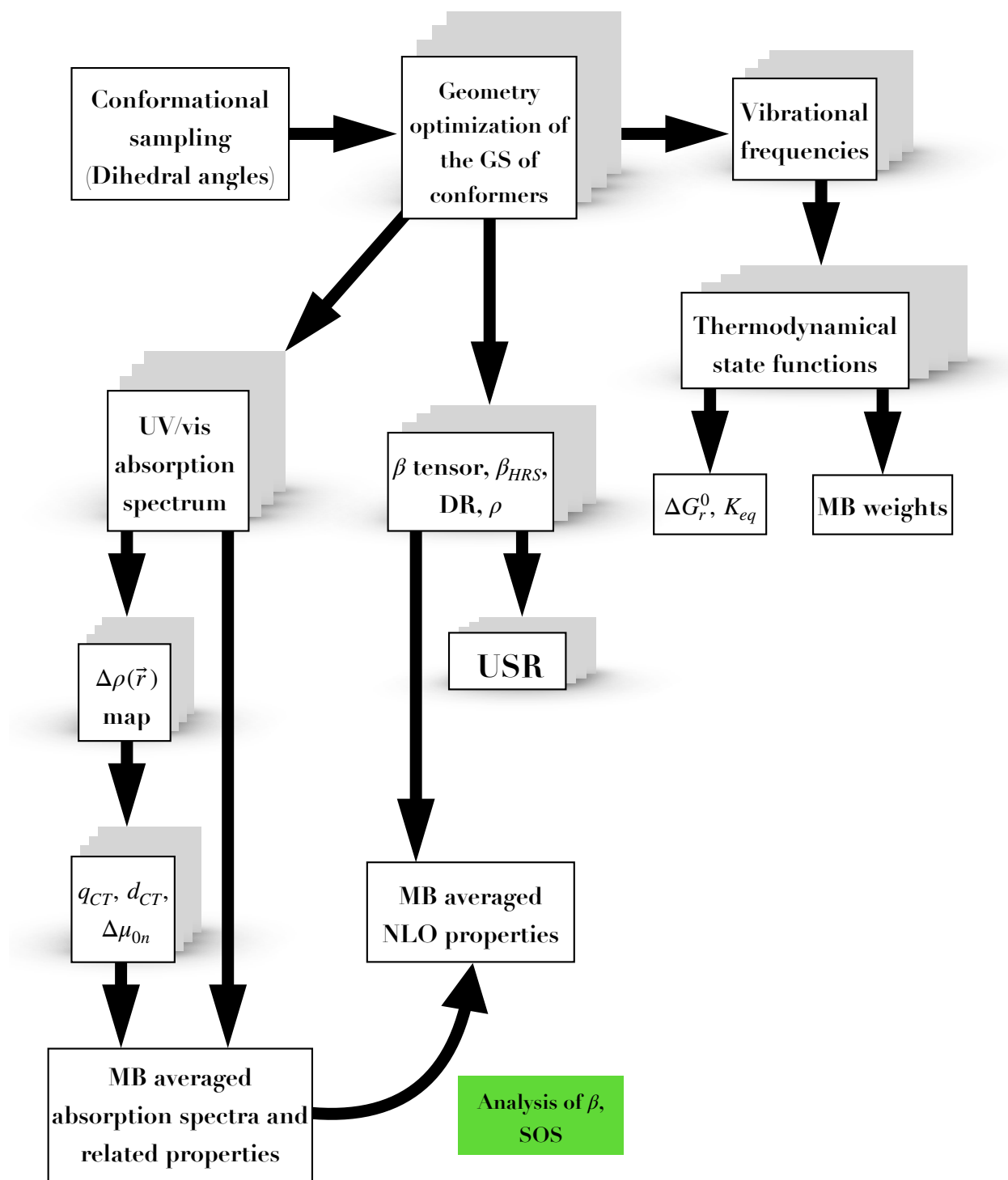
4.1 General strategies

The computational approach followed in this work to investigate the linear and second-order NLO properties is presented in Scheme 4.1. All calculations were performed at the density functional theory (DFT)^{1,2} level with the ω B97X-D exchange-correlation functional (XCF)³ and using the integral equation formalism (IEF)⁴ of the polarizable continuum model (PCM) (IEF-PCM) to describe acetonitrile solvent effects.⁵ Within IEF-PCM, the solvent is described by its dielectric permittivity (ϵ). ω B97X-D is a range-separated hybrid XCF that includes empirical atom-atom London dispersion forces using a version of Grimme’s D2 dispersion model.^{6,7} It has been shown to be suitable for predicting molecular structures and thermodynamic properties. In addition, owing to its Hartree-Fock (HF) exchange ranging from 22% at short range to 100% at long range, ω B97X-D is a reliable XC functional to compute the first hyperpolarizabilities of π -conjugated systems, because β is known as a "nonlocal" response.^{8,9} All calculations were carried out using the Gaussian16 package.¹⁰ The molecular structures, electron densities variations, and unit sphere representations were generated using the DrawMol software.¹¹ The Gaussian16 input files for the calculation of the properties were created thanks to a homemade python3 code.

The GS geometries of all conformers of all forms of the dyad were fully optimized using DFT, with the 6-311G(d) basis set.^{12,13} TIGHT convergence thresholds on the residual forces on the atoms (1.5×10^{-5} Ha/bohr or Ha/rad) were applied. $3N-6$ real vibrational frequencies demonstrate that the optimized geometries are minima on the potential energy surface.

The conformers of the DHA and VHF units that possess a non negligible weight within the Maxwell-Boltzmann (MB) statistics were identified (i) by performing relaxed potential energy scans to highlight the key dihedral angles associated with the most stable conformations and (ii) by keeping those with at least a 3% MB population. As for the merocyanine (MC or MCH), the literature informed on the eight possible conformers, and all were characterized (see, for instance, Refs. 14 and 15). The MB populations of the conformers as well as the equilibrium constants for the acid-base switching reactions were calculated using standard ($T = 298.15$ K) Gibbs free energy variations, ΔG^0 . The weight, w_i , of a given conformer with a Gibbs free energy ΔG_i^0 (kJ/mol) in an ensemble of N conformers $\{1 \leq i \leq N\}$ and within a MB statistic, is computed as:

$$w_i = \frac{\exp \frac{-\Delta G_i^0}{RT}}{\sum_j^N \exp \frac{-\Delta G_j^0}{RT}} \quad (4.1)$$



Scheme 4.1: Chart of the computational procedure followed in this work.

where R is the gas constant ($8.314 \cdot 10^{-3} \text{ kJ mol}^{-1} \text{ K}^{-1}$). The corresponding population, P_{MB_i} , for a conformer i is given by $P_i = 100w_i$. Owing to their extent, these molecules present low frequency collective vibrations, which can contaminate the calculation of the entropy, and therefore of the Gibbs free energy. These are like transverse acoustic modes in polymers,^{16–18} and their frequencies are below 50 cm^{-1} . This has the consequence that isomers with the

same GS energy have Gibbs free energies that differ by 1-2 kJ/mol. An accurate treatment of these modes requires accounting for the anharmonicity effects, which is beyond the scope of this study because it would necessitate excessive computational times. Note that additional geometry optimizations and vibrational frequency calculations (not presented in this work) were performed using SMD¹⁹ (Solvation Model Density) as an alternative implicit solvation scheme, and by modifying the tessellation of the PCM cavity to rule out the hypothesis of a poor description of solvent effects. However, similar results to those of IEF-PCM were obtained. As a matter of fact, a systematic correction was employed, which consists to withdraw the contribution to the entropy of the eight first vibrational normal modes. This correction was implemented in a homemade python3 code.

Natural bond orbitals (NBO) and natural population analysis (NPA) were performed for the most stable conformer of each form, in order to investigate the charge distribution in the GS, and hyperconjugative interactions.

The vertical excitation energies (ΔE_{0n}) and ground-to-excited state electric transition dipoles (μ_{0n}) for the 40 lowest-energy excited states (ES) n were computed using the time-dependent DFT (TDDFT) method^{20–22} and the 6-311+G(d) basis set.²³ The μ_{0n} quantities were then used to compute the oscillator strengths, $f_{0n} = 2/3\Delta E_{0n}\mu_{0n}^2$, which allowed to simulate the UV/vis absorption spectra. To plot these spectra, a Gaussian function was centered on each ΔE_{0n} , with an intensity proportional to f_{0n} , and of full width at half-maximum (FWHM) of 0.3 eV. Nonequilibrium solvation²⁴ TDDFT calculations were performed to evaluate the differences between the electronic densities of the ground state and of the key excited states, $|n\rangle$, *i.e.* those that dominate the UV/vis absorption spectra, $\Delta\rho_{0n}(\mathbf{r}) = \rho_n(\mathbf{r}) - \rho_0(\mathbf{r})$.²⁵ From $\Delta\rho_{0n}(\mathbf{r})$, the barycenters of the positive (\mathbf{R}^+) and negative (\mathbf{R}^-) electronic density variations, and the distance between the latter, d_{CT} , were calculated. The integration of $(\Delta\rho^{+/-}(\mathbf{r}))$ over the whole space gives the amount of charge transfer (q_{CT}) while the product between d_{CT} and q_{CT} equals the difference between the ground and excited state dipole moments,^{25,26}

$$\Delta\mu_{0n} = d_{CT}q_{CT} = \mu_n - \mu_0. \quad (4.2)$$

Moreover, using the Multiwfn software²⁷ for post-processing of the Gaussian16 calculations, the hole and electron densities were computed, as well as their overlap integrals and functions.

The static and dynamic (for an incident wavelength of 1907, 1500, and 1064 nm) β -tensor components were evaluated using the TDDFT method,²⁸ with the 6-311+G(d) basis set. With

respect to 6-311G(d), one set of diffuse functions was added on the atoms of the second and third rows of the periodic table, and on the hydrogen atoms, providing the best balance between accuracy (on ΔE_{0n} and β) and computational resources.²⁹ All the reported β values are given in atomic units (1 a.u. of $\beta = 3.6212 \times 10^{-42} \text{ m}^4 \text{ V}^{-1} = 3.2064 \times 10^{-53} \text{ C}^3 \text{ m}^3 \text{ J}^{-2}$) within the T convention.³⁰ When computing the β responses, the frequency dependence of ϵ is accounted. For acetonitrile, the static and optical ($\omega = \infty$) dielectric constants amount to 35.688 and 1.807, respectively.

Additional calculations were performed on the individual constitutive units, and on the four stereoisomers of the DHA-SP form of the dyad. The optimizations of their GS geometry, and the calculations of their molecular properties were done at the same level of approximation as for the complete dyads. Moreover, the trifluoroacetic acid and triethylammonium, as well as their conjugated bases, were fully optimized at the IEF-PCM/ ω B97X-D/6-311+G(d) level, and the Hessian were computed at each optimization step. Vibrational frequency calculations were performed on the equilibrium geometries to assess their thermodynamical state functions.

4.2 Interpretation of the NLO responses

First, the unit sphere representation (USR) was adopted to graphically represent the first hyperpolarizability tensor.³¹ It computes an effective induced SHG dipole,

$$\boldsymbol{\mu}_{ind} = \overleftrightarrow{\beta} : \mathbf{E}^2(\theta, \phi), \quad (4.3)$$

where $\overleftrightarrow{\beta}$ is the first hyperpolarizability tensor, and $\mathbf{E}(\theta, \phi)$ is a unit vector of incident electric field, of which the polarization is defined in spherical coordinates by the θ and ϕ angles. By sampling all possible θ and ϕ incident polarizations, the induced dipoles are plotted on a sphere centered on the molecule center of mass (for readability). This allows to highlight the directions where the second-order polarization is the strongest (it corresponds to the largest induced dipoles) and its orientation (from the donor to the acceptor direction), and to subsequently show how dipolar/octupolar the response is.

In a second step, a more spectroscopic understanding of these responses can be grasped by taking advantage of the perturbation theory, and more precisely, of the Orr-Ward-Bishop (OWB) summation over excited states (SOS) expression of β .^{32,33} Based on an friendly implementation of the OWB formula, as presented in the work of Champagne and Kirtman,³⁴ and

in the book by Boyd,³⁵ the β -tensor components are given by:

$$\beta_{\zeta\eta\xi}(-\omega_\sigma; \omega_1, \omega_2) = \sum P_{-\sigma,1,2} \sum_{n \neq 0} \sum_{m \neq 0} \frac{\mu_{0n}^\zeta \bar{\mu}_{nm}^\eta \mu_{0m}^\xi}{(E_{0n} - \omega_\sigma)(E_{0m} - \omega_2)}, \quad (4.4)$$

where the summations run over all excited states $|n\rangle$ and $|m\rangle$ of energies E_n and E_m . $\sum P_{-\sigma,1,2}$ denotes the summation over the six permutation of the pairs of frequencies and Cartesian components $(-\omega_\sigma, \zeta)$, (ω_1, η) , and (ω_2, ξ) . $|0\rangle$ is the wavefunction of the ground state of energy E_0 , so that $E_{0n} = E_n - E_0$, $\mu_{0n}^\zeta = \langle 0 | \hat{\mu}_\eta | n \rangle$ is the ζ component of the transition dipole moment between the ground state and the excited state $|n\rangle$, $\bar{\mu}_{nm}^\eta$ is the expectation value of the η component of the fluctuation operator, and reads:

$$\bar{\mu}_{nm}^\eta = \langle n | \hat{\mu}_\eta | m \rangle - \delta_{nm} \langle 0 | \hat{\mu}_\eta | 0 \rangle \quad (4.5)$$

where $\langle n | \hat{\mu}_\eta | m \rangle$ is the excited-to-excited state transition dipole moment between state $|n\rangle$ and $|m\rangle$ when $|n\rangle \neq |m\rangle$, while when $|n\rangle$ and $|m\rangle$ are the same, this quantity corresponds to the change of dipole moment between the ground and the n^{th} excited state.

However, the calculation of the excited-to-excited state transition dipoles is not implemented in most of the current quantum chemistry codes, at the TDDFT level and for the ω B97X-D exchange-correlation functional. Consequently, those transition dipoles were approximated using the Multiwfn program.²⁷ The latter employs the one-electron configuration coefficients (with five decimals), computed with Gaussian16 at the IEF-PCM/ ω B97X-D/TDDFT/6-311+G(d) level, to build the excited state wavefunctions and subsequently the unrelaxed electronic density of the excited states.³⁶ Then, feeding Eq. (4.4) with the different spectroscopic quantities, the complete dynamic β tensors were build thanks to a homemade python3 code. The workflow of the implementation is shown in Appendix A.

The accuracy of the fluctuation dipoles calculated with Multiwfn for the DHA-SP dyad was addressed by comparing these dipoles with the results obtained by computing β as a quadratic response function and its double residues with the Dalton program.^{37,38} The comparison was done for the DHA-MC form in its most stable conformation, in gas phase, and with the CAM-B3LYP XCF.³⁹ This approach consists in evaluating the single and double residues of the quadratic response function to extract the μ_{0n} and μ_{nm} terms, respectively, as discussed in Section 3.6,⁴⁰ and it is taken as the reference method. However, it was only possible to compute the transition dipoles for a maximum of 15 excited states, due to the high computational costs.

Subsequently, the contributions to β tensor of specific excited states included in the OWB formula were evaluated by employing the missing state analysis.⁴¹ It involves doing a series of incomplete SOS calculations, in which one state of a convergent sum is left out. The contribution of this missing state is determined by the effect of its absence. For instance, the relative importance of the i^{th} excited state, σ_i , to β_{HRS} is given by

$$\sigma_i = \frac{\beta_{HRS}^{tot} - \beta_{HRS}^i}{\beta_{HRS}^{tot}}, \quad (4.6)$$

where β_{HRS}^{tot} is the SOS calculation with no state missing, and β_{HRS}^i is the SOS value with state i missing. The missing state analysis was also implemented in an additional python3 code.

Bibliography

- [1] Hohenberg, P.; Kohn, W. Inhomogeneous Electron Gas. *Phys. Rev.* **1964**, *136*, 864–871.
- [2] Kohn, W.; Sham, L. J. Self-Consistent Equations Including Exchange and Correlation Effects. *Phys. Rev.* **1965**, *140*, 1133–1138.
- [3] Chai, J. D.; Head-Gordon, M. Long-Range Corrected Hybrid Density Functionals with Damped Atom-atom Dispersion Corrections. *Phys. Chem. Chem. Phys.* **2008**, *10*, 6615–6620.
- [4] Cancès, E.; Mennucci, B.; Tomasi, J. A New Integral Equation Formalism for the Polarizable Continuum Model: Theoretical Background and Applications to Isotropic and Anisotropic Dielectrics. *J. Chem. Phys.* **1997**, *107*, 3032–3041.
- [5] Tomasi, J.; Mennucci, B.; Cammi, R. Quantum Mechanical Continuum Solvation Models. *Chem. Rev.* **2005**, *105*, 2999–3093.
- [6] Grimme, S. Accurate Description of van der Waals Complexes by Density Functional Theory Including Empirical Corrections. *J. Comput. Chem.* **2004**, *25*, 1463–1473.
- [7] Grimme, S. Semiempirical GGA-type Density Functional Constructed with a Long-Range Dispersion Correction. *J. Comput. Chem.* **2006**, *27*, 1787–1799.
- [8] Johnson, L. E.; Dalton, L. R.; Robinson, B. H. Optimizing Calculations of Electronic Excitations and Relative Hyperpolarizabilities of Electrooptic Chromophores. *Acc. Chem. Res.* **2014**, *47*, 3258–3265.
- [9] Rtibi, E.; Abderrabba, M.; Ayadi, S.; Champagne, B. Theoretical Assessment of the Second-Order Nonlinear Optical Responses of Lindqvist-Type Organoimido Polyoxometalates. *Inorg. Chem.* **2019**, *58*, 11210–11219.
- [10] Frisch, M. J. et al. Gaussian 16 Revision A.03. 2016; Gaussian Inc. Wallingford CT.
- [11] Liégeois, V. UNamur. DrawMol. www.unamur.be/drawmol.
- [12] McLean, A. D.; Chandler, G. S. Contracted Gaussian Basis Sets for Molecular Calculations. I. Second Row Atoms, Z=11-18. *J. Chem. Phys.* **1980**, *72*, 5639–5648.
- [13] Krishnan, R.; Binkley, J. S.; Seeger, R.; Pople, J. A. Self-Consistent Molecular Orbital Methods. XX. A Basis Set for Correlated Wave Functions. *J. Chem. Phys.* **1980**, *72*, 650–654.

- [14] Minkin, V. I. Photo-, Thermo-, Solvato-, and Electrochromic Spiroheterocyclic Compounds. *Chem. Rev.* **2004**, *104*, 2751–2776.
- [15] Wang, P. X.; Bai, F. Q.; Zhang, Z. X.; Wang, Y. P.; Wang, J.; Zhang, H. X. The Theoretical Study of Substituent and Charge Effects in the Conformational Transformation Process of Molecular Machine Unit Spiropyran. *Org. Electron.* **2017**, *45*, 33–41.
- [16] Tashiro, K.; Kobayashi, M.; Tadokoro, H. Vibrational Spectra and Theoretical Three-Dimensional Elastic Constants of Isotactic Polypropylene Crystal: An Important Role of Anharmonic Vibrations. *Polym. J.* **1992**, *24*, 134102.
- [17] Kirtman, B.; Champagne, B.; André, J.-M. Role of Collective Modes in Vibrational Polarizabilities and Hyperpolarizabilities of Polyacetylene and Other Quasilinear Polymers. *J. Chem. Phys.* **1996**, *104*, 4125–4136.
- [18] Boulatov, A.; Burin, A. L. Crucial effect of Transverse Vibrations on the Transport through Polymer Chains. *J. Chem. Phys.* **2020**, *153*, 134102.
- [19] Marenich, A. V.; Cramer, C. J.; Truhlar, D. G. Universal Solvation Model Based on Solute Electron Density and on a Continuum Model of the Solvent Defined by the Bulk Dielectric Constant and Atomic Surface Tensions. *J. Phys. Chem. B* **2009**, *113*, 6378–6396.
- [20] Runge, E.; Gross, E. K. U. Density-Functional Theory for Time-Dependent Systems. *Phys. Rev. Lett.* **1984**, *52*, 997–1000.
- [21] Gross, E. K. U.; Dobson, J. F.; Petersilka, M. Density-Functional Theory of Time-Dependent Phenomena. *Top. Curr. Chem.* **1996**, *181*, 81–172.
- [22] Casida, M. E. *Density Functional Theory II*; Springer, Heidelberg, 1995.
- [23] Clark, T.; Chandrasekhar, J.; Spitznagel, G. W.; Von Ragué Schleyer, P. Efficient Diffuse Function-Augmented Basis Sets for Anion Calculations. III. The 3-21+G Basis Set for First-Row Elements, Li-F. *J. Comput. Chem.* **1983**, *4*, 294–301.
- [24] Scalmani, G.; Frisch, M. J.; Mennucci, B.; Tomasi, J.; Cammi, R.; Barone, V. Geometries and Properties of Excited States in the Gas Phase and in Solution: Theory and Application of a Time-Dependent Density Functional Theory Polarizable Continuum Model. *J. Chem. Phys.* **2006**, *124*, 094107.
- [25] Le Bahers, T.; Adamo, C.; Ciofini, I. A Qualitative Index of Spatial Extent in Charge-transfer Excitations. *J. Chem. Theory Comp.* **2011**, *7*, 2498–2506.
- [26] Jacquemin, D.; Le Bahers, T.; Adamo, C.; Ciofini, I. What Is the "Best" Atomic Charge

- Model to Describe Through-Space Charge-Transfer Excitations? *Phys. Chem. Chem. Phys.* **2012**, *14*, 5383–5388.
- [27] Lu, T.; Chen, F. Multiwfn: A Multifunctional Wavefunction Analyzer. *J. Comput. Chem.* **2012**, *33*, 580–592.
- [28] van Gisbergen, S. J. A.; Snijders, J. G.; Baerends, E. J. Calculating Frequency-Dependent Hyperpolarizabilities using Time-Dependent Density Functional Theory. *J. Chem. Phys.* **1998**, *109*, 10644–10656.
- [29] de Wergifosse, M.; Champagne, B. Electron Correlation Effects on the First Hyperpolarizability of Push-Pull π -Conjugated Systems. *J. Chem. Phys.* **2011**, *134*, 074113.
- [30] Shelton, D. P.; Rice, J. E. Measurements and Calculations of the Hyperpolarizabilities of Atoms and Small Molecules in the Gas Phase. *Chem. Rev.* **1994**, *94*, 3–29.
- [31] Tuer, A.; Krouglov, S.; Cisek, R.; Tokarz, D.; Barzda, V. Three-Dimensional Visualization of the First Hyperpolarizability Tensor. *J. Comput. Chem.* **2011**, *32*, 1128–1134.
- [32] Orr, B. J.; Ward, J. F. Perturbation Theory of the Non-Linear Optical polarization of an Isolated System. *Mol. Phys.* **1971**, *20*, 513–526.
- [33] Bishop, D. M. Explicit Nondivergent Formulas for Atomic and Molecular Dynamic Hyperpolarizabilities. *J. Chem. Phys.* **1994**, *100*, 6535–6542.
- [34] Champagne, B.; Kirtman, B. Evaluation of Alternative Sum-Over-States Expressions for the first Hyperpolarizability of Push-Pull Systems. *J. Chem. Phys.* **2006**, *125*, 024101.
- [35] Boyd, R. W. *Nonlinear Optics*, 4th ed.; Academic Press, Rochester, New York, 2020.
- [36] Wiberg, B.; Hadad, C. M.; LePage, T. J.; Breneman, C. M.; Frish, M. J. Analysis of the Effect of Electron Correlation on Charge Density Distributions. *J. Phys. Chem.* **1992**, *96*, 671–679.
- [37] Aidas, K. et al. The Dalton Quantum Chemistry Program System. *WIREs Comput. Mol. Sci.* **2013**, *4*, 269–284.
- [38] Dalton a Molecular Electronic Structure Program, Release DALTON2013.0 (2013). <http://daltonprogram.org/>.
- [39] Yanai, T.; Tew, D. P.; Handy, N. C. A New Hybrid Exchange–Correlation Functional Using the Coulomb-Attenuating Method (CAM-B3LYP). *Chem. Phys. Lett.* **2004**, *91*, 51–57.
- [40] Pedersen, T. B. *Introduction to Response Theory*, in: Leszczynski J. (Eds), *Handbook of Computational Chemistry*; Springer, Dordrecht, 2015; pp 269–294.

- [41] Dirk, C. W.; Kuzyk, M. G. Missing-State Analysis: A Method for Determining the Origin of Molecular Nonlinear Optical Properties. *Phys. Rev. A* **1989**, *39*, 1219–1226.

Chapter 5

Results and discussions

5.1 Structural properties

Conformational sampling

The very first step to assess the structural properties of the DHA-SP dyad is to determine the stable conformations of each form. On the one hand, the spiropyran unit only shows one conformer (but two enantiomers) while for the merocyanine constitutive unit, the thermochemical and geometrical features of the MC, E-MCH, and Z-MCH forms are given in Table B.1. On the other hand, the conformers of the full DHA-VHF dyad were identified thanks to relaxed potential energy scans. This is illustrated in Fig. 5.1 for the torsion potential between the two switching units, which exhibits two stable conformations. In this example, the energy barrier is relatively low (about 4 kJ/mol), so that the rotation is nearly free, and the two conformers can co-exist. Similar profiles were obtained for the DHA and VHF units of the dyad (Figs. B.2 and B.3). In Fig. B.3, the potential energy scan along the θ_X torsion provides a clue about the *cis-trans* isomerization activation barrier of VHF, which is of the order of 27 kJ/mol. Then, by combining the MC conformers with those of the DHA/VHF unit and the torsion between the moieties, all conformers of all states of the molecular switch were identified. Their thermochemical and geometrical parameters are presented in Tables B.2 to B.13. Note that each conformer is doubly degenerated due to pairs of θ_A and θ_B that gives two equivalent conformations. In

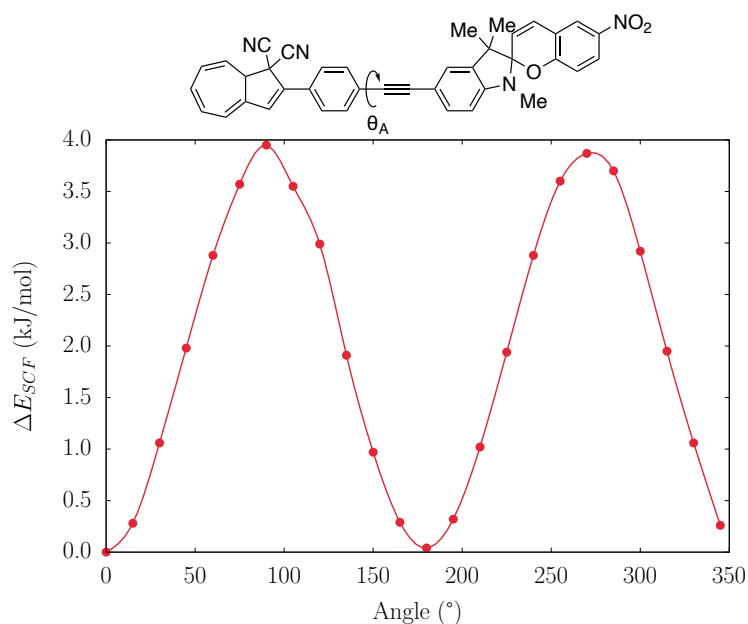


Fig. 5.1: Relaxed potential energy scan along the θ_A angle for the DHA-SP form. The reported ΔE_{SCF} values were evaluated at the IEF-PCM(acetonitrile)/ ω B97X-D/6-311G(d) level, using the most stable conformer as reference.

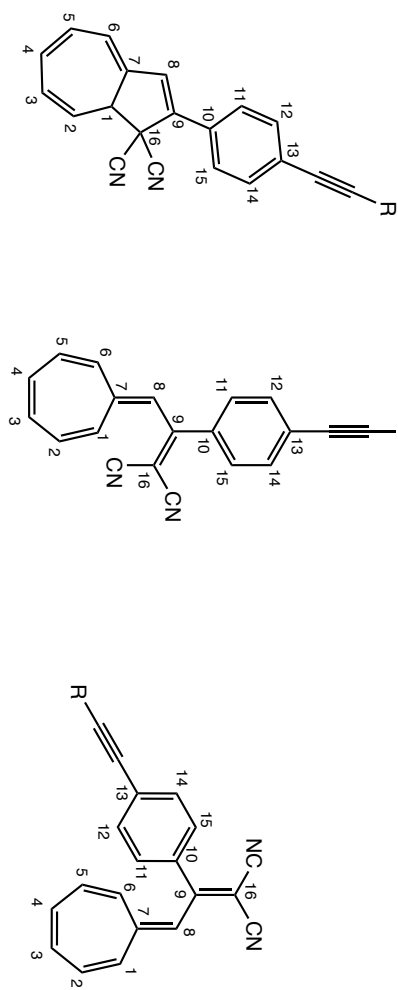
the rest of this Section, the structural analyses are done on the most stable conformations.

Ground state equilibrium geometries and charge distributions

The GS geometries of the four stereoisomers of the DHA-SP state were first optimized. The energy differences between the diastereoisomers are of the order of 10^{-3} kJ/mol (Table B.14). Their standard Gibbs free energy differences are marginally higher (at most 0.2 kJ/mol), and these differences are attributed to the numerical accuracy in the calculation of the low vibrational frequencies, and of their residual contributions to the entropy after correction. The only notable difference between the diastereoisomers is the norm of the GS dipole moment, for which the variation attains 5.8 %. A comparative analysis of their geometries (Table B.15) shows very small differences between the pairs of diastereoisomers, at most 0.001 Å on bond lengths, 0.1° on valence angles, and 1° on torsion angles. Therefore, the study can concentrate on only one of the four isomers, here chosen to be made of (S)-DHA and (R)-SP, further referred to as DHA and SP.

The GS geometries of all remaining dyads were then optimized, as well as those of the constitutive units. The results are exposed in Table 5.1 for the dyads and in Tables B.16 and B.17 for the individual parent units. The geometrical parameters of the individual constitutive units are identical (within a precision of 0.001 Å on the bond lengths) to those of the connected units. Therefore, the switching units do not influence each other geometrical structures. This fact is in agreement with the negligible energy differences between the pairs of diastereoisomers. However, a previous study¹ has shown that the geometry of DHA/VHF moieties is sensitive to the nature of the substituent, when directly grafted to the DHA/VHF unit, and that it depends in particular on whether it is an electron donor or acceptor group. In this Section, the term "substituents" refers to actual substituents/chemical functions (such as the cyano groups on C_{16}) directly grafted at different positions on the DHA/VHF (or SP/MC) backbone, but not to the second switching unit. The current lack of effect is attributed to the "neutral" role of the alkyne linker, which neither plays the role of a donor or of an acceptor. This last statement is supported by the results in Table B.18, which show how the bond lengths associated with the central alkyne linker depends on the state of the DHA/VHF and SP/MC switching units. Clearly, the impact of the switching state of the units on these bond lengths is negligible. Consequently, the following analysis is performed by decomposing the system, *i.e.*, by studying the parameters of each entity individually.

Table 5.1: Representative geometrical parameters: bond lengths (Å), bond angles ($^{\circ}$), torsion angles ($^{\circ}$) and bond length alternations (Å) for the DHA and *cis/trans*-VHF units in their most stable conformations depending on the state of the SP/MC switching unit as evaluated at the IEF-PCM(acetone)/DFT/ ω B97X-D/6-311G(d) level of theory. $BLA_1 = (d_{C_7-C_8} + d_{C_9-C_{16}} - 2d_{C_8-C_9})/2$, $BLA_2 = (d_{C_7-C_8} + d_{C_9-C_{10}} - 2d_{C_8-C_9})/2$, $BLA_3 = (d_{C_{15}-C_{10}} + d_{C_9-C_{16}} - 2d_{C_9-C_{10}})/2$, BLA_4 is associated with the bond length alternation in the six-membered ring of the DHA/VHF unit, and $BLA_5 = (d_{C_1-C_2} + 2d_{C_3-C_4} + 2d_{C_5-C_6} + d_{C_7-C_1})/6 - (2d_{C_2-C_3} + 2d_{C_4-C_5} + 2d_{C_6-C_7})/6$.

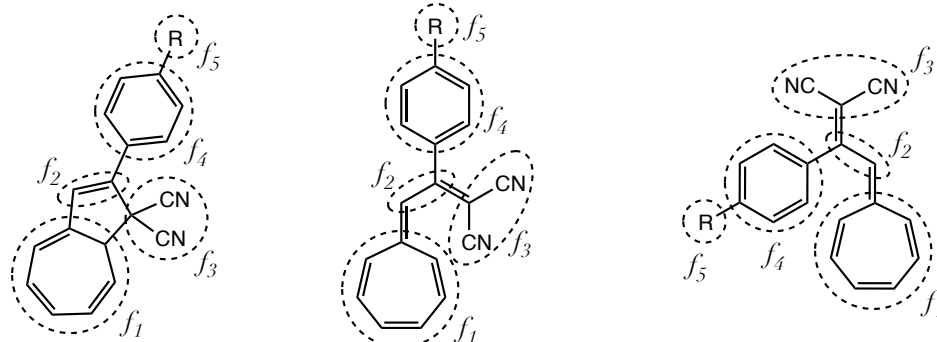
R = -C≡C-SP/MC	SP	MC	DHA				<i>cis</i> -VHF				<i>trans</i> -VHF			
			E-MCH	Z-MCH	SP	MC	E-MCH	Z-MCH	SP	MC	E-MCH	Z-MCH		
														
C7-C8	1.444	1.444	1.444	1.444	1.389	1.390	1.391	1.391	1.389	1.389	1.390	1.390		
C8-C9	1.343	1.343	1.343	1.343	1.423	1.421	1.420	1.420	1.419	1.419	1.418	1.418		
C9-C16	1.542	1.542	1.541	1.541	1.390	1.391	1.391	1.391	1.389	1.389	1.389	1.389		
C9-C10	1.466	1.467	1.467	1.467	1.484	1.485	1.486	1.486	1.485	1.486	1.486	1.486		
C8-C9-C16	108.9	109.0	109.0	109.0	125.1	125.3	125.5	125.4	120.6	120.6	120.7	120.7		
C4-C5-C6-C7	24.8	25.0	24.8	24.9	-1.5	-1.5	-1.5	-1.5	1.1	1.1	1.1	1.1		
C6-C7-C1-C2	-52.8	-53.3	-52.8	-52.9	-15.7	-15.6	-15.6	-15.4	18.4	18.6	18.1	18.3		
C7-C8-C9-C16	-6.8	-6.7	-6.8	-6.6	-33.3	-32.8	-32.2	-32.3	166.3	166.6	167.2	167.3		
C7-C8-C9-C10	176.0	175.8	176.0	176.0	150.0	150.6	151.2	151.1	-18.3	-18.0	-17.5	-17.4		
C8-C9-C10-C11	-19.4	-19.6	-20.0	-19.6	-47.8	-49.0	-49.8	-49.5	-54.1	-54.6	-55.6	-55.7		
BLA1	0.149	0.149	0.149	0.149	-0.032	-0.031	-0.029	-0.029	-0.030	-0.030	-0.028	-0.028		
BLA2	0.112	0.112	0.112	0.112	0.015	0.016	0.018	0.018	0.017	0.019	0.020	0.020		
BLA3	/	/	/	/	-0.090	-0.091	-0.092	-0.092	-0.093	-0.094	-0.094	-0.094		
BLA4	0.003	0.003	0.003	0.003	0.000	0.000	0.000	0.000	0.000	0.000	0.000	0.000		
BLA5	-0.093	-0.093	-0.093	-0.093	0.077	0.076	0.076	0.075	0.077	0.076	0.076	0.076		

First, in the DHA moiety (of all DHA-containing forms) of the molecular switch, the ($C_7 - C_8 - C_9 - C_{16}$) and ($C_7 - C_8 - C_9 - C_{10}$) torsion angles are close to 0° and 180° , respectively. The five-membered ring forms a $\simeq -20^\circ$ dihedral angle with the adjacent phenyl ring. Then, the seven-membered ring adopts a boat conformation, which is also observed in the solid state as revealed by single-crystal X-ray diffraction.^{2,3} The ($C_4 - C_5 - C_6 - C_7$) and ($C_6 - C_7 - C_1 - C_2$) dihedral angles take values of about 25° and -53° , respectively. This cycle becomes nearly planar (-2° and -16° , respectively) after the isomerization of DHA to *cis*-VHF. This planarization was also experimentally observed by Kaftory *et al.*,³ but they did not report the values for these angles. The planarization of the seven-membered ring is related to the decrease of electron density as spotlighted in Ref. 1, which is a first indication that the ring π -electron delocalization is better in VHF than in DHA. Although it was recently concluded that the planarization of this cycloheptatriene ring plays a key role in the breaking of the $C_1 - C_{16}$ bond leading to the VHF state, it is essentially a consequence of the enhancement of aromaticity following the isomerization.^{4,5}

Natural population analysis (Table 5.2) confirms the aforementioned drop of electron density on the seven-membered ring (from $+0.12 e$ to $+0.39 e$), and the simultaneous charge transfer to the $C(CN)_2$ moiety (f_3 fragment, from $-0.25 e$ to $-0.49 e$). Plaquet *et al.*¹ suggested that the charge is also transferred to the phenyl ring, no matter the donor/acceptor character of R. Nonetheless, the current results do not reproduce this last observation, indicating rather that this phenyl ring becomes slightly more positive whereas the excess charge is transferred to the f_2 fragment. This difference arises from the fact that Plaquet *et al.*¹ employed Mulliken population analysis, which displays obviously some limitations.

The DHA to VHF isomerization is associated with a reversal of the single and double $C - C$ bonds of the seven-membered and five-membered rings (the latter is now open), with changes of the bond lengths between 0.05 \AA and 0.15 \AA . In the cyclopentene, the lengths of the single ($1.444\text{--}1.542 \text{ \AA}$) and double (1.343 \AA) bonds are clearly distinguishable, while this single/double bond character difference is less marked in the VHF form, this part of the system being π -conjugated. π -conjugated segments are commonly described by the so-called bond length alternations (BLAs), which is a major parameter influencing the linear and nonlinear optical responses.^{6,7} Results for selected BLAs are also presented in Table 5.1. The opening of DHA to VHF leads to a significant decrease of BLA_1 and BLA_2 . This is interpreted as an increase of the π -electron delocalization. BLA_3 confirms that the central part of the VHF moiety involves π -conjugation. The $BLA_4 \simeq 0$ values show that the phenyl ring is weakly

Table 5.2: Natural population analysis for the five remarkable molecular fragments of the DHA-SP, *cis*-VHF-SP and *trans*-VHF-SP dyads as evaluated at the IEF-PCM(acetonitrile)/ ω B97X-D/6-311G(d) level of theory.



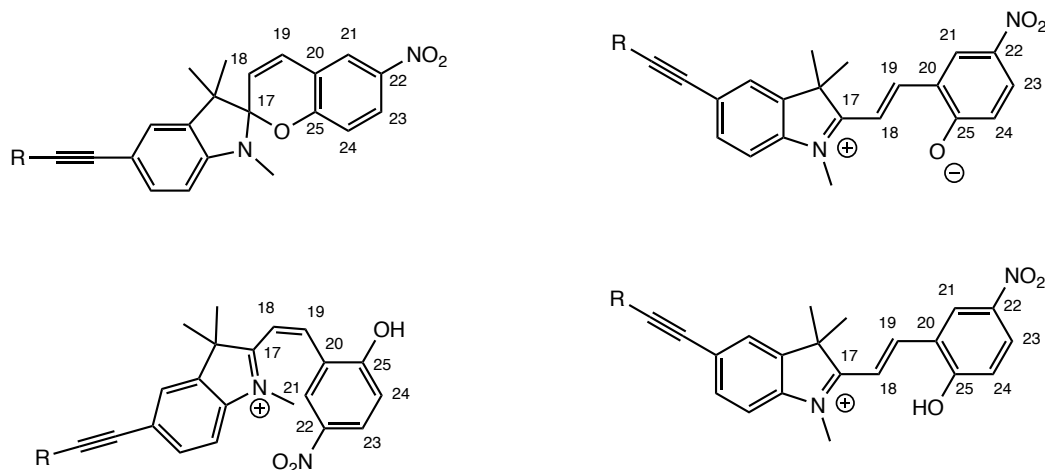
	f_1	f_2	f_3	f_4	f_5
DHA-SP	0.117	0.106	-0.250	-0.001	0.029
<i>cis</i> -VHF-SP	0.385	0.045	-0.493	0.032	0.029
<i>trans</i> -VHF-SP	0.394	0.047	-0.492	0.018	0.029

conjugated with the rest of the system (in other words, it keeps its geometrical aromaticity). Finally, BLA₅ confirms that the π -conjugation in the seven-membered ring is better in VHF than in DHA. One can also note that the DHA ring-opening is accompanied by an increase of the GS dipole moment, as illustrated in Fig. B.4.

Upon *cis-trans* isomerization of VHF, the bond lengths of the central part stay identical (variations smaller than 0.001 Å), and the seven-membered ring keeps its near-planarity. However, the global planarity of the VHF unit increases as the ($C_7 - C_8 - C_9 - C_{10}$) dihedral angle goes from $\simeq 150^\circ$ to -18° along the *cis* to *trans* transformation.

The results for the corresponding structural analysis of the second switching unit, *i.e.* SP/MC, are presented in Table 5.3. The indoline and benzopyran moieties in SP are not co-planar but approximately perpendicular to each other. As expected from crystallographic data,⁸ the $N - C_{17}$ bond in SP is shorter than those in the corresponding "isolated" five-membered heterocycles (1.44 Å compared to 1.47-1.48 Å for pyrrolidine derivatives). On the other hand, the $C_{17} - O$ bond is elongated in comparison to those in similar six-membered heterocycles such as tetrahydropyran (1.46 Å compared to 1.41-1.43 Å). These specific structural characteristics of spiropyrans have already been rationalized in the literature employing the simplistic Lewis structure model (for instance, Refs. 9 and 10). These works suggested that the weakening of the $C_{17} - O$ bond strength in the GS results from the interaction between the lone electron pair (LEP) of the N -atom and the σ^* -MO of the $C_{17} - O$ covalent bond. This interaction, known as a negative hyperconjugation¹¹ (or eventually, anomeric effect), consists in the

Table 5.3: Representative geometrical parameters: bond lengths (Å), bond angles (°), torsion angles (°), and bond length alternations (Å) for the SP, MC, E-MCH, and Z-MCH moieties in their most stable conformations depending on the state of the DHA/VHF switching unit as evaluated at the IEF-PCM(acetonitrile)/ ω B97X-D/6-311G(d) level of theory. $BLA_6 = (d_{C_{17}-C_{18}} + 2d_{C_{19}-C_{20}} + d_{C_{21}-C_{22}})/4 - (2d_{C_{18}-C_{19}} + 2d_{C_{20}-C_{21}})/4$.



R = -C \equiv C-DHA/VHF	DHA	<i>cis</i> -VHF	<i>trans</i> -VHF	DHA	<i>cis</i> -VHF	<i>trans</i> -VHF
SP				MC		
N-C ₁₇	1.440	1.440	1.440	1.337	1.337	1.337
C ₁₇ -O	1.464	1.463	1.463	/	/	/
C ₁₈ -C ₁₉	1.499	1.499	1.499	1.401	1.401	1.401
C ₁₉ -C ₂₀	1.331	1.331	1.330	1.378	1.378	1.378
C ₂₀ -C ₂₁	1.457	1.457	1.457	1.415	1.415	1.415
C ₂₅ -O	1.339	1.339	1.339	1.240	1.240	1.240
C ₁₈ -H - - O	/	/	/	2.130	2.130	2.130
C ₁₇ -C ₁₈ -C ₁₉ -C ₂₀	3.6	3.6	3.6	179.9	179.9	180.0
N-C ₁₇ -C ₁₈ -C ₁₉	-136.7	-136.7	-136.7	-179.6	-179.6	-179.9
C ₁₈ -C ₂₉ -C ₂₀ -C ₂₅	7.2	7.4	7.2	0.1	0.0	0.0
BLA ₆	0.091	0.091	0.091	0.008	0.007	0.008
E-MCH				Z-MCH		
N-C ₁₇	1.318	1.318	1.319	1.305	1.305	1.306
C ₁₇ -C ₁₈	1.428	1.428	1.429	1.453	1.453	1.453
C ₁₈ -C ₁₉	1.351	1.351	1.353	1.340	1.340	1.340
C ₁₉ -C ₂₀	1.451	1.450	1.451	1.469	1.469	1.469
C ₂₅ -O	1.336	1.336	1.335	1.340	1.340	1.340
O-H	0.962	0.961	0.962	0.961	0.961	0.961
C ₁₇ -C ₁₈ -C ₁₉ -C ₂₀	179.8	178.9	179.9	-4.4	-4.2	-4.0
N-C ₁₇ -C ₁₈ -C ₁₉	179.8	178.8	178.1	-50.6	-50.0	-49.9
C ₁₈ -C ₁₉ -C ₂₀ -C ₂₅	175.7	174.7	-1.8	138.9	137.3	137.1
BLA ₆	0.054	0.054	0.052	0.077	0.077	0.077

donation of electron density from a filled π/p -orbital or LEP to a neighboring σ^* -antibonding molecular orbital. More quantitative interpretations are provided in Table 5.4 by employing the NBO analysis. The second LEP of the O-atom, associated with π -electron density (99.3 %

Table 5.4: Occupancies of the NBOs (e), their corresponding energies (eV), and percentages of s and p characters for the DHA-SP form as evaluated at the IEF-PCM(acetonitrile)/ ω B97X-D/6-311G(d) level.

NBO	Occupancy	Energy	s and p character
LEP N	1.75	-9.12	$s(5.1)$ $p(94.9)$
LEP(1) O	1.96	-16.95	$s(32.7)$ $p(67.2)$
LEP(2) O	1.82	-11.17	$s(0.7)$ $p(99.3)$
$\sigma^* C_{17} - O$	0.09	8.52	/
$\sigma^* C_{17} - N$	0.05	12.01	/

of p character), is lower in energy than the N -atom LEP (-11.17 eV compared to -9.12 eV), in agreement with their respective electronegativity. Then, the $C_{17} - O$ σ^* -MO is found to be energetically higher (8.52 eV), and mainly located on the carbon atom (70.6 %). Hence, the $N_{LEP} \rightarrow \sigma^*_{C_{17}-O}$ electron density donation is possible, and can be emphasized by the nonzero natural population of the antibonding molecular orbital, which amounts to 0.09 e . As detailed by Reed and coworkers,¹² small occupancies of these antibonding orbitals correspond to small noncovalent corrections to the ideal Lewis structure (localized covalent bonds). The population of the $C_{17} - O$ σ^* -MO induces a weakening of the $C_{17} - O$ covalent bond, in agreement with Görner,¹³ which measured, by time-resolved spectroscopy, an activation energy of 90 kJ/mol ($\simeq 0.93$ eV) for the $C_{17} - O$ bond breaking, of a nearly identical spiropyran in acetonitrile (*i.e.*, when $R = H$). Moreover, the electron density donation is only weakly compensated by the $O_{LEP(2)} - \sigma^*_{C_{17}-N}$ interaction, due to a wider energy gap between the corresponding MOs (23.18 eV compared to 17.64 eV for the $N_{LEP} - \sigma^*_{C_{17}-O}$ gap).¹⁴ Since the second unit does not influence the geometrical parameters of the first one, a similar activation energy is expected for the system of interest in this work. Finally, the energy lowering, $\Delta E_{\sigma\sigma^*}^{(2)}$ (remind Fig. 3.1), resulting from the interaction between the N -atom LEP and the σ^* -MO was estimated by the second-order perturbation theory analysis of the Fock matrix in the NBO basis (Eq. (3.35)) and it is equal to 0.91 eV.

Contrary to the DHA/VHF unit, the SP to MC isomerization is not associated with a reversal of the single and double $C - C$ bonds. Only the initially-single $N - C_{17}$ bond adopts a double bond character following the ring opening. The changes of bond lengths range between 0.011 Å and 0.103 Å. Yet, upon ring opening, the lengths of single bonds ($C_{17} - C_{18}$, $C_{19} - C_{20}$) decrease while the length of the $C_{19} - C_{20}$ double bond increases. Turning now to the bond length alternation, the trend for BLA₆ is SP > Z-MCH > E-MCH > MC, indicating that the π -conjugation is the smallest for SP because it is broken by the spiro junction, and the largest for

MC. This would give a high contrast of first hyperpolarizability between the open (MC) and closed (SP) forms. The π -electron delocalization is weakened in the E/Z-MCH forms as a result of the phenolate donor strength reduction upon protonation. Additionally, the out-of-plane distortion in Z-MCH (the $C_{17} - C_{18} - C_{19} - C_{20}$ dihedral angle $\simeq -50.0^\circ$) also weakens the π -conjugation. Furthermore, Sheng and coworkers¹⁵ have investigated the structural effects of the substituents on spiropyrans and merocyanines (in relation to their donor/acceptor character). The presence of the nitro group in position 22, a strong electron withdrawing group stabilizing the MC form, is expected to enhance the aforementioned contrast of β between the SP and MC forms. One can also note that the GS dipole moment increases significantly upon the ring-opening (see Fig. B.4).

The distance between the *O*-atom and the hydrogen carried by C_{18} equals 2.130 Å in the MC form. A weak hydrogen bond is therefore present, although a carbon atom is not a good hydrogen bond donor, and the angle $C_{18} - H - - O$ is 105.0° . The second-order noncovalent energy describing the interaction between the LEP of the *O*-atom and the antibonding $C_{18} - H$ σ^* -MO was evaluated by NBO calculations, and it is indeed small 0.04 (eV) but not negligible.

5.2 Thermodynamical analysis

To tackle the thermodynamics of these transformations, the Gibbs free energies were calculated for the successive switching steps. This section aims at studying the opening/closing state of both switching units, following the addition of acid (trifluoroacetic acid) or base (triethylamine), or UV/vis light irradiation. The analysis separates the pH-gated switching transitions from the photochromic switching processes. Then, the attention is drawn to the consecutive reactions, from which the orthogonality and the path-dependency of the switching transitions arise.

Acid-base switching reactions

First, the reactions with the triethylamine, Et_3N , are addressed,



where AH is the acid form of the switch, A^- its conjugate base, and the indices "sol" point out the solvation in acetonitrile. Note that, in this Section, the charge of the acids (MCH^+) is explicitly added to their name, as a matter of highlighting the conservation of the charge. The

associated standard Gibbs free energies are calculated as follows:

$$\Delta G^0 = [G^0(A_{\text{sol}}^-) + G^0(\text{Et}_3\text{NH}_{\text{sol}}^+)] - [G^0(\text{AH}_{\text{sol}}) + G^0(\text{Et}_3\text{N}_{\text{sol}})]. \quad (5.2)$$

The G^0 of the $\text{Et}_3\text{NH}^+/\text{Et}_3\text{N}$ couple were evaluated using the 6-311G(d) basis set but also 6-311+G(d) to assess the impact of diffuse functions. Based on these ΔG^0 , the equilibrium constants, K_{eq} , were calculated,

$$K_{eq} = e^{\frac{-\Delta G^0}{RT}}, \quad (5.3)$$

where R is the gas constant, and T is the temperature. The results are presented in Table 5.5.

At first sight, the ΔG^0 values and equilibrium constants indicate that all the reactions induced by the addition of Et_3N are spontaneous and complete under standard conditions of temperature and concentration. Similar conclusions are drawn from the calculations with both basis sets. Indeed, the values are simply shifted by 8.7 kJ/mol between the two sets of results, which corresponds to the difference between the ΔG^0 of the $\text{Et}_3\text{NH}^+/\text{Et}_3\text{N}$ acid-base couple calculated with the two basis sets, as detailed in Table C.1. Yet, this difference emphasizes the better description of the charge using the 6-311+G(d) basis set.

Looking now more precisely at each reaction with Et_3N , a lack of influence of one unit on the other emerges, similarly to what has been observed for the geometrical features: the ΔG^0 associated with closing the Z-MCH⁺ moiety into SP, or by deprotonation of E-MCH⁺, is independent of the level of opening of the DHA/VHF unit (within a precision of 1.3 kJ/mol). Moreover, the results show that the deprotonation (and ring closing) of the Z-MCH⁺ moiety is more exergonic than that of E-MCH⁺, leading to the zwitterionic MC form.

Table 5.5: Standard ($T = 298.15$ K, $[] = 1$ M[†]) Gibbs free energy (kJ/mol) variations[‡], and equilibrium constants (unitless) following the addition of Et_3N (Eq. (5.1)) as evaluated at the IEF-PCM(acetonitrile)/ ω B97X-D level of theory.

Switching process	Et ₃ N with 6-311G(d)		Et ₃ N with 6-311+G(d)	
	ΔG^0	K_{eq}	ΔG^0	K_{eq}
<i>trans</i> -VHF-E-MCH ⁺ → <i>trans</i> -VHF-MC	-41.5	1.9×10^7	-32.8	5.6×10^5
<i>trans</i> -VHF-Z-MCH ⁺ → <i>trans</i> -VHF-SP	-91.1	9.1×10^{15}	-82.4	2.7×10^{14}
<i>cis</i> -VHF-E-MCH ⁺ → <i>cis</i> -VHF-MC	-42.1	2.4×10^7	-33.4	7.1×10^5
<i>cis</i> -VHF-Z-MCH ⁺ → <i>cis</i> -VHF-SP	-91.0	8.7×10^{15}	-82.3	2.6×10^{14}
DHA-E-MCH ⁺ → DHA-MC	-40.8	1.4×10^7	-32.1	4.2×10^5
DHA-Z-MCH ⁺ → DHA-SP	-89.4	4.6×10^{15}	-80.7	1.4×10^{14}

[†] Since the sum of the stoichiometric coefficients of the reactants and products are the same, standard conditions of pressure ($P = 1$ atm) and of concentration (1 M) give the same ΔG^0 , and equilibrium constants.

[‡] Averaged values calculated using the MB populations at 298.15 K.

Afterwards, the analysis of the switching reactions (experimentally observed) triggered by the addition of acid can be subdivided into two levels of approximation. One can already note that the aforementioned "independence" of the switching units is obviously observed for the other acid-base reactions. On the one hand, the latter can be investigated, in first approximation, by considering the half protonation reactions in solution,



with their associated ΔG^0 ,

$$\Delta G^0 = [G^0(AH_{\text{sol}})] - [G^0(A_{\text{sol}}^-) + G^0(H_{\text{sol}}^+)]. \quad (5.5)$$

The $G^0(H^+)$ in acetonitrile was adopted from Ref. 16 (-1075.3 kJ/mol), and the equilibrium constants are calculated using Eq. (5.3). Within this approach, all the switching processes considered in Table 5.6 appear to be exergonic. On the other hand, when considering the reactions with the trifluoroacetic acid which whom the geometry was optimized at the IEF-PCM(acetonitrile)/ ω B97X-D/6-311+G(d) level of approximation,



and the associated standard Gibbs free energy variations,

$$\Delta G^0 = [G^0(AH_{\text{sol}}) + G^0(CF_3COO_{\text{sol}}^-)] - [G^0(A_{\text{sol}}^-) + G^0(CF_3COOH_{\text{sol}})], \quad (5.7)$$

the formation of the protonated Z-isomer of the merocyanine becomes endergonic (ΔG^0 of about 31 kJ/mol). Consequently, the K_{eq} values for these processes are typical of equilibria shifted towards the reactants. Therefore, one can conclude on the spontaneity of the $MC \rightarrow MCH^+$ reactions, but the acido-triggered opening of SP is not spontaneous. However, the latter point, $\Delta G^0 > 0$, is consistent with the (experimental) literature, informing that large excess of trifluoroacetic acid are needed.^{17,18}

Moreover, the pH-dependency of the acidochromism varies in tandem with the molecule capacity to planarize.¹⁹ So, owing to the out-of-plane distortion of Z-MCH⁺ highlighted in Section 5.1, a limited access to the protonated Z-form is indeed expected in the presence of (relatively) weak acids, such as CF₃COOH. Furthermore, the strength of the acid also plays

Table 5.6: Standard ($T = 298.15$ K, $[] = 1$ M) Gibbs free energy (kJ/mol) variations[†], and equilibrium constants following the addition of acid as evaluated at the IEF-PCM(acetonitrile)/ ω B97X-D/6-311G(d) level of theory. The G^0 values for the TFA and its conjugated base were computed using the 6-311+G(d) basis set. Following Ref. 16, a G^0 value of -1075.3 kJ/mol was adopted for H^+ in acetonitrile.

Switching process	Reaction with H^+		Reaction with CF_3COOH	
	ΔG^0	K_{eq}	ΔG^0	K_{eq}
<i>trans</i> -VHF-SP \rightarrow <i>trans</i> -VHF-Z-MCH ⁺	-9.2	40.9	31.6	2.9×10^{-6}
<i>trans</i> -VHF-MC \rightarrow <i>trans</i> -VHF-E-MCH ⁺	-58.8	1.9×10^{10}	-18.0	1.4×10^3
<i>cis</i> -VHF-SP \rightarrow <i>cis</i> -VHF-Z-MCH ⁺	-9.3	43.0	31.5	3.0×10^{-6}
<i>cis</i> -VHF-MC \rightarrow <i>cis</i> -VHF-E-MCH ⁺	-58.2	1.6×10^{10}	-17.4	1.1×10^3
DHA-SP \rightarrow DHA-Z-MCH ⁺	-10.9	80.0	30.0	5.6×10^{-6}
DHA-MC \rightarrow DHA-E-MCH ⁺	-59.5	2.6×10^{10}	-18.7	1.9×10^3

[†] Averaged values calculated using the MB populations at 298.15 K.

a key role. This consideration was noted for the first time by Irving and colleagues²⁰ on xanthanospiropyrans, and then observed on several occasions with indolinobenzospiropyran.^{18,21}

So far, only the experimentally characterized acido-triggered switching process were considered. Nevertheless, one additional acidochromic reaction can be emphasized: the protonation of DHA-MC to DHA-E-MCH⁺. Even though the latter is not of great utility for the orthogonal and path-dependent successive transitions, it is thermodynamically favorable, since its ΔG^0 amounts of -59.5 and -18.7 kJ/mol with H^+ and CF_3COOH , respectively, as shown by the last line in Table 5.6. Those results are also in agreement with the fact that ΔG^0 is independent of the state of the DHA/VHF unit.

General thermodynamic analysis of the switching transitions

The calculated Gibbs free energy variations for the thermally- and photo-induced switching processes are shown in Table 5.7. These results, as well as the previous observations about the thermodynamical aspects of the acid-base reactions, allow to unravel the relative stability of the different states of the dyads, starting with *cis-trans* isomerization of VHF, which was overlooked in Ref. 22. The ω B97X-D calculations show that $\Delta G^0 = G_{cis}^0 - G_{trans}^0$ amounts to about 9 kJ/mol (in average over the pairs of switching processes involving *cis* and *trans*-VHF in Table 5.7), leading to a negligible MB weight for the *cis* form. A similar value (10.3 kJ/mol) is obtained for the constitutive unit, presented in Table C.2, affirming once more that the thermodynamical properties of a single unit remain consistent, regardless of the presence of the second unit. However the relaxed potential energy scan in Fig. B.3, already mentioned

Table 5.7: Standard ($T = 298.15$ K, $[] = 1$ M) Gibbs free energy (kJ/mol) variations[†] following the thermochromic and photochromic switching processes as evaluated at the IEF-PCM(acetonitrile)/ ω B97X-D/6-311G(d) level of theory.

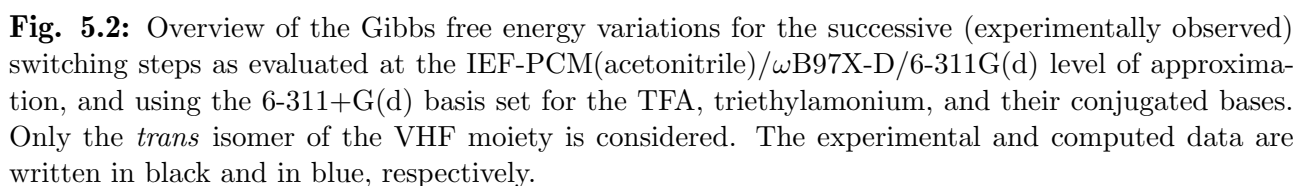
Switching process	ΔG^0
DHA-SP \rightarrow <i>trans</i> -VHF-SP	13.4
DHA-SP \rightarrow <i>trans</i> -VHF-MC	43.4
<i>trans</i> -VHF-SP \rightarrow <i>trans</i> -VHF-MC	30.0
DHA-SP \rightarrow <i>cis</i> -VHF-SP	22.6
DHA-SP \rightarrow <i>cis</i> -VHF-MC	51.8
<i>cis</i> -VHF-SP \rightarrow <i>cis</i> -VHF-MC	29.2
<i>trans</i> -VHF-Z-MCH ⁺ \rightarrow <i>trans</i> -VHF-E-MCH ⁺	-19.6
<i>trans</i> -VHF-Z-MCH ⁺ \rightarrow DHA-E-MCH ⁺	-34.0
<i>trans</i> -VHF-E-MCH ⁺ \rightarrow DHA-E-MCH ⁺	-14.4
<i>cis</i> -VHF-Z-MCH ⁺ \rightarrow <i>cis</i> -VHF-E-MCH ⁺	-19.7
<i>cis</i> -VHF-Z-MCH ⁺ \rightarrow DHA-E-MCH ⁺	-43.1
<i>cis</i> -VHF-E-MCH ⁺ \rightarrow DHA-E-MCH ⁺	-23.4
DHA-Z-MCH ⁺ \rightarrow DHA-E-MCH ⁺	-18.9
DHA-MC \rightarrow DHA-SP	-29.7

[†] Averaged values calculated using the MB populations at 298.15 K.

in Section 5.1, gives a clue on the activation barrier being approximately of 27 kJ/mol. Hence, those *cis* and *trans* isomers are taken as two different and well defined species in the rest of this work.

Fig. 5.2 summarizes the thermodynamical aspects, as obtained from our DFT calculations, of the transitions that have been previously experimentally characterized (considering only the *trans* isomer of VHF). The Gibbs free energies of the *trans*-VHF-containing forms are 13.4-14.4 kJ/mol higher than the DHA-containing ones. Consequently, all thermal back-reactions to DHA are spontaneous. As for the SP/MC unit, the ring-closed SP is the energetically most stable state, despite the better π -electron delocalization in the merocyanines, and the resonance stabilization of the phenolate in the zwitterionic ring-open form. Moreover, the Z to E isomerization of the protonated merocyanine is also accompanied by a $\Delta G^0 < 0$.

In addition, one can concentrate on the successive switching steps. Considering two consecutive reactions, if the ΔG^0 of the second reaction is more negative than that of the first one, the former drives the equilibrium to the latter. The results in Fig. 5.2 highlight that, in most of the cases, the path-dependency facilitates the transformation to a specific state. The formation of DHA-E-MCH starting from DHA-SP is driven by the spontaneous thermal isomerization of DHA-Z-MCH. Moreover, the results suggest that forming the DHA-E-MCH state is easier using VHF-SP as starting point. Another example is the access to VHF-E-MCH from VHF-SP,



5.3 UV/vis absorption spectra and related properties

On the basis of the MB populations, the ΔE_{0n} weighted averages were evaluated at the IEF-PCM/ ω B97X-D/6-311+G(d) level of theory. When combined with the calculated oscillator strengths (f_{0n}), they allow simulating the UV/vis absorption spectra (Fig. 5.3). The CT characteristics of the dominant lowest-energy excitations are also listed (Table 5.8). Additional calculations were performed on the four stereoisomers of the DHA-SP form (Table D.1) to assess the impact of the configuration of the chiral centers. The results were nearly identical (*e.g.*,

variations of ΔE_{0n} of the order of 0.02 eV or less), and consequently, the following analysis is, again, only based on the (S)-DHA and the (R)-SP isomers.

The main absorption bands in most of the UV/vis spectra of the dyads result from a quasi superposition of the spectra of the constitutive switching units. The first ($S_0 \rightarrow S_1$) excitation wavelength of the parent DHA unit equals 371 nm (reported in Table D.14), and it shifts to 381 nm in DHA-SP. Experimentally, the maximum absorption wavelength of the parent DHA, 380 nm, shifts to 392 nm when connected to SP. Dowds *et al.*²² made the assumption that the absorbing chromophore in DHA-SP includes, in addition to DHA, the neighboring

Table 5.8: Computed excitation energies (ΔE_{0n} , eV) and their associated wavelengths (λ_{0n} , nm), oscillator strengths (f_{0n}), amounts of charge transfer (q_{CT} , e), distances of charge transfer (d_{CT} , Å), and variations of dipole moment upon excitation from the GS to the n^{th} dominant lowest-energy ES ($\Delta\mu_{0n}$, D) of each state of the molecular switch[†] as evaluated at the IEF-PCM(acetonitrile)/TDDFT/ ω B97X-D/6-311+G(d) level.

Form	n	ΔE_{0n}	λ_{0n}	f_{0n}	q_{CT}	d_{CT}	$\Delta\mu_{0n}$
DHA-SP	1	3.25	381	1.50	0.47	0.74	1.66
	2	3.95	314	0.90	0.54	2.74	7.15
DHA-MC	1	2.67	465	1.70	0.50	1.01	2.46
	2	3.27	379	0.92	0.44	0.52	1.11
DHA-E-MCH	1	3.12	398	2.48	0.54	1.94	5.02
DHA-Z-MCH	1	3.23	384	1.61	0.47	1.56	3.56
	2	3.65	340	0.41	0.62	2.14	6.35
<i>trans</i> -VHF-SP	1	2.79	444	0.85	0.44	1.22	2.61
	3	3.55	349	0.96	0.87	4.38	18.31
	4	4.06	305	0.34	0.67	2.66	8.62
	6	4.16	291	0.69	0.58	3.47	9.68
<i>trans</i> -VHF-MC	1	2.68	463	1.45	0.50	1.07	2.60
	2	2.79	444	0.92	0.44	1.17	2.47
	5	3.68	336	0.67	0.63	2.50	7.61
<i>trans</i> -VHF-E-MCH	1	2.79	445	0.87	0.44	1.22	2.59
	3	3.25	382	1.82	0.57	1.34	3.70
<i>trans</i> -VHF-Z-MCH	1	2.79	445	0.88	0.44	1.20	2.55
	3	3.58	347	1.27	0.65	1.30	4.05
<i>cis</i> -VHF-SP	1	2.73	454	0.71	0.46	1.54	3.43
	3	3.58	346	1.46	0.77	5.25	19.34
<i>cis</i> -VHF-MC	1	2.66	467	1.64	0.49	0.56	1.32
	2	2.74	453	0.55	0.46	0.78	1.74
	5	3.65	336	0.86	0.56	2.20	5.92
	6	3.82	322	0.41	0.60	1.76	5.06
<i>cis</i> -VHF-E-MCH	1	2.72	456	0.74	0.46	1.58	3.46
	3	3.21	386	1.82	0.57	1.33	3.65
	4	3.89	318	0.47	0.62	3.48	10.44
<i>cis</i> -VHF-Z-MCH	1	2.72	456	0.70	0.46	1.53	3.34
	3	3.57	347	1.44	0.63	1.18	3.60

[†] Averaged values calculated using the MB populations at 298.15 K.

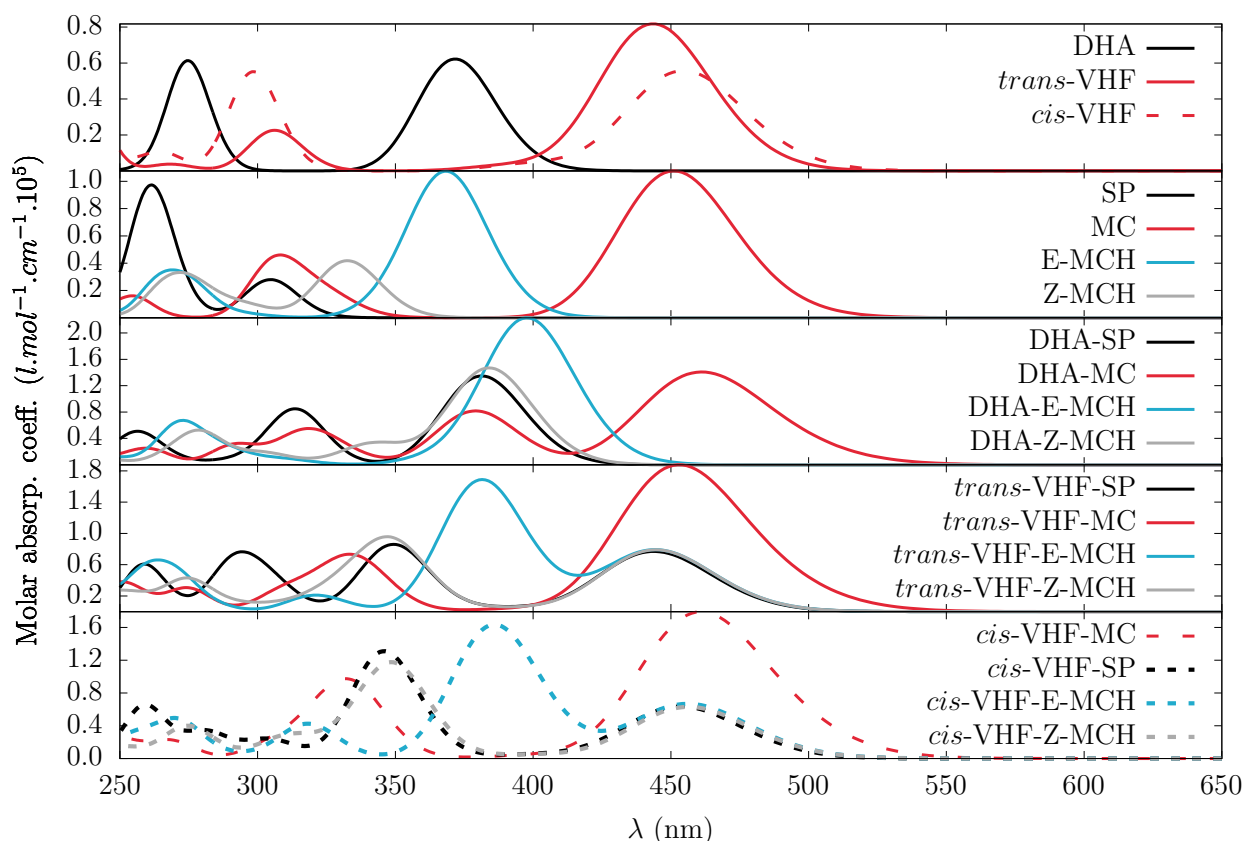


Fig. 5.3: Averaged simulated UV/vis absorption spectra of the constitutive units and of each state of the molecular dyad as evaluated at the IEF-PCM/TDDFT/ ω B97X-D/6-311+G(d) level (FWHM = 0.3 eV). The averaged values were obtained using the MB populations at 298.15 K.

phenylacetylene moiety and the nitrogen group, which would explain the observed red shift. The latter was partly confirmed by the $\Delta\rho(\mathbf{r})$ plot, further referred to as $\Delta\rho$ (Fig. 5.4a), where $\Delta\rho_{S_0 \rightarrow S_1}$ spreads mostly over both the DHA unit and the alkyne linker, with alternating positive and negative regions. This indicates that the first singlet excited state in DHA-SP is a local excited state. Hence, the transition is associated with a weak charge transfer (0.47 e over 0.74 Å, and $\Delta\mu_{0n}$ of 1.66 D), as shown by the CT vector (Fig. 5.4b). The second ($S_0 \rightarrow S_2$) absorption in the DHA-SP spectrum peaks at 314 nm, and it originates from the parent DHA too, as well as from the indole of the SP moiety (Fig. 5.4c). The S_2 excited state exhibits therefore a stronger CT (0.54 e over 2.74 Å, and $\Delta\mu_{0n}$ of 7.15 D) character (Fig. 5.4d).

The DHA-SP to VHF-SP isomerization gives rise to a red shift of the first absorption band from 381 to 454 nm and 444 nm for the *cis* and *trans*-VHF-SP, respectively. The same observation holds for the parent DHA and VHF units. These results are in agreement with the analysis of the BLAs, from which one expects a better π -electron delocalization in VHF, which redshifts the first ES of the dyad. Moreover, this absorption band is found at the same wavelength as the parent VHF (which is also the case experimentally), indicating that

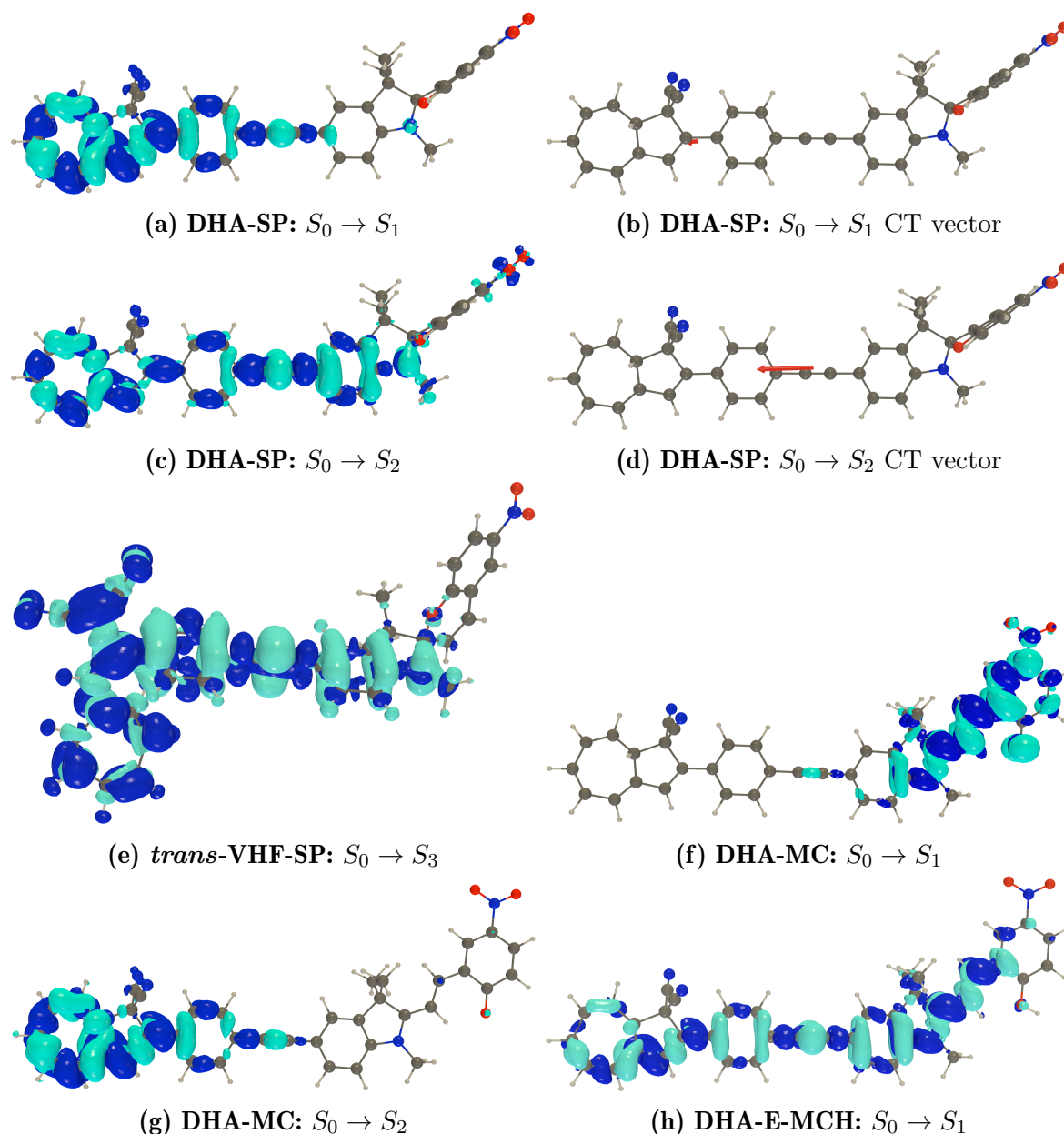


Fig. 5.4: Variation of electron density ($\Delta\rho$) and CT vector (in red) upon excitation from GS to the n^{th} ES for selected states of the molecular switch in their most stable conformation as evaluated at the IEF-PCM(acetonitrile)/TDDFT/ ω B97X-D/6-311+G(d) level; light and dark blue correspond to negative and positive $\Delta\rho$, respectively (isovalue = 0.0008 a.u.).

the excitation involves only the VHF moiety, as further substantiated by Fig. D.1. The second absorption band (346 nm and 349 nm in *cis* and *trans*-VHF-SP, respectively) is associated with a large intramolecular charge transfer (ICT), where the indole part of the SP units contribute but not its benzopyran part (Fig. 5.4e). This excitation, particularly intense in *cis*-VHF-SP ($f_{0n} = 1.46$), partially disrupts the additivity of the two switching units, as these signals are absent in the spectra of the individual constitutive units.

SP only shows a strong absorption band at about 270 nm that is slightly blue-shifted in

DHA-SP and VHF-SP. The "poor" chromophore character of SP in the visible region of the absorption spectra contrasts with the presence of the low-energy lying CT excited states in the SP-containing forms of the dyads, that involve the indole group and are associated with the large d_{CT} values. The dipole moments of the latter are significantly larger in the ES than in the GS ($\Delta\mu_{0n}$ range between 18.0 D and 19.5 D). In parallel, q_{CT} is less affected by the level of opening of the dyads, and ranges from 0.44 e to 0.87 e . Since $\Delta\mu_{0n}$ is the product of q_{CT} by d_{CT} , the variations of $\Delta\mu_{0n}$ follow, therefore, those of d_{CT} , which is often observed in π -conjugated molecular switches.^{23,24} The ring-opening to MC generates a broad signal at 451 nm, 465 nm, 467 nm, and 463 nm in the parent MC unit, in DHA-MC, and in *cis* and *trans*-VHF-MC, respectively. Its $\Delta\rho_{S_0 \rightarrow S_1}$ is localized on the MC moiety and slightly on the alkyne linker (see Fig. 5.4f for DHA-MC, and Fig. D.1 for the other MC-containing forms). The whole MC unit (and the linker) constitutes the chromophore since the π -electron delocalization is no more interrupted by the spiro junction. The observed red-shift, when going from SP to MC, arises from stronger push-pull behavior of the *p*-nitrophenolate moiety in MC, compared to the benzopyran part of SP, and was expected from the BLAs (Section 5.1). Then, the second main absorption band of DHA-MC appears at 379 nm. It is associated with a localized $\Delta\rho$ in the DHA moiety and in the linker (Fig. 5.4g). In the *cis*-VHF-MC forms, both MC and VHF units contribute to $\Delta\rho_{S_0 \rightarrow S_1}$ and $\Delta\rho_{S_0 \rightarrow S_2}$. In fact, those constitutive units present similar excitation energies (2.75 eV for MC *versus* 2.73 eV for the *cis*-VHF) so that the two first excited states of the dyads can be linear combinations of these localized excited states. This explains why the excitations are localized on both external units but not over the linker, so that their $\Delta\mu_{0n}$ are small.

The protonation of MC results in a hypsochromic shift of the first absorption band, which leads to a single dominant signal at 398 nm in DHA-E-MCH. This hypsochromic shift is, again, in agreement with the phenolate donor strength reduction upon protonation, and the analysis of the BLA₆ values previously presented. The two individual constitutive units show similar ΔE_{0n} in their first excitation bands (3.34 eV and 3.38 eV for DHA and E-MCH, respectively). Consequently, both switching units are involved in the $S_0 \rightarrow S_1$ transition when connected. Contrary to the example of *cis*-VHF-MC, $\Delta\rho_{S_0 \rightarrow S_1}$ (Fig. 5.4h) is delocalized over the whole dyad, and the $S_0 \rightarrow S_1$ transition bears a non-negligible CT character (0.54 e over 1.94 Å, and $\Delta\mu_{0n}$ of 5.02 D). This delocalization also explains the redshift (0.2 eV) of this first transition in DHA-E-MCH with respect to its constitutive units. Subsequently, this excitation is associated with the largest oscillator strength ($f_{0n} = 2.48$). Furthermore, owing to the fact that the UV/vis

absorption spectrum is mainly governed by one ES, and to Fig. D.2 suggesting that the CT occurs from the DHA to the E-MCH moiety, a one-dimensional β response is expected, *i.e.* with a DR close to 5. The first absorption wavelength of DHA-Z-MCH (384 nm) is similar to that of DHA-SP (381 nm), in agreement with the fact that the absorption band of the Z-MCH parent unit is weak in that range, in comparison to the one of the DHA unit. Similar observations are drawn for the protonation of VHF-MC. The signal at $\lambda = 467$ nm and 463 nm in *cis* and *trans*-VHF-MC, respectively, attributed to the excitation of the MC unit, is blue-shifted upon protonation. Indeed, the first main band at 445 nm in *trans*-VHF-E-MCH and *trans*-VHF-Z-MCH corresponds to a local excitation of the VHF moiety, as previously discussed in this Section. The same conclusions are drawn from the band at 456 nm in the *cis* isomers.

The nature of these low-energy excitations has been further analyzed by looking at which frontier orbitals are dominating. For most of the forms, one of the first low-energy excitations corresponds mainly to a HOMO to LUMO electronic transition, which whose topologies are represented in Fig. 5.5 for DHA-SP, and *trans*-VHF-SP. These HOMO to LUMO transitions lead to the $S_0 \rightarrow S_1$ and $S_0 \rightarrow S_3$ excitations in DHA-SP and *trans*-VHF-SP, respectively. The topology of these frontier orbitals could also help rationalizing the electronic density variations,

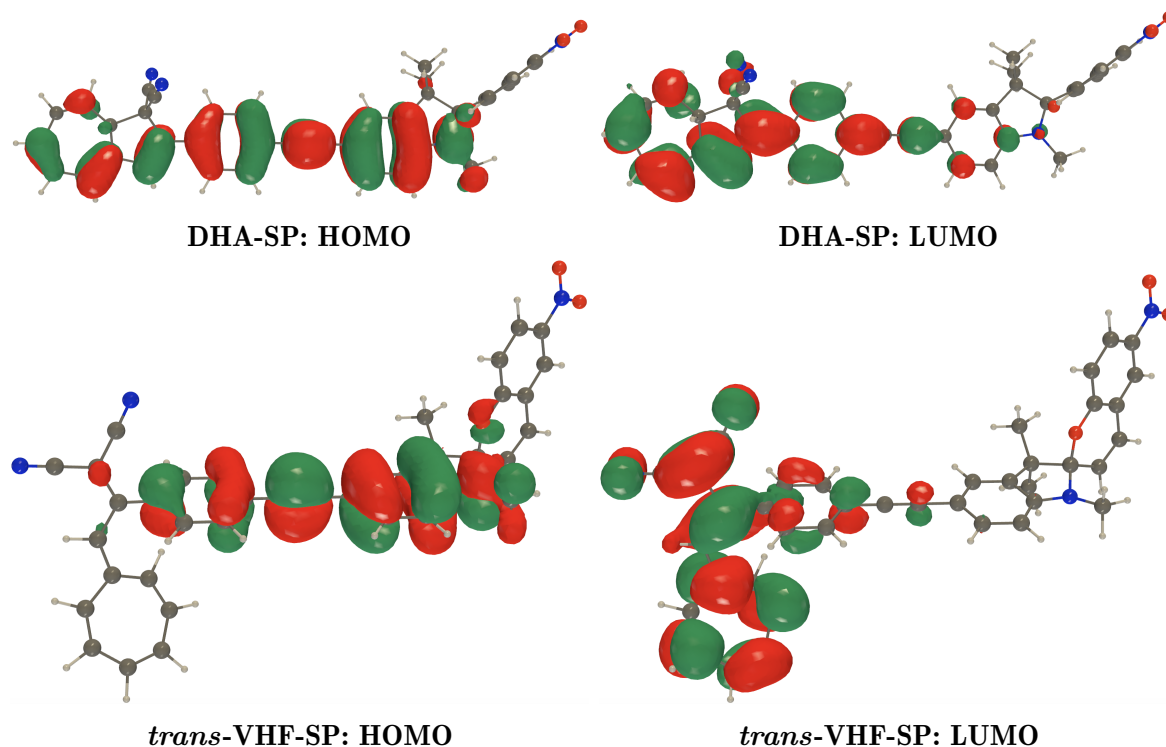


Fig. 5.5: HOMO and LUMO of selected forms of the molecular switch in their most stable conformations as evaluated at the IEF-PCM(acetonitrile)/ ω B97X-D/6-311G(d) level of approximation; green and red correspond to the regions where the orbital is negative and positive, respectively (isovalue = 0.02 a.u.).

and why they are spread over the molecule with alternative positive and negative regions. These are delocalized over the π -conjugated system but their distributions do not extend on the benzopyran part of SP in the example of DHA-SP, in particular for the LUMO. In other words, the overlap between the donor and acceptor is strong, which explains the formation of a local excited state (on the DHA moiety and the π -linker). On the contrary, the HOMO-LUMO overlap is weak in the example of *trans*-VHF-SP, leading to the aforementioned low-energy CT excited state, with a large $\Delta\mu_{0n}$. One can note that the spatial overlap between the HOMO and LUMO (the main frontier orbitals), as well as the energy gap between the latter, are often key aspects to tune π -conjugated compounds with large NLO responses.^{25,26}

The model of frontier orbitals is however very simplistic, since only one occupied and one virtual MO are accounted for in the description of the electronic transitions. In most cases, excitations have to be represented as a superposition of transitions of multiple MO pairs with corresponding weighting coefficients. A more quantitative analysis of these excitations is achieved by considering the creation of an exciton, namely, an electron-hole pair (Fig. 5.6). On the one hand, these electrons and holes confirm that the specific examples of the DHA-SP_{*S*₀→*S*₁} and *trans*-VHF-SP_{*S*₀→*S*₃} are mainly governed by HOMO to LUMO transitions, since their topologies are very close to those of the frontier orbitals. Indeed, if the excitation can be perfectly

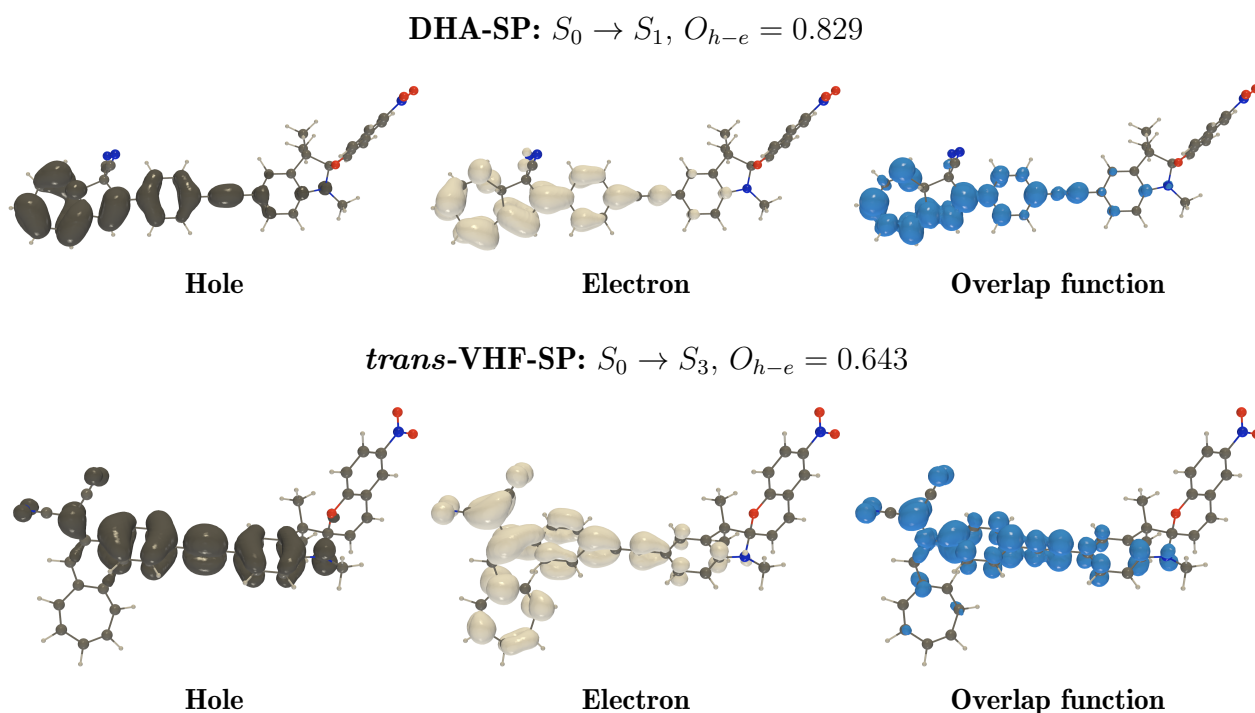


Fig. 5.6: Illustration of the holes, electrons, their overlap functions and integrals (O_{h-e}) for selected forms of the molecular switch in their most stable conformations as evaluated at the IEF-PCM(acetonitrile)/ ω B97X-D/6-311G(d) level of approximation (isovalue = 0.0008 a.u.).

described as HOMO to LUMO transition, the hole and the electron are simply represented by those frontier MOs (without the sign), respectively. In these examples, the electron-hole overlap integral for the excitation of DHA-SP (0.829) is larger than the one of *trans*-VHF-SP (0.643), which illustrates that the CT is larger in *trans*-VHF-SP_{*S*₀→*S*₃}. Furthermore, the electron-hole overlap logically correlates with d_{CT} , indicating here that the charge separation is larger following the $S_0 \rightarrow S_3$ excitation in *trans*-VHF than for DHA-SP_{*S*₀→*S*₁}.²⁷

It is now interesting to compare more quantitatively the experimental and simulated UV/vis absorption spectra. The computed vertical excitation energies are in semi-quantitative agreement with the experimental maximum absorption energies for most of the forms of the dyad (Fig. 5.7). This substantiates the selection of the ω B97X-D XC functional for the investigation of the targeted linear (and nonlinear) optical properties of this system. In general, the computed ΔE_{0n} values are slightly overestimated (0.1 to 0.2 eV) since the calculations neglect the vibronic structure.²⁸ For the DHA-MC and VHF-MC forms, a larger shift is however observed compared to the experimental results. This might originate from the presence of the negatively charged phenolate group, and the too simplistic treatment of solvent effects on that unit. Note that only the *trans*-VHF isomers were considered here, owing to the negligible MB weights of the *cis* forms at the thermodynamic equilibrium.

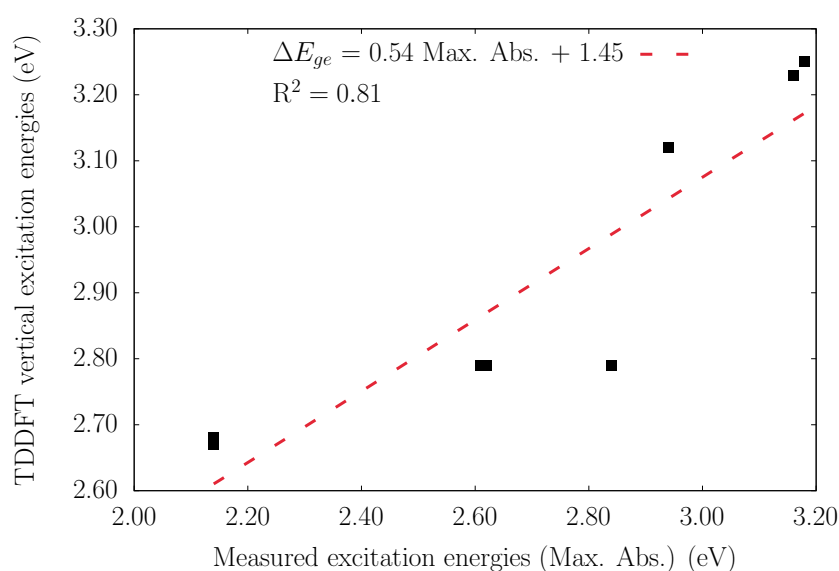


Fig. 5.7: Comparison between the vertical excitation energies computed at the IEF-PCM(acetonitrile)/TDDFT/ ω B97X-D/6-311+G(d) level and the experimental maximum absorption energies (Ref. 22).

5.4 Nonlinear optical properties

For the purpose of introducing HRS responses as an novel output signal for the dyads, the first hyperpolarizabilities of each form of the molecular switch were computed at the IEF-PCM(acetonitrile)/ ω B97X-D/6-311+G(d) level of approximation, and are listed in Table 5.9. These are MB average values over the main conformers (Tables E.3 to E.14). Additional calculations were also performed on the four stereoisomers of the DHA-SP form (Table E.1). The results are in agreement with the previous observations on geometries, thermodynamics and UV/vis absorption spectra, as the variations are negligible, *i.e.* of about 100 a.u. for β_{HRS} , and of 0.02 or less for DR and ρ . Therefore, the following analysis is, again, only based on the (S)-DHA and the (R)-SP stereoisomers. Complementary calculations on selected states of the molecular switch were performed to assess the impact on the β tensor of adding diffuse functions to the (reference) 6-311G(d) basis set (Table E.2). A convergence is reached on β_{HRS} and DR by adding one set of *sp* diffuse functions on all atoms with the exception of the hydrogen atoms, *i.e.* by employing the 6-311+G(d) basis set. This substantiates the use of the latter to compute NLO properties, as there is no need to resort to the 6-311++G(d) or more extended basis sets, which are more computationally expensive.

Table 5.9: Static and dynamic ($\lambda = 1907, 1500$ and 1064 nm) β_{HRS} values (10^3 a.u.), depolarization ratios, and nonlinear anisotropy factors of each form of the molecular switch[†] as evaluated at the IEF-PCM(acetonitrile)/(CPKS) TDDFT/ ω B97X-D/6-311+G(d) level of approximation

λ (nm)	β_{HRS}				DR				ρ			
	∞	1907	1500	1064	∞	1907	1500	1064	∞	1907	1500	1064
DHA-SP	7.2	7.0	8.1	13.3	3.93	4.13	4.18	4.36	1.10	1.04	1.03	0.99
DHA-MC	7.0	5.3	6.4	16.4	2.61	2.94	3.04	3.18	1.87	1.57	1.51	1.43
DHA-E-MCH	2.7	3.2	4.4	10.9	5.29	5.36	5.31	5.14	0.76	0.75	0.75	0.78
DHA-Z-MCH	3.3	3.4	4.2	8.1	3.52	4.00	4.10	4.39	1.26	1.08	1.04	0.97
<i>cis</i> -VHF-SP	9.2	8.6	10.0	16.3	2.67	3.15	3.08	2.67	1.79	1.44	1.48	1.78
<i>cis</i> -VHF-MC	9.5	8.0	9.7	22.9	2.37	2.77	2.80	2.80	2.16	1.70	1.68	1.72
<i>cis</i> -VHF-E-MCH	3.8	2.6	3.4	10.6	2.71	2.80	3.15	4.59	1.90	1.86	1.57	0.92
<i>cis</i> -VHF-Z-MCH	3.5	2.5	3.3	10.0	2.94	3.10	3.38	4.32	1.58	1.47	1.32	0.98
<i>trans</i> -VHF-SP	6.7	5.8	6.8	11.6	2.20	2.16	2.60	2.36	2.42	1.81	1.84	2.16
<i>trans</i> -VHF-MC	8.1	6.2	7.6	19.0	2.17	2.45	2.52	2.71	2.60	2.05	1.98	1.78
<i>trans</i> -VHF-E-MCH	3.3	2.2	2.8	7.3	2.58	3.31	3.79	4.77	1.98	1.46	1.23	0.90
<i>trans</i> -VHF-Z-MCH	3.4	2.3	2.9	7.0	3.31	4.12	4.33	4.44	1.47	1.13	1.06	1.00

[†] Averaged values calculated using the MB populations at 298.15 K.

β_{HRS} responses for the different forms of the dyad

On the one hand, based on the BLAs and previous studies conducted on the DHA/VHF parent moieties,^{1,29} it was expected that the isomerization from DHA to VHF would lead to an enhancement of the β_{HRS} values. This holds true for the parent units but, surprisingly, this trend is not observed when the DHA/VHF is connected to SP, E-MCH, and Z-MCH. The trend is however reproduced for VHF-MC *versus* DHA-MC.

On the other hand, the opening of SP to MC induces a substantial increase in β_{HRS} . The DHA-MC and VHF-MC forms, exhibiting the smallest ΔE_{0n} and local BLAs, present logically the largest β_{HRS} values (only for $\lambda = 1064$ nm for DHA-MC). An exaltation of β_{HRS} at 1064 nm is also recorded for the latter forms, indicating near-resonance effects, which is confirmed by the simulated UV/vis absorption spectra ($\lambda_{0n} = 464$ and 462 nm for DHA-MC and VHF-MC, respectively while $\lambda_{SHG} = 532$ nm for an excitation at 1064 nm). Calculations also reveal that the smallest β_{HRS} values are achieved with MCH forms, which, to a given extent, are unexpected results, because of the presence of π -electron delocalization in E/Z-MCH (yet, mostly E-MCH) while it is absent in SP (see also the BLA values). Nevertheless, the smaller first hyperpolarizabilities observed in those forms containing the E/Z-MCH moiety compared to those constituted by the MC unit is attributed to the weaker electron donating group (EDG) character of the neutral *p*-nitrophenol with respect to the negatively charged *p*-nitrophenolate moiety.

Fig. 5.8 presents the dynamic first hyperpolarizabilities at 1907 nm for each form of the dyad, along with the contributions from the parent units (also detailed in Table E.15). Contrary to the UV/vis absorption spectra, the second-order NLO responses of the dyads are not systematically a direct combination of the responses of the constitutive switching units. Indeed, on the one hand, the β values of the *trans*-VHF-MC, *trans*-VHF-Z-MCH, and to a lower extent, DHA-MC states are in good agreement with the sum of their two contributions. On the other hand, the deviation amounts to 32-47 % for *trans*-VHF-SP and *trans*-VHF-E-MCH, while for the last three states, the dyad responses are underestimated by at least a factor of 2. Similar observations are made based on the *cis*-VHF isomers but are not represented in Fig. 5.8, for clarity. The rest of this analysis is also only based on the *trans* isomers.

The β_{HRS} responses of the majority of the states exhibit an octupolar character ($\rho > 1$), with a DR ranging from 2.17 to 4.77. Moreover, the DRs of the dyads do not systematically follow the trend observed for the constitutive units. For instance, a decrease is observed for

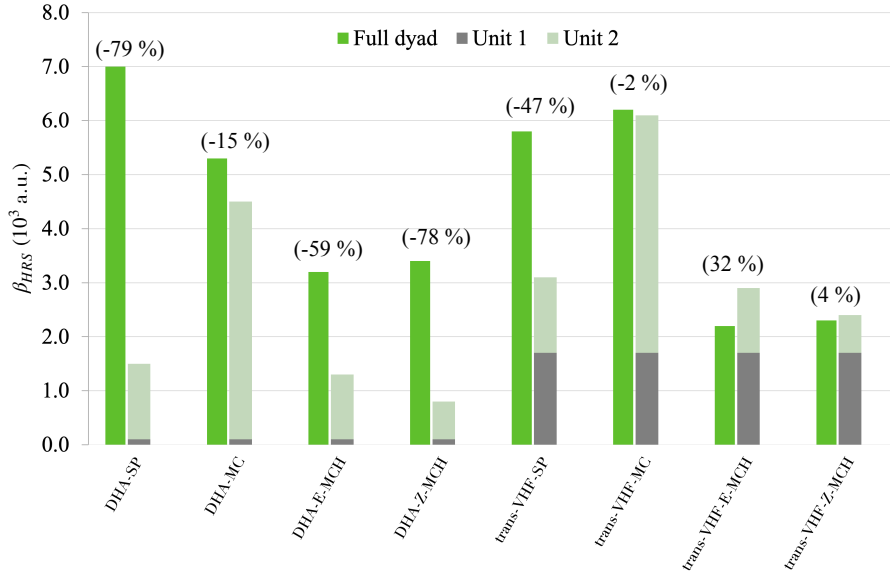


Fig. 5.8: Dynamic ($\lambda = 1907$ nm) β_{HRS} values, in comparison to those of their constitutive units (and their sums) for selected forms of the DHA-SP dyad, (unit 1 = DHA/*trans*-VHF, unit 2 = SP/MC/MCH) as evaluated at the IEF-PCM(acetonitrile)/TDDFT/ ω B97X-D/6-311+G(d) level of theory. The relative deviations with respect to the additivity are written in parenthesis (R.D. = $100[(\text{Sum} - \text{Full})/\text{Full}]$).

the opening of DHA to VHF, which is not reproduced when the DHA/VHF unit is grafted to Z-MCH. Another example is the transition from SP to MC, where MC-containing dyads exhibit generally a larger octupolar character. Hence the DRs of the dyads should decrease upon this ring opening, which is not the case at an excitation wavelength of 1907 nm or 1064 nm when the SP/MC unit is connected to *trans*-VHF. These observations suggest interferences between the β tensor of the two switching units. These interferences are not obvious and require, as presented below, detailed analysis of the β responses. The DHA-E-MCH form demonstrates a DR close to 5, which is typical of a one-dimensional NLOphore, and confirms the prediction made based on its UV/vis absorption spectrum. The trends in the nonlinear anisotropy factors of the dyads logically follow those of the DRs.

Analysis using the Unit Sphere Representation

Turning now to the unit sphere representations of the static β tensor as illustrated in Fig. 5.9 for DHA-SP, *trans*-VHF-MC forms, and their individual constitutive units, the effective induced dipole moments are oriented in different directions as a function of the orientation of the applied field. To rationalize these results, the reader should focus on the orientation of these induced dipoles, and on the color scale (at least for the constitutive units), since different USR factors are employed for clarity. Those USRs can then help qualitatively rationalizing the HRS results by

considering the oriented character of the β responses. Indeed, the *trans*-VHF and MC moieties share a common main direction in their HRS responses, which could vindicate the validity of the β additivity rule ($\beta_{MC} = 4400$ a.u., $\beta_{trans-VHF} = 1700$ a.u., $\beta_{dyad} = 6200$ a.u., and $R.D. = 2\%$ for an excitation at 1907 nm). On the contrary, the DHA and SP individual units show very distinct orientations of their β tensors, while the latter are also in a completely different direction in comparison to the USR of the DHA-SP form. Moreover, small β_{HRS} were computed for these two parent units, while as mentioned previously, a relatively large response is observed for the dyad. This is a first indication that both parent units are coupled to contribute to the NLO response. This hypothesis is reinforced by the presence of a low-energy CT (involving the two switching units) excited state, as discussed in Section 5.3. Furthermore, the induced dipoles in the USR of the DHA-SP form are mostly aligned in one direction, from the acceptor to the donor moiety, which is consistent with the direction of the CT excited state (recall Fig. 5.4d), and with a larger DR value. The aforementioned presence of a low-energy CT state in the SP-containing forms therefore explains why their HRS responses are similar/higher than those of the MC-containing forms, despite the better π -electron delocalization in MC, and the smaller ΔE_{0n} of the latter. Similar conclusions are drawn for the VHF-SP forms. Even though both *trans*-VHF and SP units share a similar orientation of their β tensors, the USR of the full dyad presents a different structure, and its main direction corresponds to the orientation of the $S_0 \rightarrow S_3$ CT vector (Fig. D.2), this excitation being associated with a large ICT.

Another aspect that USRs could rationalize is the decrease of dynamic β_{HRS} when going from DHA to *trans*-VHF. The shape of USRs of the DHA-E-MCH and DHA-Z-MCH forms are mainly oriented from the MCH to the DHA moiety. Then, the ring-opening of DHA to *trans*-VHF induces an increase of the responses in a perpendicular direction, leading to a decrease of the global dynamic responses of the dyads. This observation is in agreement with the fact that this trend was not observed for DHA-MC versus *trans*-VHF-MC, as the *trans*-VHF and MC units show a similar main direction in their USRs. Nonetheless, these observations, as well as the multidirectional character of the USRs, suggest that the local excited states also contribute significantly to the β responses of the dyads. In addition, the responses of the constitutive units are also governed by several excited states, as substantiated by their UV/vis absorption spectra (Fig. 5.3).

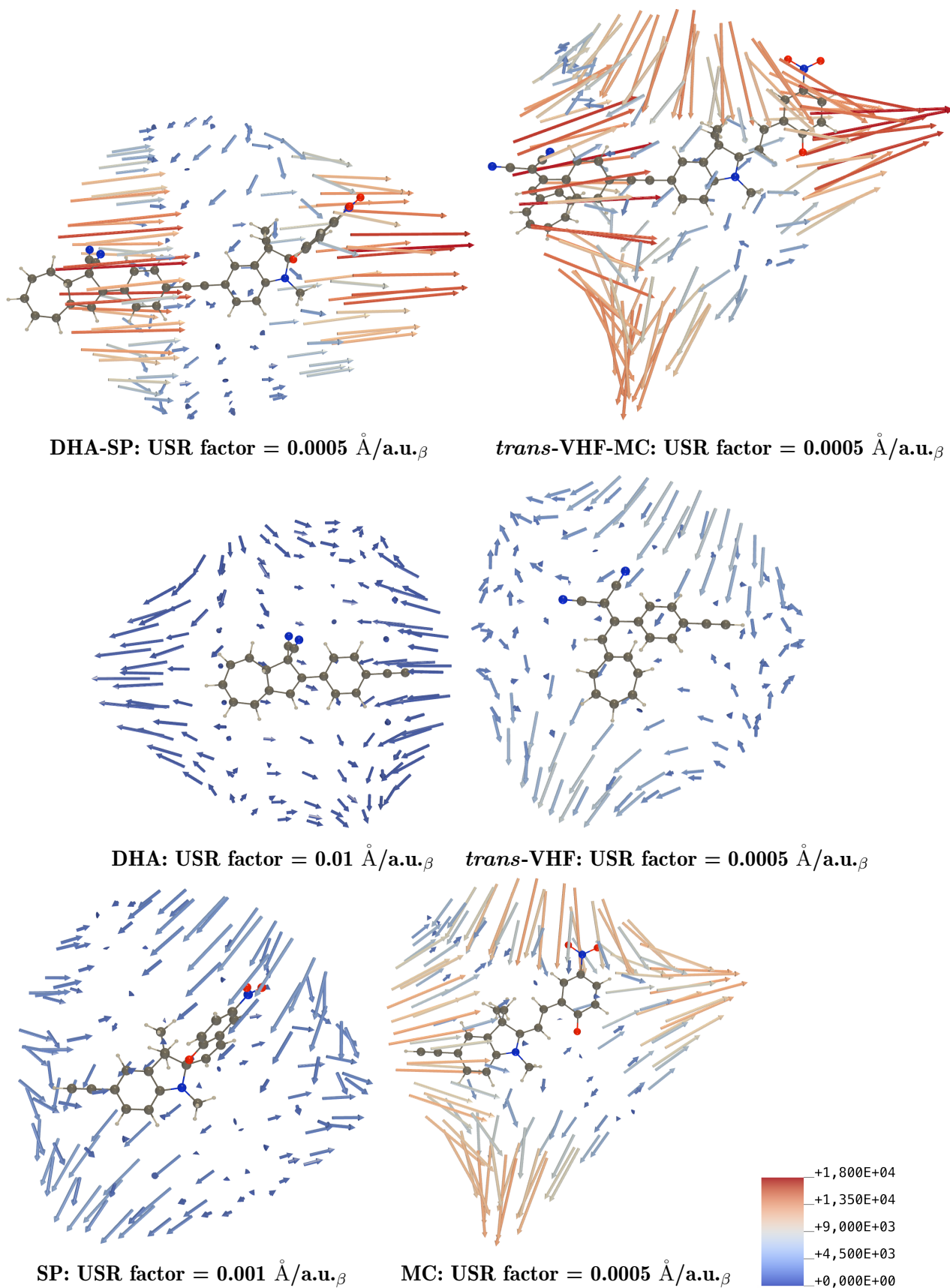


Fig. 5.9: Unit sphere representations of the static β of selected forms of the molecular switch in their most stable conformations, and of their constitutive units as evaluated at the IEF-PCM(acetonitrile)/CPKS/ ω B97X-D/6-311+G(d) level.

Second-order NLO contrasts

Considering a required β_{HRS} variation of 20 % to allow experimental assignment,³⁰ the different forms of the DHA-SP multi-state dyad should exhibit distinct first hyperpolarizabilities to act as an efficient NLO switch. At an excitation wavelength of 1907 nm, along the switching paths of the dyad, several variations of β_{HRS} (Fig. 5.10a) amount at least to 50 %. However, the β -contrasts at 1907 nm of the photo-triggered reactions are smaller, *e.g.*, the DHA-MC, VHF-SP, and VHF-MC show contrasts ranging from 1.1 to 1.3 when compared to the fully closed form (DHA-SP). Higher contrasts of β_{HRS} are observed for the acido-triggered switching reactions,

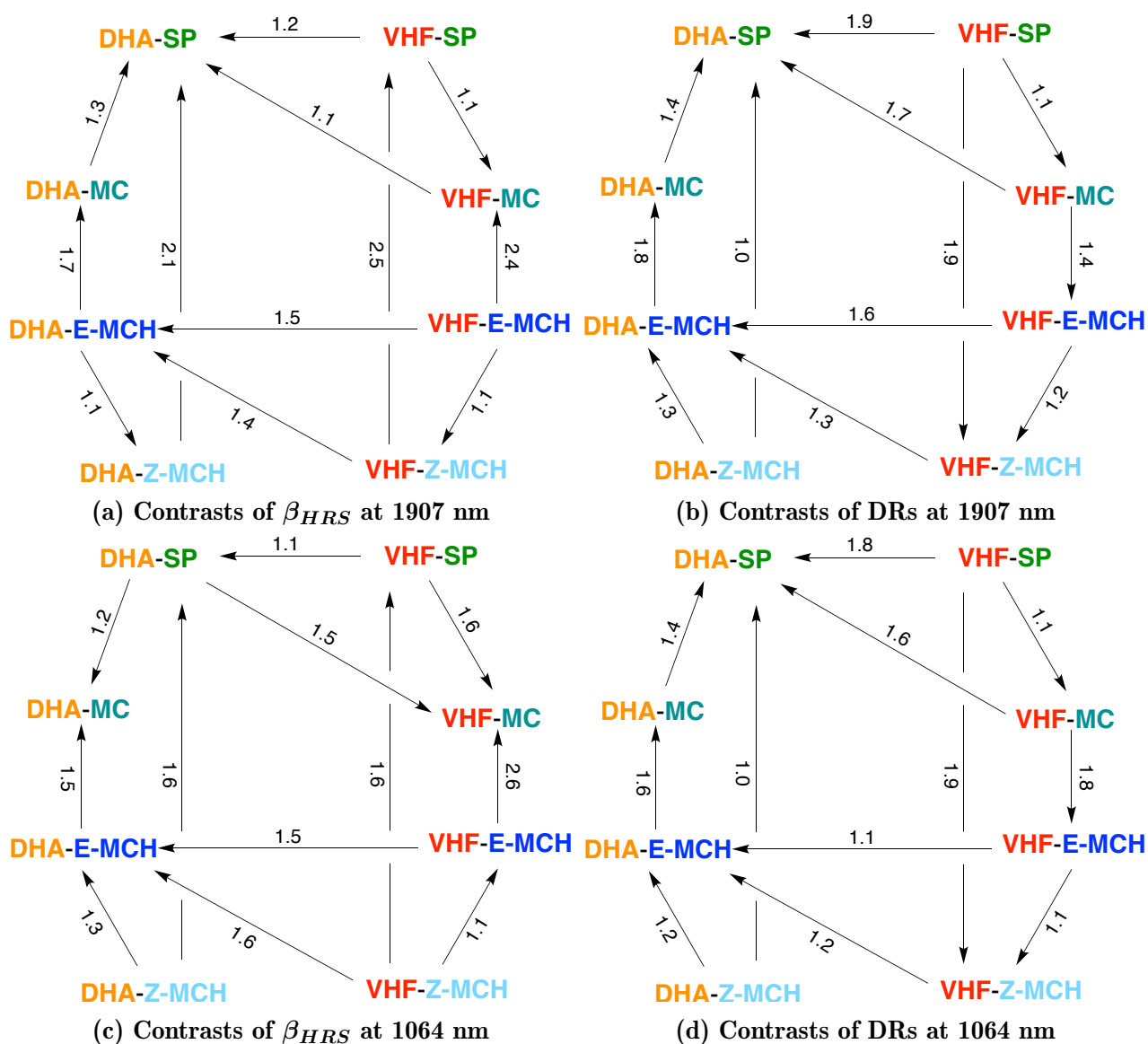


Fig. 5.10: Contrasts of dynamic ($\lambda = 1907$ nm and 1064 nm) β_{HRS} ($\beta_{end}/\beta_{start}$) and their DRs (DR_{end}/DR_{start}) between the different forms of the molecular switch for the experimentally characterized transitions as evaluated at the IEF-PCM(acetonitrile)/TDDFT/ ω B97X-D/6-311+G(d) level of theory.

ranging from 1.7 to 2.5, the latter being achieved upon protonation of VHF-MC. Nevertheless, by combining the β_{HRS} and the DR quantities, it becomes possible to distinguish between most of the different states of the DHA-SP dyad. The contrasts of DRs at 1907 nm (Fig. 5.10b) are indeed larger than those of β_{HRS} for several of the photo-induced switching transitions. Another possibility to improve the contrasts is to vary the incident excitation wavelength, notably by choosing a near-resonance regime for specific pairs of states. Figs. 5.10c and 5.10d present the contrasts of β_{HRS} and DR for an excitation at 1064 nm. In this case, the approaching-resonance effects for the MC-containing forms at the latter wavelength improve the distinction between VHF-SP and VHF-MC, reaching a contrast of 1.6 for the β_{HRS} values. Furthermore, it is also interesting to note that tuning and/or grafting additional specific chemical functions on the dyads could help enhancing the responses of some of the forms, *e.g.* by tuning the donor-acceptor character borne by the switching units.^{31–33}

In addition, the HRS responses could also help differentiating between two states obtained after consecutive switching reactions, *e.g.* in the case of an *AND* logic gate, when a UV/vis light irradiation is applied simultaneously to a pH variation. As an example, the path-dependent formation of DHA-E-MCH starting from DHA-SP results in a $\beta_{DHA-SP}/\beta_{DHA-E-MCH}$ ratio of 2.2. However, the β_{HRS} -contrast between DHA-SP and DHA-Z-MCH (the latter being an intermediate state in path to DHA-E-MCH) is of the same order of magnitude (2.1) at $\lambda = 1907$ nm. So, the β_{HRS} responses must also be combined with the DR when studying successive transitions.

Interpretation of the β values within the few-state approximation

A deeper understanding of the HRS responses can be grasped by resorting to the few-state approximation. Fig. 5.11 displays the evolutions of the dynamic ($\lambda = 1907$ nm) β_{HRS} values and their associated DRs for the DHA-MC and *trans*-VHF-SP forms in their most stable conformation, as obtained with the Orr-Ward-Bishop expression^{34,35} (Eq. (4.4)) at the SOS/IEF-PCM(acetonitrile)/TDDFT/ ω B97X-D/6-311+G(d) level of approximation. Those evolutions, as a function of the number of excited states, taken in increasing order of excitation energy, are presented in Appendix E.2 for the other forms of the molecular switch. From these graphs, it is clear that a two-state approximation is not sufficient to reproduce the HRS responses of this switching dyad, which was already deduced previously in this work, thanks to the UV/vis absorption spectra and the USRs.

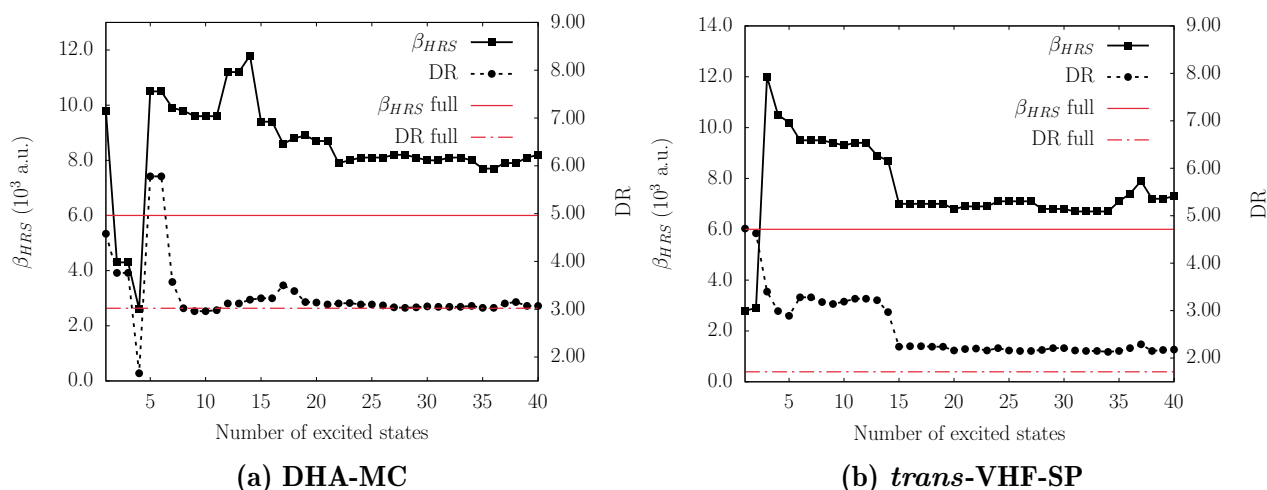
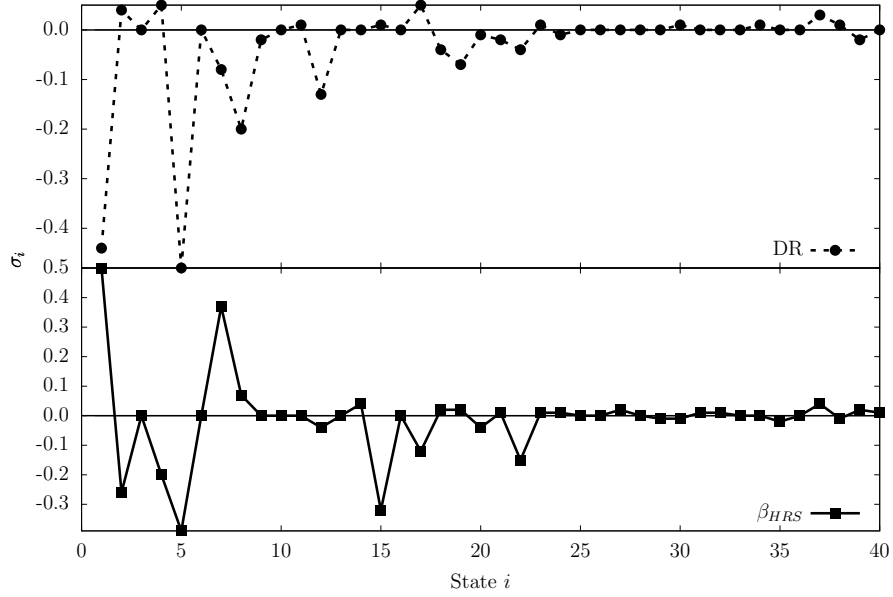


Fig. 5.11: Evolutions, as a function of the number of excited states, of the dynamic ($\lambda = 1907$ nm) β_{HRS} and DR for the DHA-MC and *trans*-VHF-SP forms of the molecular switch in their most stable conformation as evaluated at the SOS/IEF-PCM(acetonitrile)/TDDFT/ ω B97X-D/6-311+G(d) level. The full tensor values are also represented (in red). The fluctuation dipoles are approximated using the Multiwfn software.

The profiles of the evolutions of β_{HRS} also allow to rationalize the intriguing results obtained for the dyads, in comparison to those of their individual constitutive units and geometrical descriptors (BLAs, torsion angles). Considering only the contribution from the first excited state in DHA-MC (Fig. 5.11a), which corresponds to a local excitation on the MC moiety, leads to a β_{HRS} value of 9800 a.u., which is about twice larger than the response resulting from the full TDDFT calculation (indicated by the red line). Then, adding the contribution of the second excited state, which is a local excitation on the DHA unit, induces a decrease of the β_{HRS} . This is in agreement with the oriented character of the responses of the constitutive units highlighted by the USRs, since the SHG response of the DHA moiety is oriented in an opposite direction in comparison to the tensor of MC. Moreover, the SOS evolutions of both the β_{HRS} and DR suggest that the fifth ES contributes substantially to the HRS responses. Similarly, adding the contribution of the third ES for the *trans*-VHF-SP form (Fig. 5.11b) leads to a sharp increase of β_{HRS} . It is also of interest to see that the DRs converge faster than the first hyperpolarizabilities.

The relative contributions to β_{HRS} and DR of each excited state, σ_i , following the missing state analysis³⁶ (Eq. (4.6)), are plotted in Fig. 5.12 for the examples of DHA-MC and *trans*-VHF-SP. As expected from Fig. 5.11a, the first excited state of the DHA-MC form displays a major contribution to the β_{HRS} , and also to the DR (Fig. 5.12a). The local excitation on the DHA (the $S_0 \rightarrow S_2$ electronic transition) unit has however a weak impact on the depolarization ratio but contributes significantly to decrease the value of the first hyperpolarizability, even if

the response of the individual DHA is close to 0 (100 a.u. at 1907 nm). Moreover, the missing state analysis suggests that the fifth excited state dictates the DR, in addition to the first excited state. Hence, additional calculations were performed to determine the CT quantities associated with this excitation, and to plot $\Delta\rho_{S_0 \rightarrow S_5}$ for the most stable conformer (added in Fig. D.1), since it does not appear as a main band in the UV/vis absorption spectrum. The excitation wavelength and oscillator strength amount to 316 nm and 0.48, respectively. As a matter of



(a) DHA-MC

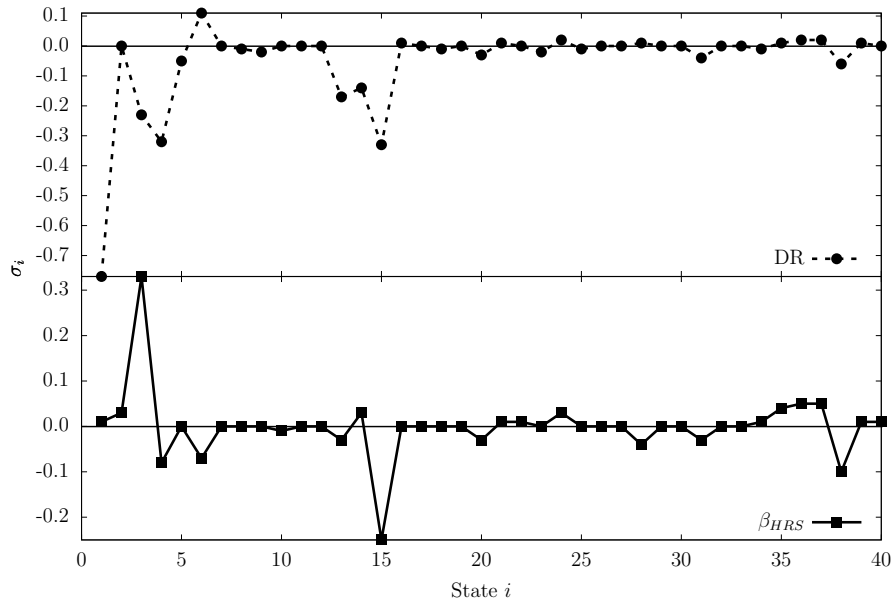
(b) *trans*-VHF-SP

Fig. 5.12: Relative importance of the state i , σ_i (dimensionless), to β_{HRS} and DR of the DHA-MC and *trans*-VHF-SP forms in their most stable conformation, as evaluated using the missing state analysis. Lines are guides for the eyes.

fact, this electronic transition, is, again, mostly associated with an excitation mostly localized on the MC unit. Since two of the criteria to achieve large β , *i.e.* a low-energy excitation and a high oscillator strength, are not fulfilled, the contribution to the HRS responses from this ES arises from its CT character (the third criterion). Despite its $\Delta\rho$ mostly localized on MC, q_{CT} , d_{CT} , and $\Delta\mu_{0n}$ amount to $0.43 e$, 2.08 \AA , and $4.33 D$, respectively. One can therefore conclude that the DR of DHA-MC is mostly governed by the response of the MC unit, also in agreement with the negligible response of DHA. In this case, the two main local excitations on MC tend to decrease the value of DR at convergence. On the contrary, while adding the contribution of the first ES to the SOS expression enhances the β_{HRS} value, including the fifth ES induces the opposite effect. Furthermore, this specific example pinpoints the participation of local ES to the HRS responses, as suggested previously, in a qualitative way, by the USRs.

Turning now to the *trans*-VHF-SP form, Fig. 5.12b confirms that the β_{HRS} is mostly guided by the third excited state, which is associated with a large ICT, as discussed in Section 5.3. As for the DR, the latter is univocally governed by the first ES, corresponding to local excitation on the VHF moiety. Furthermore, the fifteenth ES non-negligibly impacts both the β_{HRS} and the DR. Since this excitation is also nearly invisible in the absorption spectra ($\Delta E_{0n} = 4.90 \text{ eV}$, and $f_{0n} = 0.08$), its contribution arises from its large CT character, q_{CT} , d_{CT} , and $\Delta\mu_{0n}$ being equal to $0.78 e$, 5.74 \AA , and $21.36 D$, respectively. This large ICT is illustrated by the $\Delta\rho$, added to Fig. D.1. These observations support the hypothesis that the β_{HRS} of the SP-containing forms are mainly governed by CT excited states.

It is important to stress that the β_{HRS} values calculated with the SOS scheme and the few-

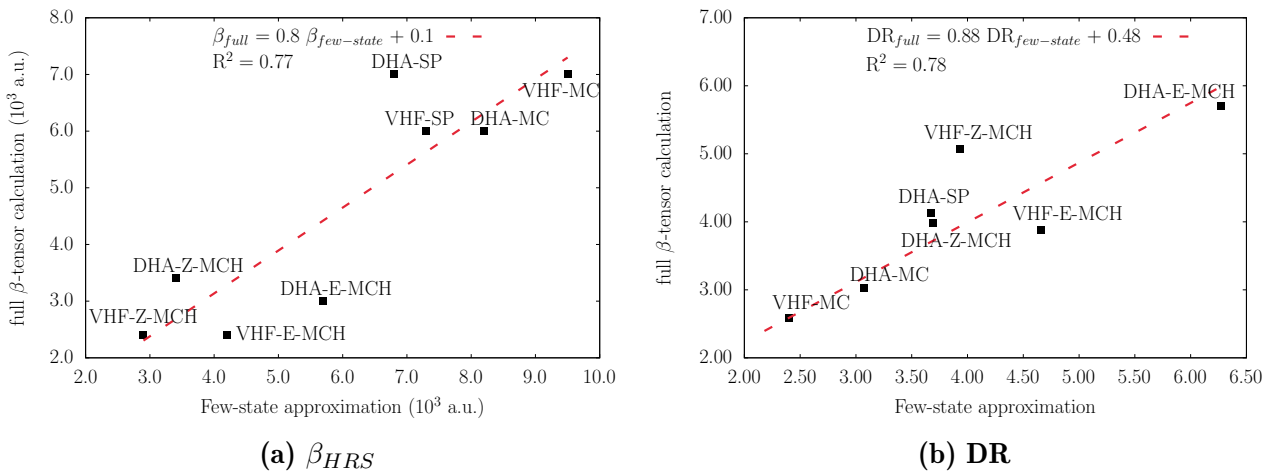


Fig. 5.13: Comparison between (a) the dynamic ($\lambda = 1907 \text{ nm}$) β_{HRS} and (b) the DRs evaluated at $\omega\text{B97X-D/6-311+G(d)}$ level and the SOS values, truncated after 40 excited states, and using the one particle transition density.

state approximation closely reproduce the results obtained with the "full" TDDFT response method. (In that scheme, there is no truncation of the excited state manifold. All excited states are implicitly included in the TDDFT response calculation). In particular, the former method reproduces the trends, observed with the latter method, in what concerns the variations of the HRS responses upon ring-opening/closing of both switching units. On the one hand, the β_{HRS} are slightly overestimated (Fig. 5.13a), but remain close to the values obtained by full the calculations. However, this is not a general statement as the SOS results for the DHA-SP, DHA-Z-MCH and *trans*-VHF-Z-MCH forms are nearly identical to those of the full TDDFT calculations (absolute deviation of maximum 500 a.u.). The largest deviations of β_{HRS} occur for the MC-containing forms. On the other hand, the SOS depolarization ratios are in quantitative agreement with the TDDFT full tensor calculations (Fig. 5.13b). Since DR is a ratio, the errors on the two rotational averages, $\langle \beta_{ZZZ}^2 \rangle$ and $\langle \beta_{ZXX}^2 \rangle$, are counterbalanced.

To assess the unrelaxed density approximation of the Multiwfn code, a first set of results were obtained for the DHA-MC form in its most stable conformation when calculating the quadratic responses and their double residues. These calculations were performed at the TDDFT/CAM-B3LYP/6-311+G(d) level using the Dalton package. The vertical excitation energies and ground-to-excited state electric transition dipoles for the 15 lowest-energy excited states were computed at the same level of approximation using the Gaussian16 package, and the fluctuation dipole moment were then approximated using Multiwfn. A comparison between

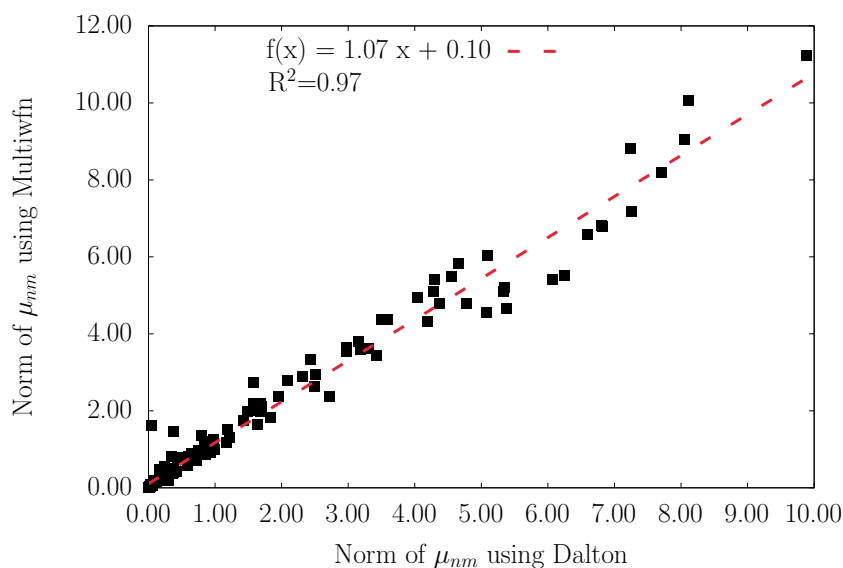


Fig. 5.14: Relationship between the norms of the fluctuation dipoles for the first 15 excited states of the DHA-MC form as evaluated approximately with Multiwfn and the reference values calculated from the quadratic response function and double residues using Dalton. All calculations were carried out in gas phase at the TDDFT/CAM-B3LYP/6-311+G(d) level.

the norms of these fluctuation dipoles calculated with the two methods is shown by Fig. 5.14. The two sets of values are in close to excellent agreement, which substantiates the use of the approximate method, that is less computationally demanding but also allows calculations with IEFPCM and the ω B97X-D XC functional.

Bibliography

- [1] Plaquet, A.; Champagne, B.; Castet, F.; Ducasse, L.; Bogdan, E.; Rodriguez, V.; Pozzo, J. L. Theoretical Investigation of the Dynamic First Hyperpolarizability of DHA-VHF Molecular Switches. *New J. Chem.* **2009**, *33*, 1349–1356.
- [2] Gobbi, L.; Seiler, P.; Diederich, F.; Gramlich, V.; Boudon, C.; Gisselbrecht, J. P.; Gross, M. Photoswitchable Tetraethynylethene-Dihydroazulene Chromophores. *Helv. Chim. Acta* **2001**, *84*, 743–777.
- [3] Kaftory, M.; Botoshansky, M.; Daub, J.; Fischer, C.; Bross, A. 2-p-Cyanophenyl-1,8a-Dihydroazulene-1,1-Dicarbonitrile and Methyl 1-Cyano-2-p-Cyanophenyl-1,8a-Dihydroazulene-1-Carboxylate. *Acta Cryst. C* **1997**, *53*, 1665–1667.
- [4] Abedi, M.; Pápai, M.; Mikkelsen, K. V.; Henriksen, N. E.; Møller, K. B. B. Mechanism of Photoinduced Dihydroazulene Ring-Opening Reaction. *J. Phys. Chem. Lett.* **2019**, *10*, 3944–3949.
- [5] Shostak, S.; Park, W.; Oh, J.; Kim, J.; Lee, S.; Nam, H.; Filatov, M.; Kim, D.; Choi, C. H. Ultrafast Excited State Aromatization in Dihydroazulene. *J. Am. Chem. Soc.* **2023**, *145*, 1638–1648.
- [6] Marder, S. R.; Cheng, L.-T.; Tiemann, B. G.; Friedli, A. C.; Blanchard-Desce, M.; Perry, J. W.; Skindhøj, J. Large First Hyperpolarizabilities in Push-Pull Polyenes by Tuning of the Bond Length Alternation and Aromaticity. *Science* **1994**, *263*, 511–514.
- [7] Lu, D.; Chen, G.; Perry, J. W.; Goddard, W. A. Valence-Bond Charge-Transfer Model for Nonlinear Optical Properties of Charge-Transfer Organic Molecules. *J. Am. Chem. Soc.* **1994**, *116*, 10679–10685.
- [8] Abe, Y.; Ebara, H.; Okada, S.; Akaki, R.; Horii, T.; Nakao, R. Molecular Structure and Photochromic Properties of 1,3-Dimethylindoline-3,3'-Alkano-2-Spiro-2'-(6'-Nitro)Benzopyrans. *Dyes Pigm.* **2002**, *52*, 23–28.
- [9] Kumar, S.; Velasco, K.; McCurdy, A. X-Ray, Kinetics and DFT Studies of Photochromic Substituted Benzothiazolinic Spiropyranes. *J. Mol. Struct.* **2010**, *968*, 13–18.
- [10] Crano, J. C., Guglielmetti, R. J., Eds. *Organic Photochromic and Thermochromic Compounds: Physicochemical Studies, Biological Applications, and Thermochromism (Topics in Applied Chemistry)*; Plenum Publishers, New York, 1999; Vol. 2.

- [11] IUPAC *Compendium of Chemical Terminology (the "Gold Book")*, 2nd ed.; Blackwell Scientific Publications, Oxford, Compiled by A. D. McNaught and A. Wilkinson, 1997.
- [12] Reed, A. E.; Curtiss, L. A.; Weinhold, F. Intermolecular Interactions from a Natural Bond Orbital, Donor-Acceptor Viewpoint. *Chem. Rev.* **1988**, *88*, 899–926.
- [13] Görner, H. Photochromism of Nitrospiropyrans : Effects of Structure, Solvent and Temperature. *Phys. Chem. Chem. Phys.* **2001**, *3*, 416–423.
- [14] Minkin, V. I. Photo-, Thermo-, Solvato-, and Electrochromic Spiroheterocyclic Compounds. *Chem. Rev.* **2004**, *104*, 2751–2776.
- [15] Sheng, Y.; Leszczynski, J.; Garcia, A. A.; Rosario, R.; Gust, D.; Springer, J. Comprehensive Theoretical Study of The Conversion Reactions of Spiropyrans: Substituent and Solvent Effects. *J. Phys. Chem. B* **2004**, *108*, 16233–16243.
- [16] Glasovac, Z.; Kovačević, B. Modeling pKa of the Brønsted Bases as an Approach to the Gibbs Energy of the Proton in Acetonitrile. *Int. J. Mol. Sci.* **2022**, *23*, 18.
- [17] Wojtyk, J. T. C.; Wasey, A.; Xiao, N.; Kazmaier, P. M.; Hoz, S.; Yu, C.; Lemieux, R. P.; Buncel, E. Elucidating the Mechanisms of Acidochromic Spiropyran-Merocyanine Interconversion. *J. Phys. Chem. A* **2007**, *111*, 2511–2516.
- [18] Kortekaas, L.; Chen, J.; Jacquemin, D.; Browne, W. R. Proton-Stabilized Photochemically Reversible E/Z Isomerization of Spiropyrans. *J. Phys. Chem. B* **2018**, *122*, 6423–6430.
- [19] Kortekaas, J.; Browne, W. R. The Evolution of Spiropyran: Fundamentals and Progress of an Extraordinary Versatile Photochrome. *Chem. Rev. Soc.* **2019**, *48*, 3406–3424.
- [20] Irving, F. CXLV.—Styrylpyrylium Salts. Part XII. Spiropyrans Derived from 9-Methyl- and 9-Ethyl-Xanthylium Salts. *J. Chem. Soc.* **1929**, 1093–1095.
- [21] Roxburgh, C. J.; Sammes, P. G. On the Acid Catalysed Isomerisation of Some Substituted Spirobenzopyrans. *Dyes Pigm.* **1995**, *27*, 63–69.
- [22] Dowds, M.; Stenspil, S. G.; de Souza, J. H.; Laursen, B. W.; Cacciarini, M.; Nielsen, M. B. Orthogonal- and Path-Dependent Photo/Acidoswitching in an Eight-State Dihydroazulene-Spiropyran Dyad. *ChemPhotoChem* **2022**, *6*, e202200152.
- [23] Quertinmont, J.; Beaujean, P.; Stiennon, J.; Aidibi, Y.; Leriche, P.; Rodriguez, V.; Sanguinet, L.; Champagne, B. Combining Benzazolo-Oxazolidine Twins toward Multi-state Nonlinear Optical Switches. *J. Phys. Chem B* **2021**, *125*, 3918–3931.
- [24] Rtibi, E.; Abderrabba, M.; Ayadi, S.; Champagne, B. Theoretical Assessment of the

- Second-Order Nonlinear Optical Responses of Lindqvist-Type Organoimido Polyoxometalates. *Inorg. Chem.* **2019**, *58*, 11210–11219.
- [25] Misra, R.; Bhattacharyya, S. P. *Intramolecular Charge Transfer, Theory and Applications*; Wiley-VCH, Weinheim, Germany, 2018.
- [26] Oudar, J. L.; Chemla, D. S. Hyperpolarizabilities of the Nitroanilines and their Relations to the Excited State Dipole Moment. *J. Chem. Phys.* **1977**, *66*, 2664–2668.
- [27] Chen, X.; Ravva, M. K.; Li, H.; Ryno, S. M.; Brédas, J.-L. Effect of Molecular Packing and Charge Delocalization on the Nonradiative Recombination of Charge-Transfer States in Organic Solar Cells. *Adv. Energy Mater.* **2016**, *6*, 1601325.
- [28] Lasorne, B.; Jornet-Somoza, J.; Meyer, H. D.; Lauvergnat, D.; Robb, M. A.; Gatti, F. Vertical Transition Energies vs. Absorption Maxima: Illustration with the UV Absorption Spectrum of Ethylene. *Spectrochim. Acta A: Mol. Biomol. Spectrosc.* **2014**, *119*, 52–58.
- [29] Bayach, I.; Al-Faiyz, Y. S. S.; Alkhalifah, M. A.; Almutlaq, N.; Ayub, K.; Sheikh, N. S. Phototunable Absorption and Nonlinear Optical Properties of Thermally Stable Dihydroazulene–Vinylheptafulvene Photochrome Pair. *ACS Omega* **2022**, *7*, 35863–35874.
- [30] Bouquiaux, C.; Beaujean, P.; Ramos, T. N.; Castet, F.; Rodriguez, V.; Benoît, B. First Hyperpolarizability of the di-8-ANEPPS and DR1 Nonlinear Optical Chromophores in Solution. An Experimental and Multi-Scale Theoretical Chemistry Study. *J. Chem. Phys.* **2023**, *159*, 174307.
- [31] Beaujean, P.; Sanguinet, L.; Rodriguez, V.; Castet, F.; Champagne, B. Multi-State Second-Order Nonlinear Optical Switches Incorporating One to Three Benzazolo-Oxazolidine Units: A Quantum Chemistry Investigation. *Molecules* **2022**, *27*, 2770.
- [32] Desmedt, E.; Woller, T.; Teunissen, L.; Vleeschouwer, F. D.; Alonso, M. Fine-Tuning of Nonlinear Optical Contrasts of Hexaphyrin-Based Molecular Switches Using Inverse Design. *Front. Chem.* **2021**, *9*, 786036.
- [33] Castet, F.; Rodriguez, V.; Pozzo, J.-L.; Ducasse, L.; Plaquet, A.; Champagne, B. Design and Characterization of Molecular Nonlinear Optical Switches. *Acc. Chem. Res.* **2013**, *46*, 2656–2665.
- [34] Orr, B. J.; Ward, J. F. Perturbation Theory of the Non-Linear Optical polarization of an isolated system. *Mol. Phys.* **1971**, *20*, 513–526.

- [35] Bishop, D. M. Explicit Nondivergent Formulas for Atomic and Molecular Dynamic Hyperpolarizabilities. *J. Chem. Phys.* **1994**, *100*, 6535–6542.
- [36] Dirk, C. W.; Kuzyk, M. G. Missing-State Analysis: A Method for Determining the Origin of Molecular Nonlinear Optical Properties. *Phys. Rev. A* **1989**, *39*, 1219–1226.

Chapter 6

Conclusions and outlooks

In this Master thesis, the dihydroazulene-spiropyran molecular switch, recently proposed by Dowds *et al.*,¹ has been studied by using quantum chemistry methods, with the final goal of assessing its second-order NLO properties, and therefore introducing a novel output signal from the viewpoint of molecular logic. First, the ground state equilibrium geometries of the selected conformers of all the forms of the dihydroazulene-spiropyran dyad have been optimized, as well as of all the stereoisomers of the fully closed DHA-SP form. It has been found that all stereoisomers of a given state (2 or 4) have the same energy and geometrical parameters. The structural analysis has highlighted an independence between the two switching units, *i.e.* switching either unit has only a negligible impact on the geometrical parameters of the other one, and the individual constitutive units present nearly identical parameters as in the dyads. This has allowed the rest of the structural analysis to be focused on each unit individually, such that their structures were compared to single crystal X-ray diffraction data.

This "additivity" or "independence" trend has then been confirmed by the Gibbs free energy of reactions. In fact, the ΔG^0 associated with the opening/closing of one unit is independent of the state of opening of the second one. For the *cis-trans* isomerization of VHF, the ΔG^0 calculations give an average value of 9 kJ/mol for all switching reactions (*i.e.* no matter what is the state of the second unit). These ΔG^0 pave also the way to discuss the spontaneity of the switching reactions, and to show how the path-dependency of the successive switching transitions could drive the thermodynamic equilibriums.

Comparable effects have been observed in the UV/vis absorption spectra simulated from TDDFT vertical excitation energies and oscillator strengths, since these spectra are, in good approximation and for most of the forms, a superposition of those from their parent units. The analysis of the excitation-induced electronic density variations, $\Delta\rho_{0n}$, has then helped to interpret the spectra and to assess the analysis of Dowds *et al.*¹ As a result, this quasi-superposition of the spectra of the constitutive units to get the spectra of the dyads is explained by the presence of excitations localized on one unit (or the other). However, for the SP-containing forms of the molecular switch, an additional absorption band is observed. Their associated $\Delta\rho_{0n}$ have shown that these electronic excitations are accompanied by large intramolecular charge transfers, encompassing both switching units. Subsequently, the analysis of the $\Delta\rho_{0n}$ was completed with the analysis of the hole and electron densities, which quantified the overlap between the electron donor and acceptor.

Though UV/vis absorption spectra could help differentiating the forms of the dyad, when the switching reactions involve UV irradiation, recording the spectra induces also these switching

reactions. In molecular logic, this corresponds to a readout process that erases the information. Thus, light absorption (to encode the information) must be combined with a detection channel of another nature. This is why the second-order NLO responses have been proposed and studied. The adequacy of this output was judged by calculating the NLO contrasts between the forms of the switch. It appears that, for several switching transitions, variations of β_{HRS} of at least 50 % are observed (*e.g.*, for the acid-base reactions). Yet, the β_{HRS} does not always provide sufficiently large contrasts to differentiate between the eight forms of the dyad. Nonetheless, combining the HRS responses and their depolarization ratios leads to discernible output signals between the different forms of the dyad. Consequently, these HRS responses are good candidates as additional readouts for this DHA-SP multi-state molecular switch.

Contrary to the absorption spectra, this additivity trend of the two switching units was not consistently observed for β_{HRS} , where, for several forms, large deviations occur. On the one hand, the results have been rationalized by considering the oriented character of the responses, which is unraveled thanks to the unit sphere representations. These USRs show why, in specific cases, the additivity was conserved. This occurs when the main orientations of the responses of the two constitutive units and therefore of the complete dyad are similar. For the cases in which the additivity was lost, two effects were pinpointed (i) the orientation of the response of one switching unit is different from the one of the full dyad, but the response of the dyad is dominated by the response of the other unit, and (ii) the responses of the two individual switching units are oriented in complete different directions in comparison to the response of the dyad. This last observation has suggested interferences between the first hyperpolarizability tensors of the constitutive units.

In addition, using the few-state approximation provides a deeper and more quantitative understanding of these HRS responses. Indeed, the SOS evaluation of β_{HRS} and DR have confirmed the impact of the orientation of the responses of the constitutive units on the responses of the dyads. Then, the missing state analysis has identified the excited states that govern the β_{HRS} and DR values. As a matter of fact, in the cases of a complete loss of additivity, the β_{HRS} of the dyad is mainly governed by charge transfer excited states. In other words, the conservation of the additivity of the constitutive units for specific forms of the dyad is induced by the fact that local excited states dictate the responses. In conclusion, the few-state approximation and the missing state analysis help to unravel the relationships between the first hyperpolarizabilities and the UV/vis spectra, as well as with the CT character of the excitations.

In the future, the combined analysis of the USR and of the few-state approximation could ultimately help tuning specific chemical functions grafted on the dyads to enhance the responses of the open forms, which would then lead to higher contrasts. Furthermore, the methodology followed in this study could be applied to other multi-state and multi-functional molecular switches. For instance, Gobbi and coworkers² proposed one of these switches, also composed by a photoswitchable dihydroazulene, connected to a tetraethynylethene. The latter also displays eight distinct states that were experimentally characterized. Owing to its π -conjugated structure and donor substituents, this compound could act as an NLO switch, to which the results obtained for the DHA-SP dyad could be confronted.

Bibliography

- [1] Dowds, M.; Stenspil, S. G.; de Souza, J. H.; Laursen, B. W.; Cacciarini, M.; Nielsen, M. B. Orthogonal- and Path-Dependent Photo/Acidoswitching in an Eight-State Dihydroazulene-Spiropyran Dyad. *ChemPhotoChem* **2022**, *6*, e202200152.
- [2] Gobbi, L.; Seiler, P.; Diederich, F.; Gramlich, V.; Boudon, C.; Gisselbrecht, J. P.; Gross, M. Photoswitchable Tetraethynylethene-Dihydroazulene Chromophores. *Helv. Chim. Acta* **2001**, *84*, 743–777.

Part III

Appendices

Appendix A

Supporting information to Chapter 4

The implementation logically begins by importing the adequate packages (Fig. A.1). Then, the SOS expression of β was defined in a function (Fig. A.2). The latter starts with the development required for the summation over the permutations of the frequencies, which is accomplished by the "permutations" library of the "itertools" package. The next lines allow to obtain the fluctuation dipoles, following Eq. (4.5). The "for" loop is applied until the chosen truncation of the OWB formula. Here, N corresponds to the number of excited states used in the Gaussian16 calculation of the vertical excitation energies.

```

1  #!/usr/bin/env python3
2
3  import itertools
4  import numpy
5  import math
6  import os

```

Fig. A.1: Necessary packages employed in the implementation of the SOS expression.

```

11 def sos(omega, cpt, N, transition_dipoles, excitation_energies):
12     # Eq. 2 of Champagne and Kirtman J. Chem. Phys. 125 024101
13     perms = [(-2*omega, cpt[0]), (omega, cpt[1]), (omega, cpt[2])]
14     beta_tensor_component = 0.0
15     for permuted in itertools.permutations(perms): # sum over permutations
16         pzeta, peta, pxi = permuted[0][1], permuted[1][1], permuted[2][1]
17         pomega_sigma = permuted[0][0]
18         pomega2 = permuted[2][0]
19
20         for n in range(1, N+1):
21             for m in range(1, N+1):
22                 fluctuation_dipole = transition_dipoles[m, n]
23                 if m == n:
24                     fluctuation_dipole = transition_dipoles[m, n] - transition_dipoles[0, 0]
25
26                 x = transition_dipoles[0, n][pzeta] * fluctuation_dipole[peta] * transition_dipoles[m, 0][pxi] / ((excitation_energies[n]+pomega_sigma) * (excitation_energies[m]-pomega2))
27                 beta_tensor_component += x
28
29     return beta_tensor_component

```

Fig. A.2: Definition of the OWB formula.

The electric transition dipole matrix is build using a "numpy array", filled by the dipole components computed with the Multiwfn software (Fig. A.3).

```

86 # Create the output file in the current directory
87 output_file = open(os.path.join(cwd, 'HRS_quantities.csv'), 'w')
88
89 # Build transition dipole matrix
90 transition_dipoles = numpy.zeros((Nb_of_excited_states+1, Nb_of_excited_states+1, 3))
91 for i in range(len(indices_1)):
92     transition_dipoles[indices_1[i], indices_2[i], :] = [x[i], y[i], z[i]]
93     transition_dipoles[indices_2[i], indices_1[i], :] = [x[i], y[i], z[i]]
94
95 HRS_quantities = []
96 for p in range(1, N+1):
97     beta = numpy.ndarray((3, 3, 3)) # create rank 3 tensor
98     for i in range(3):
99         for j in range(3):
100             for k in range(3):
101                 beta[i, j, k] = sos(0.02389, (i, j, k), p, transition_dipoles, excitation_energies)
102     # HRS quantities
103     beta2_ZZZ = 0
104     beta2_ZXX = 0
105     for i in range(3):
106         for j in range(3):
107             for k in range(3):
108                 beta2_ZZZ += 1/105*(2*beta[i, j, k]**2 + beta[i, j, j]*beta[i, k, k] + 4*beta[i, i, j]*beta[k, k, j] + 4*beta[i, j, k]*beta[j, i, k])
109                 beta2_ZXX += 1/105*(6*beta[i, j, k]**2 + 3*beta[i, j, j]*beta[i, k, k] - 2*beta[i, k, k] - 2*beta[i, j, j]*beta[k, k, j] - 2*beta[i, j, k]*beta[j, i, k])
110     beta_HRS = (math.sqrt(beta2_ZZZ + beta2_ZXX))/1000
111     DR = beta2_ZZZ/beta2_ZXX

```

Fig. A.3: Construction of the electric transition dipole matrix and of the dynamic β tensor (for an incident wavelength of 1907 nm), and derivation of the β_{HRS} and its DR. Note that the β_{HRS} values are divided by a factor 1000, in order to be consistent with the manner of presenting the results in Section 5.4.

Appendix B

Supporting information to Section 5.1

B.1 Conformational search

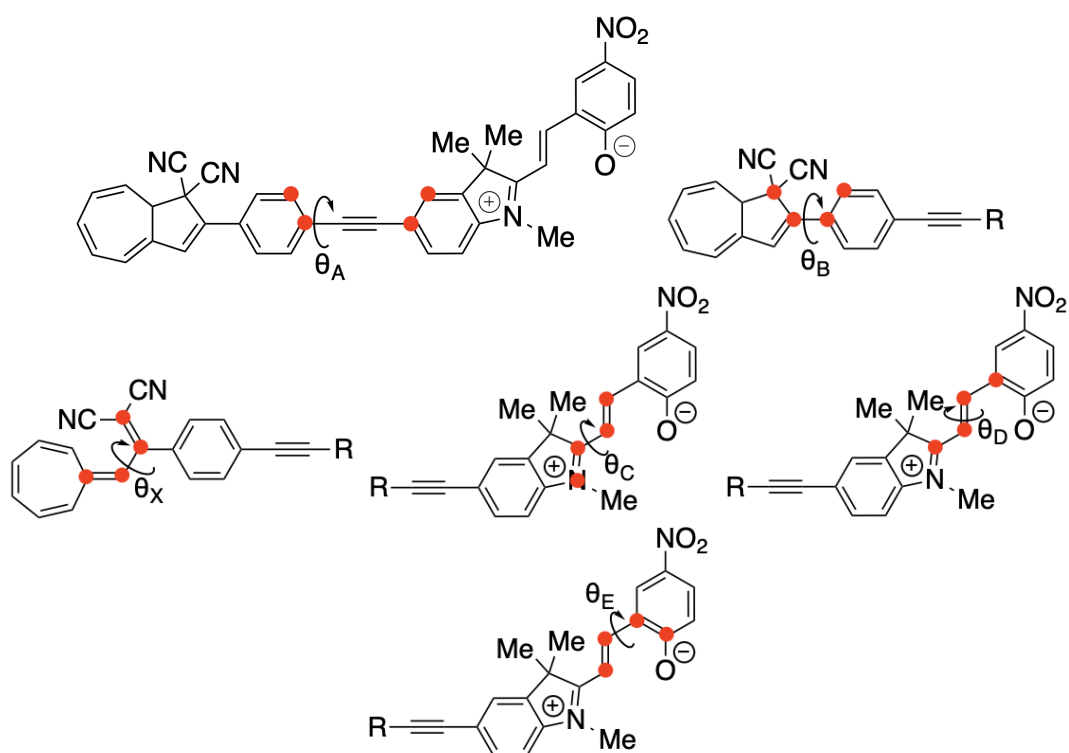


Fig. B.1: Definitions of the θ_A , θ_B , θ_X , θ_C , θ_D , θ_E torsional angles employed in the conformational sampling of the dyads and their constitutive units. The atoms determining these angles are marked in red.

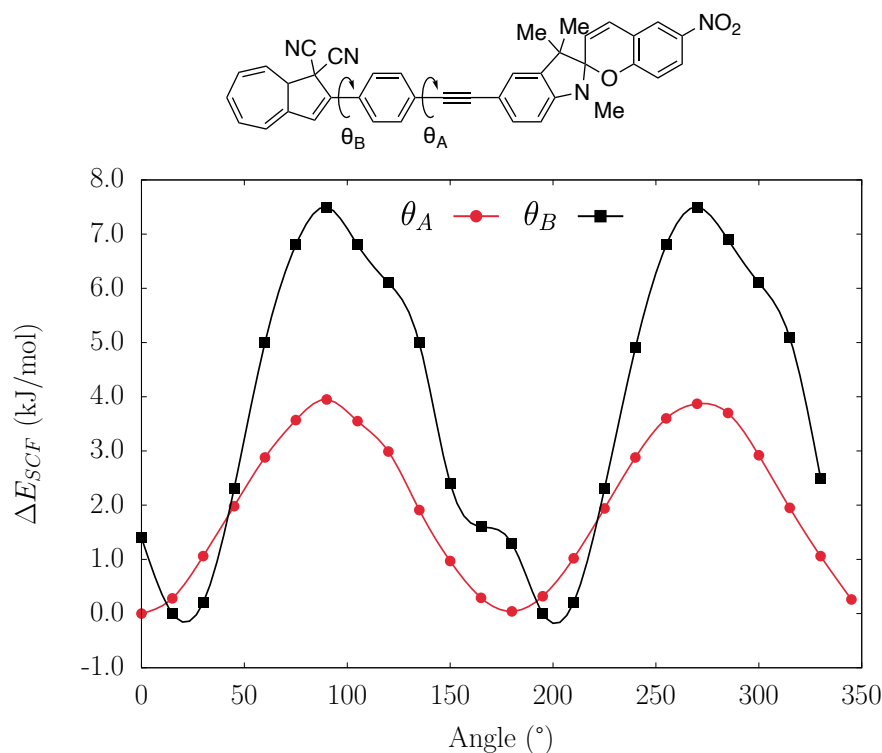


Fig. B.2: Relaxed potential energy scans along the θ_A and θ_B dihedral angles for the DHA-SP form. The reported ΔE_{SCF} values were evaluated at the IEF-PCM(acetonitrile)/ ω B97X-D/6-311G(d) level, using the most stable conformers as reference.

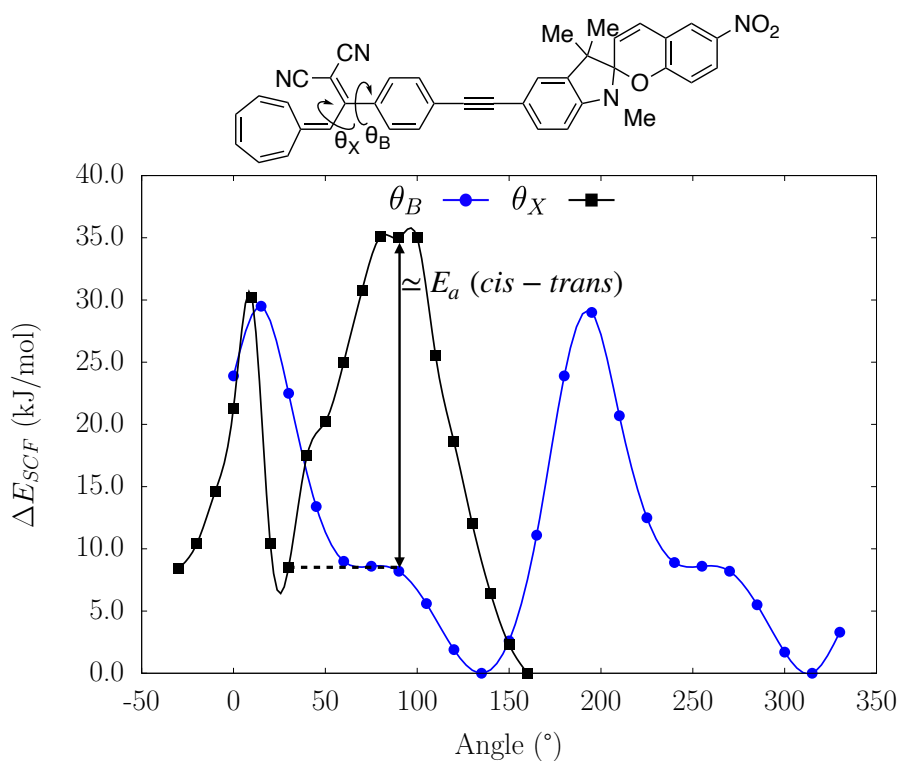
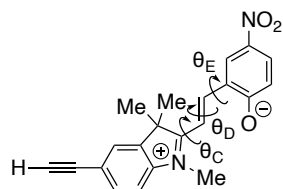


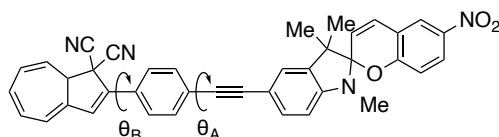
Fig. B.3: Relaxed potential energy scans along the θ_B and θ_X dihedral angles for the VHF-SP form. The reported ΔE_{SCF} values were evaluated at the IEF-PCM(acetonitrile)/ ω B97X-D/6-311G(d) level, using the most stable conformers as reference.

Table B.1: Relative conformer energies of the GS (ΔE_{SCF} , kJ/mol), standard (T = 298.15 K) relative Gibbs free energies (ΔG^0 , kJ/mol) for the constitutive merocyanine unit in its three states (MC, E-MCH and Z-MCH) with respect to the most stable conformer of each form, their corresponding MB populations at 298.15 K (P_{MB} , %), and their θ_C , θ_D , θ_E torsional angles ($^\circ$) as evaluated at the IEF-PCM(acetonitrile)/ ω B97X-D/6-311G(d) level.



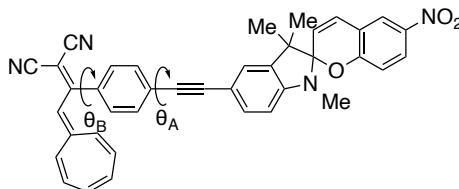
Conformer	θ_C	θ_D	θ_E	ΔE_{SCF}	ΔG^0	P_{MB}
MC						
TTC	0.0	180.0	0.0	0.0	0.0	97.6
TTT	180.0	180.0	180.0	3.0	10.5	1.4
CTC	-20.9	-176.8	-2.3	7.1	12.6	0.6
CTT	-16.9	-178.3	177.2	10.6	13.5	0.4
E-MCH						
TTC	179.0	-179.8	-1.2	0.0	0.0	60.1
TTT	-179.5	179.5	176.8	0.4	2.0	27.1
CTT	-33.8	-176.3	170.7	3.3	4.8	8.8
CTC	-36.0	-175.2	-5.2	2.4	6.7	4.0
Z-MCH						
CCT	-50.0	-4.1	138.0	0.0	0.0	74.8
TCT	106.1	-5.2	128.2	7.5	3.0	22.1
CCC	-46.3	-2.3	-49.8	5.9	8.0	2.9
TCC	112.3	-3.9	-55.8	15.6	16.0	0.1

Table B.2: Thermochemical and specific geometrical features of the main conformers of the DHA-SP form as evaluated at the IEF-PCM(acetonitrile)/ ω B97X-D/6-311G(d) level of approximation: relative conformer energies of the GS (ΔE_{SCF} , kJ/mol), standard (T = 298.15 K) relative Gibbs free energies with respect to the most stable conformers (ΔG^0 , kJ/mol), their corresponding MB populations at 298.15 K (P_{MB} , %), and their (θ_A, θ_B) torsional angles ($^\circ$).



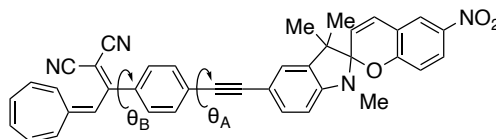
Conformer	θ_A	θ_B	ΔE_{SCF}	ΔG^0	P_{MB}
DHA(1)-SP	4.6	-15.8	0.0	0.0	55.5
DHA(2)-SP	175.7	-16.3	0.0	0.5	44.5

Table B.3: Thermochemical and specific geometrical features of the main conformers of the *trans*-VHF-SP form as evaluated at the IEF-PCM(acetonitrile)/ ω B97X-D/6-311G(d) level of approximation: relative conformer energies of the GS (ΔE_{SCF} , kJ/mol), standard (T = 298.15 K) relative Gibbs free energies with respect to the most stable conformers (ΔG^0 , kJ/mol), their corresponding MB populations at 298.15 K (P_{MB} , %), and their (θ_A, θ_B) torsional angles ($^\circ$).



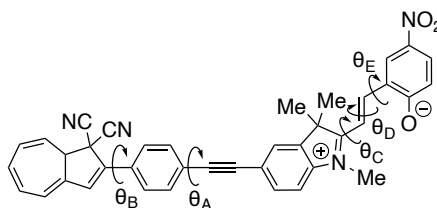
Conformer	θ_A	θ_B	ΔE_{SCF}	ΔG^0	P_{MB}
<i>trans</i> -VHF(1)-SP	0.3	-59.2	0.1	0.4	45.9
<i>trans</i> -VHF(2)-SP	1.3	121.4	0.0	0.0	54.1

Table B.4: Thermochemical and specific geometrical features of the main conformers of the *cis*-VHF-SP form as evaluated at the IEF-PCM(acetonitrile)/ ω B97X-D/6-311G(d) level of approximation: relative conformer energies of the GS (ΔE_{SCF} , kJ/mol), standard (T = 298.15 K) relative Gibbs free energies with respect to the most stable conformers (ΔG^0 , kJ/mol), their corresponding MB populations at 298.15 K (P_{MB} , %), and their (θ_A, θ_B) torsional angles ($^\circ$).



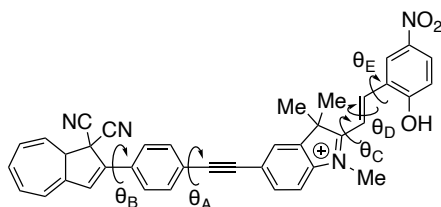
Conformer	θ_A	θ_B	ΔE_{SCF}	ΔG^0	P_{MB}
<i>cis</i> -VHF-SP	-3.2	-47.2	0.0	1.0	40.3
<i>cis</i> -VHF-SP	1.7	135.3	0.0	0.0	59.7

Table B.5: Thermochemical and specific geometrical features of the main conformers of the DHA-MC form as evaluated at the IEF-PCM(acetonitrile)/ ω B97X-D/6-311G(d) level of approximation: relative conformer energies of the GS (ΔE_{SCF} , kJ/mol), standard (T = 298.15 K) relative Gibbs free energies with respect to the most stable conformers (ΔG^0 , kJ/mol), their corresponding MB populations at 298.15 K (P_{MB} , %), and their ($\theta_A, \theta_B, \theta_C, \theta_D, \theta_E$) torsional angles ($^\circ$).



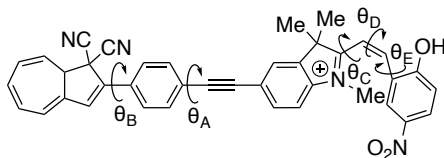
Conformer	θ_A	θ_B	θ_C	θ_D	θ_E	ΔE_{SCF}	ΔG^0	P_{MB}
DHA(1)-MC/TTC	2.1	-16.1	-179.6	179.9	0.1	0.0	0.0	42.9
DHA(2)-MC/TTC	178.4	-17.0	-180.0	179.9	0.1	-0.1	0.7	32.7
DHA(1)-MC/TTT	-0.9	-16.4	-179.7	-180.0	-179.8	3.4	2.8	13.9
DHA(2)-MC/TTT	178.7	-16.6	-179.6	-179.9	-179.9	3.4	3.5	10.4

Table B.6: Thermochemical and specific geometrical features of the main conformers of the DHA-E-MCH form as evaluated at the IEF-PCM(acetonitrile)/ ω B97X-D/6-311G(d) level of approximation: relative conformer energies of the GS (ΔE_{SCF} , kJ/mol), standard (T = 298.15 K) relative Gibbs free energies with respect to the most stable conformers (ΔG^0 , kJ/mol), their corresponding MB populations at 298.15 K (P_{MB} , %), and their ($\theta_A, \theta_B, \theta_C, \theta_D, \theta_E$) torsional angles ($^\circ$).



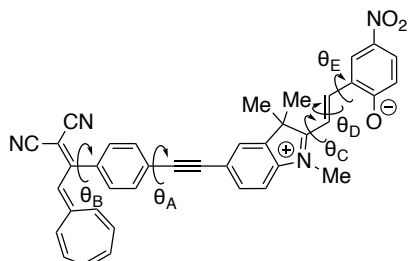
Conformer	θ_A	θ_B	θ_C	θ_D	θ_E	ΔE_{SCF}	ΔG^0	P_{MB}
DHA(1)-MCH/TTC	0.7	-16.5	-179.4	179.8	0.0	-0.1	1.7	19.0
DHA(2)-MCH/TTC	176.9	-17.1	-179.3	179.8	0.3	-0.1	1.5	20.9
DHA(1)-MCH/TTT	-1.2	-16.4	179.8	179.8	175.7	0.0	0.0	37.7
DHA(2)-MCH/TTT	177.8	-16.5	-179.3	-179.9	178.6	0.0	1.3	22.3

Table B.7: Thermochemical and specific geometrical features of the main conformers of the DHA-Z-MCH form as evaluated at the IEF-PCM(acetonitrile)/ ω B97X-D/6-311G(d) level of approximation: relative conformer energies of the GS (ΔE_{SCF} , kJ/mol), standard (T = 298.15 K) relative Gibbs free energies with respect to the most stable conformers (ΔG^0 , kJ/mol), their corresponding MB populations at 298.15 K (P_{MB} , %), and their ($\theta_A, \theta_B, \theta_C, \theta_D, \theta_E$) torsional angles ($^\circ$).



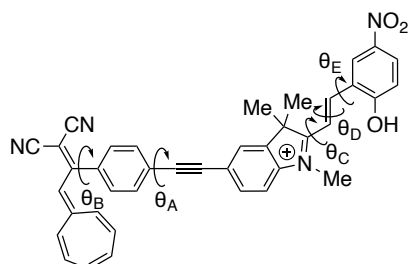
Conformer	θ_A	θ_B	θ_C	θ_D	θ_E	ΔE_{SCF}	ΔG^0	P_{MB}
DHA(1)-MCH/CCT	3.0	-16.0	-50.6	-4.4	138.7	0.0	0.0	45.4
DHA(2)-MCH/CCT	-178.8	-15.6	-50.2	-4.3	137.5	0.0	0.0	44.9
DHA(1)-MCH/TCT	2.3	-16.4	-104.2	5.0	-127.7	7.7	4.9	6.2
DHA(2)-MCH/TCT	-176.0	-16.7	-104.4	5.4	-127.8	7.5	9.6	3.4

Table B.8: Thermochemical and specific geometrical features of the main conformers of the *trans*-VHF-MC form as evaluated at the IEF-PCM(acetonitrile)/ ω B97X-D/6-311G(d) level of approximation: relative conformer energies of the GS (ΔE_{SCF} , kJ/mol), standard (T = 298.15 K) relative Gibbs free energies with respect to the most stable conformers (ΔG^0 , kJ/mol), their corresponding MB populations at 298.15 K (P_{MB} , %), and their ($\theta_A, \theta_B, \theta_C, \theta_D, \theta_E$) torsional angles ($^\circ$).



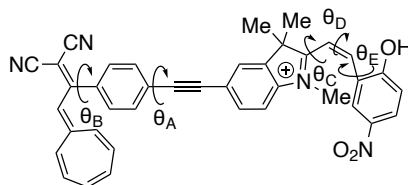
Conformer	θ_A	θ_B	θ_C	θ_D	θ_E	ΔE_{SCF}	ΔG^0	P_{MB}
<i>trans</i> -VHF(1)-MC/TTC	-2.8	-60.2	-180.0	179.8	0.0	0.0	0.0	45.9
<i>trans</i> -VHF(2)-MC/TTC	-176.9	-59.7	-180.0	180.0	0.0	0.1	0.9	31.3
<i>trans</i> -VHF(1)-MC/TTT	1.9	-60.0	-179.8	-179.7	-179.8	3.4	3.2	12.7
<i>trans</i> -VHF(2)-MC/TTT	175.1	-60.4	179.9	179.7	-179.8	3.4	3.8	10.1

Table B.9: Thermochemical and specific geometrical features of the main conformers of the *trans*-VHF-E-MCH form as evaluated at the IEF-PCM(acetonitrile)/ ω B97X-D/6-311G(d) level of approximation: relative conformer energies of the GS (ΔE_{SCF} , kJ/mol), standard (T = 298.15 K) relative Gibbs free energies with respect to the most stable conformers (ΔG^0 , kJ/mol), their corresponding MB populations at 298.15 K (P_{MB} , %), and their ($\theta_A, \theta_B, \theta_C, \theta_D, \theta_E$) torsional angles ($^\circ$).



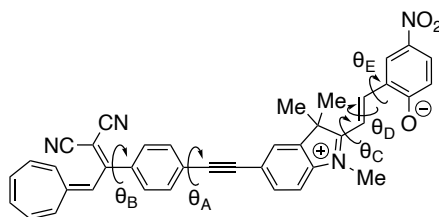
Conformer	θ_A	θ_B	θ_C	θ_D	θ_E ($^\circ$)	ΔE_{SCF}	ΔG^0	P_{MB}
<i>trans</i> -VHF(1)-MCH/TTC	-6.6	-60.6	178.1	179.9	-1.8	0.0	0.0	34.1
<i>trans</i> -VHF(2)-MCH/TTC	-179.4	-60.3	177.4	179.5	1.3	0.7	0.2	31.2
<i>trans</i> -VHF(1)-MCH/TTT	2.1	-60.3	-178.3	-179.5	179.1	0.4	1.4	19.0
<i>trans</i> -VHF(2)-MCH/TTT	174.9	-60.7	179.3	179.4	-179.0	0.6	1.9	15.7

Table B.10: Thermochemical and specific geometrical features of the main conformers of the *trans*-VHF-Z-MCH form as evaluated at the IEF-PCM(acetonitrile)/ ω B97X-D/6-311G(d) level of approximation: relative conformer energies of the GS (ΔE_{SCF} , kJ/mol), standard (T = 298.15 K) relative Gibbs free energies with respect to the most stable conformers (ΔG^0 , kJ/mol), their corresponding MB populations at 298.15 K (P_{MB} , %), and their ($\theta_A, \theta_B, \theta_C, \theta_D, \theta_E$) torsional angles ($^\circ$).



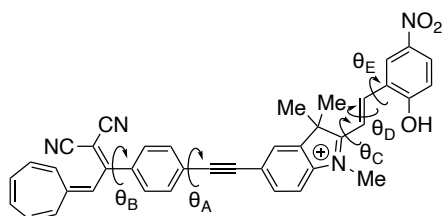
Conformer	θ_A	θ_B	θ_C	θ_D	θ_E	ΔE_{SCF}	ΔG^0	P_{MB}
<i>trans</i> -VHF(1)-MCH/CCT	-2.0	-60.6	-49.9	-4.0	137.1	0.0	0.0	50.9
<i>trans</i> -VHF(2)-MCH/CCT	-179.6	-60.7	-50.8	-3.9	138.2	-0.5	1.1	33.0
<i>trans</i> -VHF(1)-MCH/TCT	3.0	-60.5	-107.6	5.3	-128.9	7.3	4.1	9.8
<i>trans</i> -VHF(2)-MCH/TCT	179.8	-60.7	-105.3	5.0	-126.8	7.1	5.1	6.4

Table B.11: Thermochemical and specific geometrical features of the main conformers of the *cis*-VHF-MC form as evaluated at the IEF-PCM(acetonitrile)/ ω B97X-D/6-311G(d) level of approximation: relative conformer energies of the GS (ΔE_{SCF} , kJ/mol), standard (T = 298.15 K) relative Gibbs free energies with respect to the most stable conformers (ΔG^0 , kJ/mol), their corresponding MB populations at 298.15 K (P_{MB} , %), and their ($\theta_A, \theta_B, \theta_C, \theta_D, \theta_E$) torsional angles ($^\circ$).



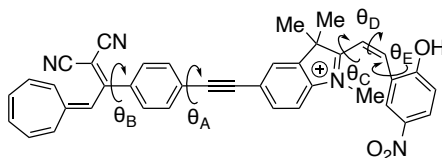
Conformer	θ_A	θ_B	θ_C	θ_D	θ_E	ΔE_{SCF}	ΔG^0	P_{MB}
<i>cis</i> -VHF(1)-MC/TTC	-2.2	-47.5	-179.9	-179.8	0.1	-0.1	2.0	22.7
<i>cis</i> -VHF(2)-MC/TTC	178.9	-47.5	179.7	179.9	0.0	0.0	0.0	51.9
<i>cis</i> -VHF(1)-MC/TTT	-2.9	-47.5	179.8	179.7	-179.8	3.4	4.4	8.9
<i>cis</i> -VHF(2)-MC/TTT	-177.3	-47.2	-179.9	-179.8	-179.8	3.5	2.8	16.4

Table B.12: Thermochemical and specific geometrical features of the main conformers of the *cis*-VHF-E-MCH form as evaluated at the IEF-PCM(acetonitrile)/ ω B97X-D/6-311G(d) level of approximation: relative conformer energies of the GS (ΔE_{SCF} , kJ/mol), standard (T = 298.15 K) relative Gibbs free energies with respect to the most stable conformers (ΔG^0 , kJ/mol), their corresponding MB populations at 298.15 K (P_{MB} , %), and their ($\theta_A, \theta_B, \theta_C, \theta_D, \theta_E$) torsional angles ($^\circ$).



Conformer	θ_A	θ_B	θ_C	θ_D	θ_E	ΔE_{SCF}	ΔG^0	P_{MB}
<i>cis</i> -VHF(1)-MCH/TTC	-2.3	-47.9	-179.7	179.9	-0.1	-0.4	0.9	28.5
<i>cis</i> -VHF(2)-MCH/TTC	-174.3	-47.3	179.0	179.3	1.3	-0.3	1.8	20.1
<i>cis</i> -VHF(1)-MCH/TTT	-3.9	-48.0	-180.0	-179.8	-173.8	0.3	3.6	9.8
<i>cis</i> -VHF(2)-MCH/TTT	172.4	-48.3	178.8	178.9	174.7	0.0	0.0	41.6

Table B.13: Thermochemical and specific geometrical features of the main conformers of the *cis*-VHF-Z-MCH form as evaluated at the IEF-PCM(acetonitrile)/ ω B97X-D/6-311G(d) level of approximation: relative conformer energies of the GS (ΔE_{SCF} , kJ/mol), standard (T = 298.15 K) relative Gibbs free energies with respect to the most stable conformers (ΔG^0 , kJ/mol), their corresponding MB populations at 298.15 K (P_{MB} , %), and their ($\theta_A, \theta_B, \theta_C, \theta_D, \theta_E$) torsional angles ($^\circ$).



Conformer	θ_A	θ_B	θ_C	θ_D	θ_E	ΔE_{SCF}	ΔG^0	P_{MB}
<i>cis</i> -VHF(1)-MCH/CCT	-2.2	-48.0	-50.0	-4.2	137.3	0.0	0.0	43.8
<i>cis</i> -VHF(2)-MCH/CCT	170.4	-48.7	-50.7	-4.6	138.5	0.0	0.0	44.3
<i>cis</i> -VHF(1)-MCH/TCT	2.4	-47.8	-105.0	5.3	-127.1	7.3	4.5	7.3
<i>cis</i> -VHF(2)-MCH/TCT	-178.3	-47.7	-105.3	5.1	-127.8	7.4	4.8	5.6

B.2 Geometry optimizations

Table B.14: Relative GS energies (ΔE_{SCF} , kJ/mol), standard ($T = 298.15$ K) Gibbs free energies (ΔG^0 , kJ/mol) with respect to the (S)-DHA-(R)-SP form, and norm of the GS dipole moment (μ_g , D) as evaluated at the IEF-PCM(acetonitrile)/ ω B97X-D/6-311G(d) level.

Stereoisomer	ΔE_{SCF}	ΔG^0	μ_g
(S)-DHA-(R)-SP	0.0	0.0	10.3
(R)-DHA-(S)-SP	0.0	0.0	10.3
(R)-DHA-(R)-SP	0.0	-0.2	9.7
(S)-DHA-(S)-SP	0.0	-0.2	9.7

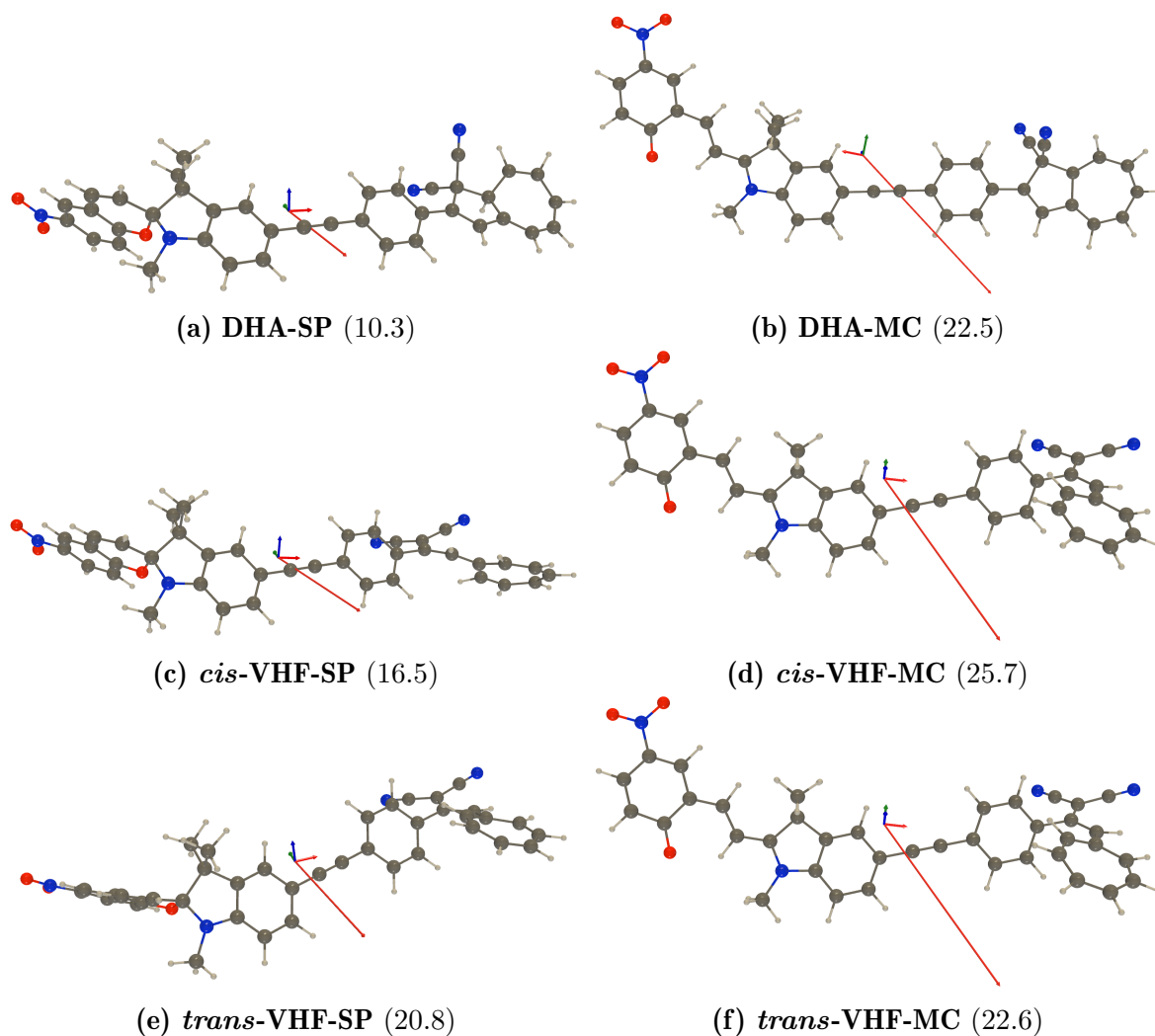
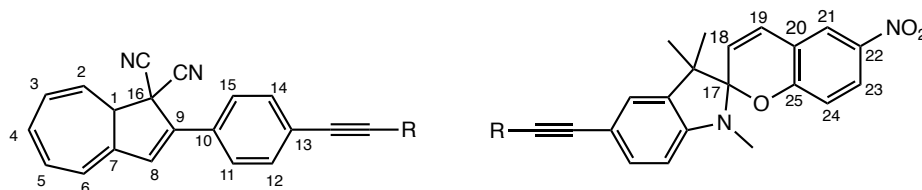


Fig. B.4: GS dipole moment vectors (in red) of all neutral forms of the DHA-SP molecular switch in their most stable conformations as evaluated at the IEF-PCM(acetonitrile)/ ω B97X-D/6-311G(d) level of theory. The norms are written in parenthesis (in D).

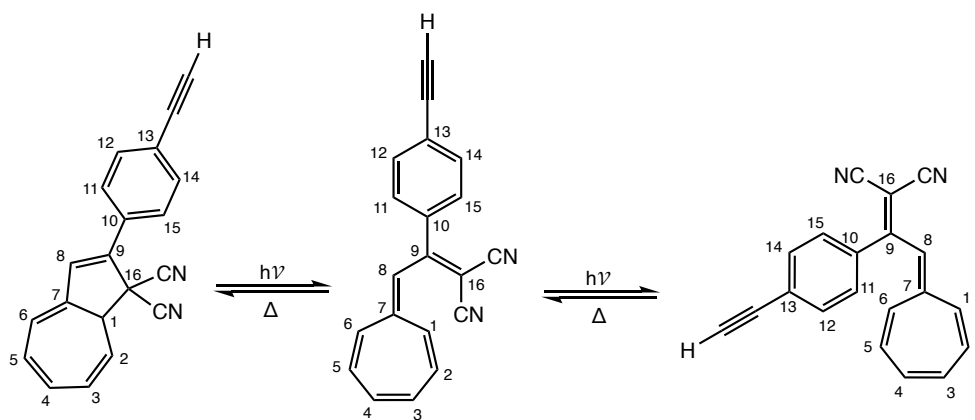
Table B.15: Representative geometrical parameters: bond lengths (Å), bond angles (°), torsion angles (°)[†], and bond length alternations (Å) for the main stereoisomers of the DHA-SP form as evaluated at the IEF-PCM(acetonitrile)/ ω B97X-D/6-311G(d) level of theory. $BLA_1 = (d_{C_7-C_8} + d_{C_9-C_{16}} - 2d_{C_8-C_9})/2$, $BLA_2 = (d_{C_7-C_8} + d_{C_9-C_{10}} - 2d_{C_8-C_9})/2$, $BLA_3 = (d_{C_{15}-C_{10}} + d_{C_9-C_{16}} - 2d_{C_9-C_{10}})/2$, BLA_4 is associated with the bond length alternation in the six-membered ring of the DHA/VHF unit, $BLA_5 = (d_{C_1-C_2} + 2d_{C_3-C_4} + 2d_{C_5-C_6} + d_{C_7-C_1})/6 - (2d_{C_2-C_3} + 2d_{C_4-C_5} + 2d_{C_6-C_7})/6$, and $BLA_6 = (d_{C_{17}-C_{18}} + 2d_{C_{19}-C_{20}} + d_{C_{21}-C_{22}})/4 - (2d_{C_{18}-C_{19}} + 2d_{C_{20}-C_{21}})/4$.



(R/S)-DHA, R	(S)-DHA, -C \equiv C-(R)-SP	(R)-DHA, -C \equiv C-(S)-SP	(R)-DHA, -C \equiv C-(R)-SP	(S)-DHA, -C \equiv C-(S)-SP
C ₇ -C ₈	1.444	1.444	1.444	1.443
C ₈ -C ₉	1.343	1.343	1.343	1.343
C ₉ -C ₁₆	1.542	1.542	1.542	1.542
C ₉ -C ₁₀	1.466	1.466	1.467	1.467
C ₈ -C ₉ -C ₁₆	108.9	108.9	109.0	109.0
C ₄ -C ₅ -C ₆ -C ₇	24.8	-24.8	-25.3	25.5
C ₆ -C ₇ -C ₁ -C ₂	-52.8	53.0	53.8	-54.3
C ₇ -C ₈ -C ₉ -C ₁₆	-6.8	6.8	6.6	-6.5
C ₇ -C ₈ -C ₉ -C ₁₀	176.0	-175.8	-175.6	175.8
C ₈ -C ₉ -C ₁₀ -C ₁₁	-19.4	19.5	19.5	-18.4
BLA ₁	0.149	0.149	0.150	0.150
BLA ₂	0.112	0.112	0.112	0.112
BLA ₃	0.004	0.004	0.004	0.004
BLA ₄	0.003	0.003	0.003	0.003
BLA ₅	-0.093	-0.093	-0.093	-0.093
(R/S)-SP, R	(R)-SP, -C \equiv C-(S)-DHA	(S)-SP, -C \equiv C-(R)-DHA	(R)-SP, -C \equiv C-(R)-DHA	(S)-SP, -C \equiv C-(S)-DHA
N-C ₁₇	1.440	1.440	1.440	1.440
C ₁₇ -O	1.464	1.464	1.464	1.464
C ₁₇ -C ₁₈	1.499	1.499	1.499	1.499
C ₁₈ -C ₁₉	1.331	1.331	1.331	1.331
C ₁₉ -C ₂₀	1.457	1.457	1.457	1.457
C ₂₅ -O	1.339	1.339	1.339	1.339
C ₁₇ -C ₁₈ -C ₁₉ -C ₂₀	3.6	-3.6	3.6	-3.6
N-C ₁₇ -C ₁₈ -C ₁₉	-136.8	136.8	-136.8	136.8
C ₁₈ -C ₁₉ -C ₂₀ -C ₂₅	7.3	-7.3	7.3	-7.3
BLA ₆	0.091	0.091	0.091	0.091

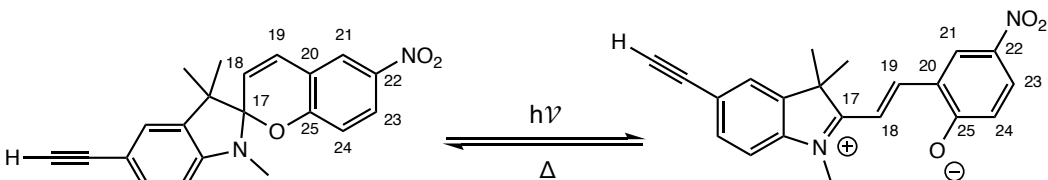
[†] The very small differences in the bond lengths (0.001 Å), valence (1.0°) and torsion angles (1.0°) arise from numerical precision of the method.

Table B.16: Representative geometrical parameters: bond lengths (Å), bond angles (°), torsion angles (°) and bond length alternations (Å) for the (S)-DHA, (R)-DHA, *cis*-VHF and *trans*-VHF individual units (R = -C≡C-H) in their most stable conformations as evaluated at the IEF-PCM(acetonitrile)/ωB97X-D/6-311G(d) level of theory. $BLA_1 = (d_{C_7-C_8} + d_{C_9-C_{16}} - 2d_{C_8-C_9})/2$, $BLA_2 = (d_{C_7-C_8} + d_{C_9-C_{10}} - 2d_{C_8-C_9})/2$, $BLA_3 = (d_{C_{15}-C_{10}} + d_{C_9-C_{16}} - 2d_{C_9-C_{10}})/2$, BLA_4 is associated with the bond length alternation in the six-membered ring of the DHA/VHF unit, and $BLA_5 = (d_{C_1-C_2} + 2d_{C_3-C_4} + 2d_{C_5-C_6} + d_{C_7-C_1})/6 - (2d_{C_2-C_3} + 2d_{C_4-C_5} + 2d_{C_6-C_7})/6$.



	(S)-DHA	(R)-DHA	<i>cis</i> -VHF	<i>trans</i> -VHF
C ₇ -C ₈	1.444	1.444	1.390	1.390
C ₈ -C ₉	1.343	1.343	1.421	1.418
C ₉ -C ₁₆	1.541	1.541	1.390	1.389
C ₉ -C ₁₀	1.467	1.467	1.486	1.486
C ₈ -C ₉ -C ₁₆	108.9	108.9	125.3	120.7
C ₄ -C ₅ -C ₆ -C ₇	24.5	-24.5	-1.5	1.2
C ₆ -C ₇ -C ₁ -C ₂	-52.1	52.1	-15.6	-18.7
C ₇ -C ₈ -C ₉ -C ₁₆	-6.8	6.8	-32.8	167.4
C ₇ -C ₈ -C ₉ -C ₁₀	176.1	-176.1	150.3	-17.4
C ₈ -C ₉ -C ₁₀ -C ₁₁	-20.7	20.7	-49.2	-55.5
BLA ₁	0.149	0.149	-0.031	-0.029
BLA ₂	0.112	0.112	0.017	0.020
BLA ₃	/	/	-0.092	-0.094
BLA ₄	0.003	0.003	0.000	0.001
BLA ₅	-0.093	-0.093	0.076	0.076

Table B.17: Representative geometrical parameters: bond lengths (Å), bond angles (°), torsion angles (°) and bond length alternations (Å) for the (R)-SP, (S)-SP, MC, E-MCH and Z-MCH individual units (R = -C≡C-H) in their most stable conformations as evaluated at the IEF-PCM(acetonitrile)/ωB97X-D/6-311G(d) level of theory. $BLA_6 = (d_{C_{17}-C_{18}} + 2d_{C_{19}-C_{20}} + d_{C_{21}-C_{22}})/4 - (2d_{C_{18}-C_{19}} + 2d_{C_{20}-C_{21}})/4$.



	(R)-SP	(S)-SP	MC	E-MCH	Z-MCH
N-C ₁₇	1.440	1.440	1.337	1.319	1.305
C ₁₇ -O	1.464	1.464	/	/	/
C ₁₇ -C ₁₈	1.499	1.499	1.401	1.429	1.453
C ₁₈ -C ₁₉	1.331	1.331	1.378	1.353	1.340
C ₁₉ -C ₂₀	1.457	1.457	1.415	1.451	1.469
C ₂₅ -O	1.339	1.339	1.240	1.335	1.340
O-H	/	/	/	0.962	0.961
C ₁₇ -C ₁₈ -C ₁₉ -C ₂₀	3.6	-3.6	180.0	-179.8	-4.1
N-C ₁₇ -C ₁₈ -C ₁₉	-136.6	136.6	-180.0	179.0	-50.0
C ₁₈ -C ₁₉ -C ₂₀ -C ₂₅	7.2	-7.2	0.0	-1.2	138.0
BLA ₆	0.091	0.091	0.008	0.051	0.077

Table B.18: Bond lengths (Å) involving the alkyne linker as a function of the DHA/VHF and SP/MC switching unit states in their most stable conformations as evaluated at the IEF-PCM(acetonitrile)/ωB97X-D/6-311G(d) level of theory.

(R ₁)C—C ₁ ≡C ₂ —C(R ₂)				
R ₁ , R ₂	DHA, SP	DHA, MC	DHA, E-MCH	DHA, Z-MCH
(R ₁)C-C ₁	1.426	1.427	1.427	1.427
(R ₂)C-C ₂	1.426	1.427	1.427	1.427
C ₁ -C ₂	1.207	1.206	1.206	1.205
R ₁ , R ₂	<i>cis</i> -VHF, SP	<i>cis</i> -VHF, MC	<i>cis</i> -VHF, E-MCH	<i>cis</i> -VHF, Z-MCH
(R ₁)C-C ₁	1.427	1.428	1.428	1.428
(R ₂)C-C ₂	1.426	1.427	1.427	1.427
C ₁ -C ₂	1.207	1.206	1.205	1.205
R ₁ , R ₂	<i>trans</i> -VHF, SP	<i>trans</i> -VHF, MC	<i>trans</i> -VHF, E-MCH	<i>trans</i> -VHF, Z-MCH
(R ₁)C-C ₁	1.427	1.428	1.428	1.428
(R ₂)C-C ₂	1.426	1.427	1.427	1.427
C ₁ -C ₂	1.207	1.206	1.205	1.205

Appendix C

Supporting information to Section 5.2

Table C.1: Relative energy of the GS, (ΔE_{SCF} , kJ/mol), and standard ($T = 298.15$ K, $[] = 1$ M) Gibbs free energy (ΔG^0 , kJ/mol) of formation of the conjugated base of each acid-base couple as evaluated at the IEF-PCM/ ω B97X-D level of theory, with the 6-311G(d) and 6-311+G(d) basis sets, and their absolute difference ($A.D. = \text{value}_{(6-311G(d))} - \text{value}_{(6-311+G(d))}$, kJ/mol).

	6-311G(d)		6-311+G(d)		<i>A.D.</i>	
	ΔE_{SCF}	ΔG^0	ΔE_{SCF}	ΔG^0	ΔE_{SCF}	ΔG^0
CF ₃ COOH CF ₃ COO ⁻	1189.2	1154.8	1150.3	1116.1	38.9	38.7
Et ₃ NH ⁺ Et ₃ N	1219.5	1175.6	938.0	1166.9	281.5	8.7

Table C.2: Standard ($T = 298.15$ K, $[] = 1$ M) Gibbs free energy (kJ/mol) and equilibrium constants for all the switching processes of the constitutive units as evaluated at the IEF-PCM(acetonitrile)/ ω B97X-D/6-311G(d) level of theory. The G^0 values for the CF₃COOH/CF₃COO⁻ and Et₃NH⁺/Et₃N acid-base couples were computed using the 6-311+G(d) basis set.

Switching process	ΔG^0	K_{eq}
DHA \rightarrow <i>trans</i> -VHF	13.4	/
DHA \rightarrow <i>cis</i> -VHF	23.7	/
SP \rightarrow MC	37.7	/
Z-MCH ⁺ \rightarrow E-MCH ⁺	-24.1	/
MC + CF ₃ COOH \rightarrow E-MCH ⁺ + CF ₃ COO ⁻	-25.6	3.1×10^4
E-MCH ⁺ + Et ₃ N \rightarrow MC + Et ₃ NH ⁺	-25.1	2.5×10^4
SP + CF ₃ COOH \rightarrow Z-MCH ⁺ + CF ₃ COO ⁻	36.2	4.6×10^{-7}
Z-MCH ⁺ + Et ₃ N \rightarrow SP + Et ₃ NH ⁺	-87.0	4.6×10^{15}

Appendix D

Supporting information to Section 5.3

Table D.1: Computed excitation energies (ΔE_{0n} , eV) and their associated wavelengths (λ_{0n} , nm), oscillator strengths (f_{0n}), amounts of charge transfer (q_{CT} , e), distances of charge transfer (d_{CT} , Å), and variations of dipole moment upon excitation from the GS to the n^{th} dominant lowest-energy ES ($\Delta\mu_{0n}$, D) of each stereoisomer of the DHA-SP form. All calculations were performed at the IEF-PCM(acetonitrile)/TDDFT/ ω B97X-D/6-311+G(d) level.

Form	n	ΔE_{0n}	λ_{0n}	f_{0n}	q_{CT}	d_{CT}	$\Delta\mu_{0n}$
(S)-DHA-(R)-SP	1	3.26	380	1.50	0.47	0.73	1.63
	2	3.96	313	0.90	0.54	2.76	7.19
(R)-DHA-(S)-SP	1	3.24	383	1.49	0.47	0.73	1.63
	2	3.92	316	0.95	0.54	2.76	7.19
(R)-DHA-(R)-SP	1	3.24	382	1.51	0.47	0.77	1.71
	2	3.93	315	0.94	0.54	2.71	7.05
(S)-DHA-(S)-SP	1	3.24	382	1.51	0.47	0.77	1.71
	2	3.93	315	0.94	0.54	2.71	7.05

Table D.2: Computed excitation energies (ΔE_{0n} , eV) and their associated wavelengths (λ_{0n} , nm), oscillator strengths (f_{0n}), amounts of charge transfer (q_{CT} , e), distances of charge transfer (d_{CT} , Å), and variations of dipole moment upon excitation from the GS to the n^{th} dominant lowest-energy ES ($\Delta\mu_{0n}$, D) of the main conformers of the DHA-SP form as evaluated at the IEF-PCM(acetonitrile)/TDDFT/ ω B97X-D/6-311+G(d) level. The last two lines contain averaged values using the MB populations at 298.15 K.

Form	n	ΔE_{0n}	λ_{0n}	f_{0n}	q_{CT}	d_{CT}	$\Delta\mu_{0n}$
DHA(1)-SP	1	3.26	380	1.50	0.47	0.73	1.63
	2	3.96	313	0.90	0.54	2.76	7.19
DHA(2)-SP	1	3.24	382	1.50	0.47	0.76	1.69
	2	3.93	315	0.90	0.54	2.73	7.10
avg.	1	3.25	381	1.50	0.47	0.74	1.66
	2	3.95	314	0.90	0.54	2.74	7.15

Table D.3: Computed excitation energies (ΔE_{0n} , eV) and their associated wavelengths (λ_{0n} , nm), oscillator strengths (f_{0n}), amounts of charge transfer (q_{CT} , e), distances of charge transfer (d_{CT} , Å), and variations of dipole moment upon excitation from the GS to the n^{th} dominant lowest-energy ES ($\Delta\mu_{0n}$, D) of the main conformers of the DHA-MC form as evaluated at the IEF-PCM(acetonitrile)/TDDFT/ ω B97X-D/6-311+G(d) level. The last two lines contain averaged values using the MB populations at 298.15 K.

Form	n	ΔE_{0n}	λ_{0n}	f_{0n}	q_{CT}	d_{CT}	$\Delta\mu_{0n}$
DHA(1)-MC/TTC	1	2.70	458	1.77	0.51	1.11	2.70
	2	3.27	379	0.89	0.44	0.51	1.08
DHA(2)-MC/TTC	1	2.71	458	1.75	0.51	1.08	2.65
	2	3.27	379	0.87	0.44	0.51	1.08
DHA(1)-MC/TTT	1	2.56	485	1.50	0.49	0.75	1.78
	2	3.26	380	1.10	0.44	0.57	1.20
DHA(2)-MC/TTT	1	2.56	485	1.50	0.50	0.76	1.80
	2	3.26	380	1.00	0.44	0.57	1.21
avg.	1	2.67	465	1.70	0.50	1.01	2.46
	2	3.27	379	0.92	0.44	0.52	1.11

Table D.4: Computed excitation energies (ΔE_{0n} , eV) and their associated wavelengths (λ_{0n} , nm), oscillator strengths (f_{0n}), amounts of charge transfer (q_{CT} , e), distances of charge transfer (d_{CT} , Å), and variations of dipole moment upon excitation from the GS to the n^{th} dominant lowest-energy ES ($\Delta\mu_{0n}$, D) of the main conformers of the DHA-E-MCH form as evaluated at the IEF-PCM(acetonitrile)/TDDFT/ ω B97X-D/6-311+G(d) level. The last line contains averaged values using the MB populations at 298.15 K.

Form	n	ΔE_{0n}	λ_{0n}	f_{0n}	q_{CT}	d_{CT}	$\Delta\mu_{0n}$
DHA(1)-E-MCH/TTC	1	3.14	395	2.52	0.53	1.99	5.09
DHA(2)-E-MCH/TTC	1	3.14	395	2.47	0.53	1.99	5.05
DHA(1)-E-MCH/TTT	1	3.10	400	2.48	0.55	1.90	5.00
DHA(2)-E-MCH/TTT	1	3.10	400	2.47	0.55	1.90	4.99
avg.	1	3.12	398	2.48	0.54	1.94	5.02

Table D.5: Computed excitation energies (ΔE_{0n} , eV) and their associated wavelengths (λ_{0n} , nm), oscillator strengths (f_{0n}), amounts of charge transfer (q_{CT} , e), distances of charge transfer (d_{CT} , Å), and variations of dipole moment upon excitation from the GS to the n^{th} dominant lowest-energy ES ($\Delta\mu_{0n}$, D) of the main conformers of the DHA-Z-MCH form as evaluated at the IEF-PCM(acetonitrile)/TDDFT/ ω B97X-D/6-311+G(d) level. The last two lines contain averaged values using the MB populations at 298.15 K.

Form	n	ΔE_{0n}	λ_{0n}	f_{0n}	q_{CT}	d_{CT}	$\Delta\mu_{0n}$
DHA(1)-MCH/CCT	1	3.23	384	1.64	0.48	1.58	3.61
	2	3.62	342	0.38	0.62	2.06	6.16
DHA(2)-MCH/CCT	1	3.23	384	1.64	0.48	1.59	3.63
	2	3.62	342	0.38	0.63	2.07	6.22
DHA(1)-MCH/TCT	1	3.25	381	1.38	0.46	1.34	2.94
	2	3.88	319	0.73	0.58	2.86	7.93
DHA(2)-MCH/TCT	1	3.25	382	1.36	0.46	1.33	2.93
	2	3.88	319	0.71	0.58	2.85	7.90
avg.	1	3.23	384	1.61	0.47	1.56	3.56
	2	3.65	340	0.41	0.62	2.14	6.35

Table D.6: Computed excitation energies (ΔE_{0n} , eV) and their associated wavelengths (λ_{0n} , nm), oscillator strengths (f_{0n}), amounts of charge transfer (q_{CT} , e), distances of charge transfer (d_{CT} , Å), and variations of dipole moment upon excitation from the GS to the n^{th} dominant lowest-energy ES ($\Delta\mu_{0n}$, D) of the main conformers of the *cis*-VHF-SP form as evaluated at the IEF-PCM(acetonitrile)/TDDFT/ ω B97X-D/6-311+G(d) level. The last two lines contain averaged values using the MB populations at 298.15 K.

Form	n	ΔE_{0n}	λ_{0n}	f_{0n}	q_{CT}	d_{CT}	$\Delta\mu_{0n}$
<i>cis</i> -VHF(1)-SP	1	2.73	454	0.73	0.46	1.54	3.41
	3	3.59	345	1.42	0.77	5.26	19.41
<i>cis</i> -VHF(2)-SP	1	2.73	454	0.69	0.47	1.55	3.45
	3	3.58	346	1.48	0.77	5.25	19.30
avg.	1	2.73	454	0.71	0.46	1.54	3.43
	3	3.58	346	1.46	0.77	5.25	19.34

Table D.7: Computed excitation energies (ΔE_{0n} , eV) and their associated wavelengths (λ_{0n} , nm), oscillator strengths (f_{0n}), amounts of charge transfer (q_{CT} , e), distances of charge transfer (d_{CT} , Å), and variations of dipole moment upon excitation from the GS to the n^{th} dominant lowest-energy ES ($\Delta\mu_{0n}$, D) of the main conformers of the *cis*-VHF-MC form as evaluated at the IEF-PCM(acetonitrile)/TDDFT/ ω B97X-D/6-311+G(d) level. The last four lines contain averaged values using the MB populations at 298.15 K.

Form	n	ΔE_{0n}	λ_{0n}	f_{0n}	q_{CT}	d_{CT}	$\Delta\mu_{0n}$
<i>cis</i> -VHF(1)-MC/TTC	1	2.69	460	2.12	0.49	0.48	1.13
	2	2.74	452	0.12	0.46	0.54	1.19
	5	3.52	335	0.89	0.56	2.31	6.21
	6	3.70	322	0.27	0.60	1.78	5.09
<i>cis</i> -VHF(2)-MC/TTC	1	2.69	461	1.50	0.49	0.48	1.13
	2	2.74	452	0.74	0.47	0.52	1.17
	5	3.70	335	0.87	0.56	2.40	6.45
	6	3.86	322	0.32	0.59	2.04	5.82
<i>cis</i> -VHF(1)-MC/TTT	1	2.56	484	1.59	0.50	0.79	1.87
	2	2.73	455	0.46	0.46	1.55	3.40
	5	3.67	338	0.77	0.56	1.70	4.53
	6	3.85	322	0.77	0.61	1.17	3.44
<i>cis</i> -VHF(2)-MC/TTT	1	2.56	484	1.45	0.50	0.79	1.87
	2	2.73	455	0.59	0.46	1.54	3.39
	5	3.67	338	0.81	0.56	1.73	4.61
	6	3.85	322	0.72	0.62	1.18	3.48
avg.	1	2.66	467	1.64	0.49	0.56	1.32
	2	2.74	453	0.55	0.46	0.78	1.74
	5	3.65	336	0.86	0.56	2.20	5.92
	6	3.82	322	0.41	0.60	1.76	5.06

Table D.8: Computed excitation energies (ΔE_{0n} , eV) and their associated wavelengths (λ_{0n} , nm), oscillator strengths (f_{0n}), amounts of charge transfer (q_{CT} , e), distances of charge transfer (d_{CT} , Å), and variations of dipole moment upon excitation from the GS to the n^{th} dominant lowest-energy ES ($\Delta\mu_{0n}$, D) of the main conformers of the *cis*-VHF-E-MCH form as evaluated at the IEF-PCM(acetonitrile)/TDDFT/ ω B97X-D/6-311+G(d) level. The last three lines contain averaged values using the MB populations at 298.15 K.

Form	n	ΔE_{0n}	λ_{0n}	f_{0n}	q_{CT}	d_{CT}	$\Delta\mu_{0n}$
<i>cis</i> -VHF(1)-MCH/TTC	1	2.72	456	0.78	0.46	1.59	3.47
	3	3.24	382	1.82	0.57	1.54	4.22
	4	3.91	317	0.45	0.63	3.88	11.76
<i>cis</i> -VHF(2)-MCH/TTC	1	2.72	456	0.71	0.46	1.57	3.46
	3	3.24	382	1.94	0.57	1.43	3.92
	4	3.91	317	0.41	0.63	3.83	11.62
<i>cis</i> -VHF(1)-MCH/TTT	1	2.72	456	0.78	0.46	1.61	3.54
	3	3.22	384	1.76	0.57	1.07	2.96
	4	3.88	319	0.53	0.62	3.33	9.84
<i>cis</i> -VHF(2)-MCH/TTT	1	2.72	456	0.72	0.46	1.56	3.43
	3	3.18	390	1.78	0.57	1.20	3.29
	4	3.88	319	0.50	0.62	3.08	9.10
avg.	1	2.72	456	0.74	0.46	1.58	3.46
	3	3.21	386	1.82	0.57	1.33	3.65
	4	3.89	318	0.47	0.62	3.48	10.44

Table D.9: Computed excitation energies (ΔE_{0n} , eV) and their associated wavelengths (λ_{0n} , nm), oscillator strengths (f_{0n}), amounts of charge transfer (q_{CT} , e), distances of charge transfer (d_{CT} , Å), and variations of dipole moment upon excitation from the GS to the n^{th} dominant lowest-energy ES ($\Delta\mu_{0n}$, D) of the main conformers of the *cis*-VHF-Z-MCH form as evaluated at the IEF-PCM(acetonitrile)/TDDFT/ ω B97X-D/6-311+G(d) level. The last two lines contain averaged values using the MB populations at 298.15 K.

Form	n	ΔE_{0n}	λ_{0n}	f_{0n}	q_{CT}	d_{CT}	$\Delta\mu_{0n}$
<i>cis</i> -VHF(1)-MCH/CCT	1	2.72	456	0.71	0.46	1.55	3.40
	3	3.54	350	1.39	0.64	1.18	3.62
<i>cis</i> -VHF(2)-MCH/CCT	1	2.72	456	0.69	0.45	1.51	3.28
	3	3.55	349	1.44	0.64	1.33	4.05
<i>cis</i> -VHF(1)-MCH/TCT	1	2.72	456	0.70	0.46	1.52	3.35
	3	3.74	331	1.56	0.61	0.51	1.51
<i>cis</i> -VHF(2)-MCH/TCT	1	2.71	456	0.67	0.46	1.54	3.40
	3	3.74	331	1.63	0.61	0.83	2.44
avg.	1	2.72	456	0.70	0.46	1.53	3.34
	3	3.57	347	1.44	0.63	1.18	3.60

Table D.10: Computed excitation energies (ΔE_{0n} , eV) and their associated wavelengths (λ_{0n} , nm), oscillator strengths (f_{0n}), amounts of charge transfer (q_{CT} , e), distances of charge transfer (d_{CT} , Å), and variations of dipole moment upon excitation from the GS to the n^{th} dominant lowest-energy ES ($\Delta\mu_{0n}$, D) of the main conformers of the *trans*-VHF-SP form as evaluated at the IEF-PCM(acetonitrile)/TDDFT/ ω B97X-D/6-311+G(d) level. The last four lines contain averaged values using the MB populations at 298.15 K.

Form	n	ΔE_{0n}	λ_{0n}	f_{0n}	q_{CT}	d_{CT}	$\Delta\mu_{0n}$
<i>trans</i> -VHF(1)-SP	1	2.79	444	0.87	0.45	1.23	2.63
	3	3.55	349	0.93	0.87	4.40	18.39
	4	4.06	305	0.34	0.67	2.56	8.23
	6	4.25	291	0.70	0.58	3.46	9.64
<i>trans</i> -VHF(2)-SP	1	2.79	444	0.84	0.44	1.22	2.59
	3	3.55	349	0.98	0.87	4.37	18.24
	4	4.06	305	0.34	0.68	2.75	8.96
	6	4.09	291	0.68	0.58	3.48	9.71
avg.	1	2.79	444	0.85	0.44	1.22	2.61
	3	3.55	349	0.96	0.87	4.38	18.31
	4	4.06	305	0.34	0.67	2.66	8.62
	6	4.16	291	0.69	0.58	3.47	9.68

Table D.11: Computed excitation energies (ΔE_{0n} , eV) and their associated wavelengths (λ_{0n} , nm), oscillator strengths (f_{0n}), amounts of charge transfer (q_{CT} , e), distances of charge transfer (d_{CT} , Å), and variations of dipole moment upon excitation from the GS to the n^{th} dominant lowest-energy ES ($\Delta\mu_{0n}$, D) of the main conformers of the *trans*-VHF-MC form as evaluated at the IEF-PCM(acetonitrile)/TDDFT/ ω B97X-D/6-311+G(d) level. The last three lines contain averaged values using the MB populations at 298.15 K.

Form	n	ΔE_{0n}	λ_{0n}	f_{0n}	q_{CT}	d_{CT}	$\Delta\mu_{0n}$
<i>trans</i> -VHF(1)-MC/TTC	1	2.71	457	1.57	0.51	1.15	2.80
	2	2.79	444	0.84	0.44	1.16	2.46
	5	3.69	336	0.69	0.64	2.57	7.86
<i>trans</i> -VHF(2)-MC/TTC	1	2.71	457	1.35	0.51	1.16	2.83
	2	2.79	444	1.06	0.44	1.14	2.42
	5	3.69	336	0.68	0.64	2.68	8.21
<i>trans</i> -VHF(1)-MC/TTT	1	2.56	484	1.36	0.50	0.80	1.90
	2	2.79	444	0.86	0.44	1.23	2.60
	5	3.66	338	0.61	0.62	2.14	6.40
<i>trans</i> -VHF(2)-MC/TTT	1	2.56	484	1.30	0.49	0.79	1.87
	2	2.79	444	0.91	0.44	1.20	2.55
	5	3.66	338	0.64	0.62	2.05	6.10
avg.	1	2.68	463	1.45	0.50	1.07	2.60
	2	2.79	444	0.92	0.44	1.17	2.47
	5	3.68	336	0.67	0.63	2.50	7.61

Table D.12: Computed excitation energies (ΔE_{0n} , eV) and their associated wavelengths (λ_{0n} , nm), oscillator strengths (f_{0n}), amounts of charge transfer (q_{CT} , e), distances of charge transfer (d_{CT} , Å), and variations of dipole moment upon excitation from the GS to the n^{th} dominant lowest-energy ES ($\Delta\mu_{0n}$, D) of the main conformers of the *trans*-VHF-E-MCH form as evaluated at the IEF-PCM(acetonitrile)/TDDFT/ ω B97X-D/6-311+G(d) level. The last three lines contain averaged values using the MB populations at 298.15 K.

Form	n	ΔE_{0n}	λ_{0n}	f_{0n}	q_{CT}	d_{CT}	$\Delta\mu_{0n}$
<i>trans</i> -VHF(1)-MCH/TTC	1	2.79	445	0.90	0.44	1.22	2.58
	3	3.25	382	1.80	0.57	1.49	4.11
<i>trans</i> -VHF(2)-MCH/TTC	1	2.79	445	0.85	0.44	1.21	2.58
	3	3.28	378	1.94	0.57	1.41	3.89
<i>trans</i> -VHF(1)-MCH/TTT	1	2.79	445	0.89	0.44	1.23	2.60
	3	3.22	385	1.70	0.58	1.13	3.12
<i>trans</i> -VHF(2)-MCH/TTT	1	2.79	444	0.85	0.44	1.22	2.58
	3	3.22	384	1.79	0.58	1.14	3.16
avg.	1	2.79	445	0.87	0.44	1.22	2.59
	3	3.25	382	1.82	0.57	1.34	3.70

Table D.13: Computed excitation energies (ΔE_{0n} , eV) and their associated wavelengths (λ_{0n} , nm), oscillator strengths (f_{0n}), amounts of charge transfer (q_{CT} , e), distances of charge transfer (d_{CT} , Å), and variations of dipole moment upon excitation from the GS to the n^{th} dominant lowest-energy ES ($\Delta\mu_{0n}$, D) of the main conformers of the *trans*-VHF-Z-MCH form as evaluated at the IEF-PCM(acetonitrile)/TDDFT/ ω B97X-D/6-311+G(d) level. The last three lines contain averaged values using the MB populations at 298.15 K.

Form	n	ΔE_{0n}	λ_{0n}	f_{0n}	q_{CT}	d_{CT}	$\Delta\mu_{0n}$
<i>trans</i> -VHF(1)-MCH/CCT	1	2.79	445	0.89	0.44	1.20	2.54
	3	3.54	350	1.25	0.65	1.37	4.27
<i>trans</i> -VHF(2)-MCH/CCT	1	2.79	444	0.86	0.44	1.21	2.57
	3	3.55	349	1.32	0.65	1.34	4.15
<i>trans</i> -VHF(1)-MCH/TCT	1	2.79	444	0.88	0.44	1.22	2.59
	3	3.74	332	1.22	0.66	0.90	2.87
<i>trans</i> -VHF(2)-MCH/TCT	1	2.79	445	0.86	0.44	1.21	2.55
	3	3.74	331	1.27	0.66	1.16	3.68
avg.	1	2.79	445	0.88	0.44	1.20	2.55
	3	3.58	347	1.27	0.65	1.30	4.05

Table D.14: Computed excitation energies (ΔE_{0n} , eV) and their associated wavelengths (λ_{0n} , nm), oscillator strengths (f_{0n}), amounts of charge transfer (q_{CT} , e), distances of charge transfer (d_{CT} , Å), and variations of dipole moment upon excitation from the GS to the n^{th} dominant lowest-energy ES ($\Delta\mu_{0n}$, D) of the individual constitutive units of the molecular switch[†] as evaluated at the IEF-PCM(acetonitrile)/TDDFT/ ω B97X-D/6-311+G(d) level.

Form	n	ΔE_{0n}	λ_{0n}	f_{0n}	q_{CT}	d_{CT}	$\Delta\mu_{0n}$
DHA	1	3.34	371	0.69	0.44	0.97	2.05
	2	4.51	275	0.68	0.42	0.68	1.37
<i>cis</i> -VHF	1	2.73	455	0.62	0.45	1.45	3.16
	3	4.15	298	0.61	0.70	3.54	11.91
<i>trans</i> -VHF	1	2.80	444	0.91	0.44	1.16	2.42
	3	4.05	306	0.25	0.84	2.72	11.01
SP	1	4.07	305	0.28	0.68	2.76	8.99
	4	4.62	268	0.16	0.77	3.83	14.07
	6	4.71	263	0.38	0.47	0.73	1.64
	7	4.75	261	0.36	0.66	3.38	10.66
	8	4.75	257	0.36	0.48	0.84	1.93
MC	1	2.75	451	1.21	0.50	1.32	3.20
	3	3.82	325	0.18	0.50	2.63	6.32
	4	4.04	306	0.47	0.49	0.20	0.47
E-MCH	1	3.38	367	1.29	0.56	0.36	0.97
	4	4.49	276	0.22	0.63	3.16	9.65

[†] Averaged values calculated using the MB populations at 298.15 K.

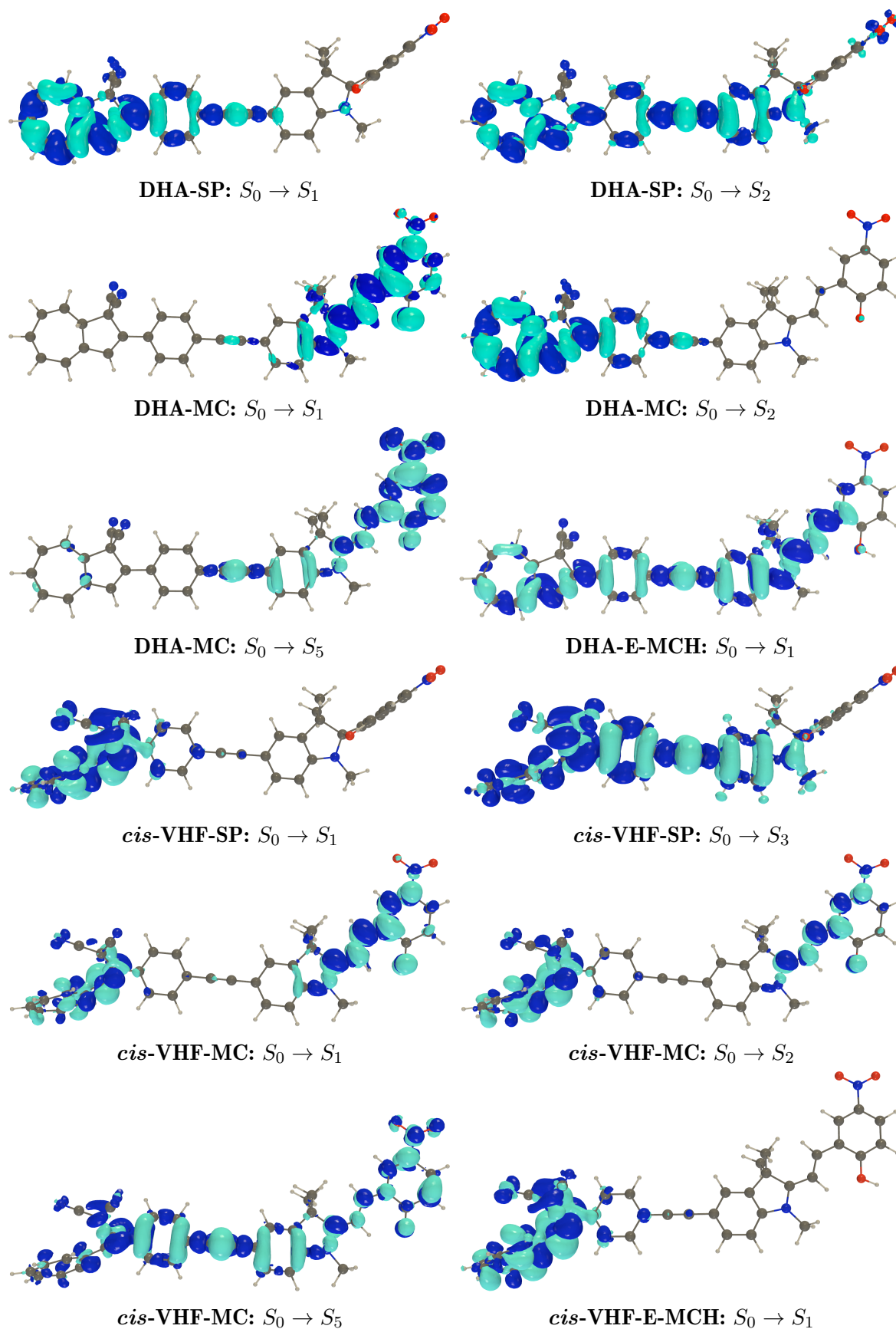
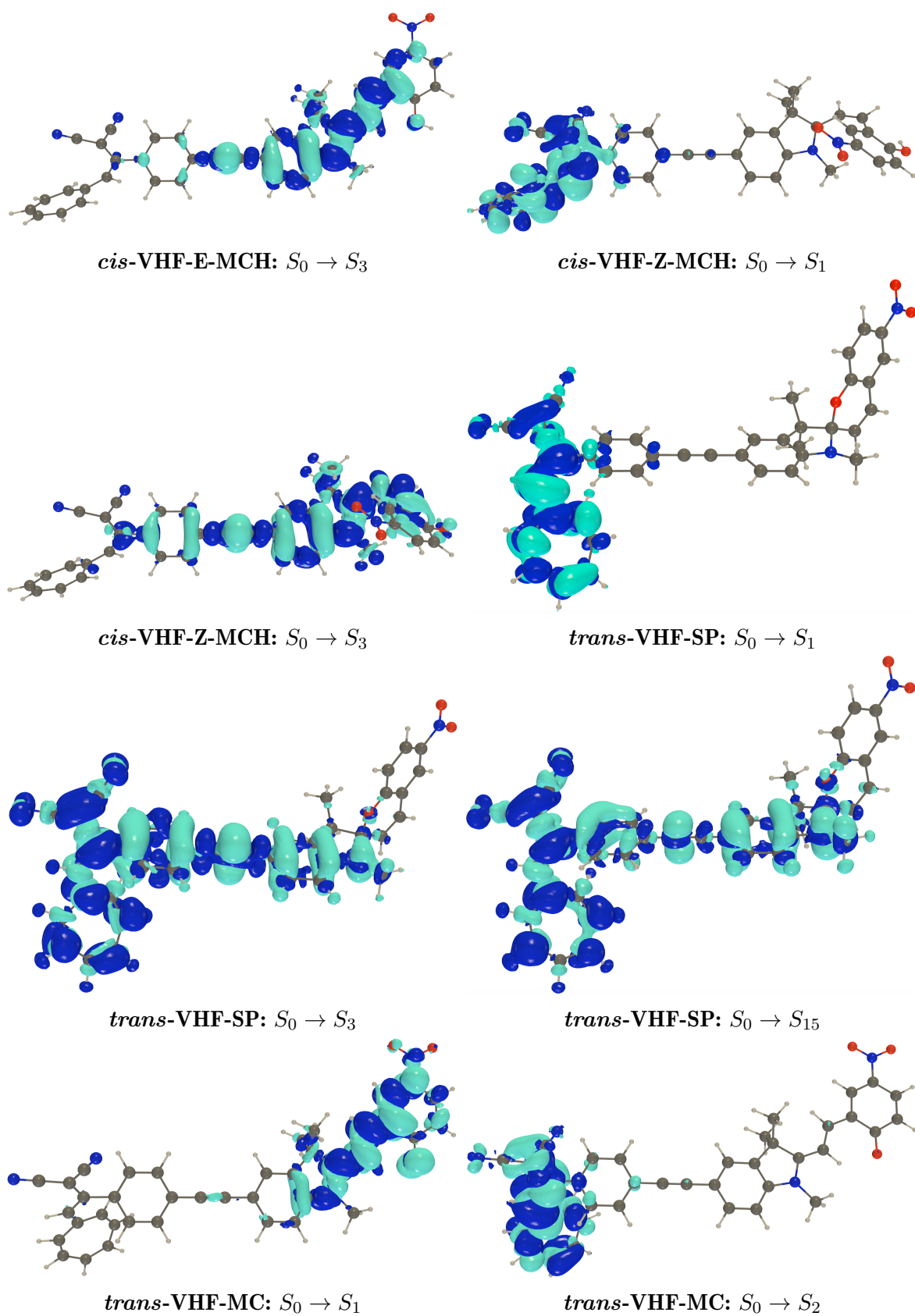


Fig. D.1: Variation of electron density ($\Delta\rho$) upon excitation from GS to the n^{th} ES for each state of the molecular switch in their most stable conformations as evaluated at the IEF-PCM(acetonitrile)/TDDFT/ ω B97X-D/6-311+G(d) level; light and dark blue correspond to negative and positive $\Delta\rho$, respectively (isovalue = 0.0008 a.u.).

**Fig. D.1:** Continued from previous page.

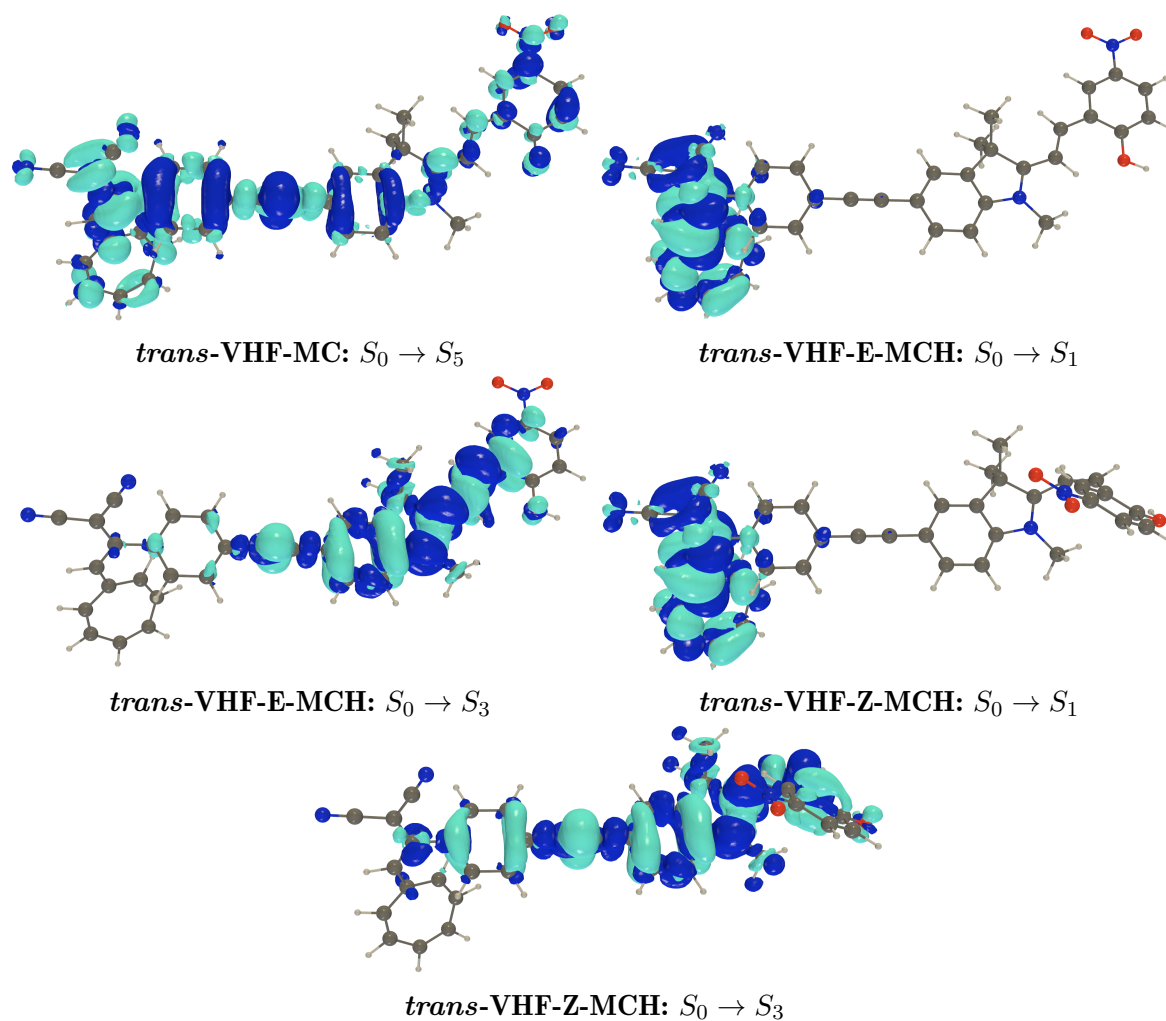


Fig. D.1: Continued from previous pages.

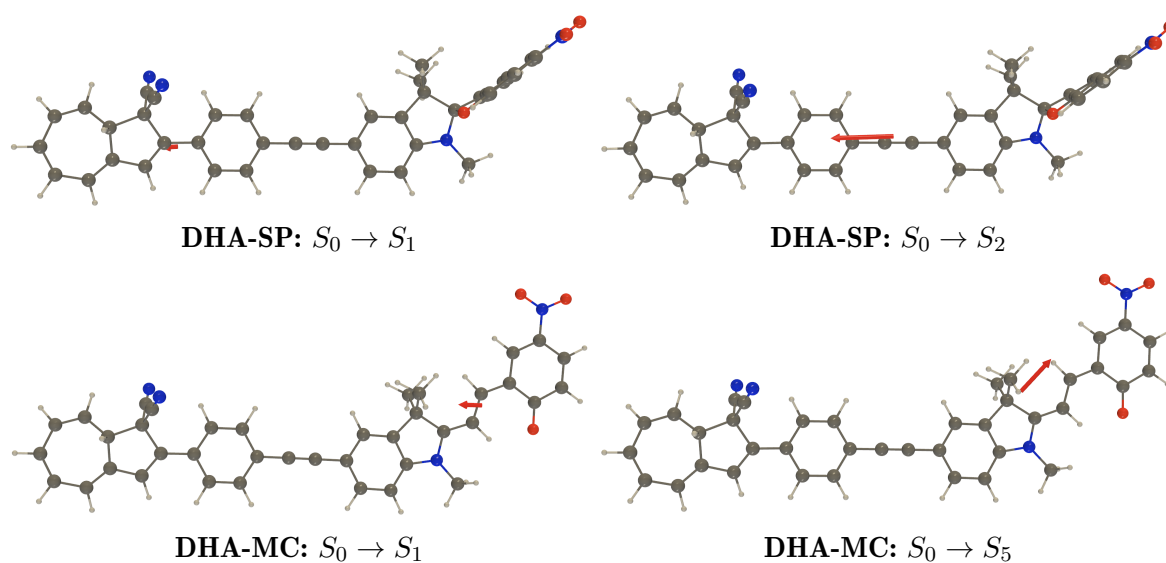
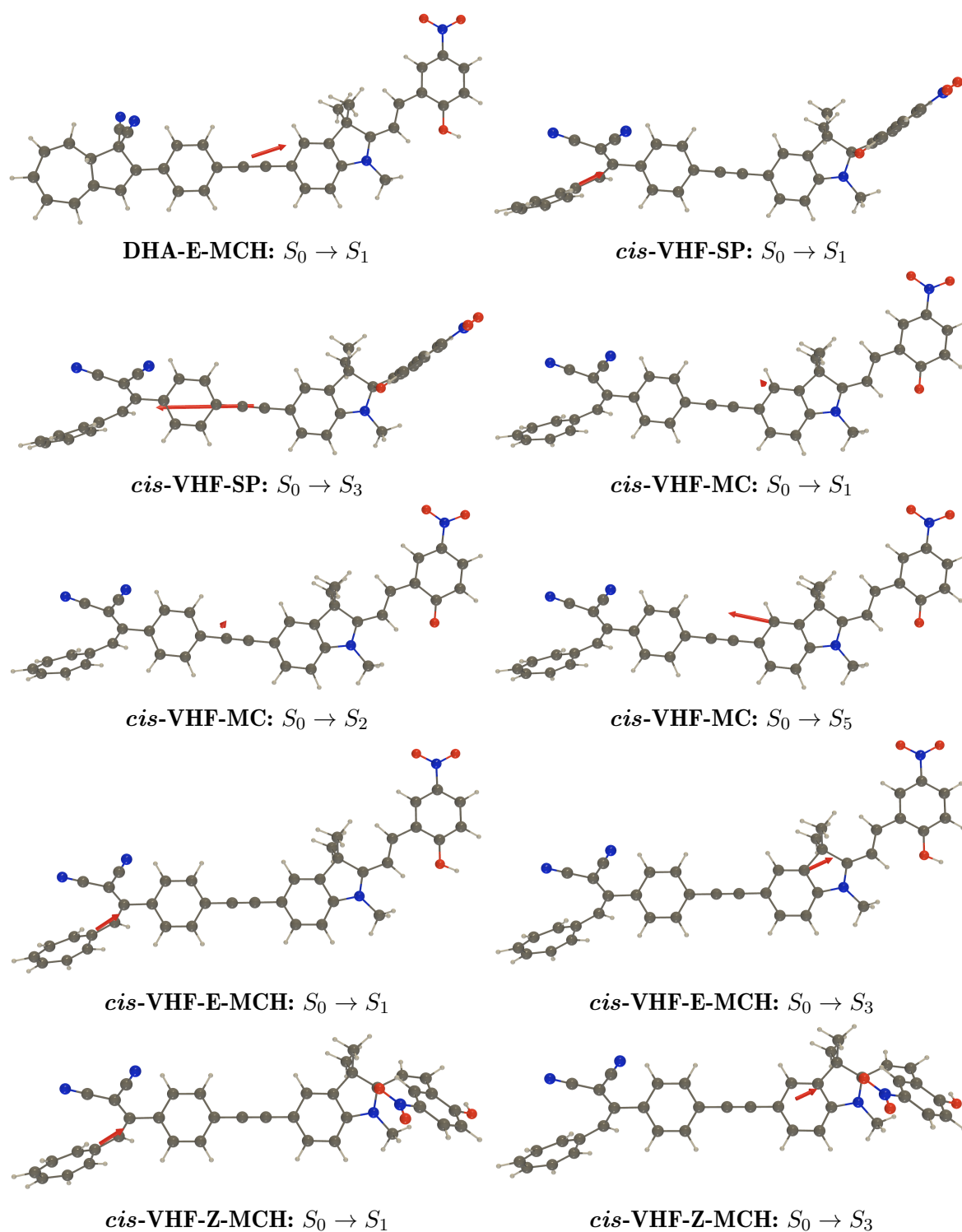


Fig. D.2: CT vector upon excitation from GS to the n^{th} ES for each state of the molecular switch in their most stable conformations as evaluated at the IEF-PCM(acetonitrile)/TDDFT/ ω B97X-D/6-311+G(d) level. Note that the CT vector for the $S_0 \rightarrow S_2$ in DHA-MC is too small, and therefore is not represented.

**Fig. D.2:** Continued from previous page.

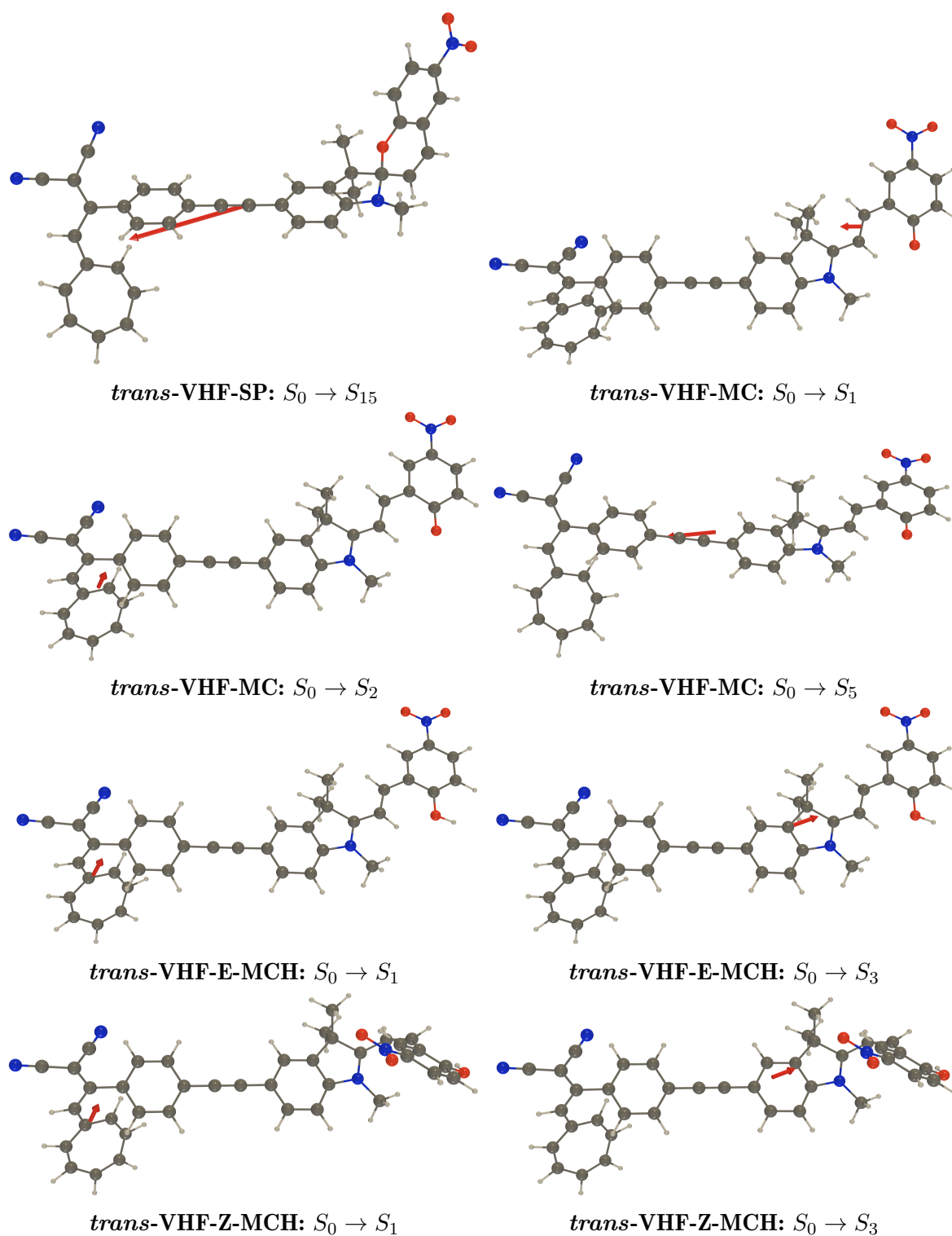


Fig. D.2: Continued from previous pages.

Appendix E

Supporting information to Section 5.4

E.1 HRS quantities

Table E.1: Static and dynamic ($\lambda = 1907, 1500$ and 1064 nm) β_{HRS} values (10^3 a.u.), depolarization ratios, and nonlinear anisotropy factors of the four stereoisomers of the DHA-SP form as evaluated at the the IEF-PCM(acetonitrile)/(CPKS) TDDFT/ ω B97X-D/6-311+G(d).

λ (nm)	β_{HRS}				DR				ρ			
	∞	1907	1500	1064	∞	1907	1500	1064	∞	1907	1500	1064
(S)-DHA-(R)-SP	7.2	7.0	8.1	13.3	3.93	4.13	4.18	4.36	1.10	1.04	1.02	0.99
(R)-DHA-(S)-SP	7.2	7.0	8.1	13.3	3.93	4.13	4.18	4.36	1.10	1.04	1.02	0.97
(R)-DHA-(R)-SP	7.3	6.9	8.1	13.3	3.92	4.12	4.18	4.35	1.10	1.04	1.02	0.98
(S)-DHA-(S)-SP	7.3	7.0	8.1	13.3	3.92	4.12	4.18	4.35	1.10	1.04	1.02	0.98

Table E.2: Static and dynamic ($\lambda = 1907, 1500$ and 1064 nm) β_{HRS} values (10^3 a.u.), depolarization ratios of selected forms of the molecular switch in their most stable conformations as evaluated at the IEF-PCM(acetonitrile)/(CPKS) TDDFT/ ω B97X-D level using the 6-311G(d), 6-311+G(d) and 6-311++G(d) basis sets.

		β_{HRS}				DR			
λ (nm)		∞	1907	1500	1064	∞	1907	1500	1064
DHA-SP	6-311G(d)	7.0	6.7	7.8	12.6	4.03	4.22	4.28	4.45
	6-311+G(d)	7.2	7.0	8.1	13.3	3.93	4.13	4.18	4.36
	6-311++G(d)	7.3	7.0	8.1	13.3	3.93	4.13	4.18	4.36
<i>cis</i> -VHF-SP	6-311G(d)	8.8	8.2	9.5	15.2	2.88	3.28	3.24	2.87
	6-311+G(d)	9.4	8.6	10.0	16.4	2.81	3.22	3.17	2.80
	6-311++G(d)	9.4	8.6	10.0	16.4	2.81	3.22	3.17	2.80
DHA-MC	6-311G(d)	7.3	5.8	7.1	17.4	2.90	3.26	3.38	3.67
	6-311+G(d)	7.9	6.0	7.2	17.2	2.72	3.02	3.12	3.31
	6-311++G(d)	7.9	6.0	7.2	17.2	2.72	3.02	3.12	3.31

Table E.3: Static and dynamic ($\lambda = 1907, 1500$ and 1064 nm) β_{HRS} values (10^3 a.u.), depolarization ratios, and nonlinear anisotropy factors of the main conformers of the DHA-SP form as evaluated at the IEF-PCM(acetonitrile)/(CPKS) TDDFT/ ω B97X-D/6-311+G(d) level. The last line contains average values obtained using the MB populations at 298.15 K.

β_{HRS}					DR				ρ			
λ (nm)	∞	1907	1500	1064	∞	1907	1500	1064	∞	1907	1500	1064
DHA(1)-SP	7.2	7.0	8.1	13.3	3.93	4.13	4.18	4.37	1.10	1.04	1.03	0.99
DHA(2)-SP	7.3	7.0	8.1	13.3	3.94	4.13	4.18	4.35	1.10	1.04	1.02	0.98
avg.	7.2	7.0	8.1	13.3	3.93	4.13	4.18	4.36	1.10	1.04	1.03	0.99

Table E.4: Static and dynamic ($\lambda = 1907, 1500$ and 1064 nm) β_{HRS} values (10^3 a.u.), depolarization ratios, and nonlinear anisotropy factors of the main conformers of the DHA-MC form as evaluated at the IEF-PCM(acetonitrile)/(CPKS) TDDFT/ ω B97X-D/6-311+G(d) level. The last line contains average values obtained using the MB populations at 298.15 K.

β_{HRS}					DR				ρ			
λ (nm)	∞	1907	1500	1064	∞	1907	1500	1064	∞	1907	1500	1064
DHA(1)-MC/TTC	7.9	6.0	7.2	17.2	2.72	3.02	3.12	3.31	1.73	1.52	1.46	1.35
DHA(2)-MC/TTC	7.8	5.9	7.2	17.0	2.78	3.07	3.17	3.35	1.68	1.48	1.43	1.33
DHA(1)-MC/TTT	4.6	3.3	4.1	14.4	2.18	2.62	2.71	2.74	2.42	1.82	1.74	1.71
DHA(2)-MC/TTT	4.4	3.2	3.9	14.0	2.22	2.67	2.76	2.74	2.34	1.77	1.70	1.71
avg.	7.0	5.3	6.4	16.4	2.61	2.94	3.04	3.18	1.87	1.57	1.51	1.43

Table E.5: Static and dynamic ($\lambda = 1907, 1500$ and 1064 nm) β_{HRS} values (10^3 a.u.), depolarization ratios, and nonlinear anisotropy factors of the main conformers of the DHA-E-MCH form as evaluated at the IEF-PCM(acetonitrile)/(CPKS) TDDFT/ ω B97X-D/6-311+G(d) level. The last line contains average values obtained using the MB populations at 298.15 K.

λ (nm)	β_{HRS}				DR				ρ			
	∞	1907	1500	1064	∞	1907	1500	1064	∞	1907	1500	1064
DHA(1)-MCH/TTC	2.5	3.0	4.1	10.3	5.60	5.70	5.59	5.29	0.70	0.68	0.70	0.75
DHA(2)-MCH/TTC	2.4	2.9	4.0	10.1	5.28	5.54	5.47	5.24	0.76	0.71	0.72	0.77
DHA(1)-MCH/TTT	2.8	3.4	4.6	11.4	5.20	5.19	5.18	5.07	0.77	0.78	0.78	0.80
DHA(2)-MCH/TTT	2.8	3.4	4.6	11.5	5.17	5.17	5.15	5.05	0.78	0.78	0.78	0.80
avg.	2.7	3.2	4.4	10.9	5.29	5.36	5.31	5.14	0.76	0.75	0.75	0.78

Table E.6: Static and dynamic ($\lambda = 1907, 1500$ and 1064 nm) β_{HRS} values (10^3 a.u.), depolarization ratios, and nonlinear anisotropy factors of the main conformers of the DHA-Z-MCH form as evaluated at the IEF-PCM(acetonitrile)/(CPKS) TDDFT/ ω B97X-D/6-311+G(d) level. The last line contains average values obtained using the MB populations at 298.15 K.

λ (nm)	β_{HRS}				DR				ρ			
	∞	1907	1500	1064	∞	1907	1500	1064	∞	1907	1500	1064
DHA(1)-MCH/CCT	3.3	3.4	4.3	8.2	3.52	3.98	4.09	4.38	1.26	1.09	1.05	0.97
DHA(2)-MCH/CCT	3.4	3.5	4.3	8.3	3.49	3.97	4.08	4.38	1.27	1.09	1.05	0.97
DHA(1)-MCH/TCT	2.9	2.9	3.4	6.2	3.69	4.19	4.29	4.54	1.19	1.02	0.99	0.92
DHA(2)-MCH/TCT	2.9	2.9	3.4	6.2	3.70	4.17	4.27	4.52	1.19	1.03	1.00	0.93
avg.	3.3	3.4	4.2	8.1	3.52	4.00	4.10	4.39	1.26	1.08	1.04	0.97

Table E.7: Static and dynamic ($\lambda = 1907, 1500$ and 1064 nm) β_{HRS} values (10^3 a.u.), depolarization ratios, and nonlinear anisotropy factors of the main conformers of the *cis*-VHF-SP form as evaluated at the IEF-PCM(acetonitrile)/(CPKS) TDDFT/ ω B97X-D/6-311+G(d) level. The last line contains average values obtained using the MB populations at 298.15 K.

λ (nm)	β_{HRS}				DR				ρ			
	∞	1907	1500	1064	∞	1907	1500	1064	∞	1907	1500	1064
<i>cis</i> -VHF-SP	9.4	8.6	10.0	16.4	2.81	3.22	3.17	2.80	1.66	1.40	1.43	1.66
<i>cis</i> -VHF-SP	9.0	8.6	10.0	16.3	2.57	3.10	3.02	2.58	1.87	1.47	1.51	1.86
avg.	9.2	8.6	10.0	16.3	2.67	3.15	3.08	2.67	1.79	1.44	1.48	1.78

Table E.8: Static and dynamic ($\lambda = 1907, 1500$ and 1064 nm) β_{HRS} values (10^3 a.u.), depolarization ratios, and nonlinear anisotropy factors of the main conformers of the *cis*-VHF-MC form as evaluated at the IEF-PCM(acetonitrile)/(CPKS) TDDFT/ ω B97X-D/6-311+G(d) level. The last line contains average values obtained using the MB populations at 298.15 K.

λ (nm)	β_{HRS}				DR				ρ			
	∞	1907	1500	1064	∞	1907	1500	1064	∞	1907	1500	1064
<i>cis</i> -VHF(1)-MC/TTC	10.5	8.7	10.5	23.4	2.72	2.99	3.04	2.99	1.73	1.53	1.50	1.54
<i>cis</i> -VHF(2)-MC/TTC	10.4	8.7	10.6	24.2	2.20	2.61	2.61	2.50	2.38	1.83	1.83	1.95
<i>cis</i> -VHF(1)-MC/TTT	5.7	5.0	5.9	15.1	2.20	2.83	2.83	2.79	2.38	1.65	1.65	1.68
<i>cis</i> -VHF(2)-MC/TTT	7.4	6.2	7.6	22.2	2.53	2.96	3.05	3.46	1.92	1.55	1.50	1.28
avg.	9.5	8.0	9.7	22.9	2.37	2.77	2.80	2.80	2.16	1.70	1.68	1.72

Table E.9: Static and dynamic ($\lambda = 1907, 1500$ and 1064 nm) β_{HRS} values (10^3 a.u.), depolarization ratios, and nonlinear anisotropy factors of the main conformers of the *cis*-VHF-E-MCH form as evaluated at the IEF-PCM(acetonitrile)/(CPKS) TDDFT/ ω B97X-D/6-311+G(d) level. The last line contains average values obtained using the MB populations at 298.15 K.

λ (nm)	β_{HRS}				DR				ρ			
	∞	1907	1500	1064	∞	1907	1500	1064	∞	1907	1500	1064
<i>cis</i> -VHF(1)-MCH/TTC	4.2	3.2	4.1	12.4	3.18	3.26	3.52	4.48	1.42	1.38	1.26	0.94
<i>cis</i> -VHF(2)-MCH/TTC	3.6	2.4	3.0	9.1	1.93	1.90	2.10	3.79	3.10	3.22	2.60	1.15
<i>cis</i> -VHF(1)-MCH/TTT	3.3	2.3	3.2	11.0	2.48	2.66	3.11	4.47	1.97	1.78	1.46	0.94
<i>cis</i> -VHF(2)-MCH/TTT	3.7	2.4	3.1	9.9	2.83	2.96	3.41	5.09	1.64	1.56	1.30	0.80
avg.	3.8	2.6	3.4	10.6	2.71	2.80	3.15	4.59	1.90	1.86	1.57	0.92

Table E.10: Static and dynamic ($\lambda = 1907, 1500$ and 1064 nm) β_{HRS} values (10^3 a.u.), depolarization ratios, and nonlinear anisotropy factors of the main conformers of the *cis*-VHF-Z-MCH form as evaluated at the IEF-PCM(acetonitrile)/(CPKS) TDDFT/ ω B97X-D/6-311+G(d) level. The last line contains average values obtained using the MB populations at 298.15 K.

λ (nm)	β_{HRS}				DR				ρ			
	∞	1907	1500	1064	∞	1907	1500	1064	∞	1907	1500	1064
<i>cis</i> -VHF(1)-MCH/CCT	4.2	3.1	4.0	11.3	3.14	3.21	3.40	4.18	1.44	1.40	1.31	1.02
<i>cis</i> -VHF(2)-MCH/CCT	2.8	1.9	2.6	8.7	2.78	3.06	3.44	4.55	1.68	1.49	1.29	0.92
<i>cis</i> -VHF(1)-MCH/TCT	4.0	2.9	3.7	10.5	2.65	2.75	2.96	3.85	1.80	1.70	1.56	1.13
<i>cis</i> -VHF(2)-MCH/TCT	3.5	2.2	2.9	8.9	3.02	2.94	3.20	4.20	1.52	1.57	1.41	1.02
avg.	3.5	2.5	3.3	10.0	2.94	3.10	3.38	4.32	1.58	1.47	1.32	0.98

Table E.11: Static and dynamic ($\lambda = 1907, 1500$ and 1064 nm) β_{HRS} values (10^3 a.u.), depolarization ratios, and nonlinear anisotropy factors of the main conformers of the *trans*-VHF-SP form as evaluated at the IEF-PCM(acetonitrile)/(CPKS) TDDFT/ ω B97X-D/6-311+G(d) level. The last line contains average values obtained using the MB populations at 298.15 K.

λ (nm)	β_{HRS}				DR				ρ			
	∞	1907	1500	1064	∞	1907	1500	1064	∞	1907	1500	1064
<i>trans</i> -VHF-SP	7.0	6.0	7.1	12.2	2.36	1.71	2.72	2.55	2.12	1.71	1.73	1.89
<i>trans</i> -VHF-SP	6.5	5.7	6.6	11.1	2.06	2.55	2.50	2.20	2.68	1.89	1.94	2.38
avg.	6.7	5.8	6.8	11.6	2.20	2.16	2.60	2.36	2.42	1.81	1.84	2.16

Table E.12: Static and dynamic ($\lambda = 1907, 1500$ and 1064 nm) β_{HRS} values (10^3 a.u.), depolarization ratios, and nonlinear anisotropy factors of the main conformers of the *trans*-VHF-MC form as evaluated at the IEF-PCM(acetonitrile)/(CPKS) TDDFT/ ω B97X-D/6-311+G(d) level. The last line contains average values obtained using the MB populations at 298.15 K.

λ (nm)	β_{HRS}				DR				ρ			
	∞	1907	1500	1064	∞	1907	1500	1064	∞	1907	1500	1064
<i>trans</i> -VHF(1)-MC/TTC	9.1	7.0	8.5	20.2	2.34	2.58	2.64	2.76	2.15	1.86	1.80	1.70
<i>trans</i> -VHF(2)-MC/TTC	8.5	6.7	8.1	19.3	2.10	2.43	2.48	2.64	2.58	2.03	1.97	1.81
<i>trans</i> -VHF(1)-MC/TTT	5.6	4.2	5.2	16.4	1.71	1.98	2.00	2.22	4.49	2.93	2.86	2.34
<i>trans</i> -VHF(2)-MC/TTT	5.4	4.0	5.0	15.9	2.22	2.55	2.72	3.33	2.34	1.89	1.73	1.34
avg.	8.1	6.2	7.6	19.0	2.17	2.45	2.52	2.71	2.60	2.05	1.98	1.78

Table E.13: Static and dynamic ($\lambda = 1907, 1500$ and 1064 nm) β_{HRS} values (10^3 a.u.), depolarization ratios, and nonlinear anisotropy factors of the main conformers of the *trans*-VHF-E-MCH form as evaluated at the IEF-PCM(acetonitrile)/(CPKS) TDDFT/ ω B97X-D/6-311+G(d) level. The last line contains average values obtained using the MB populations at 298.15 K.

λ (nm)	β_{HRS}				DR				ρ			
	∞	1907	1500	1064	∞	1907	1500	1064	∞	1907	1500	1064
<i>trans</i> -VHF(1)-MCH/TTC	3.5	2.4	3.0	7.9	2.86	3.88	4.47	5.62	1.62	1.12	0.94	0.69
<i>trans</i> -VHF(2)-MCH/TTC	3.1	2.0	2.5	6.7	2.09	2.42	2.74	3.60	2.62	2.05	1.71	1.22
<i>trans</i> -VHF(1)-MCH/TTT	3.4	2.2	2.9	7.6	2.47	3.20	3.75	4.94	1.98	1.40	1.17	0.83
<i>trans</i> -VHF(2)-MCH/TTT	3.3	2.1	2.7	7.1	3.09	3.99	4.45	5.05	1.47	1.08	0.95	0.80
avg.	3.3	2.2	2.8	7.3	2.58	3.31	3.79	4.77	1.98	1.46	1.23	0.90

Table E.14: Static and dynamic ($\lambda = 1907, 1500$ and 1064 nm) β_{HRS} values (10^3 a.u.), depolarization ratios, and nonlinear anisotropy factors of the main conformers of the *trans*-VHF-Z-MCH form as evaluated at the IEF-PCM(acetonitrile)/(CPKS) TDDFT/ ω B97X-D/6-311+G(d) level. The last line contains average values obtained using the MB populations at 298.15 K.

λ (nm)	β_{HRS}				DR				ρ			
	∞	1907	1500	1064	∞	1907	1500	1064	∞	1907	1500	1064
<i>trans</i> -VHF(1)-MCH/CCT	3.4	2.4	3.1	7.4	3.98	5.07	5.32	5.23	1.08	0.80	0.75	0.77
<i>trans</i> -VHF(2)-MCH/CCT	3.3	2.2	2.8	6.6	2.46	2.94	3.10	3.47	2.00	1.56	1.46	1.28
<i>trans</i> -VHF(1)-MCH/TCT	3.4	2.3	2.8	6.9	3.07	3.93	4.17	4.32	1.49	1.10	1.03	0.98
<i>trans</i> -VHF(2)-MCH/TCT	3.5	2.2	2.7	6.4	2.66	2.92	3.03	3.28	1.79	1.58	1.51	1.37
avg.	3.4	2.3	2.9	7.0	3.31	4.12	4.33	4.44	1.47	1.13	1.06	1.00

Table E.15: Static and dynamic ($\lambda = 1907, 1500$ and 1064 nm) β_{HRS} values (10^3 a.u.), depolarization ratios, and nonlinear anisotropy factors of the constitutive units[†] as evaluated at the IEF-PCM(acetonitrile)/(CPKS) TDDFT/ ω B97X-D/6-311+G(d) level. The last line contains average values obtained using the MB populations at 298.15 K

λ (nm)	β_{HRS}				DR				ρ			
	∞	1907	1500	1064	∞	1907	1500	1064	∞	1907	1500	1064
DHA	0.2	0.1	0.2	0.5	2.04	2.95	3.38	4.28	2.74	1.56	1.32	1.00
cis-VHF	3.3	2.2	2.8	7.9	2.70	2.72	2.92	3.83	1.75	1.73	1.58	1.14
trans-VHF	2.9	1.7	2.2	5.9	2.35	2.61	2.81	3.29	2.14	1.83	1.66	1.36
SP	1.8	1.4	1.5	1.9	2.69	2.87	2.93	3.12	1.76	1.61	1.57	1.46
MC	6.8	4.4	5.4	12.3	2.45	2.57	2.66	2.90	2.02	1.87	1.79	1.59
E-MCH	1.6	1.2	1.2	1.5	2.52	2.61	2.63	2.70	1.94	1.83	1.82	1.76
Z-MCH	1.0	0.7	0.8	1.1	2.15	2.12	2.13	2.19	2.76	2.86	2.82	2.65

[†] Averaged values calculated using the MB populations at 298.15 K.

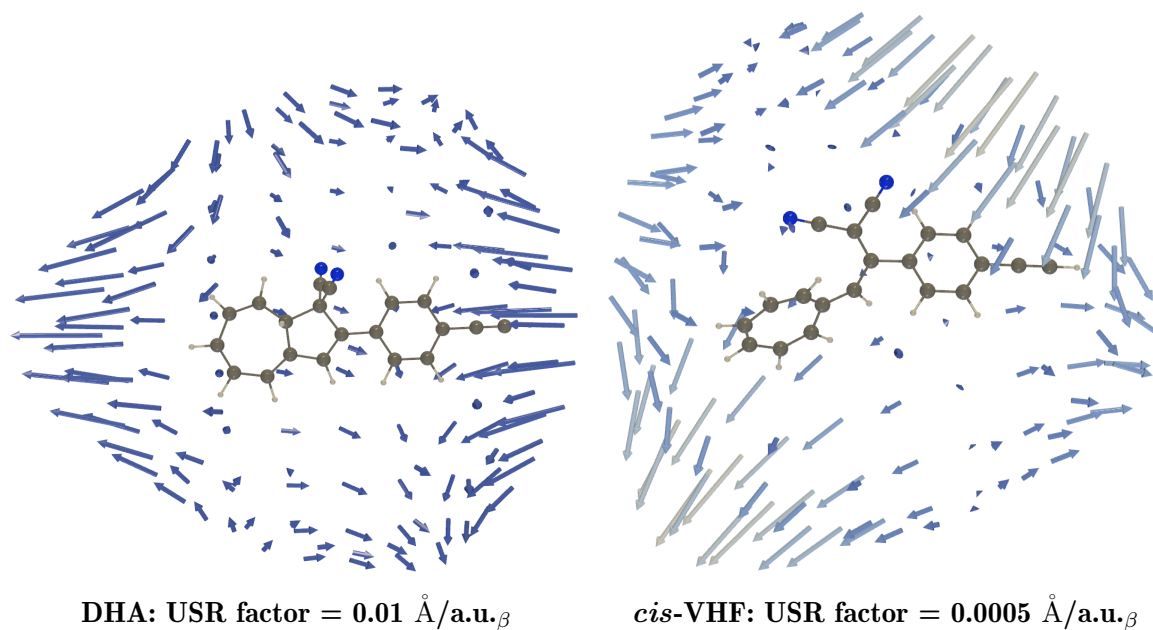


Fig. E.1: Unit sphere representation of the static β of the constitutive units in their most stable conformations as evaluated at the IEF-PCM(acetonitrile)/CPKS/ ω B97X-D/6-311+G(d) level.

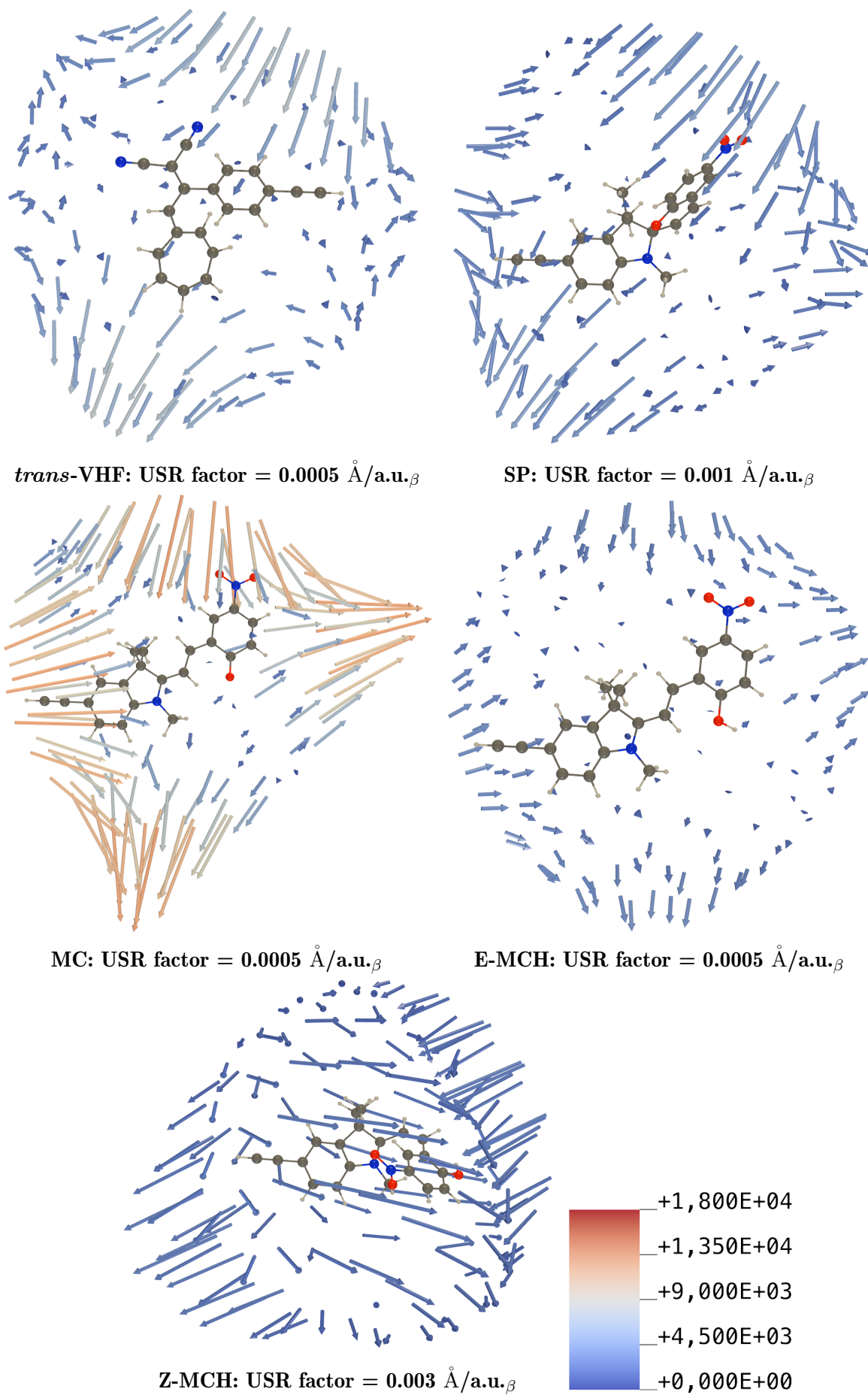


Fig. E.1: Continued from previous page.

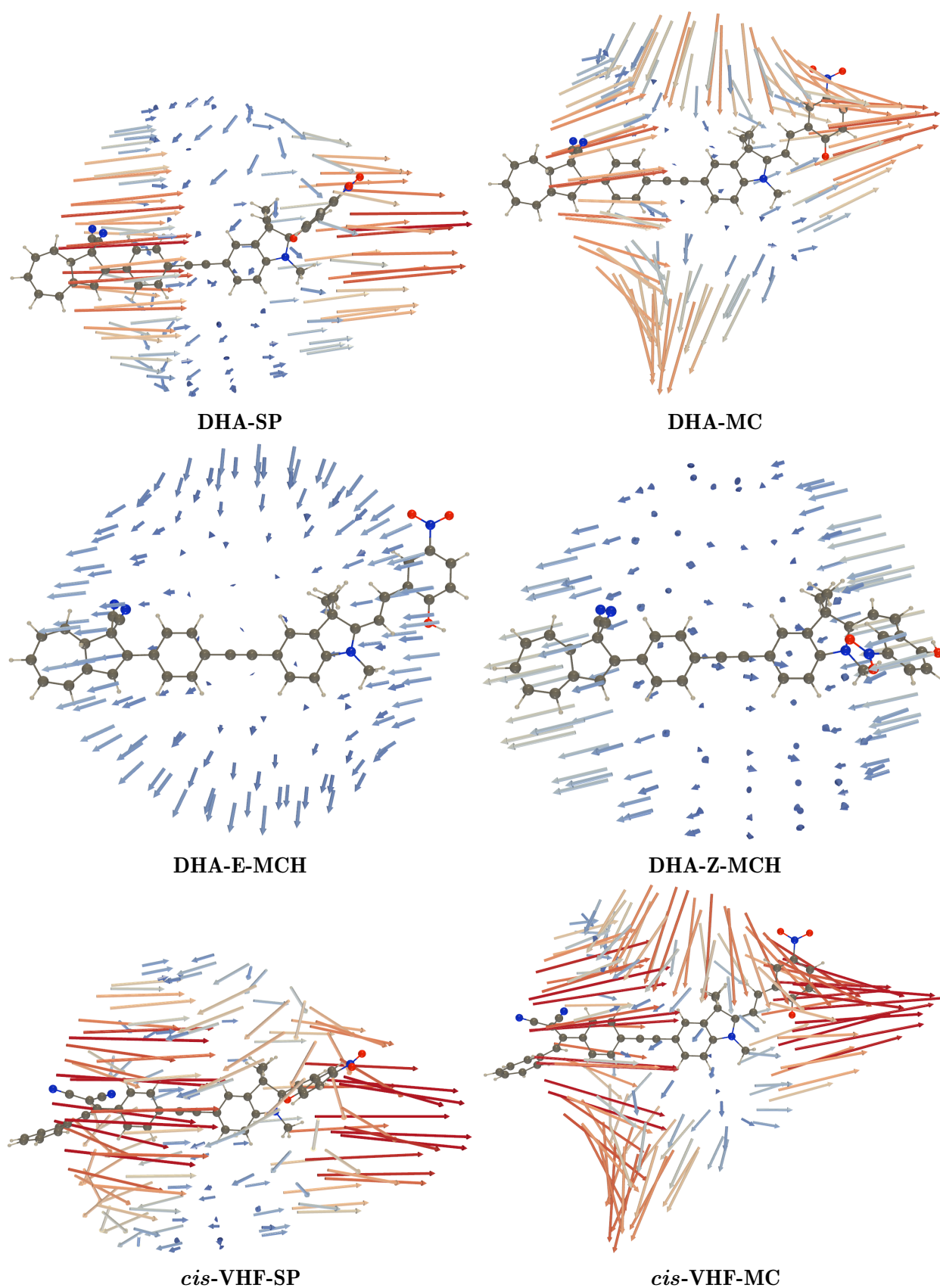


Fig. E.2: Unit sphere representation of the static β of each form of the molecular switch in their most stable conformations as evaluated at the IEF-PCM(acetonitrile)/CPKS/ ω B97X-D/6-311+G(d) level (USR factor = 0.0005 Å/a.u. $_{\beta}$). The color scale is identical as in Appendix E.1.

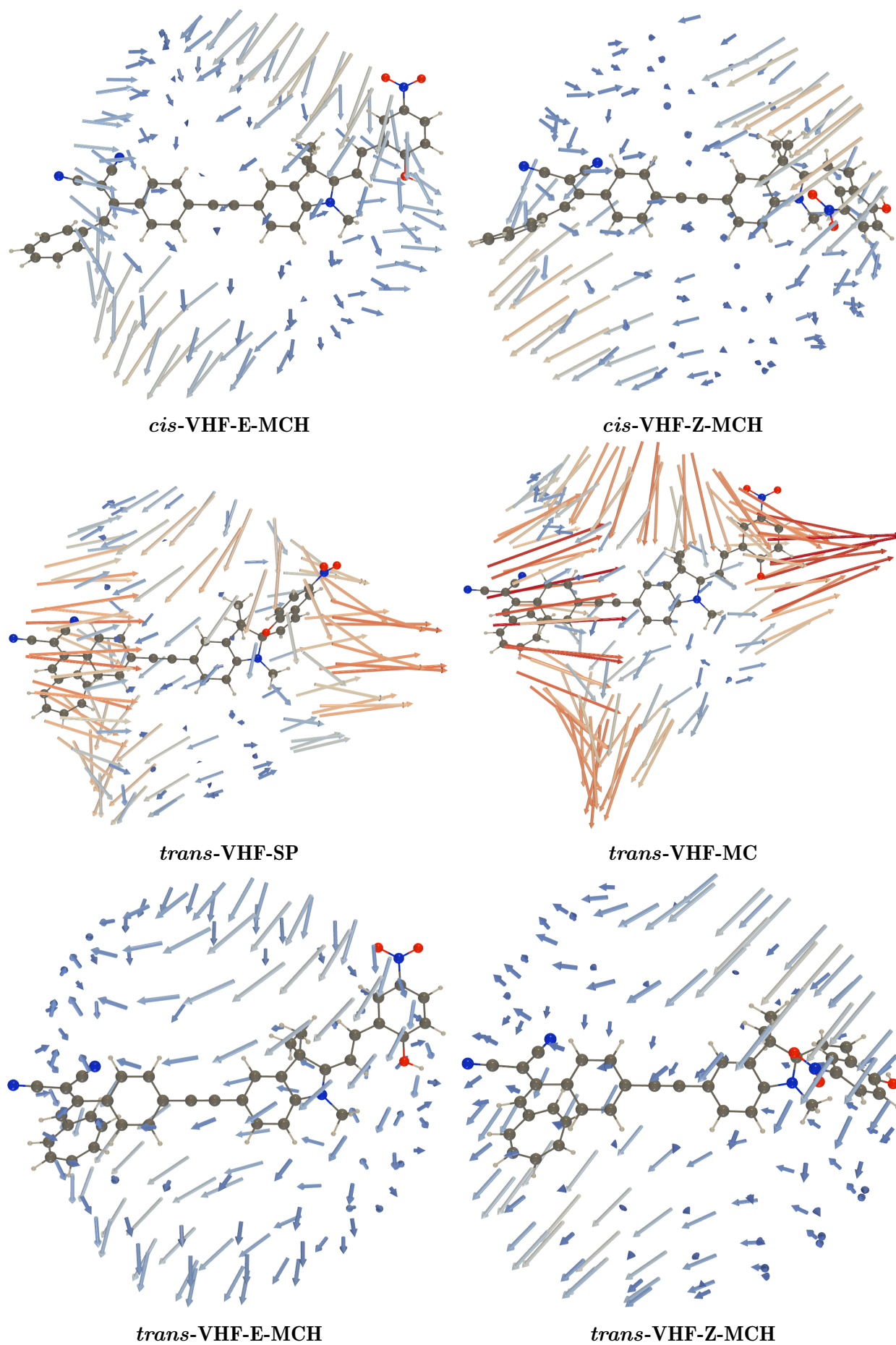


Fig. E.2: Continued from previous page.

E.2 Few-state approximation

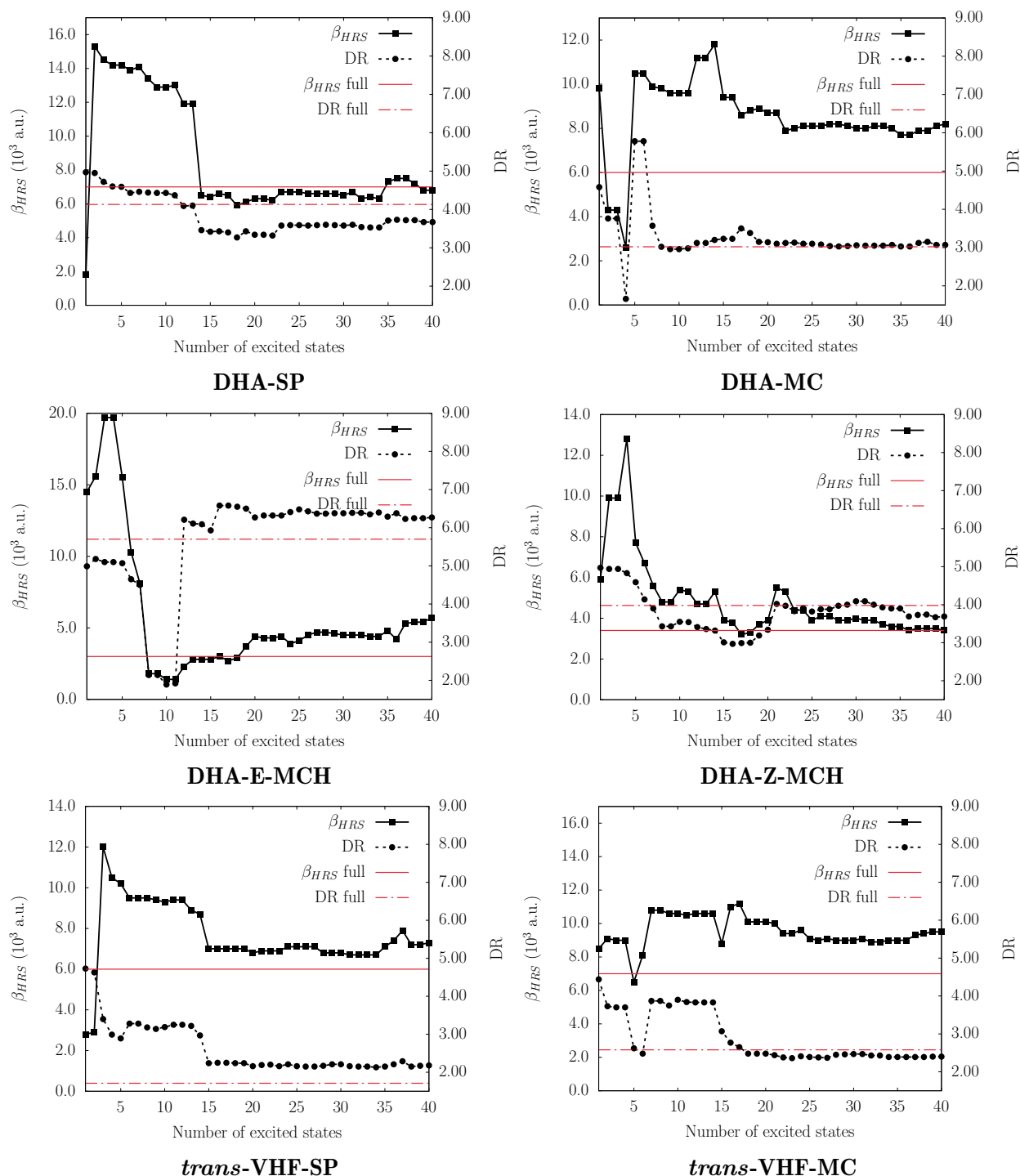


Fig. E.3: Evolutions, as a function of the number of excited states, of the dynamic ($\lambda = 1907$ nm) β_{HRS} and DR for selected forms of the molecular switch in their most stable conformation as evaluated at the SOS/IEF-PCM(acetonitrile)/TDDFT/ ω B97X-D/6-311+G(d) level. The full tensor values are also represented (in red). The fluctuation dipoles are approximated using the Multiwfn software.

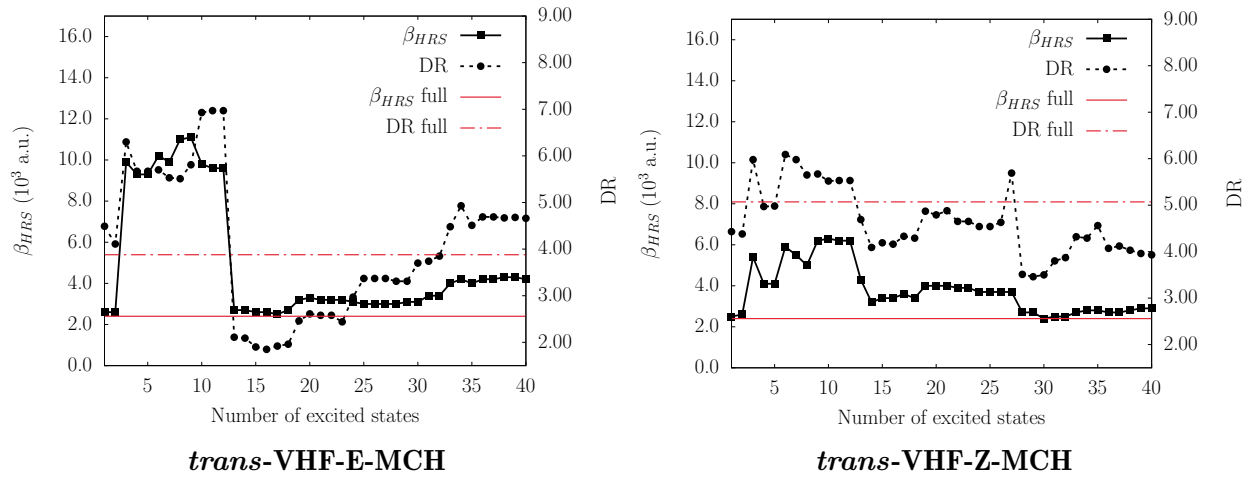


Fig. E.3: Continued from previous page